Abstract

A First Principles Study on Oxide Interfaces

Hanghui Chen
2012

Both theoretically and experimentally, enormous progress has been made toward understanding and controlling materials at the atomic scales. The advances in thin film deposition techniques make it possible to grow artificially designed heterostructures that do not exist in nature. The theoretical developments of *ab initio* calculations combined with the rapid increase of computational capability enable scientists to analyze data, make predictions and even design experiments from numerical simulations.

In this thesis, as a good demonstration, we use Density Functional Theory to investigate structural, electronic and magnetic properties of oxide interfaces. Transition metal oxides are complex materials in which charge, spin, orbital and lattice are all coupled to each other, resulting in many competing phases. Oxide interfaces are more intriguing because unexpected novel phenomena emerge that are absent in both bulk constituents. We study three interesting and representative oxide interfaces. The first is the interface between band insulators $SrTiO_3$ and $LaAlO_3$. A comprehensive investigation of electronic and atomic reconstructions at the interface is presented and different scenarios of formation of two dimensional electron gas at the interface are provided. The second example is the interface between ferroelectrics and manganites. The couplings of ferroelectric polarization to charge, spin and orbital occupancy in manganites are studied in details. Comparisons to existent experiments and predictions for new experiments are presented. The last interface investigated is the one between simple metals and binary oxides. We show that when the interface structure is carefully engineered, a pair of unstable metal-O bonds could induce ferroelectricity in otherwise paraelectrics. If this interfacial ferroelectricity is combined with magnetic insulators, multiferroics can be formed in ultra thin films.

A First Principles Study on Oxide Interfaces

A Dissertation
Presented to the Faculty of the Graduate School
of
Yale University
in Candidacy for the Degree of
Doctor of Philosophy

Hanghui Chen

Dissertation Director: Sohrab Ismail-Beigi

May 2012

Contents

List of Figures

List of Tables

Acknowledgements

acknowledgement

Chapter 1

Introduction

Transition metal oxides exhibit rich and unusual physical properties such as ferroelectricity, magnetism, colossal magnetoresistance and superconductivity (see Fig. 1.1) [1]. The reason that they display complex phenomena is that different degrees of freedom in transition metal oxides, such as charge, spin, orbital and lattice, couple to each other, leading to various competing phases [2]. Though their bulk properties are already intriguing, the interface between two dissimilar transition metal oxides plays host to various electronic or atomic reconstructions, yielding novel properties that are absent in either bulk constituent [3]. During the past decade, with advances in techniques to control thin film growth on atomic scales [4], such as pulsed laser deposition and molecular beam epitaxy, along with breakthroughs in preparing well-defined, single-terminated surfaces [5], oxide heterostructures with an atomically sharp interface can now be routinely prepared in laboratories [6]. A much broader spectrum of possibilities can be anticipated when atomically sharp interfaces between two or more transition metal oxides are formed in artificial heterostructures [7]. A microscopic exploration of interfacial phenomena not only deepens our understanding of basic sciences, but also has new possible applications in electronic devices and technology.

However, conventional theoretical approaches such as model Hamiltonian calculations are usually insufficient to accurately describe transition metal oxide interfaces due to their complexity. For example, various structural distortions, such as Jahn-Teller modes [8], $GdFeO_3$ modes [9], antiferrodistortive modes [10], could coexist at one interface and couple to each other. Model calculations have to first assume what types of distortions are in

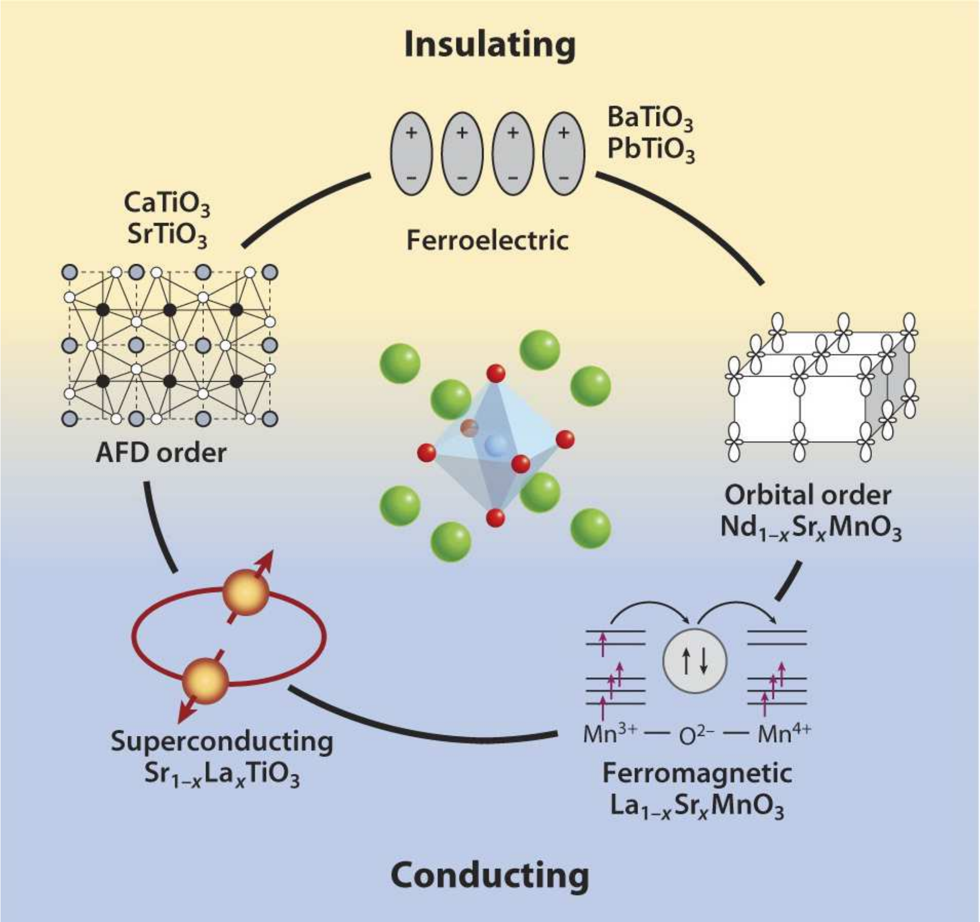

Figure 1.1: **A)** Rich and unusual physical properties of transition metal oxides: from insulating to metallic to superconducting. Phase competition between ferroelectric distortion and oxgen rotations (antiferrodistortive mode) in Ti-based oxides. Phase coexistence of charge ordering and magnetic ordering in Mn-based oxides. Figure is from Ref. [1].

play and introduce unknown fitting parameters for each coupling. Exact solution of those model Hamiltonians is difficult (or impossible) and typically different types of mean-field approximations are employed. In addition, atomic relaxation at the interface could lead to completely new electronic structures that are not derivable from any bulk parameters. At this respect, Density Function Theory (DFT) [11, 12] proves to be a powerful tool to studying the complex phenomena at transition metal oxide interfaces. DFT is a ground state theory of interacting electron systems. With no fitting parameters or *a priori* assumptions, DFT provides reliable predictions of atomic structures, electronic and magnetic properties, as well as phonon spectrums from realistic simulations. Numerous examples of excellent agreement between DFT simulations and experiment measurements not only confirm the accuracy and suitability of DFT for microscopic investigations of physics and chemistry, but also open a new field: theoretical material design [13], which employs DFT simulations to search for proper materials and engineer their interfaces or heterostructures for a specific purpose or function. For transition metal oxide interfaces, DFT has provided invaluable information on new interfacial phenomena and guidance to engineering functional oxide heterostructures. However, DFT has its own problem when handling magnetic properties that originate from localized $3d$ orbitals, which we will dwell on in the last chapter Outlook.

In this thesis, we use Density Functional Theory to investigate three oxide interfaces, each of which displays novel phenomena that are missing in bulk phases. We will demonstrate that DFT not only offers detailed microscopic information to help explain the phenomena, but also predicts new functional properties that should stimulate further experiments.

The first oxide interface is $LaAlO_3/SrTiO_3$. Both $LaAlO_3$ and $SrTiO_3$ are conventional band insulators with band gap 5.6 eV and 3.2 eV, respectively. Depositing a few unit cells of $LaAlO_3$ on TiO_2 terminated $SrTiO_3$ substrates leads to the formation of a high-mobility two dimensional electron gas [14]. In addition to the emergence of unexpected metallic states at the interface, magnetism [15] and superconductivity [16] are also found in experiment. Moreover, the sheet carrier density and mobility [17], as well as the superconducting transition temperature [18], can be modulated by back-gate voltages [19]. Recently, atomic force microscopy (AFM) has been used to "write" and "erase" conductance at the interface [20, 21]. Such a nanoscale switch is a promising candidate for oxide-based electronics. However, despite both intensive theoretical [22] and experimental [23] investigations on the $LaAlO_3/SrTiO_3$ interface, there is still controversy on the origin of the conducting electron gas. We use DFT to simulate the interface and carefully study the electronic and atomic reconstructions and their possible interplay [24, 25]. We also propose a variant of $LaAlO_3/SrTiO_3$ interface to quantum-confine the mobile electrons [26].

The second oxide interface is a ferroelectric/manganite interface [27]. Manganites (i.e. oxide compounds that include manganese) exhibit rich and complicated magnetic phases as well as intriguing colossal magneto resistance [28]. The manganite we focus on in this thesis is $LaMnO_3$, which is an antiferromagnetic Mott insulator. By chemically doping La with Sr, hole carriers are injected into the host material and $La_{1-x}Sr_xMnO_3$ becomes metallic at $x \simeq 0.15$ and ferromagnetic at $x \simeq 0.2$. With the hole doping x further increasing, the manganite is turned into an antiferromagnetic metal at $x \simeq 0.5$. At the ferroelectric/$La_{1-x}Sr_xMnO_3$ interface, due to the polarization of the ferroelectric, surface charges are formed at the interface, which induce screening charges in $La_{1-x}Sr_xMnO_3$. Not only the carrier density is modulated by ferroelectrics, the magnetic ordering could also be changed at the interface, because hole doping sensitively affects the magnetic properties in manganites. In addition, ferroelectrics have strong rumplings in each atomic layer. Such rumplings induce Jahn-Teller distortions at the interface, which could modulate the occupancy of different orbitals [29]. We use DFT to carefully investigate the coupling of ferroelectrics to charge, spin and orbital occupancy in manganites, demonstrating rich new phenomena at oxide interfaces [30, 31].

The last oxide interface is metal/ferroelectric and metal/paraelectric interfaces. Simple electrostatic analysis shows that for realistic electrodes, their finite screening length results in the occurance of depolarization field, which significantly reduces ferroelectric polarization when the size of ferroelectrics can be comparable to the screening length [32]. Recently, it was found that at Pt/$BaTiO_3$ (BaO-terminated) interfaces, the ferroelectric instability of $BaTiO_3$ is enhanced rather than suppressed by a pair of unstable Pt-O bonds [33]. Based on this discovery, we construct a microscopic theory of interfacial bonds [34]. We use DFT to demonstrate that the instability of bonds are mainly related to the giant size of A cation (e.g. Ba^{2+} in $BaTiO_3$) and the mechanism is general and not restricted to perovskite oxides. We take binary oxides (alkaline earth metal) and fluorides (alkaline metal) as examples to show that unstable interfacial bonds could induce ferroelectricity in otherwise “dull” paraelectrics. Furthermore, when electrodes are properly chosen, the magnetic insulator EuO could be turned into a ferroelectric and a novel form of multiferroic can be formed in ultra thin EuO films.

The thesis is organized as follows. Chapter 2 introduces Density Functional Theory, the main tool we use throughout this thesis. We also dicuss some special topics on methodologies. Chapter 3 is devoted to the study of $LaAlO_3$/$SrTiO_3$ interfaces. Chapter 4 focuses on ferroelectric/manganite interfaces. Chapter 5 discusses interfacial ferroelectricity. We finally make comments on the future of oxide interfaces, especially the theoretical challenges, in Chapter 6. In addition, there are three appendices. Appendix A, B and C are related to Chapter 3, Chapter 4 and Chapter 5, respectively. In these appendices, some computational details and theoretical derivations are provided for interested readers.

Chapter 2

Density Functional Theory

2.1 Introduction

Solids are composed of atoms and atoms are composed of interacting nuclei and electrons. Since nuclei are around one thousand times heavier than electrons, we can use the Born-Oppenheimer approximation [35], i.e. treat nuclei as static point charges. This means that instead of a system of dynamic and interacting nuclei and electrons, the nuclei can be frozen out and their positions are treated as parameters, so only the electrons are dynamic. This greatly simplifies the solution of the total interacting problem to one of only interacting electrons moving in the field created by nuclei. Therefore the electronic Hamiltonian of the solid is written as follows:

$$H = T + V_{ee} + V_{ei} \tag{2.1}$$

where T is the kinetic energy of electrons of mass m:

$$T = -\frac{\hbar^2}{2m}\sum_i \nabla_i^2 \tag{2.2}$$

and V_{ee} is the repulsive interaction between electrons:

$$V_{ee} = \frac{1}{2}\sum_{i\neq j}\frac{e^2}{|\mathbf{r}_i - \mathbf{r}_j|} \tag{2.3}$$

and V_{ei} is the attractive interaction between electrons and ions:

$$V_{ei} = \sum_i V_{ion}(\mathbf{r}_i) = -\sum_{iI} \frac{Z_I e^2}{|\mathbf{r}_i - \mathbf{R}_I|} \tag{2.4}$$

and $e > 0$ is the quantum of charge and $\{\mathbf{R}_I\}$ are the positions of fixed nuclei.

The electron density is defined as follows:

$$n(\mathbf{r}) = N \int d\mathbf{r}_2 ... d\mathbf{r}_N |\Psi(\mathbf{r}, \mathbf{r}_2 ... \mathbf{r}_N)|^2 \tag{2.5}$$

where N is the number of electrons and $\Psi(\mathbf{r}, \mathbf{r}_2, ...\mathbf{r}_N)$ is the eigenfuction of H. For the ground state of H, the eigen function is denoted by Ψ_0 and its associated electron density is $n_0(\mathbf{r})$ defined by Eq. (2.5).

2.2 Hohenberg-Kohn theorems

Directly solving the Schrödinger's equation of the solid Hamiltonian Eq. (2.1) is formidable. Hohenberg and Kohn [11] proposed an alternative to the ground state solution. The interacting electrons are moving in the ionic potential created by the nuclei $V_{ion}(\mathbf{r})$:

Theorem I: Up to a trivial additive constant, the ionic potential $V_{ion}(\mathbf{r})$ has a one-to-one correspondence to the *ground state* electron density $n_0(\mathbf{r})$, that is different ionic potentials must have different ground state electron densities.

Proof: By contradiction. Let us assume two ionic potentials $V_{ion}(\mathbf{r})$ and $V'_{ion}(\mathbf{r})$ whose difference is not a constant. Since the Hamiltonians are different (because $V_{ion}(\mathbf{r})$ are different), we have two different ground state wave functions Ψ_0 and Ψ'_0 associated with ground state energies E_0 and E'_0. But both of them lead to the same ground state electron density $n_0(\mathbf{r})$. By definition, we have

$$E_0 = \langle \Psi_0 | H | \Psi_0 \rangle \tag{2.6}$$

$$E'_0 = \langle \Psi'_0 | H' | \Psi'_0 \rangle \tag{2.7}$$

The ground state energy E_0, by variation principle, is the lowest possible energy for any wave functions, and therefore we must have:

$$E_0 = \langle\Psi_0|H|\Psi_0\rangle < \langle\Psi_0'|H|\Psi_0'\rangle = \langle\Psi_0'|H' - (V_{ei}' - V_{ei})|\Psi_0'\rangle = E_0' - \langle\Psi_0'|V_{ei}' - V_{ei}|\Psi_0'\rangle \quad (2.8)$$

The inequality is due to the fact that V_{ei} and V_{ei}' differ in a nontrivial way. However the last term reads:

$$\langle\Psi_0'|V_{ei}' - V_{ei}|\Psi_0'\rangle = \sum_i \langle\Psi_0'|V_{ion}'(\mathbf{r}_i) - V_{ion}(\mathbf{r}_i)|\Psi_0'\rangle = \int d\mathbf{r} n_0(\mathbf{r}) \left(V_{ion}'(\mathbf{r}) - V_{ion}(\mathbf{r})\right) \quad (2.9)$$

Combining Eq.(2.8) and Eq.(2.9), we obtain:

$$E_0 < E_0' - \int d\mathbf{r} n_0(\mathbf{r}) \left(V_{ion}'(\mathbf{r}) - V_{ion}(\mathbf{r})\right) \quad (2.10)$$

Reversing the order of Ψ_0 and Ψ_0' and making use of the fact that Ψ_0 and Ψ_0' lead to the same ground state electron density, we easily get:

$$E_0' < E_0 - \int d\mathbf{r} n_0(\mathbf{r}) \left(V_{ion}(\mathbf{r}) - V_{ion}'(\mathbf{r})\right) \quad (2.11)$$

Adding Eq. (2.10) and Eq. (2.11) leads to the contradiction:

$$E_0 + E_0' < E_0' + E_0 \quad (2.12)$$

Therefore the ionic potential $V_{ion}(\mathbf{r})$ is *uniquely* determined by the ground state electron density $n_0(\mathbf{r})$. Specifying $V_{ion}(\mathbf{r})$ uniquely determines the Hamiltonian H in Eq. (2.1) and thus all the quantities, so all ground-state properties of interest are functionals of $n(\mathbf{r})$, that is $\Psi_0[n(\mathbf{r})]$.

The universal functional is defined as:

$$F[n] = \langle\Psi_0[n]|T + V_{ee}|\Psi_0[n]\rangle \quad (2.13)$$

where T and V_{ee} are defined in Eq. (2.2) and Eq. (2.3), respectively.

Theorem II: For a given ionic potential $V_{ion}(\mathbf{r})$, we define an energy functional $E[n]$

as

$$E[n] = \int d\mathbf{r} n(\mathbf{r}) V_{ext}(\mathbf{r}) + F[n] \tag{2.14}$$

This functional takes its minimum value at the ground state electron density $n_0(\mathbf{r})$ and its value is the ground state energy E_0.

Proof: The proof uses the variational principle and theorem I. For any trial electron density $n(\mathbf{r})$, the variational principle says that:

$$E_0 = E[n_0(\mathbf{r})] = \langle \Psi_0[n_0] | H | \Psi_0[n_0] \rangle \leq \langle \Psi_0[n] | H | \Psi_0[n] \rangle \tag{2.15}$$

The equality sign occurs as $n(\mathbf{r}) = n_0(\mathbf{r})$.

2.3 Kohn-Sham equations

We now map a many-electron interacting system onto a *non-interacting* system with same external (i.e. ionic) potential, but enforce that the two systems have identical ground state electron density. The non-interacting system can be described by single-particle equations and the ground state solution is the corresponding Slater determinant. Following this idea, we can now derive the Kohn-Sham equations [12], which are the basis of Kohn-Sham density functional theory to describe the realistic solid systems.

Given a single-particle description, we can first write out the energy functional Eq. (2.14) explicitly:

$$E[n(\mathbf{r})] = -\frac{\hbar^2}{2m} \sum_i \langle \psi_i | \nabla^2 | \psi_i \rangle + \frac{e^2}{2} \iint d\mathbf{r} d\mathbf{r}' \frac{n(\mathbf{r}) n(\mathbf{r}')}{|\mathbf{r} - \mathbf{r}'|} + E_{xc}[n(\mathbf{r})] + \int d\mathbf{r} n(\mathbf{r}) V_{ion}(\mathbf{r}) \tag{2.16}$$

where the electron density is constructed as:

$$n(\mathbf{r}) = \sum_i |\psi_i(\mathbf{r})|^2 \tag{2.17}$$

Here i refers to single-particle states and the sum is over all the occupied states. $E_{xc}[n(\mathbf{r})]$ is called exchange-correlation functional, which is whatever is left to make Eq. (2.17) exact. Taking functional derivative $\delta E[n(\mathbf{r})]/\delta\psi_i^*(\mathbf{r})$ with the constraint that each $\psi_i(\mathbf{r})$ is normalized to unit leads to:

$$\left(-\frac{\hbar^2}{2m}\nabla^2 + V_{KS}\right)\psi_i(\mathbf{r}) = \epsilon_i\psi_i(\mathbf{r}) \tag{2.18}$$

where $V_{KS}(\mathbf{r})$ is composed of:

$$V_{KS}(\mathbf{r}) = \int d\mathbf{r}'\frac{n(\mathbf{r}')}{|\mathbf{r}-\mathbf{r}'|} + V_{ion}(\mathbf{r}) + V_{xc}(\mathbf{r}) \tag{2.19}$$

The first term is the Hartree potential. The second term is the local ionic potential. The last term is the exchange-correlation potential which is defined as:

$$V_{xc}(\mathbf{r}) = \frac{\delta E_{xc}[n]}{\delta n(\mathbf{r})} \tag{2.20}$$

Once the equations Eq. (2.18-2.20) are solved self-consistently (the solutions are denoted by $\{\tilde{\psi}_i\}$), we obtain the ground state electron density:

$$n_0(\mathbf{r}) = \sum_i |\tilde{\psi}_i(\mathbf{r})|^2 \tag{2.21}$$

and the total ground state energy is given by:

$$E_0 = -\frac{\hbar^2}{2m}\sum_i\langle\tilde{\psi}_i|\nabla^2|\tilde{\psi}_i\rangle + \frac{e^2}{2}\int d\mathbf{r}d\mathbf{r}'\frac{n_0(\mathbf{r})n_0(\mathbf{r}')}{|\mathbf{r}-\mathbf{r}'|} + E_{xc}[n_0] + \int d\mathbf{r}n_0(\mathbf{r})V_{ion}(\mathbf{r}) \tag{2.22}$$

Note that the preceding result for total energy does not include the ion-ion interaction E_{ii}. For a given ion configuration, E_{ii} is just a constant and a mere sum over Coulombic pair repulsions. However, when we move the ions and calculate the forces on ions, we need to take this term E_{ii} into account.

2.4 Exchange-correlation functional

The *exact* form of exchange-correlation functional is unknown. Various approximations have been made. The most widely used approximations in the solid-state calculations are Local Density Approximation (LDA) [12] and Generalized Gradient Approximation (GGA) [36, 37, 38]. We detail LDA in this section, where one models each small region of space around $\mathbf{r}$ as a uniform electron gas at the electron density $n(\mathbf{r})$.

$$E_{xc}[n] \simeq E_{xc}^{\mathrm{LDA}} = \int d\mathbf{r} n(\mathbf{r}) \varepsilon_{xc}(n(\mathbf{r})) \tag{2.23}$$

where $\varepsilon_{xc}(n)$ is the exchange-correlation energy per atom in a uniform density at n. However even $\varepsilon_{xc}(n)$ can not be calculated analytically. Usually we split $\varepsilon_{xc}(n)$ into exchange part and correlation part, i.e.

$$\varepsilon_{xc}(n) = \varepsilon_x(n) + \varepsilon_c(n) \tag{2.24}$$

For a uniform distributed electron gas, using the Hartree-Fock approximation, the exchange energy can be analytically calculated [1]

$$\varepsilon_x(n) = -\frac{3e^2}{4\pi} \left(3\pi^2 n\right)^{1/3} \tag{2.25}$$

The correlation part is more difficult to calculate analytically. In the high density limit ($r_s \ll a_0$), we have the following serial expansion from many body perturbation theory in the unit of Ry:

$$\varepsilon_c(n) = 0.0622 \ln(r_s/a_0) - 0.096 + O(r_s/a_0) \tag{2.26}$$

The most important result is the Ceperley and Alder monte carlo calculations that numerically computed the correlation part to high accuracy. Based on that, Perdue and Zunger further parametrize the $\varepsilon_c(n)$ [36] as

$$\varepsilon_c(n) = \begin{cases} 0.0622 \ln(r_s/a_0) - 0.096 + 0.0040(r_s/a_0) \ln(r_s/a_0) - 0.0232(r_s/a_0) & (r_s < a_0) \\ -0.2846 \left(1 + 1.0529\sqrt{r_s/a_0} + 0.3334(r_s/a_0)\right)^{-1} & (r_s > a_0) \end{cases} \tag{2.27}$$

The exchange-correlation potential of LDA follows from Eq.(2.20):

---

[1] This is the so-called jellium model.

$$V_{xc}^{\text{LDA}}(\mathbf{r}) = \frac{\delta E_{xc}^{\text{LDA}}[n]}{\delta n(\mathbf{r})} = \left(\frac{d[n\varepsilon_{xc}(n)]}{dn} \right) \Big|_{n(\mathbf{r})} \tag{2.28}$$

2.5 Hellmann-Feynman theorem

For a given ion configuration (so that V_{ion} is uniquely determined), the Kohn-Sham equations calculate the self-consistent electron density for the ground state. Now we turn to the question of how to calculate the force on ions. The total energy for the ground state is given by Eq. (2.22). However, since we need to consider the forces on ions, the ion-ion interaction E_{ii} which explicitly depends on the ion positions should be taken into account. The force on the ion I is by definition:

$$F_I = -\frac{\partial}{\partial R_I}(E_0 + E_{ii}) \tag{2.29}$$

The second term is straightforward, though the explicit expression could be complicated. The tricky term is the first one, in which V_{ion} (given by Eq. (2.4)) explicitly depends on R_I but the Kohn-Sham states $\{\tilde{\psi}_i\}$ implicitly depend on the R_I. Therefore when we take the full derivative, we have three contributions:

$$\frac{\partial E_0}{\partial R_I} = \frac{\partial E_0}{\partial R_I}\Big|_{\{\tilde{\psi}_i\}} + \sum_i \int d\mathbf{r} \left\{ \frac{\delta E_0}{\delta \tilde{\psi}_i^*(\mathbf{r})} \frac{\partial \tilde{\psi}_i^*(\mathbf{r})}{\partial R_I} + \frac{\delta E_0}{\delta \tilde{\psi}_i(\mathbf{r})} \frac{\partial \tilde{\psi}_i(\mathbf{r})}{\partial R_I} \right\} \tag{2.30}$$

We can see that the functional derivative $\delta E_0 / \delta \tilde{\psi}_i^*(\mathbf{r})$ gives the Kohn-Sham equations:

$$\frac{\delta E_0}{\delta \tilde{\psi}_i^*(\mathbf{r})} = \left[-\frac{\hbar^2}{2m}\nabla^2 + V_{ion}(\mathbf{r}) + \int d\mathbf{r}' \frac{n(\mathbf{r}')}{|\mathbf{r}-\mathbf{r}'|} + V_{xc}(\mathbf{r}) \right] \tilde{\psi}_i(\mathbf{r}) = \epsilon_i \tilde{\psi}_i(\mathbf{r}) \tag{2.31}$$

The second equality holds because $\{\tilde{\psi}_i\}$ are a set of solutions to the Kohn-Sham equations. By taking the complex conjugate, we obtain:

$$\frac{\partial E_0}{\partial R_I} = \frac{\partial E_0}{\partial R_I}\Big|_{\{\tilde{\psi}_i\}} + \sum_i \int d\mathbf{r} \left\{ \epsilon_i \tilde{\psi}_i(\mathbf{r}) \frac{\partial \tilde{\psi}_i^*(\mathbf{r})}{\partial R_I} + \epsilon_i \tilde{\psi}_i^*(\mathbf{r}) \frac{\partial \tilde{\psi}_i^*(\mathbf{r})}{\partial R_I} \right\} = \frac{\partial E_0}{\partial R_I}\Big|_{\{\tilde{\psi}_i\}} + \sum_i \epsilon_i \frac{\partial}{\partial R_I} \langle \tilde{\psi}_i | \tilde{\psi}_i \rangle \tag{2.32}$$

However, since $\{\tilde{\psi}_i\}$ are normalized, the second term in the last equation disappears. In fact, if we recall that the solutions $\{\tilde{\psi}_i\}$ are those wave functions that minimize the total energy functional, then it is natural that the first derivative of E_0 with respect to $\tilde{\psi}_i$ yields zero. Finally, we have a simple expression for the force on ions:

$$F_I = -\frac{\partial E_0}{\partial R_I}\bigg|_{\{\tilde{\psi}_i\}} - \frac{\partial E_{ii}}{\partial R_I} = -\int d\mathbf{r} n_0(\mathbf{r}) \frac{\partial V_{ion}}{\partial R_I} - \frac{\partial E_{ii}}{\partial R_I} \tag{2.33}$$

Eq.(2.33) is called Hellman-Feynman theorem [39].

2.6 Plane wave basis and pseudopotential

Once the Kohn-Sham equations are subject to periodic boundary conditions, we can identify the quantum i to be $n\mathbf{k}$ where n is the band index and $\mathbf{k}$ is the crystal momentum. The equations now explicitly read:

$$\left(-\frac{\hbar^2}{2m}\nabla^2 + V_{KS}\right)\psi_{n\mathbf{k}}(\mathbf{r}) = \epsilon_{n\mathbf{k}}\psi_{n\mathbf{k}}(\mathbf{r}) \tag{2.34}$$

where V_{KS} is

$$V_{KS}(\mathbf{r}) = V_{ion}(\mathbf{r}) + \int d\mathbf{r}' \frac{n(\mathbf{r}')}{|\mathbf{r} - \mathbf{r}'|} + V_{xc}(\mathbf{r}) \tag{2.35}$$

and the electron density is:

$$n(\mathbf{r}) = \sum_{n\mathbf{k}} |\psi_{n\mathbf{k}}(\mathbf{r})|^2 \tag{2.36}$$

Given an explicit V_{KS}, we now have the practical issue on how to solve these coupled equations *efficiently*.

2.6.1 Plane wave basis

Numerically, in order to solve the Kohn-Sham equations, we need to choose a basis to expand the wave functions $\psi_{n\mathbf{k}}$ and then make a truncation in the basis (so that the calculation time is finite). The most natural choice of basis is plane waves because the Bloch states $\psi_{n\mathbf{k}}$ have a periodic part, which can be expanded naturally in Fourier series.

$$\psi_{n\mathbf{k}}(\mathbf{r}) = e^{i\mathbf{k}\cdot\mathbf{r}} u_{n\mathbf{k}}(\mathbf{r}) = e^{i\mathbf{k}\cdot\mathbf{r}} \sum_{\mathbf{G}} c_{n\mathbf{k}}(\mathbf{G}) \frac{e^{i\mathbf{G}\cdot\mathbf{r}}}{\sqrt{\Omega}} \tag{2.37}$$

where Ω is the volume of the unit cell. Insert Eq. (2.37) into the Kohn-Sham equations Eq. (2.34) to find that $c_{n\mathbf{k}}(\mathbf{G})$ satisfy:

$$\frac{|\mathbf{k}+\mathbf{G}|^2}{2} c_{n\mathbf{k}}(\mathbf{G}) + \sum_{\mathbf{G}'} \tilde{V}_{KS}(\mathbf{G}-\mathbf{G}') c_{n\mathbf{k}}(\mathbf{G}') = \epsilon_{n\mathbf{k}} c_{n\mathbf{k}}(\mathbf{G}) \tag{2.38}$$

where $\tilde{V}_{KS}$ is the Fourier transform of V_{KS}. We need to set up a cutoff to get finite number of $\{\mathbf{G}\}$ basis:

$$\frac{|\mathbf{k}+\mathbf{G}|^2}{2} \leq E_{cut} \tag{2.39}$$

By Eq. (2.38) and Eq. (2.39), though *in principle* any accuracy can be achieved by increasing E_{cut}, *in practice* this method does not work. The reason is as follows: in solids or molecules, the core electrons are tightly bound to the nuclei. Their wave functions change rapidly in the core region and quickly decay away. In order to accurately describe those wave functions, we need many plane waves (i.e. large $\mathbf{G}$) to expand those functions. However, on the other side, those core electrons are so tightly bound to the nuclei that they participate little in the bonding of solids or molecules. Therefore by simply using plane wave basis, we waste a lot of efforts to describe those electrons that do not play important roles in the properties which we are interested in.

2.6.2 Pseudopotentials

As explained in the previous section, the bonding properties of materials largely depend on valence electrons rather than core electrons. As a good approximation, we treat core electrons as immobile entities stuck to nucleus. This is called the frozen core approximation. The distinction of core versus valence electrons is not unambiguous. For heavy elements, the polarization of core electrons could be important for an accurate description of electronic properties and therefore we need to consider more electrons as valence. For example, titanium (Ti) has an argon (Ar) core. The obvious choice of valence is $3d^2 4s^2$.

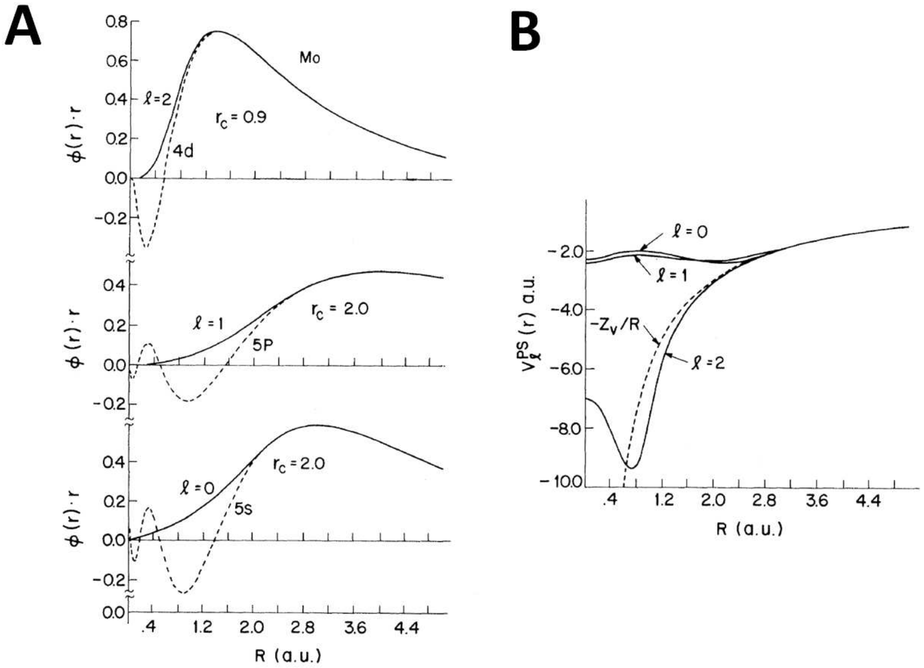

Figure 2.1: **A)** Comparison of all electron and pseudo radial wave functions for Mo. **b)** Mo pseudo-potentials of $l = 0, 1, 2$ channels. The figure is taked from Ref. [40].

However, in order to describe $SrTiO_3$ accurately, $3s^2 3p^6$ electrons also need to be included in the valence. The inclusion of these semi-core states is generally necessary for transition metals.

Even with the frozen core approximation and removal of core electrons from the computation, numerical calculations that involve the raw wave functions of valence electrons could still be very intensive. The reason is that in order to be orthogonal to core electrons, the wave functions of valence electrons must have nodes in the core region, which leads to rapid oscillations. Just like core electrons, describing rapid oscillation of wave functions in the core region needs many plane wave basis, which is the bottleneck for realistic computation. To circumvent this osbstacle, we need to notice that most bonding takes place in the interstitial region rather than in the core region. If we can construct an artificial potential which accurately reproduces the wave functions of valence electrons in the interstitial region but replaces the oscillating part of wave functions by a smooth one, we expect the chemical properties of solids or molecules to be reasonably well described. In fact, this idea is formalized into the so-called pseudo-potentials [41, 42]. Numerous tests show that implementation of pseudo-potential in realistic simulations not only significantly reduces computation cost but also furnishes good description of chemical bonding.

There are quite a few different algorithms concerning the generation of a pseudo-potential, which can be found in the literature [40, 43, 44, 45]. Fig. 2.1 shows the comparison of true and pseudo radial wave functions for Mo as well as the pseudo-potentials for Mo of $l = 0, 1, 2$ channels. Once the pseduo-potential is obtained, the implementation into the Kohn-Sham equations is straightforward. In Eq. (2.18) and Eq. (2.19), the local ionic potential $V_{ion}(\mathbf{r})$ is replaced by a pseudo-potential $V_{ps}(\mathbf{r})$, and every other term remains the same.

2.7 Special topics

In this section, we dwell on some special topics which are normally not covered in the framework of standard DFT-based self-consistent calculations. The techniques in these special topics have been used in this thesis work.

2.7.1 Saw-tooth potential

The standard Kohn-Sham equations Eq. (2.18) and Eq. (2.19) do not include the effect from an external probing field (i.e. electric or magnetic field). However, sometimes we are interested in how an external electric field would modify the electronic properties of isolated systems (i.e. molecules or solid slabs). The inclusion of a constant external electric field into Kohn-Sham Hamiltonian is as follows. Given the external electric field E along the z direction (the choice of direction is for convenience), the interaction of electron with this external field is:

$$U_{ext}(\mathbf{r}) = -e\mathbf{E} \cdot \mathbf{r} \tag{2.40}$$

The notation U is to distinguish from any potential terms V in the standard Kohn-Sham Hamiltonian Eq. (2.19). Such a potential changes monotonically and must violate periodic boundary conditions. In order to satisfy periodic boundary conditions, we need to change

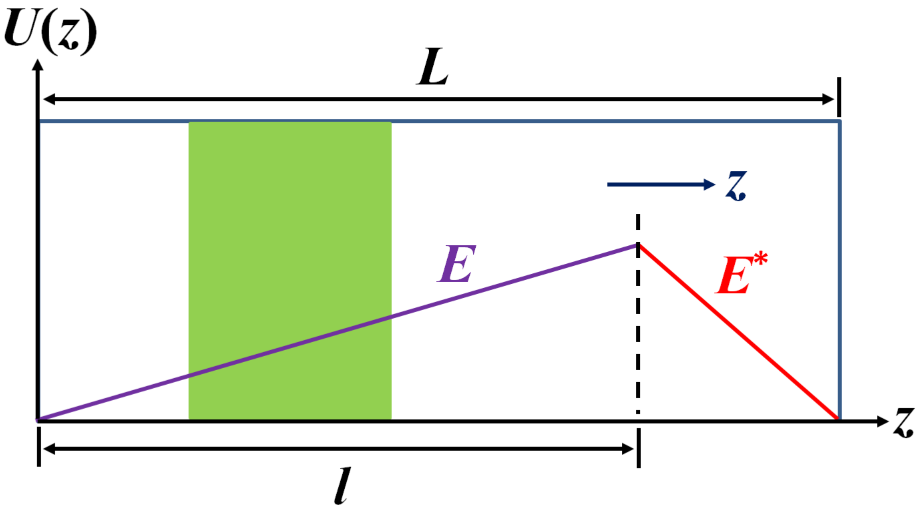

Figure 2.2: Schematics of how to arrange saw-tooth potentials. The shaded green area represents the system under investigation and the empty white space is the vacuum. The purple and red solid lines denote the linear external electric potential and its counterpart. L is the size of the periodic cell along z direction.

the electric field in some irrelevant region (e.g. in the vacuum far from any surfaces), so that the potential restores its original value on the boundary. Fig. 2.2 shows the schematic of how the external electric field changes abruptly in the vaccum and where to properly place the system under investigation. From Fig. 2.2, it is easy to derive that if the desired external electric field E exists from 0 to l, and the size of simulation cell is L along the z direction, then the artificial field E^* is

$$E^* = -E\frac{l}{L} \tag{2.41}$$

The sign indicates that the direction of E^* is always opposite to E.

2.7.2 Berry phase method

The Berry phase method [46] is a theoretical approach to define and calculate the polarization in bulk phases, i.e. under periodic boundary conditions. With Born-Oppenheimer approximation, the ions can be considered as point charges. Compared to valence electrons, they are moving much more slowly and can approximately be considered as static. Valence electrons, on the other hand, have to be treated quantum mechanically. Therefore, we can physically separate the polarization into two parts:

$$\mathbf{P} = \mathbf{P}_{ion} + \mathbf{P}_{ele} \tag{2.42}$$

where $\mathbf{P}_{ion}$ is the ionic contribution and $\mathbf{P}_{ele}$ is the electronic contribution. The ionic contribution is easy to define:

$$\mathbf{P}_{ion} = \frac{e}{\Omega}\sum_I Z_I \mathbf{R}_I \tag{2.43}$$

where $e > 0$ is the elementary charge. Ω is the volume of unit cell. Z_I is the ionic charge of Ith ion. Since the origin of unit cell is arbitrary, the ionic positions $\mathbf{R}_I$ are not unambiguously defined. However, up to an integer multiple of $\mathbf{a}_I$ where $\mathbf{a}_I$ is the lattice vector of unit cell, $\mathbf{P}_{ion}$ is well-defined. The problem is $\mathbf{P}_{ele}$ where the valence electrons are described by Bloch states, rather than as point charges. For a finite system in an infinite space, the polarization is defined as:

$$\mathbf{P} = \int d\mathbf{r}\rho(\mathbf{r})\mathbf{r} \tag{2.44}$$

where $\rho(\mathbf{r})$ is the electron density. The difficulty arises when the system is under periodic boundary conditions. The operator $\mathbf{r}$ is not well-defined in a periodic system.

In order to circumvent the difficulty, we need to give a new definition of $\mathbf{r}$ operator under periodic boundary conditions. For simplicity, we start in one dimension. Consider a periodic system with unit cell of length $L = Na$ where a is the size of unit cell and N is a large integer. We introduce

$$\eta = \exp\left(-2\pi i \frac{x}{L}\right) \tag{2.45}$$

and equivalently

$$x = \frac{iL}{2\pi}\ln(\eta) \tag{2.46}$$

Making use of Eq. (2.46), we *define* the expectation value of x with respect to Bloch states via calculating the expectation value of η which is periodic with the period L. That is:

$$\langle nk|x|n'k'\rangle \triangleq \frac{iL}{2\pi}\ln\left(\langle nk|\eta|n'k'\rangle\right) \tag{2.47}$$

The argument in the logarithmic function is well defined and can be evaluated as follows:

$$\langle nk|\eta|n'k'\rangle = \frac{1}{N}\int_0^{Na} dx u_{nk}^*(x)e^{-ikx}e^{-2\pi ix/L}u_{n'k'}(x)e^{ik'x} \tag{2.48}$$

Noting that $u_{nk}(x)$ has the following periodic property: $u_{nk}(x+a) = u_{nk}(x)$, we can simplify Eq. (2.48) into:

$$\langle nk|\eta|n'k'\rangle = \frac{1}{N}\left(\sum_{m=0}^{N-1} e^{i(k'-k-2\pi/L)ma}\right)\int_0^a dx u_{nk}^*(x)u_{n'k'}(x)e^{i(k'-k-2\pi/L)x} \tag{2.49}$$

Periodic boundary conditions constrain that k can only take values $p\pi/N$ with $p = -N, -N+1, ...N-1$. The parenthesis in Eq. (2.49) is simply:

$$\sum_{m=0}^{N-1} e^{i(k'-k-2\pi/L)ma} = N\delta_{k',k+2\pi/L} \tag{2.50}$$

Finally, we obtain:

$$\langle nk|\eta|n'k'\rangle = \delta_{k',k+2\pi/L}\int_0^a dx u_{nk}^*(x)u_{n'k'}(x)e^{i(k'-k-2\pi/L)x} \tag{2.51}$$

and after imposing Kronecker delta,

$$\langle nk|\eta|n'k'\rangle = \delta_{k',k+2\pi/L}\langle u_{nk}|u_{n'k+2\pi/L}\rangle \tag{2.52}$$

In the limit of large L (i.e. large N), we can expand $u_{nk+2\pi/L}$ into:

$$u_{nk+2\pi/L} = u_{nk} + \frac{\partial}{\partial k}u_{nk}\cdot\frac{2\pi}{L} + O\left(\frac{1}{L^2}\right) \tag{2.53}$$

Inserting Eq. (2.52) and Eq. (2.53) back into Eq. (2.47) and with a little algebra, we find:

$$\langle nk|x|n'k'\rangle \triangleq \delta_{k',k+2\pi/L}\cdot\frac{iL}{2\pi}\ln\left(1 + \frac{2\pi}{L}\langle u_{nk}|\frac{\partial}{\partial k}u_{n'k}\rangle\right) \tag{2.54}$$

Taking into account that $\ln(1+t) \simeq t$ as $|t| \ll 1$, we can further simplify Eq. (2.54) into:

$$\langle nk|x|n'k\rangle \triangleq \delta_{k',k+2\pi/L} \cdot i\langle u_{nk}|\frac{\partial}{\partial k}u_{n'k}\rangle \tag{2.55}$$

As $L \to \infty$, the difference between k and k' becomes neglegible and Eq. (2.55) formally turns into:

$$\langle nk|x|n'k\rangle \triangleq i\langle u_{nk}|\frac{\partial}{\partial k}u_{n'k}\rangle \tag{2.56}$$

Eq. (2.56) is the definition of x operator expectation value with respect to Bloch states. The right hand side of Eq. (2.56) can be calculated within the density function theory by sampling a very dense k point along the direction of polarization. In three dimensions, Eq. (2.56) is straightforwardly generalized into:

$$\langle n\mathbf{k}|\mathbf{r}|n'\mathbf{k}\rangle \triangleq i\langle u_{n\mathbf{k}}|\nabla_{\mathbf{k}}u_{n'\mathbf{k}}\rangle \tag{2.57}$$

In practice, however, one uses the more pragmatic equation Eq. (2.52) and takes the logarithm. By making L larger, convergence is achieved to the infinite periodic system.

2.7.3 Hubbard U and LDA+U

Though the local density approximation (LDA) and the local spin density approximation (LSDA) have achieved great success in describing the electronic properties of s and p orbitals, they have found to be insufficient to correctly predict the electronic and magnetic properties of localized electrons, such as those occupying d and f orbitals. In order to improve LDA or LSDA, we need to design a new exchange correlation functional which includes some corrections to the standard LDA exchange correlation functional. The most common correction is an onsite Hubbard-like interaction [47, 48].

$$E_{\mathrm{LDA}+U}[n(\mathbf{r})] = E_{\mathrm{LDA}}[n(\mathbf{r})] + E_U[n^{i\sigma}_{mm'}] \tag{2.58}$$

where i labels the atom and m refers to the localized orbitals on atom i. $n^{i\sigma}_{mm'}$ is defined as:

$$n^{i\sigma}_{mm'} = \langle im\sigma|\hat{\rho}|im'\sigma\rangle = \sum_{n\mathbf{k}} f_{n\mathbf{k}}\langle im\sigma|n\mathbf{k}\rangle\langle n\mathbf{k}|im'\sigma\rangle \tag{2.59}$$

where $f_{n\mathbf{k}}$ is the occupancy of Bloch state $|n\mathbf{k}\rangle$. In the rotationally invariant scheme, $E_U[n^{i\sigma}_{mm'}]$ is as follows:

$$E_U[n^{i\sigma}_{mm'}] = \frac{U}{2}\sum_{i,\sigma}\sum_{m}\left[n^{i\sigma}_{mm} - \sum_{m'} n^{i\sigma}_{mm'}n^{i\sigma}_{m'm}\right] \tag{2.60}$$

We define an occupancy matrix $\mathbf{n}^{i\sigma}$. Eq. (2.58) can be formally simplified into:

$$E_U[\mathbf{n}^{i\sigma}] = \frac{U}{2}\sum_{i,\sigma}\mathrm{Tr}\left[\mathbf{n}^{i\sigma}(1-\mathbf{n}^{i\sigma})\right] \tag{2.61}$$

Diagonalizing the matrix $\mathbf{n}^{i\sigma}(1-\mathbf{n}^{i\sigma})$ leads to:

$$\mathbf{n}^{i\sigma}\mathbf{v}^{i\sigma}_{\mu} = \lambda^{i\sigma}_{\mu}\mathbf{v}^{i\sigma}_{\mu} \tag{2.62}$$

where $\lambda^{i\sigma}_{\mu}$ and $\mathbf{v}^{i\sigma}_{\mu}$ are eigenvalues and eigenvectors, respectively. Since $\lambda^{i\sigma}_{\mu}$ are the eigenvalues of an occupancy matrix, we have the following constraints:

$$0 \le \lambda^{i\sigma}_{\mu} \le 1 \tag{2.63}$$

The Hubbard correction can then be rewritten as:

$$E_U[\mathbf{n}^{i\sigma}] = \frac{U}{2}\sum_{i,\sigma}\sum_{\mu}\left[\lambda^{i\sigma}_{\mu}\left(1-\lambda^{i\sigma}_{\mu}\right)\right] \tag{2.64}$$

Because of Eq. (2.63), the Hubbard correction is non-negative. which means a penalty is exerted on partial occupancy of the localized orbitals. Finally, let us apply Janak theorem [49] to Eq. (2.64): The Kohn-Sham single-particle eigenvalues can be obtained through the derivative of Eq. (2.64) with respect to the occupancy $f_{n\mathbf{k}}$:

$$\epsilon_{n\mathbf{k}} = \frac{\partial E_{\mathrm{LDA}+U}}{\partial f_{n\mathbf{k}}} = \langle n\mathbf{k}|H^{\mathrm{LDA}}|n\mathbf{k}\rangle + \sum_{i,\sigma}\sum_{\mu} U\left(\frac{1}{2}-\lambda^{i\sigma}_{\mu}\right)\frac{\partial\lambda^{i\sigma}_{\mu}}{\partial f_{n\mathbf{k}}} \tag{2.65}$$

Note that $\lambda^{i\sigma}_{\mu}$ has a similar definition of $n^{i\sigma}_{mm'}$ as in Eq. (2.59):

$$\lambda_{\mu}^{i\sigma} = \langle i\mu\sigma|\hat{\rho}|i\mu\sigma\rangle = \sum_{n\mathbf{k}} f_{n\mathbf{k}} \langle i\mu\sigma|n\mathbf{k}\rangle\langle n\mathbf{k}|i\mu\sigma\rangle \tag{2.66}$$

Therefore we have:

$$\frac{\partial \lambda_{\mu}^{i\sigma}}{\partial f_{n\mathbf{k}}} = \langle i\mu\sigma|n\mathbf{k}\rangle\langle n\mathbf{k}|i\mu\sigma\rangle = |\langle i\mu\sigma|n\mathbf{k}\rangle|^2 \tag{2.67}$$

Combining everything, we obtain:

$$\epsilon_{n\mathbf{k}} = \frac{\partial E_{\mathrm{LDA}+U}}{\partial f_{n\mathbf{k}}} = \langle n\mathbf{k}|H^{\mathrm{LDA}}|n\mathbf{k}\rangle + \sum_{i,\sigma}\sum_{\mu} U\left(\frac{1}{2} - \lambda_{\mu}^{i\sigma}\right)|\langle i\mu\sigma|n\mathbf{k}\rangle|^2 \tag{2.68}$$

We can see that the Hubbard correction lowers the energy of states occupying the localized manifold and raises those not occupying them: completely filled and complete empty ones are lowered and raised by $U/2$, respectively, which is a total splitting of mimicking upper and lower Hubbard bands.

2.7.4 Self-consistent linear response theory of Hubbard U

In this section, we introduce an approach to calculate Hubbard U based on self-consistent linear response theory [48]. Within a supercell calculations, we turn on some perturbations (specified below) on atom site i (here for simplicity, we assume single localized orbital per site, therefore the quantum number m is omitted) and the self-consistent U associated with site i can be calculated as follows:

$$U = -\left(\chi^{-1} - \chi_0^{-1}\right)_{ii} \tag{2.69}$$

where χ_0 and χ are understood as matrices. Each of their entry is defined as:

$$\chi_{ij} = \left.\frac{\partial^2 E}{\partial \alpha_i \alpha_j}\right|_{\alpha=0} \tag{2.70}$$

$$\chi_{ij}^{0} = \left.\frac{\partial^2 E^{\mathrm{KS}}}{\partial \alpha_i \alpha_j}\right|_{\alpha=0} \tag{2.71}$$

where

$$E[\{\alpha_i\}] = \min_{n(\mathbf{r})} \{E^{\mathrm{KS}}[n(\mathbf{r})]\} + \sum_i \alpha_i n_i \tag{2.72}$$

$$E^{\mathrm{KS}}[\{\alpha_i\}] = \min_{n(\mathbf{r})} \left\{ E^{\mathrm{KS}}[n(\mathbf{r})] + \sum_i \alpha_i n_i \right\} \tag{2.73}$$

where n_i is the occupation of localized orbital on site i and α_i is the corresponding prefactor. $\alpha_i n_i$ is the perturbation we make on site i, which changes the onsite potential of site i by α_i. The difference between $E[\{\alpha_i\}]$ and $E^{\mathrm{KS}}[\{\alpha_i\}]$ is that for a given structure, Eq. (2.72) is the total energy with perturbations added but the charge self-consistency is not allowed. Eq. (2.73) is the total energy with perturbations added and the self-consistency is re-achieved after electrons are relaxed. The Hubbard U is the cost of double occupancy on a site including screening effects. Modifying α_i changes the occupancy n_i of site i since it changes the local potential for electrons and thus it is sensible that U should be obtainable by derivatives of energy versus the α. However, there are effects of changing α that are not related to screening or double occupancy and must be subtracted off: for example, changing the onsite potential also modifies the bonding of the site with neighboring atoms and this changes the n_i as well. Those effects need to be subtracted out from Hubbard U and hence we have Eq. (2.69).

2.8 Computation codes

In this section, I give a brief introduction to the codes that are used throughout my thesis.

2.8.1 Quantum ESPRESSO package

The density functional theory calculations in my thesis are performed using the software package Quantum ESPRESSO[2], which stands for *opEn Source Package for Research in Electronic Structure, Simulation, and Optimization.* It is freely available to researchers around the world under the terms of the GNU General Public License. The package includes functions such as self-consistent calculations and atomic relaxation (pw.x), post-processing (pp.x), atomic-projection (projwfc.x), phonon calculation (ph.x) and Wannier

---

[2] http://www.quantum-espresso.org/

generation (wannier90.x).

Quantum ESPRESSO is an initiative of the DEMOCRITOS National Simulation Center(Trieste) and SISSA (Trieste), in collaboration with CINECA National Supercomputing Center in Bologna, Ecole Polytechnique Fdrale de Lausanne, Universit Pierre et Marie Curie, Princeton University, Massachusetts Institute of Technology, and Oxford University. Courses on modern electronic-structure theory with hands-on tutorials on the Quantum ESPRESSO codes are offered on a regular basis in developed as well as devoloping countries, in collaboration with the Abdus Salam International Centre for Theoretical Physics in Trieste.

2.8.2 USPP pseudopotential generator

Throughout my thesis, the pseudo potentials are ultrasoft pseudo potentials (USPP)[3]. The USPP generator is developed by Professor David Vanderbilt's group at Rutgers University. The latest version is USPP-736. All the pseudo potentials I use are generated with the local density approximation.

---

[3] http://www.physics.rutgers.edu/ dhv/uspp/

Chapter 3

$LaAlO_3/SrTiO_3$ Interfaces and Their Variants

3.1 Introduction

With the advance of techniques to control thin film growth on the atomic scale, the study of epitaxial oxide heterostructures is a rapidly developing area of materials science [4]. Due to the ability to produce a well-defined single terminated substrate surfaces [5], interfaces that are nearly atomically sharp can be formed. In many cases, the properties of these interfaces turn out to be much richer than those of the bulk constituents. One of the most interesting examples is the (001) interface between $LaAlO_3$ (LAO) and $SrTiO_3$ (STO), both of which are conventional band insulators in the bulk. Among the intriguing phenomena observed at this interface is the presence of a high-mobility quasi two-dimentional electron gas [14], which is sensitive to the $LaAlO_3$ film thickness on the nanoscale [19, 15, 50], and can be tuned via an external field [19, 18]. In addition, both magnetism [51] and superconductivity [16] have been observed at $LaAlO_3/SrTiO_3$ interfaces.

Due to these interface properties, the $LaAlO_3/SrTiO_3$ system shows great promise for the development of novel applications in nano-scale oxide electronics [20, 21]. However, though significant efforts have been made theoretically [52, 53, 54, 55, 56, 9, 57] and experimentally [58, 59, 60, 61, 62, 63, 64], the origin of the new phases emerging at the $LaAlO_3/SrTiO_3$ interface is still elusive. In part, this is due to the fact that more than one mechanism may play a role in determining the behavior, and furthermore, the dominant mechanism can depend on external or growth conditions [65].

Generally speaking, we can divide the driving mechanisms into two categories: electronic reconstructions and atomic reconstructions. For ideal heterostructures, electronic reconstructions are believed to play the dominating role in the formation of the two-dimensional electron gas, known as the "polar catastophe" mechanism. This mechanism is a direct result of the charge discontinuity that occurs at an abrupt interface between a nonpolar ($SrTiO_3$) and a polar ($LaAlO_3$) material. Both materials are perovskite oxides with an ABO_3 structure that forms alternating planes of AO and BO_2 stacked along the (001) direction. Consequently, there are two types of $LaAlO_3/SrTiO_3$ interfaces along this direction: TiO_2/LaO (known as the n-type interface) and SrO/AlO_2 (the p-type interface) [14, 66]. In the ionic limit, $SrTiO_3$ is composed of charge neutral atomic layers $(SrO)^0$ and $(TiO_2)^0$, while $LaAlO_3$ consists of positively charged $(LaO)^+$ and negatively charged $(AlO)^-$ atomic layers. When stoichiometric $LaAlO_3$ is grown epitaxially on $SrTiO_3$ along the (001) direction, an internal electric field directed from $(LaO)^+$ to $(AlO_2)^-$ is formed through the $LaAlO_3$, resulting in a potential difference that, mathematically, diverges with increasing $LaAlO_3$ thickness. In reality, to offset the diverging potential, an electronic reconstruction is expected to occur, with electrons transferring from the film surface (or a p-type interface) to the n-type interface. This polar catastrophe mechanism [14, 66] has been confirmed in density functional theory (DFT) calculations [57, 24, 67, 68] and might be responsible for the presence of the two-dimensional electron gas at the atomically sharp n-type interface (i.e., one with no defects).

However, the polar catastrophe mechanism alone can not explain all of the electronic properties of the $LaAlO_3/SrTiO_3$ interface, such as the observed confinement of the transferred electrons within several nanometers of the n-type interface [69]. We show [24, 26] that the electrons are bound to the n-type interface as a result of the chemical environment of the interface, which produces a large hopping matrix element between La and Ti.

Some experimental observations even contradict the predictions of pure electronic reconstructions. For example, the polar catastrophe mechanism predicts the coexistence of electrons at the interface and holes on the surface above the critical thickness [57, 24].

However, so far we are still lacking definitive evidence of surface holes in transport measurements. Theoretical predictions of the critical thickness for the reconstruction based on density functional theory (DFT) calculations place it at 6 unit cells of $LaAlO_3$ [57, 67, 26], once one takes into account the DFT underestimation of the $SrTiO_3$ band gap. Experimentally, the insulating-to-metallic transition occurs only at 4 unit cells of $LaAlO_3$ [19, 70]. More importantly, recent x-ray photoemission measurements [71] fail to detect the internal polar field through $LaAlO_3$, casting doubt on the polar catastrophe mechanism. On the other hand, various experiments [72, 60, 61, 58, 73] show that atomic reconstructions, such as cation intermixtures and oxygen vacancies, do exist at $LaAlO_3/SrTiO_3$ interfaces and could significantly affect the electronic properties of the system [54, 55, 74, 75].

Here we present studies on both electronic and atomic reconstructions of $LaAlO_3/SrTiO_3$ interfaces. We use both DFT and phenomenological modeling to provide a detailed and complete picture of the electronic reconstruction at ideal $LaAlO_3/SrTiO_3$ interfaces. We predict the behavior of the sheet carrier density as a function of the $LaAlO_3$ thickness by constructing a continuous model which approximates the $LaAlO_3$ as a homogeneous media. We also use both DFT and model calculations to give a simple yet quantitative picture of the external field effect that has been experimentally realized at the n-type interface [19, 18]. In addition, we propose a new class of quantum well systems, based on the polar catastrophe mechanism, at which the spatial extent of the two-dimensional electron gas can be manually controlled. On the other hand, we also study various important atomic reconstructions at the $LaAlO_3/SrTiO_3$ interface. The defects we focus on are either experimentally observed or potentially relevant to the origin of conducting electron gas. For each type of defect, we use DFT to find the most thermodynamically stable configuration and compare its effects on the pristine structure. We aim to find those atomic reconstructions which are more favorable thermodynamically than pure electronic reconstructions and to provide different scenarios for conducting electron gas formation at the interface other than the polar catastrophe mechanism.

3.2 Computational Details

Our calculations are performed using density functional theory within the *ab initio* supercell plane-wave approach [76], with the code PWscf in the Quantum-ESPRESSO package [1]. We employ the local density approximation (LDA) [12] and ultrasoft pseudopotentials [45], which include semi-core states in Sr, Ti and La. The reference configurations of the pseudopotentials are: Sr $4s^2 4p^6 5s^2$ ($r_c^s = 2.0a_0, r_c^p = 1.8a_0$), Ti $3s^2 3p^6 3d^1 4s^2$ ($r_c^s = r_c^p = r_c^d = 1.8a_0$), La $5s^2 5p^6 5d^1 6s^{1.5} 6p^{0.5}$ ($r_c^s = r_c^d = 2.2a_0, r_c^p = 2.0a_0$), Al $3s^2 3p^1$ ($r_c^s = 1.8a_0, r_c^p = 1.82a_0$) and O $2s^2 2p^4$ ($r_c^s = r_c^p = 1.3a_0$), where a_0 is the Bohr radius. The plane wave basis energy cutoff and charge cutoff are 30 Ry and 180 Ry, respectively. We use a Gaussian smearing width of 5 mRy when sampling the Brillouin zone. The k-grid sampling of the Brillouin zone is $10 \times 10 \times 1$ where the z-axis is orthogonal to the interface. The convergence of the total energy and total charge density has been checked with k-grids of up to $20 \times 20 \times 1$. Periodic copies are separated by ∼15 Å of vacuum. We also extend the vacuum to 30 Å to check the convergence. The effect of the artifical electric fields in the vacuum due to the periodic boundary condition, which turns out to be quite small, is discussed in Appendix A.2.1. The force convergence threshold is 26 meV/Å. In some key results we reduce the threshold to 13 meV/Å to check the convergence.

In all our calculations, the interfaces are along the (001) direction so that the z axis is perpendicular to the interface. The x and y directions of the simulation cell are subject to periodic boundary conditions and their lengths are fixed to the theoretical lattice constant of $SrTiO_3$ $a = 3.85$ Å (1.5% smaller than the experimental value). The atomic coordinates are relaxed [2] until every force component is smaller than the convergence threshold. The detailed configurations for different calculations are specified in each section below.

3.3 Electronic reconstructions: DFT results

In this section, we systematically present the DFT-LDA results of electronic reconstructions at $LaAlO_3/SrTiO_3$ interfaces.

---

[1] See http://www.quantum-espresso.org

[2] Some atoms are fixed in order to simulate the bulk-like substrate. This is specified in each section.

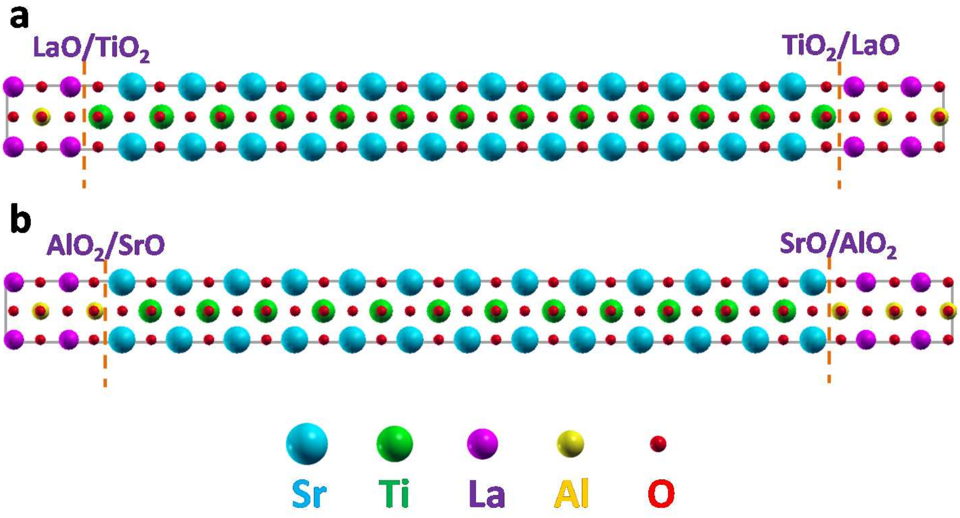

Figure 3.1: Schematics of symmetric superlattices. **a)** The double n-type superlattice. **b)** The double p-type superlattice. The interface is highlighted by the dashed line.

3.3.1 Symmetric double n-type and p-type superlattices

The simplest approach to studying the n-type or p-type $SrTiO_3/LaAlO_3$ interface is to use a symmetric superlattice approach [52, 53, 54, 55, 77, 78, 56, 79, 9], as exemplified by Fig. 3.1, which shows a simulation cell without vacuum in which a number of $SrTiO_3$ unit cells are adjacent to a number of $LaAlO_3$ unit cells and periodic boundary conditions are imposed. Therefore, a non-stoichiometric supercell contains two identical $SrTiO_3/LaAlO_3$ interfaces: *e.g.* in Fig. 3.1a, we have an additional TiO_2 layer in $SrTiO_3$ and an additional LaO layer in $LaAlO_3$, and in Fig. 3.1b, there is an additional SrO layer in $SrTiO_3$ and an additional AlO_2 in $LaAlO_3$. In this way, the superlattice contains two n-type interfaces (TiO_2/LaO) or two p-type interfaces (SrO/AlO_2).

The advantage of the superlattice approach is that no vacuum is needed in the simulation cell, making computation easier. However, due to the imposed symmetry and non-stoichiometry of the $LaAlO_3$ film, this geometry does not result in a polar field, so the evolution of the polar catastrophe can not be modeled. In addition, the non-stoichiometry of the $LaAlO_3$ also imposes a fixed carrier doping: in the ionic limit, an LaO (AlO_2) layer has a charge of +1 (-1), and there is one extra electron (hole) present in the conduction (valence) band of $LaAlO_3$, which is shared evenly by the two interfaces. Therefore each interface is doped by 0.5 electrons (n-type) or 0.5 holes (p-type) per two-dimensional unit cell. These values are precisely those needed to fully compensate the polar field of $LaAlO_3$ [66], so the symmetric supercell approach is equivalent to studying the properties of the interfaces when the $LaAlO_3$ film is very thick (infinite thickness limit).

We briefly present results on the symmetric interfaces and highlight some key observations and questions that we will answer in later sections. We show in Fig. 3.2a the xy-plane integrated *conduction* electron density for the double n-type superlattice, and in Fig 3.2b the hole density for the double p-type superlattice. The method of calculation of these densities is detailed in Appendix A.1. The integrated densities are 0.49 electrons per n-type interface and 0.49 holes per p-type interface, showing that the ionic picture for $LaAlO_3$ is highly accurate, and that one should expect 0.5 electrons (holes) at the fully compensated n-type (p-type) interface for very thick $LaAlO_3$ films.

The density profiles in Fig. 3.2 display an interesting asymmetry. One can characterize the electrons in the double n-type system as being bound to the interface. As the figure shows, they are confined in the $SrTiO_3$, with the density decreasing away from the interface. On the other hand, in the double p-type system, the holes reside in both the $LaAlO_3$ and $SrTiO_3$, do not show a strong preference for the interface itself, and have a slightly higher amplitude in the $LaAlO_3$.

Our calculated band offsets place the $LaAlO_3$ valence band maximum $\simeq 0.1$ eV above the $SrTiO_3$ valence band maximum (p-type) and the $LaAlO_3$ conduction band minimum ~ 2 eV above the $SrTiO_3$ conduction band minimum (n-type) [55, 53]. *A priori*, one would expect that any introduced carriers would occupy the most energetically favorable band edge available, *i.e.* holes would migrate to the $LaAlO_3$ valence band edge and electrons to the $SrTiO_3$ conduction band edge. Furthermore, the minimization of kinetic energy would lead to a relatively uniform distribution of carriers. In Fig. 3.2, we see that, overall, the holes prefer to be in the $LaAlO_3$ at the p-type interface, while the electrons reside in $SrTiO_3$ at the n-type interface. For the p-type interface, the small value of the band offset and the large hole density result in some "leakage" into the $SrTiO_3$ valence band states.

However, the binding of the electrons at the n-type interface cannot be explained by the above arguments. As no polar fields are present in this system to create a potential that

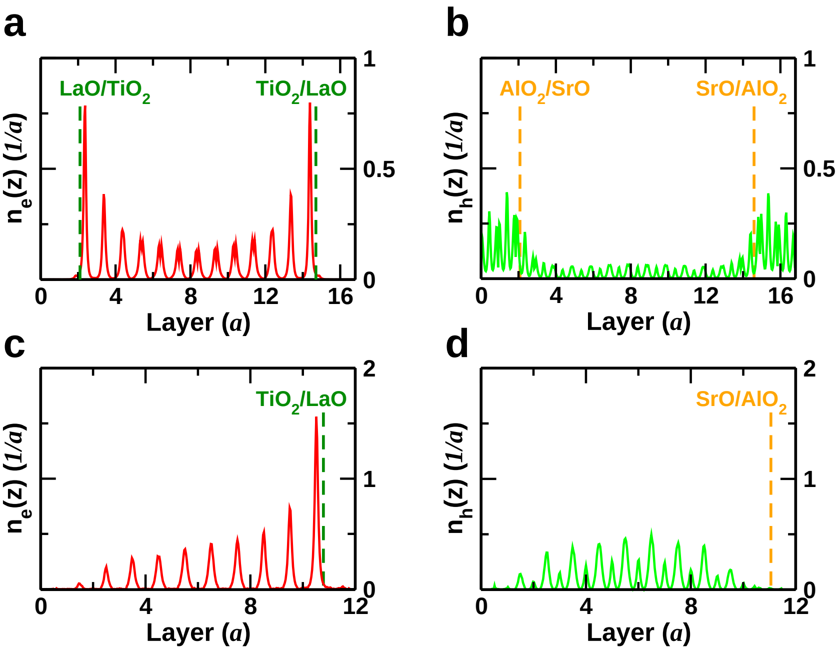

Figure 3.2: Transferred electron and hole densities integrated over the xy plane. In each panel, the integral of the conduction electron/hole density is normalized to unity. The layers are measured in units of the $SrTiO_3$ lattice constant a. **a)** The symmetric n-type superlattice. The electrons are bound to the n-type interface. **b)** The symmetric p-type superlattice. The holes reside in both the $SrTiO_3$ and $LaAlO_3$ layers. **c)** The n-type interface with 4 u.c. of $LaAlO_3$. The electrons decay away from the n-type interface. **d)** The p-type interface with 5 u.c. of $LaAlO_3$. The holes, driven by the polar field through $LaAlO_3$, diffuse into the $SrTiO_3$ substrate. Appendix A.1 explains in detail how to calculate these transferred charge densities.

will bind the electrons, what mechanism overcomes the kinetic cost inherent in localizing them to the interface? Whatever mechanism is present is absent for the holes, whose spatial profile is relatively uniform in both materials. We provide the answer to this fundamental question in Section 3.3.3, when we discuss the tight-binding hopping matrix elements across both interfaces.

Before we move onto the next section, we would like to give a short discussion on the valence band offset (VBO) of $LaAlO_3/SrTiO_3$ interfaces. The VBO of the n-type interface has been calculated by several groups [55, 80, 53, 20, 79]. Although all of the computed values place the conduction band edge of $LaAlO_3$ significantly higher than that of $SrTiO_3$

Table 3.1: The valence band offset (VBO) of $LaAlO_3/SrTiO_3$ *n*-type and *p*-type interfaces in eV. Each value is followed by the method used to determine it in parentheses.

	n-type (TiO_2/LaO)	*p*-type (SrO/AlO_2)
present study	-0.47 (MA) -0.39 (LDOS)	-0.02 (MA) 0.11 (LDOS)
Ref. [55]	0.51 (MA) 0.39 (LDOS)	0.19 (MA) 0.10 (LDOS)
Ref. [20]	1.1	NA
Ref. [53]	-0.15 (LDOS)	NA
Ref. [79]	-0.9 (LDOS)	NA
Ref. [80]	-0.1 (MA)	NA
Expt. [71]	-0.35±0.18	NA

at the *n*-type interface, the large range of computed VBO values (shown in Table I), is puzzling. To investigate this issue, we use two different approaches to calculate the VBO of the *n*-type interface and the *p*-type interface. The valence band offset is defined by:

$$E_{\mathrm{VBO}} = E_{\mathrm{V}}^{\mathrm{LAO}} - E_{\mathrm{V}}^{\mathrm{STO}} \tag{3.1}$$

where $E_{\mathrm{V}}^{\mathrm{LAO}}$ and $E_{\mathrm{V}}^{\mathrm{STO}}$ are the valence band edges of $LaAlO_3$ and $SrTiO_3$, respectively. The simulation cell is a symmetric nonstoichiometric superlattice with 12.5 layers of $SrTiO_3$ and 4.5 layers of $LaAlO_3$. The first method to determine the VBO is to analyze the local density of states, referred to as the LDOS approach [81, 55]. The other method is to use the macroscopic average potential, denoted further as the MA approach [82, 83, 55]. We compare our results with other theoretical calculations and the recent experiment in Table 3.1.

We can see from Table 3.1 that for the *n*-type interface not only the magnitude of VBO differs, but the sign is not unanimous. One possible origin for the range of theoretical values is likely that the lattice constants have minute differences (due to different pseudopotentials), which causes a variation in strain and probably affects the alignment of valence band edges. Another possibility is that we, as well as a few other groups [55, 80, 53, 79], use symmetric nonstoichiometric superlattices, in which the macroscopic average potentials are flat in both $LaAlO_3$ and $SrTiO_3$, to perform the calculations. However, if a stoichiometric $LaAlO_3$ slab is employed [20] so that a net internal electric field results, the determined

VBO will likely be different from the symmetric nonstoichiometric case. Although our results for the n-type interface agree well with the available experiments, the value as well as variations of the VBO for the n-type interface is not a closed subject and needs further work. In contrast, the computed values of the VBO for the p-type interface are in general agreement and $\simeq 0.1$ eV.

3.3.2 The polar catastrophe

n-type, p-type and np-type interfaces

As discussed in the Introduction, there are two types of $LaAlO_3/SrTiO_3$ interfaces: the n-type (TiO_2/LaO) interface and the p-type (SrO/AlO_2) interface. If a stoichiometric $LaAlO_3$ layer on an $SrTiO_3$ substrate also has a $SrTiO_3$ capping layer, then we have both n-type and p-type interfaces in the same system. Below, we refer to this type of geometry as the np-type interface. Experimentally, the n-type, p-type and np-type interfaces have all been fabricated. In this study, we simulate all three types of interfaces, the configurations of which are illustrated in Fig. 3.3. For the np-type interface, we use 5 unit cells of $SrTiO_3$ to simulate the substrate and another 5 unit cells of $SrTiO_3$ as a capping layer. For both the n-type and p-type interfaces, we use 11 unit cells of $SrTiO_3$ to simulate the substrate. In all cases, the thickness of $LaAlO_3$ is varied from 1 to 7 unit cells. In addition, the first two $SrTiO_3$ unit cells in the substrate are fixed at the ideal perovskite positions to simulate the bulk-like interior of the substrate [24]. The termination of the $SrTiO_3$ substrate and capping layers is always SrO. As illustrated in our previous work [3], the TiO_2 termination has a surface O-p state which is $\simeq 0.5$ eV higher than the valence band edge of bulk $SrTiO_3$, while the SrO termination does not have this surface state. Since we are interested in the evolution of polar fields of $LaAlO_3$ on very thick $SrTiO_3$ substrates, this pure surface state should be avoided when simulating the $SrTiO_3$ substrate and thick $SrTiO_3$ capping layers. However, for thin $SrTiO_3$ capping layers, the presence of this O-p state on the TiO_2-terminated surface will lower the critical separation, which has recently been discussed [84].

---

[3] See the EPACS Document No. E-PRBMDO-79-R12912 for a detailed discussion of surface effects of TiO_2 termination.

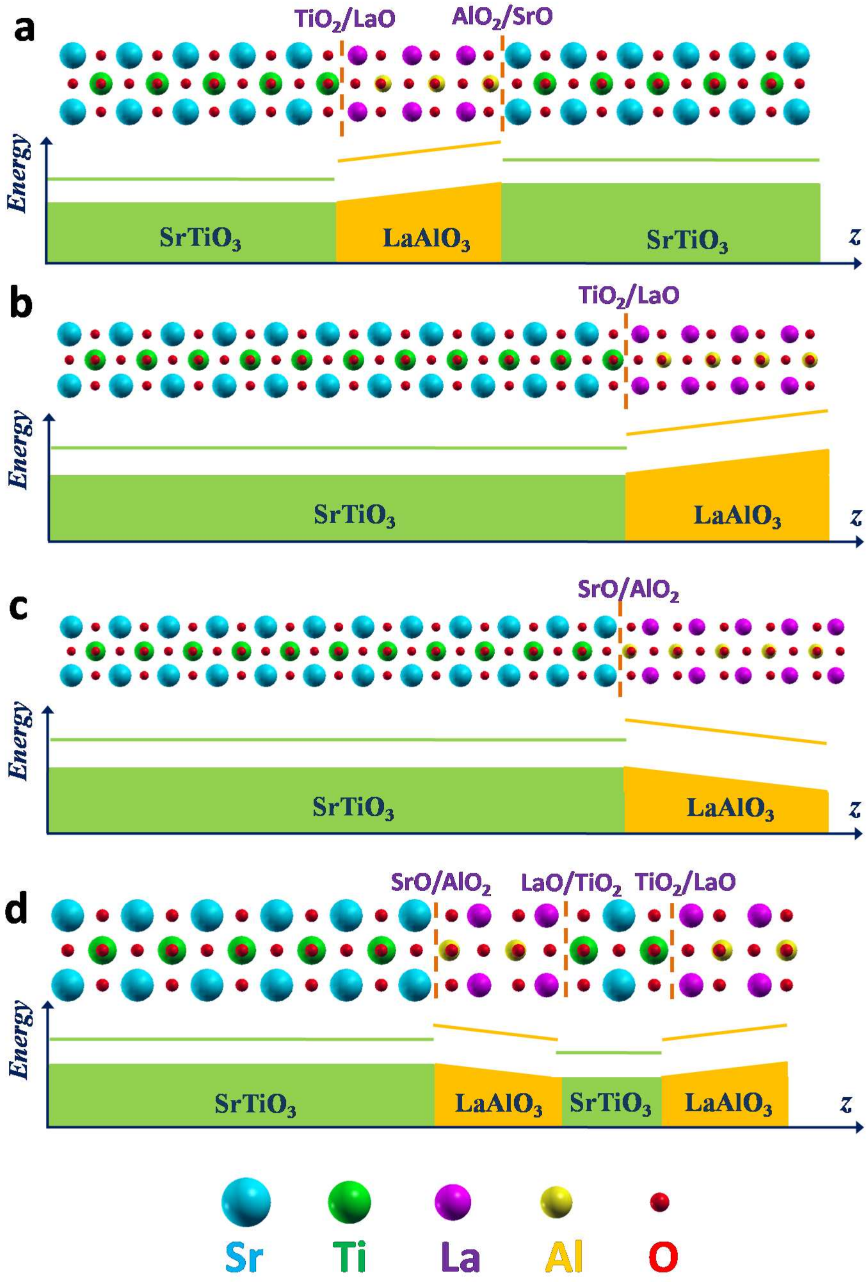

Figure 3.3: Schematics of the supercells and energy diagrams for different types of interfaces. **a)** The *np*-type interface. **b)** The *n*-type interface. **c)** The *p*-type interface. **d)** The new quantum well systems.

We observe that an insulating-to-metallic transition occurs in our simulations when the LaAlO$_3$ film reaches a critical thickness, the value of which depends on the system geometry. The phase transition can be explained in terms of an energy diagram shown in Fig. 3.3. For the *np*-type and *n*-type interfaces, due to the polar structure of $LaAlO_3$, the electric field through the $LaAlO_3$ film lifts up the band edges of the $LaAlO_3$ and reduces the energy gap. The energy gap of the *np*-type interface is the energy difference between the Ti-*d* states of the $SrTiO_3$ substrate and the O-*p* states of the $SrTiO_3$ capping layer, while the energy gap of the *n*-type interface is given by the energy difference between the Ti-*d* states of the $SrTiO_3$ substrate and the O-*p* states on the surface. For the *p*-type interface, since the polarity of $LaAlO_3$ is reversed, the electric field through the $LaAlO_3$ film decreases the valence band edge of the $LaAlO_3$. However, the energy gap of the *p*-type interface is not the most relevant quantity to monitor for the insulating-to-metallic transition. Rather, the $LaAlO_3$ film reduces the energy difference between the La states on the surface [4] and the O *p*-states of the $SrTiO_3$ substrate, which from now on we call the 'La-O energy difference'. In all three cases, the energy gap (*np*-type and *n*-type) or La-O energy difference (*p*-type) diminishes with the $LaAlO_3$ film thickness, finally disappearing when the insulating-to-metallic transition occurs. The minimum number of $LaAlO_3$ unit cells necessary to induce this phase transition is referred to as the 'critical separation'.

Our DFT calculations, as well as previous studies [57, 24, 67, 68], support the above schematics. The values of the calculated energy gap versus the $LaAlO_3$ thickness are listed in Table 3.2 for the *np*-type, *n*-type and *p*-type interfaces. The corresponding 'critical separation' is the smallest thickness of $LaAlO_3$ that makes the interface conducting. The increasing thickness of the $LaAlO_3$ film reduces the energy gap until it disappears and the interface becomes metallic. However, the critical separation depends on the band gap of $SrTiO_3$, which is underestimated in DFT calculations (the calculated band gap is 1.85 eV and the experimental band gap is 3.2 eV). Taking into account the difference between the calculated and experimental band gaps, the realistic critical separation is two more unit cells of $LaAlO_3$ in addition to the calculated one, resulting in 5, 6 and 8 u.c. for the *np*-type, *n*-type and *p*-type interfaces, respectively.

In order to give a clearer illustration of how the polar field reduces the energy gap, we show in the left column of Fig. 3.4, the *xy* planar average electrostatic potential [82]

---

[4] Detailed calculations show that the surface states have character of La 5*d*, 6*s* and 6*p*.

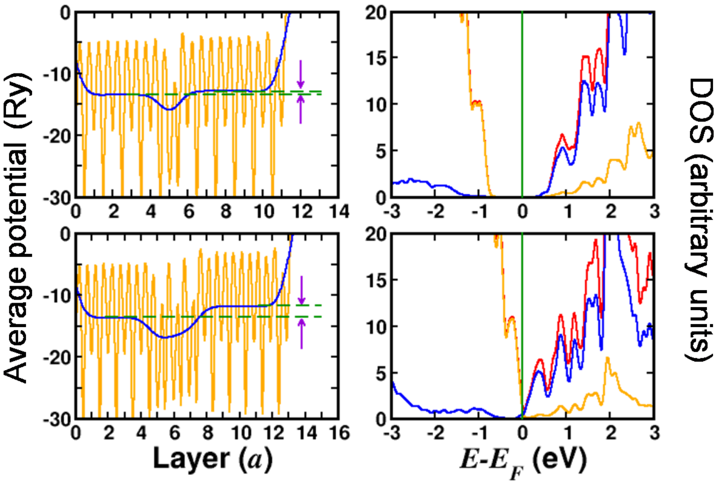

Figure 3.4: The average potential (left) and density of states (right) of the np-type interface with different thicknesses. The upper two panels correspond to the np-type interface with 1 unit cell of $LaAlO_3$, and the lower two panels correspond to the np-type interface with 3 unit cells of $LaAlO_3$. In the right panels, the red, blue, and orange lines are the total density of states (DOS), the atomic projected DOS of Ti-d states, and the atomic projected DOS of O p-states, respectively. The vertical green line in the right panels is the Fermi level.

and the associated smoothed potential along the direction perpendicular to the interface for the np-type geometry. The xy planar average potential is obtained by averaging the raw three-dimensional total potential over the interface plane. The associated smoothed potential is from convoluting the xy planar average potential along z direction with a Gaussian function using a width $\simeq 0.6$Å. As the figure shows, the smoothed potential in $SrTiO_3$ is flat, indicating that there is no internal electric field through the $SrTiO_3$ (*i.e.*, it is nonpolar). In the $LaAlO_3$ layers, the macro-averaged smoothed potential is increasing and lifts up the valence band edge of the capping $SrTiO_3$. The energy difference between the O-p states of the $SrTiO_3$ capping layer and those of the $SrTiO_3$ substrate increases with increasing $LaAlO_3$ film thickness. The right column of Fig. 3.4 shows the corresponding density of states (DOS). As the upper panel shows, since the potential increase by 1 unit cell of $LaAlO_3$ is not large enough to overcome the band gap of $SrTiO_3$, the system is still insulating. In the lower panel, the potential increase by 3 unit cells of $LaAlO_3$ is larger than the band gap of $SrTiO_3$, so that the Ti-d states in the $SrTiO_3$ substrate and O-p states in the capping $SrTiO_3$ layer overlap. Then the system becomes metallic.

Further evidence of the insulating-to-metallic transition is shown by the local density of states (LDOS) at the Fermi level of the n-type interface in Fig. 3.5a. From the character of these states, we can see that we have Ti-d states in the $SrTiO_3$ substrate and O-p states on the surface. Fig. 3.2 shows the spatial distributions of the conducting electrons and holes integrated over xy-plane at the n-type and p-type interfaces, respectively. The details of how to calculate these densities are provided in Appendix A.1. From Fig. 3.2, it is clear that the conducting electrons and holes behave very differently in the $SrTiO_3$ substrate. The conducting electrons, which occupy Ti-d states, decay away from the n-type interface over a length scale of $\simeq 10$ unit cells, indicating that the conducting electron gas is several nm thick. This result is in qualitative agreement with experimental measurements of the superconducting electron gas [16] and other theoretical calculations [56, 68]. Unlike the conducting electrons, the spatial distribution of the holes resembles that of a particle in a box, implying that the holes are very weakly bound to the interface. As elucidated in our previous work [24], the reason for this asymmetry is that the conducting electron gas is trapped at the n-type interface due to a large interfacial hopping matrix element. We will discuss this phenomenon further in Section 3.3.3.

The quantum well system

Though the conduction electrons are bound to the n-type interface, they still spread over several nanometers. The observed thickness of the electron gas at the n-type interface varies widely in experiments, from nanometers to microns, depending on the growth conditions [22]. Thus it would be desirable to be able to manually control the thickness of the electron gas. Based on the polar catastrophe mechanism, we propose a new class of quantum well systems that will allow this functionality. The quantum well system, which is illustrated in Fig. 3.3d, has the following composition: $SrTiO_3$ substrate/2 u.c. $LaAlO_3$ /m u.c. $SrTiO_3$ /$LaAlO_3$ capping layer, where m can be varied to control the thickness of the conducting electron gas, as we discuss below. Along the (001) direction, this configuration results in three interfaces: one p-type interface between the $SrTiO_3$ substrate

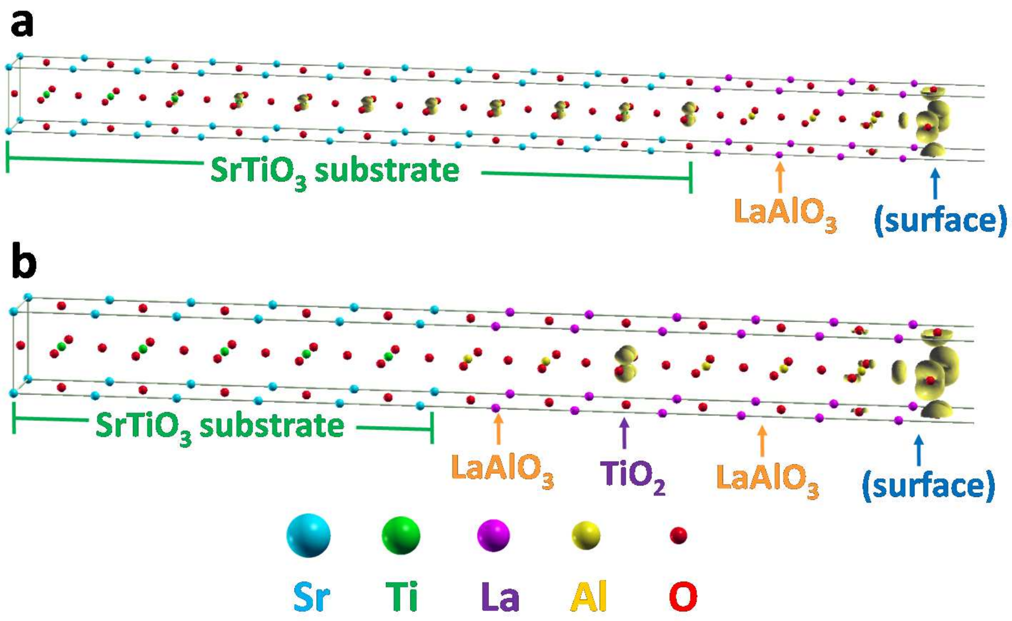

Figure 3.5: 3D isovalue surfaces (yellow contour) showing the local density of states at the Fermi level for **a)** the n-type interface and **b)** the new quantum well systems. The conduction electrons (occupying Ti-d orbitals) extend into the $SrTiO_3$ substrate at the n-type interface, but are localized in the embedded TiO_2 layer at the QW. Holes occupy the O-p states on the surface in both cases.

and the 2 u.c. $LaAlO_3$ buffer layer, and two n-type interfaces on both sides of the inserted thin $SrTiO_3$ film. Both of the $LaAlO_3$ thin films are stoichiometric in this sytem, while the embedded $SrTiO_3$ thin film is not. As we have two n-type interfaces, the quantum well systems have one extra TiO_2 layer in the inserted $SrTiO_3$ film. Like the n-type and np-type interfaces, the two $SrTiO_3$ unit cells of the substrate facing the vacuum are fixed to simulate a bulk-like substrate and all the other atoms are fully relaxed.

The reason that this configuration forms a quantum well can also be explained in terms of an energy diagram. Fig. 3.3d shows that the polar fields in the two $LaAlO_3$ thin films point in opposite directions. Therefore, the energy of the Ti-d states in the embedded $SrTiO_3$ thin film is lowered relative to the conduction band edge of the $SrTiO_3$ substrate. (We choose two unit cells of $LaAlO_3$ as the buffer layer in order to bring down the Ti-d states of the embedded $SrTiO_3$ film into the band gap of the $SrTiO_3$ substrate). As the capping $LaAlO_3$ layer thickens, the energy of the O-p states eventually becomes higher than that of the Ti-*d* states of the embedded $SrTiO_3$ film, and hence an insulating-to-metallic transition occurs. The difference between the quantum well systems and the *n*-type interface is that once the insulating-to-metallic transition happens, the conduction electrons get trapped in the Ti-*d* states of the embedded $SrTiO_3$ film rather than those of the $SrTiO_3$ substrate. Therefore, by changing the thickness of the embedded $SrTiO_3$ film, we can manually control the spatial extent of the electron gas while holding the number of transferred electrons constant. Consequently, we have two parameters to vary: 1) the thickness of embedded $SrTiO_3$ film to control the spatial extent of electron gas, and 2) the thickness of $LaAlO_3$ capping layer to control the insulating-to-metallic transition. For simplicity, in the following, we focus on one particular subclass in which the embeded $SrTiO_3$ is narrowed down to a single TiO_2 layer. The thickness of the $LaAlO_3$ capping layer will be varied. The quantum wells (QW) in the following refer to this particular subclass.

Like the *p*-type interface, at this new class of quantum well systems, the energy gap is not the most direct quantity to monitor for the insulating-to-metallic transition. As the $LaAlO_3$ capping layer is thin, the energy gap of the QW is the energy difference between the Ti-*d* states of the embedded TiO_2 layer and the O-*p* states of the $SrTiO_3$ substrate, which remains at a constant energy. The more relevant quantity is the energy difference between the Ti-*d* states of the embedded TiO_2 layer and the O-*p* states on the surface. We refer to this quantity as the 'Ti-O energy difference' in the following. Increasing the thickness of the $LaAlO_3$ capping layer reduces the Ti-O energy difference until it disappears and electron transfer occurs. The minimum thickness of the $LaAlO_3$ capping layer that enables this electron transfer is defined as the critical separation of the QW systems.

Table 3.2 shows the Ti-O energy difference and the critical separation of the QW systems. The critical separation of the QW coincides with that of the *n*-type interface, reflecting the fact that the band gap of $SrTiO_3$ is mainly determined by the Ti-*d* states and the O-*p* states. Therefore, the absence of Sr atoms does not change the critical separation. The local density of states at the Fermi level of the QW are shown in Fig. 3.5b. Unlike the *n*-type interface, at which the filled Ti *d*-states extend over ∼10 unit cells in the $SrTiO_3$ substrate, the only metallic states in the QW systems are localized in the single embedded

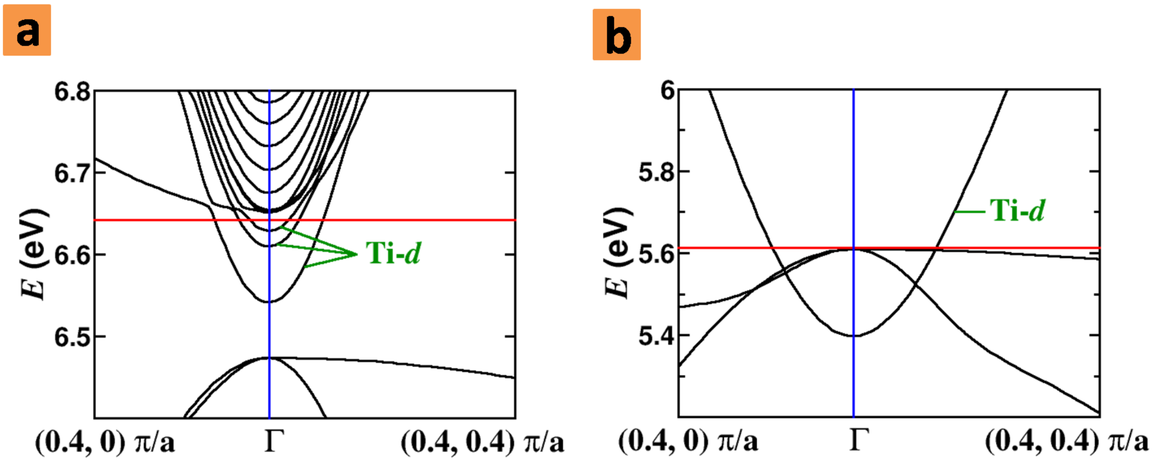

Figure 3.6: A comparison of the band structures of **a)** the n-type interface and **b)** the new QW. The n-type interface has 5 unit cells of $LaAlO_3$ and the QW has a capping layer of 6 unit cells of $LaAlO_3$. The red solid line is the Fermi level.

TiO_2 layer, as anticipated.

This new class of quantum wells displays a number of appealing properties that are absent at the $LaAlO_3/SrTiO_3$ n-type interface. First, the thickness of conduction electrons is controlled by the inserted $SrTiO_3$ film and can be in principle reduced to a single atomic TiO_2 layer. Second, the electronic properties of the new quantum wells largely depend on the polar structure of $LaAlO_3$. Therefore, the $SrTiO_3$ substrate can be replaced by other materials on which $LaAlO_3$ can be epitaxially grown, *e.g.* LSAT ($La_{0.29}Sr_{0.71}Al_{0.65}Ta_{0.35}O_3$). This provides more choices of substrates on which to grow this new quantum well structure. Finally, the new quantum well serves as a practical way to test the recently proposed hypothesis that some electrons do not contribute to transport due to Anderson localization. Popović *et al.* [79] argued that since all two dimensional states are Anderson localized by disorder, the electrons that occupy the lowest Ti-d bands do not conduct and therefore the observed sheet carrier density should be much smaller than the $0.5e$ per two-dimensional unit cell predicted by the polar catastrophe mechanism [66]. Nevertheless, it is not trivial to distinguish from which band conduction electrons originate. The thinnest of this new type of quantum wells has only one Ti-d band at the Fermi level, corresponding to the single embedded TiO_2 layer, which has a strong

Table 3.2: DFT-LDA computed energy gaps and potential changes versus the number of $LaAlO_3$ layers i for the np-type, n-type and p-type interfaces (i=0 refers to a pure $SrTiO_3$ substrate). Δ is the energy gap of the interface systems (np-type and n-type) with the corresponding number of $LaAlO_3$ layers. δ is the 'La-O energy difference' (p-type interface) or 'Ti-O energy difference' (quantum well) with the corresponding number of $LaAlO_3$ layers. V_i is the macroscopic potential change due to adding the i-th $LaAlO_3$ layer. Note that 'La-O energy difference' is not well defined when $i = 0$ (no $LaAlO_3$ layer).

np-type			n-type			p-type			QW		
i	Δ(eV)	V_i(eV)	i	Δ(eV)	V_i(eV)	i	δ(eV)	V_i(eV)	i	δ(eV)	V_i(eV)
0	1.85		0	1.85		0	N/A		0	1.85	
1	1.25	0.60	1	1.71	0.14	1	2.59		1	1.83	0.02
2	0.55	0.70	2	1.28	0.43	2	1.89	0.70	2	1.30	0.53
3	metallic		3	0.57	0.71	3	1.18	0.71	3	0.59	0.71
			4	metallic		4	0.49	0.69	4	metallic	
						5	metallic				

two-dimensional Ti-d_{xy} character. Therefore it should show strong localization and not contribute to conductivity. By thickening the embedded $SrTiO_3$, one should be changing only the extent of the wave functions and see the localization properties. Fig. 3.6 shows a comparison of the band structures of the n-type interface and the QW. These two systems both have approximately $0.1e$ per two-dimensional unit cell (from Fig. 3.9). However, the Fermi level of the n-type interface crosses three Ti-d bands, while the QW system has only one Ti-d band at the Fermi level, as expected.

3.3.3 Bound versus unbound carriers at the interfaces

In this section, we provide a microscopic picture of the quantum states inhabited by the carriers at the n-type and p-type interfaces, based on a first-principles extraction of tight-binding parameters. As reported in our previous work [24], the main result is that a significant Ti-La interfacial hopping element unique to the n-type interface causes electron to bind there. No such mechanism is operative at the p-type interface, explaining the delocalization of the holes into the $SrTiO_3$ substrate. As shown below, the Ti-La hopping is significantly enhanced at the n-type interface due to the relatively large size of La d-orbitals as well as the spatial proximity of the La and Ti atoms in the neighboring atomic planes. Here we provide an expanded and more detailed explanation and analysis of the hopping elements.

To calculate the on-site and hopping matrix elements, we employ Löwdin atomic orbitals [85], which are a set of orthonormalized atomic-like orbitals. A Löwdin orbital of type α localized around lattice position $\mathbf{R}$ is given by:

$$\langle \mathbf{r}|\alpha\mathbf{R}\rangle = \phi_\alpha(\mathbf{r}-\mathbf{R}) \tag{3.2}$$

However, as the Kohn-Sham wave functions are Bloch states indexed by wave vectors $\mathbf{k}$, it is more fruitful to employ Bloch-like superpositions $\varphi_\alpha^{\mathbf{k}}(\mathbf{r})$ defined as

$$\varphi_\alpha^{\mathbf{k}}(\mathbf{r}) = \frac{1}{\sqrt{N_{\mathbf{k}}}}\sum_{\mathbf{R}} e^{i\mathbf{k}\cdot\mathbf{R}}\phi_\alpha(\mathbf{r}-\mathbf{R})\,. \tag{3.3}$$

$N_{\mathbf{k}}$ is the total number of k-points in the Brillouin zone sampling. To extract a tight-binding model for the Bloch states at $\mathbf{k}$, we need to calculate the matrix elements $\langle\varphi_\alpha^{\mathbf{k}}|H|\varphi_\beta^{\mathbf{k}}\rangle$. Making use of the completeness of the Hamiltonian, we obtain:

$$\langle\varphi_\alpha^{\mathbf{k}}|H|\varphi_\beta^{\mathbf{k}}\rangle = \sum_n \langle\varphi_\alpha^{\mathbf{k}}|n\mathbf{k}\rangle E_{n\mathbf{k}}\langle n\mathbf{k}|\varphi_\beta^{\mathbf{k}}\rangle \tag{3.4}$$

where $\langle\mathbf{r}|n\mathbf{k}\rangle = \psi_{n\mathbf{k}}(\mathbf{r})$ are the actual Bloch eigenstates of the Hamiltonian H. The overlap $\langle\varphi_\alpha^{\mathbf{k}}|n\mathbf{k}\rangle$ can be recast easily as follows:

$$\langle\varphi_\alpha^{\mathbf{k}}|n\mathbf{k}\rangle = \sqrt{N_{\mathbf{k}}}\int d\mathbf{r}\phi_\alpha^*(\mathbf{r})\psi_{n\mathbf{k}}(\mathbf{r}) = \langle\alpha\mathbf{0}|n\mathbf{k}\rangle \tag{3.5}$$

where $\langle\mathbf{r}|\alpha\mathbf{R}\rangle = \phi_\alpha(\mathbf{r}-\mathbf{R})$. Our final operational formula is

$$\langle\varphi_\alpha^{\mathbf{k}}|H|\varphi_\beta^{\mathbf{k}}\rangle = \sum_n \langle\alpha\mathbf{0}|n\mathbf{k}\rangle E_{n\mathbf{k}}\langle n\mathbf{k}|\beta\mathbf{0}\rangle \tag{3.6}$$

where the overlaps $\langle\alpha\mathbf{0}|n\mathbf{k}\rangle$ are automatically computed and reported by the PWscf code. Choosing $\alpha = \beta$ gives the on-site energies while $\alpha \neq \beta$ are the hopping elements. The orthonormality relation can also be obtained by replacing H with the identity I operator:

$$\langle \varphi_\alpha^{\mathbf{k}} | \varphi_\beta^{\mathbf{k}} \rangle = \sum_n \langle \alpha \mathbf{0} | n\mathbf{k} \rangle \langle n\mathbf{k} | \beta \mathbf{0} \rangle = \delta_{\alpha\beta} \tag{3.7}$$

Eq.(3.7) is a good criterion to check the truncation in the infinite summation over the band index n. In our calculations, we include bands with energies up to 29 eV above the Fermi level, so that $|\langle \varphi_\alpha^{\mathbf{k}} | \varphi_\alpha^{\mathbf{k}} \rangle| > 0.99$ for all Löwdin orbitals considered and $|\langle \varphi_\alpha^{\mathbf{k}} | \varphi_\beta^{\mathbf{k}} \rangle| < 5 \times 10^{-4}$ for all the pairs of two different atomic orbitals.

At the n-type interface, direct projection of the Bloch states $\psi_{n\mathbf{k}}$ onto the Löwdin orbitals shows that the character of the lowest band accommodating the conduction electrons is mainly Ti-d_{xy} with a small component of La-d_{xy}. The minimum of these occupied bands is at Γ ($\mathbf{k} = \mathbf{0}$). Therefore we build our tight-binding model on the subspace composed of Ti-d_{xy} and La-d_{xy} orbitals and calculate the following on-site and hopping matrix elements:

$$H_{00} = \langle \varphi^{\Gamma}_{\text{La-}d_{xy}} | H | \varphi^{\Gamma}_{\text{La-}d_{xy}} \rangle \tag{3.8}$$

$$H_{jj} = \langle \varphi^{\Gamma}_{\text{Ti}^j\text{-}d_{xy}} | H | \varphi^{\Gamma}_{\text{Ti}^j\text{-}d_{xy}} \rangle \tag{3.9}$$

$$H_{0j} = H^*_{j0} = \langle \varphi^{\Gamma}_{\text{La-}d_{xy}} | H | \varphi^{\Gamma}_{\text{Ti}^j\text{-}d_{xy}} \rangle \tag{3.10}$$

$$H_{ij} = H^*_{ji} = \langle \varphi^{\Gamma}_{\text{Ti}^i\text{-}d_{xy}} | H | \varphi^{\Gamma}_{\text{Ti}^j\text{-}d_{xy}} \rangle \tag{3.11}$$

where 'La' in Eq. (3.8) and Eq. (3.10) is the La atom in the $LaAlO_3$ layer at the n-type interface. i (or j) labels the Ti atoms in the $SrTiO_3$ where $i = 1$ (or $j = 1$) is in the very TiO_2 layer at the n-type interface, and increasing i (or j) refers to the TiO_2 layers that are further away from the interface.

The n-type interface with 2 u.c. of $LaAlO_3$ is insulating (before the polar catastrophe) and that with 4 u.c. of $LaAlO_3$ is conducting (after the polar catastrophe). Table 3.3 shows the on-site and hopping matrix elements of the n-type interface before and after the polar catastrophe, respectively. The on-site matrix elements are also shown in Fig. 3.7. We can see that the polar catastrophe does not result in significant difference in either the on-site or the hopping matrix elements. Therefore, in the following we mainly focus on the tight-binding Hamiltonian after the polar catastrophe, which is more relevant to describe the conduction electron gas.

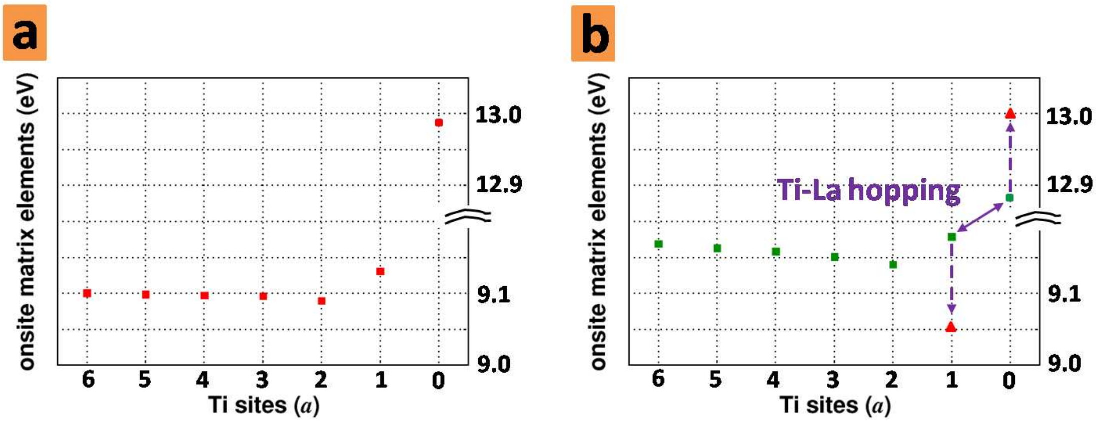

Figure 3.7: The on-site matrix elements of the n-type interface. The squares are the on-site matrix elements. Site 0 is the La atom. Sites 1-6 are the Ti atoms. The triangles are the 'new' onsite matrix elements after taking into account the hopping effects. The data can be read from Table 3.3. a is the lattice constant of SrTiO$_3$. **a)** The n-type interface with 2 unit cells of LaAlO$_3$. **b)** The n-type interface with 4 unit cells of LaAlO$_3$. The purple arrows illustrate the effect of Ti-La hopping as per Eq. (3.13) and Eq. (3.14).

Fig. 3.7 and Table 3.3 show that the on-site matrix element of the first Ti atom (closest to the interface) is *not* the lowest one before or after the polar catastrophe; instead, the second Ti atom has the lowest potential. Therefore, one would expect to find the highest electron density on the second Ti atom, in direct contrast to what is actually found in Fig. 3.2c. However, there is a very large hopping matrix element between the La and Ti atoms at the interface, at least 100 times larger than all the other hopping matrix elements between Ti atoms. This is due to two factors: one is that La-5d orbitals are more extended than Ti-3d orbitals, which leads to a larger overlap, and the other is that the distance between La and Ti atom at the n-type interface is $\sqrt{3}/2$ times the distance between neighboring Ti atoms [24]. Consequently, to the leading order [5], we neglect the hopping between adjacent Ti atoms and other higher order hopping matrix elements. The Hamiltonian becomes block-diagonal and the only block we need to diagonalize is the

---

[5] We in fact perform the exact diagonalization and find that neglecting the hopping between adjacent Ti atoms and other higher order hopping matrix elements is an excellent approximation. More importantly, this leading order approximation described in the text shows that the Ti-La hopping is crucial in trapping the electrons at the n-type interface.

leading 2 × 2 Ti-La submatrix right at the interface:

$$h = \begin{pmatrix} H_{00} & H_{01} \\ H_{10} & H_{11} \end{pmatrix} \tag{3.12}$$

Diagonalization of Eq. (3.12) with the tabulated values gives the following eigenvalues and eigenvectors:

$$\varepsilon_1 = 12.99\text{eV}, \quad |\xi_1\rangle = 0.98|\text{La-}d_{xy}\rangle - 0.18|\text{Ti}^1\text{-}d_{xy}\rangle \tag{3.13}$$

$$\varepsilon_2 = 9.04\text{eV}, \quad |\xi_2\rangle = 0.18|\text{La-}d_{xy}\rangle + 0.98|\text{Ti}^1\text{-}d_{xy}\rangle \tag{3.14}$$

After diagonalization, we find a pair of bonding and anti-bonding states at the n-type interface. The energy of the binding state ε_2 is even lower than H_{22}, showing that the electrons prefer the Ti site right at the interface. Therefore, after the insulating-to-metallic transition occurs, most electrons reside in this bonding state, which leads to an electron gas bound to the interface. In other words, the large Ti-La hopping matrix element is critical in creating a strongly bound state for the electrons at the interface. Moreover, this hopping is intrinsic to the n-type interface geometry as it does not significantly change its magnitude before and after the polar catastrophe. This also explains the overall similarity of the electron distributions at the symmetric double n-type superlattice (Fig. 3.2a) and the stoichiometric n-type interface (Fig. 3.2c). Despite differing in the lack or presence of oppositely charged carriers and polar fields, the two systems share the same Ti-La hopping and thus the same binding force to the interface.

On the other hand, at the p-type interface, holes are found to occupy bands with essentially pure O-p characters and the maximum of those bands is located at M ($\mathbf{k} = (\frac{\pi}{a}, \frac{\pi}{a}, 0)$). The tight-binding model is based on the following matrix elements:

$$H_{ij}^{\mu\nu} = \langle \varphi^{\text{M}}_{\text{O}^i\text{-}p_\mu} | H | \varphi^{\text{M}}_{\text{O}^j\text{-}p_\nu} \rangle \tag{3.15}$$

where i, j refer to different O atoms and $\mu, \nu = x, y, z$ refer to different O-p orbitals. We

Table 3.3: On-site and hopping matrix elements of the n-type interface before and after the polar catastrophe, respectively. l is the thickness of $LaAlO_3$. $l = 2$ and 4 unit cells (u.c.) correspond to before and after the polar catastrophe, respectively. We list all the nearest neighbor hopping matrix elements and the largest next nearest neighbor hopping matrix element. The first and third columns are the on-site matrix elements of Ti d-states and hopping matrix elements before the polar catastrophe. The second and fourth columns are the on-site matrix elements of Ti d-states and hopping matrix elements after the polar catastrophe.

H_{ii} (eV)			H_{ij} (meV)		
i	$l = 2$ u.c.	$l = 4$ u.c.	ij	$l = 2$ u.c.	$l = 4$ u.c.
0	12.99	12.87	0 1	-697	-696
1	9.13	9.18	1 2	-6.39	-1.3
2	9.09	9.14	2 3	-6.80	-0.2
3	9.10	9.15	3 4	-7.03	-0.3
4	9.10	9.19	4 5	-7.07	-0.3
5	9.10	9.16	5 6	-7.07	-0.4
6	9.10	9.17	6 7	-7.05	-0.4
7	9.10	9.18	7 8	-7.03	-0.5
8	9.10	9.19	8 9	-6.98	-0.5
9	9.10	9.19	0 2	-0.87	-7.2

calculate all these matrix elements at the p-type interface before and after the polar catastrophe. We find that the hopping elements between nearest neighbor O atoms are all close to 0.6 eV, that there is no order of magnitude difference in the hopping elements, and that there is no discontinuity in going across the p-type interface. This is no surprise because the O atoms form a continuous network across the p-type interface and the hopping matrix elements do not sensitively depend on the nature of the surrounding cations. Therefore, the only difference we expect from the symmetric double p-type results (compare Fig. 3.2b and Fig. 3.2d) is that the presence of the polar field at the p-type interface will drive the holes from the $LaAlO_3$ into the $SrTiO_3$. However, once in the $SrTiO_3$, the holes do not feel any strong preference for the interface and therefore diffuse further into the $SrTiO_3$ substrate. As our calculations have finite film thicknesses, we expect that the profile of holes resembles the lowest state of a free particle in a box and thus have a maximum density in the middle of the film, as borne out by Fig. 3.2d.

3.3.4 Oxygen vacancies repulsion from the interfaces

The theoretical results we have discussed to this point have concerned ideal interfaces with sharp boundaries and 1 × 1 in-plane periodicity. An important question is whether these assumptions are reasonable for describing the experimentally realized interfaces. This question is obviously very difficult to answer in general as the number of possible ways of perturbing the ideal interfaces is enormous and includes intermixtures, impurities, vacancies, interstitials, off-stoichiometry, etc. Below, we focus on answering one simple but important question for the most prevalent type of imperfections: do oxygen vacancies present in the $SrTiO_3$ substrate have a strong preference for the $SrTiO_3$ region close to the interface? Based on both our first principles results and general physical considerations, the answer appears to be no. As we show below, the interface $SrTiO_3$ region should be relatively free of oxygen vacancies compared to the bulk $SrTiO_3$ substrate.

Our approach is motivated by experiments that infer a concentration of one oxygen vacancy per four two-dimensional unit cells at the p-type interface [66]. If one assumes each oxygen vacancy donates fully two electrons, this is precisely the amount required to compensate the 0.5 holes per two-dimensional unit cell from the polar catastrophe. The same experiments are also used to infer a non-zero (but smaller) concentration of oxygen vacancies at the n-type interface [66]. To determine the most energetically favorable position for oxygen vacancies, we compute the formation energy of one monolayer of oxygen vacancies at the same areal density (1/4 per two-dimensional unit cell) at various positions inside the $SrTiO_3$ close to the interface with $LaAlO_3$. We perform calculations on both p-type and n-type interfaces using the unit cells shown in Fig. 3.8.

Our simulation cells include a $2 \times 2 \times 5$ $SrTiO_3$ film and a $2 \times 2 \times 1$ $LaAlO_3$ film and $\simeq$ 25 Å of vacuum. The substrate termination is SrO in order to minimize any surface effects [24]. The $SrTiO_3$ unit cell next to the vacuum is fixed to simulate the bulk-like substrate and all the other atoms are relaxed. For a reference, we compute the formation energy of an isolated oxygen vacancy in bulk $SrTiO_3$ in a $2 \times 2 \times 5$ supercell with one oxygen vacancy. Starting from the interface, we place the oxygen vacancy in the SrO or TiO_2 layer of the first three $SrTiO_3$ unit cells and compute the formation energy (see Fig. 3.8 for the numbering nomenclature of the layers). We show the results in Table 3.4. As the oxygen vacancies move away from the p-type interface, the formation energy decreases, approaching a constant value of 5.4-5.5 eV in the bulk-like regions of the $SrTiO_3$ films. The computed bulk formation energy is slightly lower (5.18 eV); presumably the small difference is due to the fact that the $SrTiO_3$ films in the interface geometry are rather thin (only 5 unit cells) and not yet fully in the substrate limit. Nevertheless the energetic *trend* clearly shows the interface region repels the vacancies.

Our results show that there is no energetically favorable binding of oxygen vacancies to either the p-type or n-type interface. A simple physical picture can explain the repulsion of the oxygen vacancies from both types of interface. An isolated, neutral oxygen vacancy in $SrTiO_3$ is a donor that binds two electrons (O has formal charge O^{2-}). The electrons reside on localized states composed of the d-orbitals of the vacancy's surrounding Ti atoms; the energy of these states is close to the $SrTiO_3$ conduction band edge. Thus, oxygen vacancies can be described as a type of hydrogenic system with bound electrons. As the vacancy approaches the interface, the bound electrons experience what are essentially hard wall boundary conditions since the conduction band edge of $LaAlO_3$ is $\sim$ 2 eV higher than that of $SrTiO_3$. As the vacancy approaches the hard wall, its energy increases due to the electron confinement effect [86]. Given the basic physical principles behind this argument, it is clear that it applies to both interfaces. Futhermore, it suggests that even though our first principles results are for relatively high densities of oxygen vacancies in a particular configuration, lower densities and more positionally disordered oxygen vacancies in the $SrTiO_3$ will still be repelled from the interface region.

The fact that oxygen vacancies are repelled from the interfaces provides a self-consistent picture for our computations of ideal interfaces. Namely, the dominant defects (oxygen vacancies) should not be present in the immediate vicinity of the interfaces. For example, for the p-type interface, our theory predicts extended band states for the holes that diffuse substantially into the $SrTiO_3$ substrate. Since the vacancies are themselves in the bulk of the substrate, they can trap the holes, rendering them immobile. For a relatively thick $SrTiO_3$ substrate, this situation is likely since only one oxygen vacancy per four two-dimensional unit cells, distributed over the three-dimensional volume of the substrate, is required to provide the compensating number of electrons.

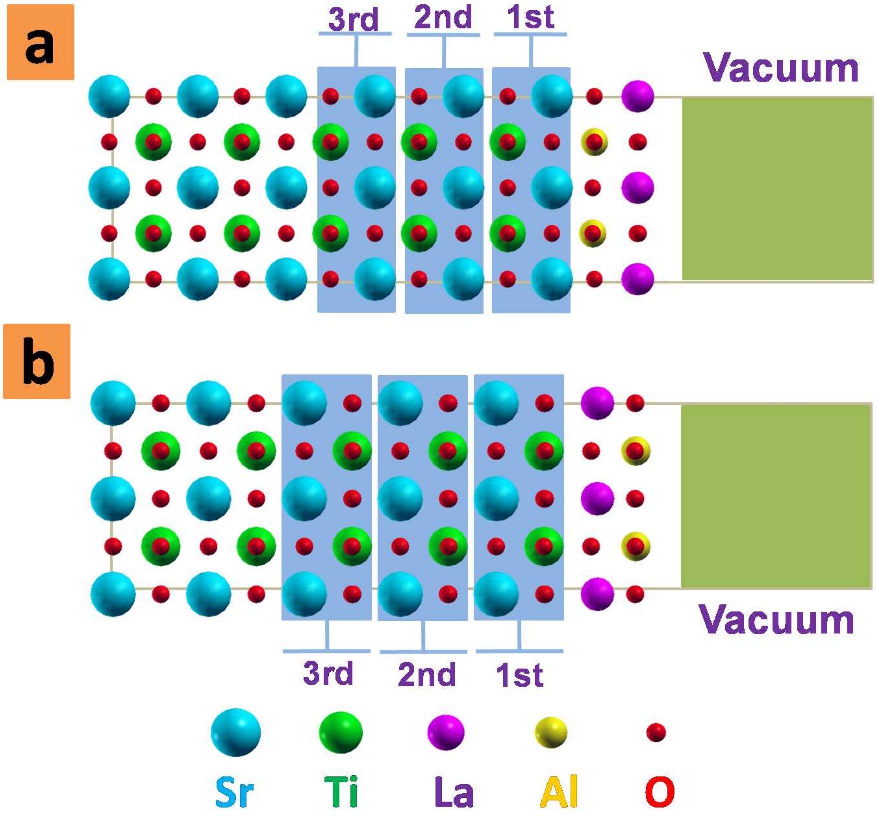

Figure 3.8: Schematics of the simulation cell for $\frac{1}{4}$ monolayer oxygen vacancy calculations. One oxygen vacancy is placed in either SrO and TiO_2 of the first, second and third layer, respectively. **a)** The p-type interface. **b)** The n-type interface.

We would like to comment that experimentally Nakagawa *et al.* [66] found $32 \pm 6\%$ of oxygen vacancies per two-dimensional unit cell at the p-type interface. Their conclusion is based on a least-square fit of EELS spectra to the reference spectra of bulk $SrTiO_3$, bulk $LaAlO_3$ and oxygen-deficient $SrTiO_{3-\delta}$ with $\delta = 1/4$. The discrepancy between our results and those experiments may be due to the following two non-mutually exclusive reasons. One is that in our simulations, we include only one unit cell of $LaAlO_3$ owing to the computational limitations. More realistic simulations would include thicker $LaAlO_3$ films to simulate the system after the polar catastrophe when carriers appear in the vicinity of the interfaces. The presence of carriers might in principle affect the formation energy of oxygen vacancies, which needs to be checked in much larger calculations in future work. The other reason is the interpretation of EELS spectra in experiment. The experimental

Table 3.4: Formation energies E of $\frac{1}{4}$ monolayer of oxygen vacancy at the p-type and n-type interface. $\frac{1}{4}$ monolayer of oxygen vacancy is in either ith SrO atomic layer or ith TiO_2 atomic layer. For reference, the formation energy in the bulk is 5.18 eV.

p-type		n-type	
position of oxygen vacancy	E (eV)	position of oxygen vacancy	E (eV)
1st SrO layer	6.25	1st TiO_2 layer	5.65
1st TiO_2 layer	5.85	1st SrO layer	5.65
2nd SrO layer	5.69	2nd TiO_2 layer	5.56
2nd TiO_2 layer	5.56	2nd SrO layer	5.46
3rd SrO layer	5.60	3rd TiO_2 layer	5.57
3rd TiO_2 layer	5.50	3rd SrO layer	5.41

fitting is based on the assumption that any deviation of O-K edge EELS from the bulk $SrTiO_3$ is caused by the presence of oxygen vacancies. However, even without oxygen vacancies at the p-type interface, we observe in our calculations that the atoms close to the interface move away from their bulk positions due to the broken symmetry at the interface. The EELS spectra of the distorted $SrTiO_3$ could be different from that of the reference bulk structure. Therefore, a more accurate (and more difficult) fit would take into account the deviation of the EELS spectra of distorted $SrTiO_3$ from the bulk and other possible factors which could also affect the EELS spectra, such as intermixture and nonstoichiometry.

3.3.5 Thickness dependence of sheet carrier density

In experiment, the sheet carrier density was observed to display a thickness dependence, but a range of results exist. The sheet carrier density depends on both sample growth conditions and post-annealing [22]. In this section, we present first-principles calculations of the sheet carrier density for different $LaAlO_3$ film thicknesses. We study the np-type, n-type and QW systems, and discuss the similarities between these different interface systems.

We define the 'sheet carrier density' as the sum of all the conduction electrons per square unit cell in the Ti d-states of the $SrTiO_3$ substrate (for n-type and np-type interfaces) or in the Ti d-states of the single embedded TiO_2 layer (for the QW systems). Fig. 3.9

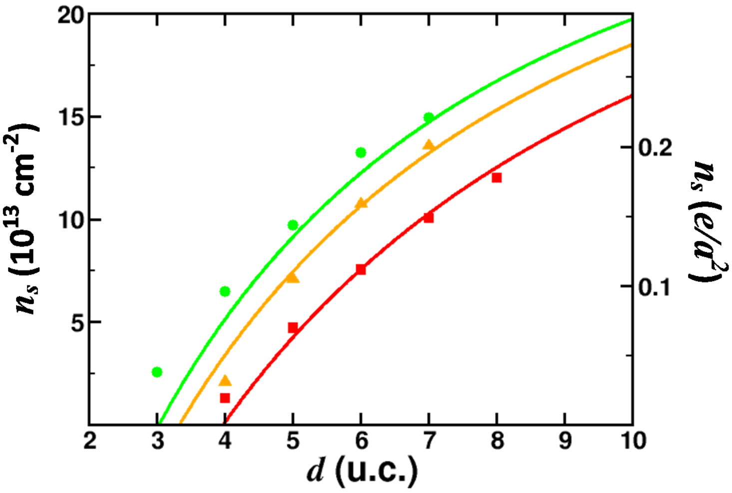

Figure 3.9: Comparison of the sheet carrier density computed with the continuous model (see Section 3.4.1) and DFT simulations. The red, orange and green lines are the model calculations of the QW, the n-type and the np-type interfaces, respectively. The squares, triangles and circles are the DFT results of the QW, the n-type and the np-type interfaces, respectively.

shows the sheet carrier density at different thicknesses for all three types of interface. The results of n-type interface are similar to what Son *et al.* recently obtained [68]. Below the critical separation in each system, there are no mobile carriers since the system is insulating. Above the critical separation, the sheet carrier densities increase in all three cases, following a similar manner. In order to further reveal the similarities among these interface systems, we show in Fig. 3.10 the relation of the sheet carrier density σ_s versus the internal electric field E through the LaAlO$_3$. The internal electric field is determined as follows. We calculate the smoothed total potential along the (001) direction. The internal electric field is the slope of the smoothed potential. Though the geometry details differ, the figure shows that the (E, σ_s) relations are almost identical for all three interface types. This suggests that a single continuous model will be able to describe the behavior of all three interfaces. We discuss such a model in Section 3.4.1.

We note that in our calculations of the sheet carrier density, we include all of the electrons in the conduction bands, regardless of whether they in fact contribute to the observed conductivity or not. We find that after the critical separation, the sheet carrier

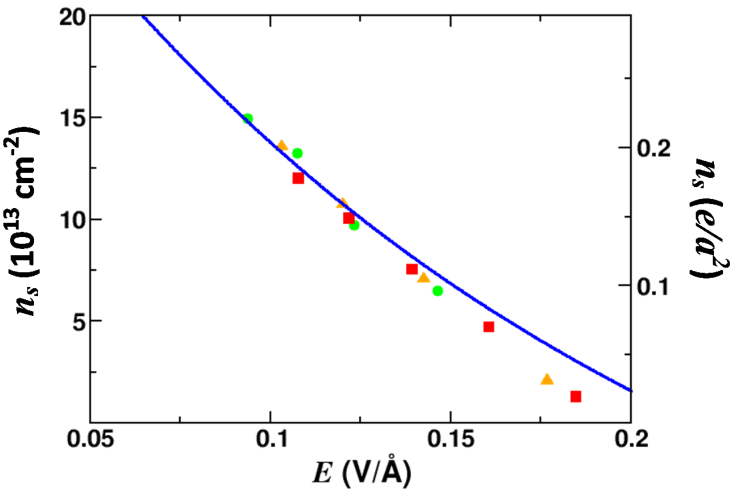

Figure 3.10: The sheet carrier density versus the internal electric field through the $LaAlO_3$ thin film. The red squares, orange triangles, and green circles are for the quantum well, the n-type, and the np-type interfaces, rspectively. The blue line is the result of the continuous model described in Section 3.4.1 .

density increases continuously with the thickness of the $LaAlO_3$ film, asymptoting to 0.5 e/a^2. This behavior qualitatively agrees with some experiments [15, 62], but conflicts with others [19], in which the sheet carrier density remains almost constant (15 times smaller than 0.5 e/a^2) after the critical separation. It is possible that the low sheet carrier density in Ref. [19] may be explained in terms of Anderson localization induced by disorder [79, 68].

3.3.6 External Field Effect

We have shown that there is an insulating-to-metallic transition as a function of $LaAlO_3$ thickness both in the $SrTiO_3/LaAlO_3$ interface and the quantum well (QW) systems. In this section, we examine the effects of inducing this transition at subcritical thicknesses via an applied electric field. We focus on the n-type interface and the QW system with 3 u.c. of $LaAlO_3$ (for both systems, the critical separation is 4 u.c. in the DFT simulations). To study the field effect, we apply a homogeneous electric field perpendicular to the interface. In order to avoid artificial effects from periodic boundary conditions (see Appendix A.2), we apply two electric fields of equal magnitude and opposite direction to each half of a symmetric simulation cell (see Fig. 3.11). Since the system is mirror symmetric, for

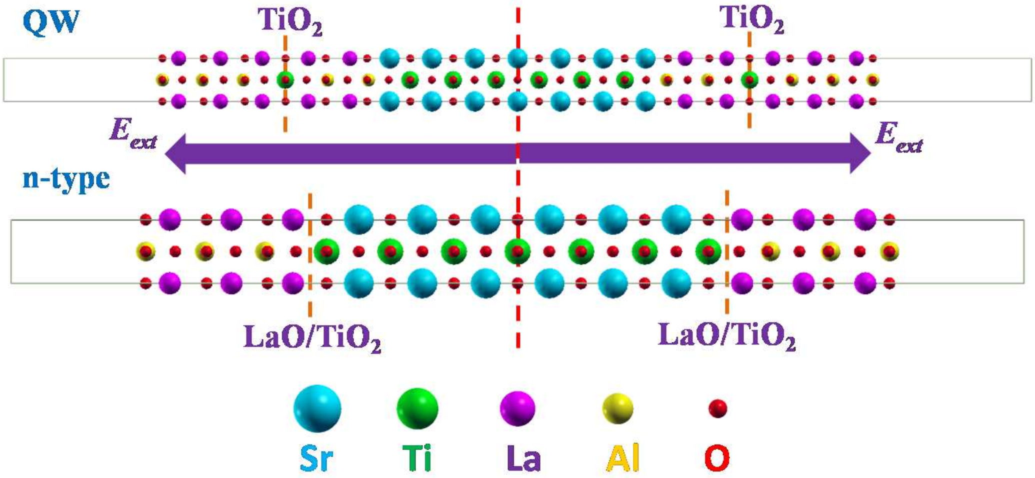

Figure 3.11: The supercells used for the field effect calculations. For the QW and the n-type interface, both simulation cells are mirror-symmetric. The external electric field is also mirror-symmetric. The dashed line in the middle is the symmetry axis. The embedded TiO_2 layer in the QW and the n-type interface LaO/TiO_2 are also highlighted by the dashed line.

simplicity we only focus on half of the simulation cell. At the n-type interface, the external electric field is parallel to the intrinsic electric field through the $LaAlO_3$ film, and in the QW systems, the direction is parallel to the field through the $LaAlO_3$ capping layer. Based on the polar catastrophe picture, such external electric fields will add to intrinsic electric fields and further reduce the energy gap, so that the insulating-to-metallic transition will occur at a subcritical separation.

We performed the simulations with different magnitudes of external electric field on both the n-type interface and QW systems. We need to elucidate a subtle point here: in the QW, the external electric field reduces the energy difference between the Ti d-states of the embedded TiO_2 layer and O p-states on the surface. This is the 'Ti-O energy difference' introduced in Section 3.3.2. Once this energy difference disappears, the insulating-to-metallic transition occurs. This energy difference is well defined because we can identify two Bloch states, one which characterizes the Ti d-states of the embedded TiO_2 layer and the other which characterizes the O p-states on the surface, and simply take their energy difference. At the n-type interface, the external electric field also reduces the energy difference between the Ti d-states of the first Ti atom at the interface and the

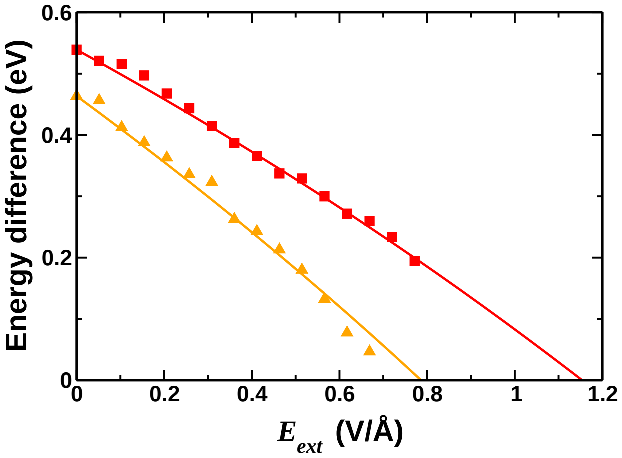

Figure 3.12: Energy differences versus the external electric field. The red squares and orange triangles correspond to the DFT-computed Ti-O energy difference for the QW systems and the energy gap of the n-type interface, respectively. The solid lines are the results of the continuous model described in Section 3.4.2.

O p-states on the surface. However, this energy difference is not easily identified because the external electric field also exists throughout the $SrTiO_3$ substrate, so the Bloch states that accept the transferred electrons are now composed of a mixture of all the Ti d-states in the $SrTiO_3$ thin film. For the purposes of this section, we simply extract the energy gap of this n-type interface system (between the O p-states on the surface and the lowest occupied Ti d-states) versus the external field. In Section 3.4.2, we will discuss more fully the relation of this energy gap and what would happen in an actual experiment.

In Fig. 3.12 we show the computed energy gap of the n-type interface and the Ti-O energy difference of the QW as a function of external electric field. As the figure shows, both monotonically decrease with increasing external electric field. Thus, the DFT simulations demonstrate how an external electric field can induce an insulating-to-metal transition.

3.4 Electronic reconstructions: continuous model

In order to shed more light on the nature of the $LaAlO_3/SrTiO_3$ interface, we develop a simple model which approximates the $LaAlO_3$ film as a homogeneous continuous medium. This model shows that the polar and dielectric properties of $LaAlO_3$ largely determine the

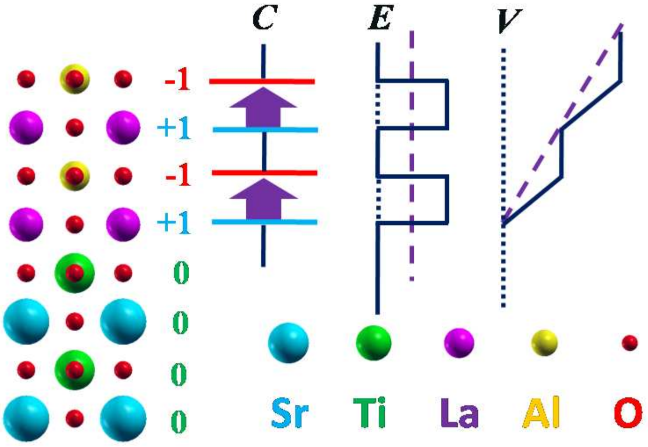

Figure 3.13: Schematic illustration of the continuous model. In the ionic limit, the $LaAlO_3$ thin film can be considered as a serial connection of capacitors. The electric field through $LaAlO_3$ is like an impulse and the resulting potential takes a stair shape.

thickness dependence of the sheet carrier density and the external field effect behavior.

3.4.1 Thickness dependence of sheet carrier density

In this section, we use model calculations, aided by DFT results, to quantitatively describe the insulating-to-metallic transition that occurs at the n-type and np-type interfaces and the quantum well (QW) systems. As detailed below, we find that the electric field dependence of dielectric constant of $LaAlO_3$ ϵ_L is critical to obtaining quantitative accuracy.

Before the insulating-to-metallic transition occurs, the alternating positively charged $(LaO)^+$ and negatively charged $(AlO_2)^-$ layers in the $LaAlO_3$ film can be idealized as a series of capacitors (see Fig. 3.13). As the figure illustrates, the thickness of each capacitor is only half of the unit cell of $LaAlO_3$ (there is zero voltage drop across the other half). Therefore the inner electric field through the $LaAlO_3$ behaves like an impulse and the resulting potential takes the shape of a stair function. If we approximate the $LaAlO_3$ thin film as a continuous homogeneous media and average this electric field, we can determine the average internal electric field:

$$\overline{E} = \frac{1}{2}\frac{4\pi\sigma_0}{\epsilon_L} = \frac{4\pi\overline{\sigma}}{\epsilon_L}, \tag{3.16}$$

where $\sigma_0 = e/a^2$ is an electron per two-dimensional unit cell, ϵ_L is the dielectric constant of $\mathrm{LaAlO_3}$, and

$$\overline{\sigma} = \frac{\sigma_0}{2} = \frac{e}{2a^2}. \tag{3.17}$$

Once the insulating-to-metallic transition occurs, some electrons transfer across the interface to counteract the internal electric field through the $\mathrm{LaAlO_3}$ thin film. The new average internal electric field through the $\mathrm{LaAlO_3}$ film is then given by:

$$\overline{E} = \frac{4\pi(\overline{\sigma} - \sigma_s)}{\epsilon_L}, \tag{3.18}$$

where σ_s is the transferred electron density, or sheet carrier density. It is easy to recast Eq. (3.18) into:

$$\sigma_s(\overline{E}) = \overline{\sigma} - \frac{\overline{E}\epsilon_L}{4\pi}, \tag{3.19}$$

where $\overline{\sigma} = 0.5e/a^2$. We also take into account that the dielectric constant ϵ_L depends on the internal electric field $\overline{E}$. The field dependence can be phenomenologically described by the Landau theory, and takes the following approximate form [87, 88] (also see Appendix A.3):

$$\epsilon_L(\overline{E}) \simeq \epsilon_0 \left(1 + \left(\frac{\overline{E}}{\mathcal{E}_0}\right)^2\right)^{-1/3}, \tag{3.20}$$

where ϵ_0 is the dielectric constant of $\mathrm{LaAlO_3}$ at vanishing electric field and $\mathcal{E}_0$ is a characteristic electric field. Eq. (3.19) and Eq. (3.20) establish a relation between the internal electric field $\overline{E}$ through the $\mathrm{LaAlO_3}$ and the sheet carrier density σ_s, both of which can be calculated independently from DFT simulations. We also performed a separate slab calculation (see Appendix A.3.1 for details) and determined the parameters ϵ_0 and $\mathcal{E}_0$ in Eq. (3.20) as:

$$\epsilon_0 = 40.95, \;\; \mathcal{E}_0 = 0.15\mathrm{V/Å} \tag{3.21}$$

Fig. 3.10 compares (E, σ_s) computed via DFT and the model. We can see from Fig. 3.10 that (E, σ_s) almost lies on the same curve in all three cases, which does not depend on the details of the structure. The continuous model shows a good agreement with the DFT results, and as the internal electric field decreases (i.e. the thickness of the $LaAlO_3$ increases), the continuous model becomes almost exact. This is expected because in the limit of an infinitely thick $LaAlO_3$ film, the interface and surface regions become neglegible. Our results show that even with only 7 u.c. of $LaAlO_3$ (*i.e.* the internal electric field $<$ 0.12 V/Å), the continuous model already works very well.

However, it is not easy to directly measure the internal electric field through the $LaAlO_3$ experimentally because the $LaAlO_3$ film is only a few unit cells thick. It is more useful to relate the sheet carrier density to the nominal thickness of the $LaAlO_3$ film (*i.e.* the number of $LaAlO_3$ unit cells grown on top of the $SrTiO_3$ substrate). Therefore, we need to find how the internal electric field through the $LaAlO_3$ depends on the $LaAlO_3$ thickness.

When the polar catastrophe takes place at the n-type interface, electrons leave the surface O-p states and are transfered into the Ti-d states. The charge transfer is halted once a common Fermi level is reached. Approximately, this means that the Ti-d conduction band edge of the $SrTiO_3$ substrate is at the same energy as the O-p surface valence band edge. Looking back at Fig. 3.3, we can see that there is a remanent field through the $LaAlO_3$ film and thus a potential difference. The existence of the electric field is also visible in Fig. 3.10 from our calculations. The potential difference across the $LaAlO_3$ thin film, denoted by K, can be related to the remanent internal electric field by:

$$e\overline{E}d = K \tag{3.22}$$

where d is the thickness of $LaAlO_3$. In principle K could depend on the thickness of $LaAlO_3$. But the detailed calculations show (see Fig. 3.14) that K quickly saturates to a constant as the thickness d gets larger. This could be understood because K is essentially determined by the energies of the relevant electronic states and the band offsets, which are interface properties and have little dependence on the thickness of $LaAlO_3$. We therefore approximate K as a constant. We illustrate later that this approximation does not significantly change the physics in the continuous model.

Inserting Eq. (3.22) into Eq. (3.19) and Eq. (3.20), we eliminate $\overline{E}$ and obtain:

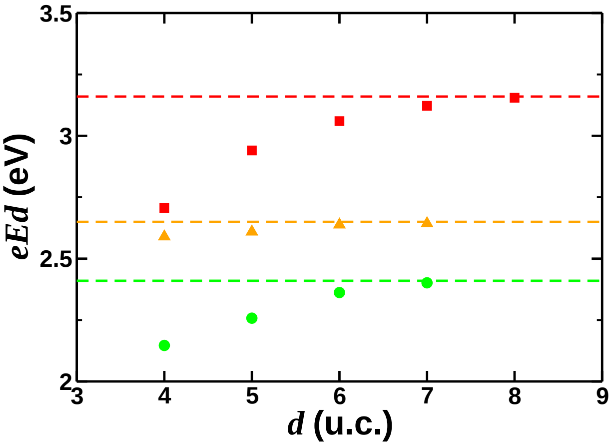

Figure 3.14: The potential difference across the $LaAlO_3$ thin film, defined by $e\overline{E}d$, of the quantum well (QW), the n-type and the np-type interfaces. Squares, triangles, and circles correspond to the QW, the n-type, and the np-type interfaces, respectively. $\overline{E}$ is the average internal electric field along the (001) direction through the $LaAlO_3$ thin film and d is the nominal number of $LaAlO_3$ unit cells (note that the $SrTiO_3$-strained $LaAlO_3$ lattice constant $a_{\rm LAO} = 0.953 a_{\rm STO}$). The dashed lines highlight the data point of the largest thickness in each interface configuration.

$$\sigma_s = \overline{\sigma} - \frac{K}{4\pi e d}\epsilon_0 \left(1 + \left(\frac{K}{e\mathcal{E}_0 d}\right)^2\right)^{-1/3} \tag{3.23}$$

Eq. (3.23) highlights some qualitative features of the sheet carrier density. The critical separation is the smallest d which makes $\sigma_s > 0$. Below the critical separation, the sheet carrier density is zero. Above the critical separation, the sheet carrier density gradually increases and then saturates to $\overline{\sigma} = 0.5e/a^2$ in the limit of large d.

The parameter K in Eq. (3.23) is determined as follows. We simulate n-type, np-type interfaces and QW with different thicknesses and calculate the macro-averaged smoothed electric field through the $LaAlO_3$ at each thickness. In Fig. 3.14, we show the potential difference across the $LaAlO_3$ thin film, defined by $e\overline{E}d$. We can see that in all three cases, $e\overline{E}d$ quickly saturates as d gets larger. Since we do not have a microscopic model to describe how the potential difference $e\overline{E}d$ changes with the thickness d, we use the last data (corresponding to the largest d) to determine the values of K, which are highlighted by the dashed line in Fig. 3.14. In each case, we find that

$$K_{\mathrm{QW}} = 3.16 \text{ eV}, \;\; K_n = 2.64 \text{ eV}, \;\; K_{np} = 2.40 \text{ eV}. \tag{3.24}$$

The K in all three cases turn out to be different from each other and larger than the DFT-computed band gap of $\mathrm{SrTiO_3}$ (1.85 eV). This is partly because the band offsets of these three cases are not the same. However, the small valence band offsets alone [55, 53] can not explain the big difference between the K value and $\mathrm{SrTiO_3}$ band gap. A more important factor is that we treat $\overline{E}$ as a uniform electric field throughout the $\mathrm{LaAlO_3}$ thin film. However, close to the interface and surface, the internal electric field should be different from that in the middle of the $\mathrm{LaAlO_3}$ film but difficult to average in those regions. Therefore we use an approximate relation ($K = e\overline{E}d$) to determine the potential difference, but as shown later, this approximation is good enough to reproduce the DFT-calculated thickness dependence of sheet carrier density.

Equipped with K, ϵ_0 and $\mathcal{E}_0$, we can calculate the sheet carrier density at different thicknesses using Eq. (3.23). We compare the sheet carrier densities calculated from the continuous model with those from the DFT simulations. The results are shown in Fig. 3.9. The agreement is good in all three cases even though Eq. (3.22) is not exact.

We would like to comment that recently Son *et al.* [68] also calculated the thickness dependence of sheet carrier density and they made a similar model by assuming that the dielectric constant of $\mathrm{LaAlO_3}$ has no field dependence and is simply constant. Rather than Eq.(3.23), they had a simpler formula

$$\sigma_s = \overline{\sigma}\left(1 - \frac{d_c}{d}\right) \tag{3.25}$$

where $\overline{\sigma}$ and d_c are two constants determined by fitting. They found $\overline{\sigma} = 0.455e/a^2$, close to the ideal value $0.5e/a^2$. Our analysis is different in that we fix $\overline{\sigma} = 0.5e/a^2$, which is necessitated by the polar catastrophe mechanism, but take into account that the dielectric constant of $\mathrm{LaAlO_3}$ has a strong field dependence, as confirmed by the DFT calculations.

3.4.2 External electric field

In order to get a more quantitative description of the external field effect, we apply the continuous model established in the previous section. In principle, at the subcritical separation (3 u.c.), the continuous model should break down because the $\mathrm{LaAlO_3}$ film is so thin that the interface and surface regions cannot be neglected and the $\mathrm{LaAlO_3}$ is no longer uniform. However, we simplify the situation by assuming that $\mathrm{LaAlO_3}$ is still a homogeneous media with the dielectric constant given by Eq. (3.20) with the parameters Eq. (3.21), but has an effective thickness d_{eff}. In order to simplify our notations, we use E instead of $\overline{E}$ to denote the averaged macroscropic fields.

Based on the above argument, for the quantum well systems we have:

$$\Delta = \Delta_0 - (E^L - E_0^L) d_{eff}^L, \tag{3.26}$$

where 'L' stands for $\mathrm{LaAlO_3}$. Δ is the Ti-O energy difference at a given E_{ext} and E^L is the internal electric field. Δ_0 and E_0^L indicate the values of Δ and E^L, respectively, at vanishing external electric field:

$$E^L = \frac{4\pi\overline{\sigma} + E_{ext}}{\epsilon_L(E^L)} \tag{3.27}$$

and

$$E_0^L = \frac{4\pi\overline{\sigma}}{\epsilon_L(E_0^L)} \tag{3.28}$$

Equations (3.26, 3.27, and 3.28) establish the relation between Δ and E_{ext}. The effective thickness cannot be given *a priori* from the model. Instead, we fit the data and find $d_{eff}^L = 5.9\text{Å} = 1.6$ u.c. A comparison of (E_{ext}, Δ) for the quantum well systems using DFT calculations and the model calculations is shown in Fig. 3.12.

For the n-type interface, we also need to account for the potential drop in the $\mathrm{SrTiO_3}$ due to the external electric field. Therefore we have:

$$\Delta = \Delta_0 - (E^L - E_0^L) d_{eff}^L - E^S d_{eff}^S \tag{3.29}$$

where 'S' stands for $SrTiO_3$. Δ is the energy gap of the system and Δ_0 is the value of Δ at vanishing external electric field. Note that in the absence of an external electric field, the $SrTiO_3$ film is unpolarized in the continuous model. E^S and E_{ext} are related by:

$$E^S = \frac{E_{ext}}{\epsilon_S(E^S)} \tag{3.30}$$

We use the Berry phase method [89] to calculate $\epsilon_S(E)$ and fit the data using Eq. (3.20) (see Appendix A.3.2 for details). The results of the fit are:

$$\epsilon_0^S = 309.6, \mathcal{E}_0^S = 49.2\text{V}/\mu\text{m} = 4.92 \times 10^{-2}\text{V/Å} \tag{3.31}$$

We find that the values of d_{eff}^L in different systems are different. Hence, in principle we have two fitting parameters in Eq. (3.29): d_{eff}^L and d_{eff}^S. However, it turns out that Eq. (3.29) very insensitively depends on d_{eff}^S. This is expected because the dielectric constant of $SrTiO_3$ is at least 10 times larger than that of $LaAlO_3$ and the nominal thicknesses of $LaAlO_3$ and $SrTiO_3$ are both 3 u.c. in the DFT calculations (see Fig. 3.11), and thus the potential drop across the $SrTiO_3$ is much smaller than that across the $LaAlO_3$ film. Therefore we just use the real thickness of $SrTiO_3$ $d_{eff}^S = 11.1$ Å (from the relaxed structure) and fit the data with d_{eff}^L. We find: $d_{eff}^L = 7.5$ Å$\simeq$ 2 u.c. Fig. 3.12 compares the values of (E_{ext}, Δ) of the n-type interface computed by DFT and the model, respectively.

Fig. 3.12 shows that the critical electric fields E_{ext}^c extracted from the DFT calculations for the n-type interface and the QW are 0.79 and 1.15 V/Å, respectively. In the continuous model, the critical voltage across the whole sample is given by:

$$V_c = \frac{E_{ext}^c + 4\pi\overline{\sigma}}{\epsilon_{\text{LAO}}} d_{\text{LAO}} + \frac{E_{ext}^c}{\epsilon_{\text{STO}}} d_{\text{STO}} \tag{3.32}$$

where d_{LAO} and d_{STO} are the thickness of $LaAlO_3$ and $SrTiO_3$, respectively. $\overline{\sigma} = 0.5e/a^2$ and E_{ext}^c is the critical external electric field. In order to estimate the critical voltage for the experimental setup, we need to use the thickness of the $SrTiO_3$ substrate in experiment.

Here we need to clarify some subtleties: in the presence of applied external field, DFT simulations do not realistically represent the spatial distribution of conduction electrons.

Fig. 3.15 illustrates the reason for the discrepancy. In the DFT simulations, the conduction electrons fill the lowest energy states. Since the "external" field bends the $SrTiO_3$ conduction bands, these states are located at the bottom surface of the $SrTiO_3$ substrate, as shown schematically in Fig. 3.15a. Although in principle the experimental situation is the same, realistically, electrons can only tunnel a few unit cells from the surface; thus they get trapped at the n-type interface, as illustrated in Fig. 3.15b. The trapping mechanism is the Ti-La interfacial hopping, which lowers the energy of the Ti atom closest to the interface and creates the energy barrier through which the electrons must tunnel. Hence, the real critical field has to be larger than the computed one, so that the energy of surface states equals that of the interface states (Fig. 3.15b). The critical external field E_{ext}^c we obtain from DFT simulations is therefore only a lower bound.

Now we make a simple estimation of the lower bound: at low temperatures (< 5 K), the dielectric constant of $SrTiO_3$ can be as large as 2.5×10^4 [90] and the thickness of the $SrTiO_3$ substrate is typically $\simeq 1$ mm. Considering that $\epsilon_{\mathrm{LAO}} \simeq 30$ and $d_{\mathrm{LAO}} \simeq 10$ Å, the second term in Eq.(3.32) is dominant. Therefore, for the n-type interface, we have:

$$V_c^{n\text{-type}} \simeq \frac{E_{ext}^c}{\epsilon_{\mathrm{STO}}} d_{\mathrm{STO}} \simeq 320 \text{ V} \tag{3.33}$$

and for the QW,

$$V_c^{\mathrm{QW}} \simeq \frac{E_{ext}^c}{\epsilon_{\mathrm{STO}}} d_{\mathrm{STO}} \simeq 480 \text{ V} \tag{3.34}$$

As these estimates are based on data from DFT simulations in which the band gap of $SrTiO_3$ is underestimated, they provide only lower bounds on the critical voltage. Experimentally, the critical voltage of the n-type interface with a 1 mm thick $SrTiO_3$ substrate has been measured to be $\simeq 70$ V at low temperature [19], which is much smaller than our estimates. The discrepancy may imply that the simple model of an ideally sharp interface is not sufficient to model the external field doping, due to additional details that play an important role at the n-type interface. Various types of atomic reconstructions, such as cation intermixtures at the interface [66] or oxygen vacancies on the surface [20] may possibly trigger an insulating-to-metallic transition, leading to a smaller critical voltage.

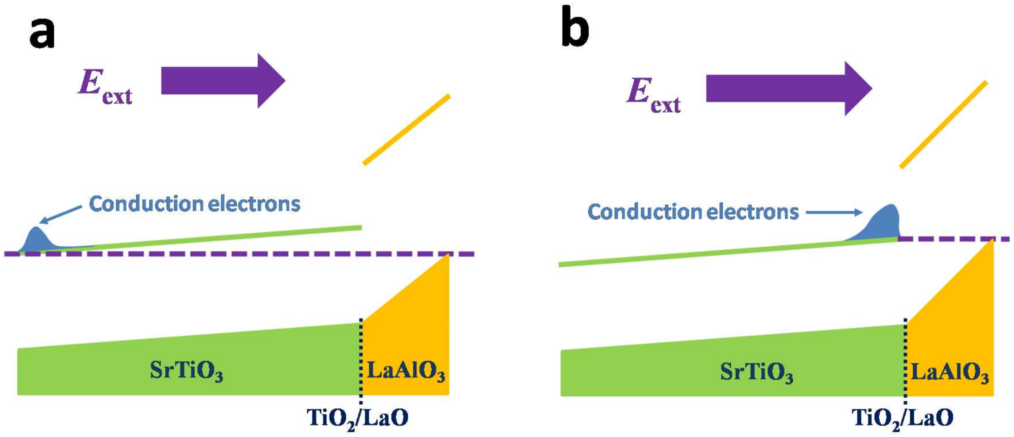

Figure 3.15: **a)** The spatial distribution of conduction electrons in the DFT simulations. The conduction electrons occupy the lowest energy states available, which are located at the bottom surface. **b)** The spatial distribution of conduction electrons in the actual experiment. The conduction electrons get trapped at the n-type interface by the tunneling barrier due to the self-consistent potential well formed at the interface that largely stems from the Ti-La hopping. The length of arrows illustrates the magnitude of external field.

3.5 Atomic reconstructions

In this section, we start our discussion on atomic reconstructions at SrTiO$_3$/LaAlO$_3$ interfaces. We focus on the n-type interface, since this interface shows interesting electronic properties that are missing in both bulk constituents. Each of the following three subsections is devoted to one type of defect. In every subsection, a brief description of methodology is presented, followed by DFT results and modelling, as well as discussion on the effect of electronic structures.

3.5.1 Cation intermixtures

Methodology

In order to calculate the total energy with various cation intermixture configurations, we include four unit cells of SrTiO$_3$ to simulate the substrate. The one unit cell of SrTiO$_3$ facing the surface is fixed at ideal positions to simulate the bulk-like region. A schematic of supercell is shown in Fig. 3.16. To study the position dependence, we employ a $c(2 \times 2)$ in-plane cell to accommodate 50% mixing. For the investigation of concentration dependence,

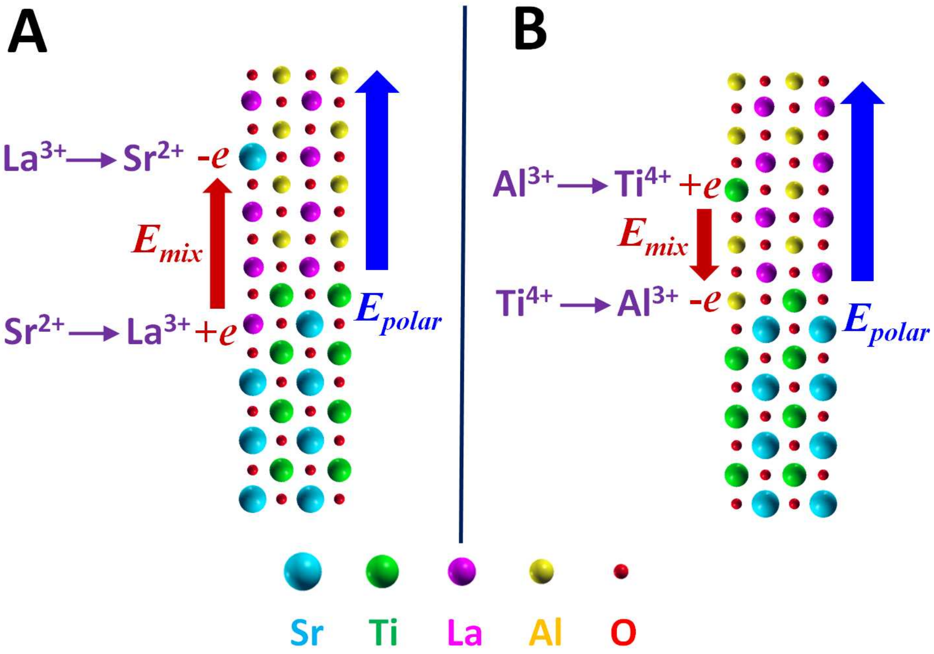

Figure 3.16: Schematic of simulation cell for cation intermixtures. **A**) Sr-La intermixture and **B**) Ti-Al intermixture. In **A**), the induced electric field by cation mixing is parallel to the polar field through $LaAlO_3$ thin films, while in **B**) the two electric fields are anti-parallel.

we choose various in-plane cells: 1 × 1, 1 × 2 and 1 × 3 to simulate 0%, 33%, 50%, 67% and 100% cation intermixing.

Results

In this section, we discuss the energetics of cation intermixtures. Cation intermixtures are common at oxides interface [91]. At the $LaAlO_3/SrTiO_3$ interface, two types of cation intermixtures are considered: Sr-La intermixture and Ti-Al intermixture, both of which were observed in experiment [58]. In our simulations, we considered one type of cation intermixtures at a time. Before we go into the details of the calculations, we qualitatively analyze how cation intermixtures change the electrostatics at the n-type interface. Fig. 3.16 shows a schematic of internal electric field at the $LaAlO_3/SrTiO_3$ interface. At ideal interfaces, a constant electric field generated by half an electron is through $LaAlO_3$ thin films. Both types of cation intermixtures (Sr-La and Ti-Al) induce an additional electric

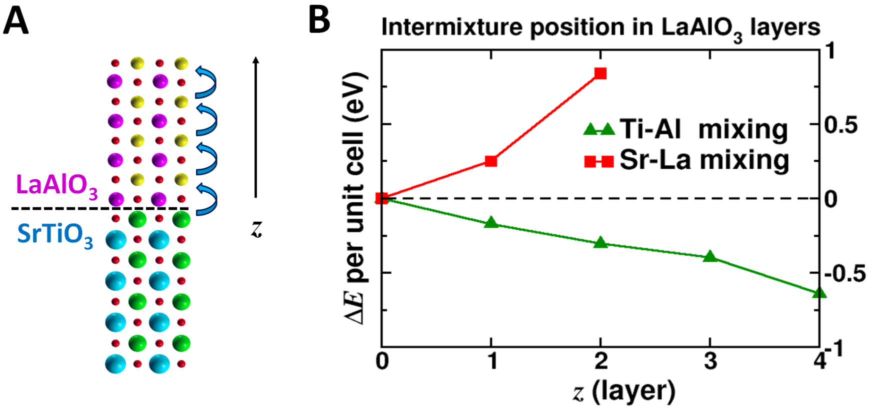

Figure 3.17: **A**) Schematic of a $c(2 \times 2)$ simulation cell in which one Sr(Ti) atom is switched with another La(Al) atom. The switched La(Al) atom is at the interface while the intermixing Sr(Ti) atom gradually moves to the surface of LaAlO$_3$. **B**) Energetics of Sr-La and Ti-Al intermixtures ($\eta = 50\%$). ΔE is the energy difference between the structure with the cation intermixture and the ideal structure. Layer 0 is the interface.

field, the direction of which could be either parallel or anti-parallel to the original internal electric field. Sr-La intermixtures always enhance the internal field and therefore thermodynamically they are unfavorable. Ti-La intermixtures counteract the original internal field. Since every Ti-La intermixture induces an additional field equivalent to that generated by e, and the original field is produced by $0.5e$, we can argue that when the concentration of Ti-Al intermixtures is less than 50%, the internal field is suppressed as the concentration increases and therefore Ti-Al intermixtures are energetically favorable; if the concentration exceeds 50%, the internal field increases again with the opposite direction and Ti-Al intermixutures are thus unfavorable thermodynamically. In order to quantitatively verify the preceding picture, we perform *ab initio* calculations on both types of cation intermixtures. We try to answer two questions: one is that given a concentration, denoted by η, where is the most preferred position for intermixtures? The other is that given the position of intermixtures z, how does the concentration affect the energetics?

For the first question, we perform calculations with a $c(2 \times 2)$ in-plane cell and with one Sr(Ti) atom being switched with another La(Al) atom. The switched La(Al) atom is in the first unit cell closest to the interface, and the intermixing Sr(Ti) atom is moving from the interface to the surface of LaAlO$_3$, as is illustrated in Fig. 3.17A. For each position of intermixture z, we relax all the atoms (except for the bottom unit cell of $SrTiO_3$ to simulate the bulk-like substrate) and obtain the total energies, which are summarized in Fig. 3.17B. We can see that as expected from the preceding simple electrostatic argument, 50% Sr-La intermixture enhances the internal field through $LaAlO_3$ and increases the total energy as its position gets further away from the interface. On the other hand, 50% Ti-Al intermixture reduces the internal field and with its position approaching the surface, the total energy monotonically decreases.

Now we study the concentration dependence to answer the second question. For simplicity, we assume the intermixture is always in the surface layer. We use the ideal structure as the reference and calculate the energy difference per interface cell for both types of intermixture. The data are collected in Fig. 3.18. Consistent with the simple electrostatic analysis, Sr-La intermixtures (Fig. 3.18A) strengthen the internal polar field and monotonically increase the total energy with intermixture concentration and thickness of $LaAlO_3$. For Ti-Al intermixtures (Fig. 3.18B), the general trend of energy difference agrees with the electrostatic argument in that the polar field is reduced as the concentration is less than 50%, and above 50% the polar field is restored again. Accordingly, the total energy decreases and then increases again. However, though the nominal charge at the ideal interface is $0.5e$, at 100% Ti-Al is supposed to completely reverse the polar field with the same magnitude as the ideal case, DFT calculations show that the total energy is not fully restored to the ideal one, which can not be explained from the simple electrostatic model. The total energy at 100% Ti-Al intermixture is lower than the ideal structure by almost a constant amount regardless of $LaAlO_3$ thickness, which indicates this is a surface effect. With the Ti atom switched with Al atom on the surface, an extra energy gain occurs, which is proportional to the concentration but independent of $LaAlO_3$ thickness. Combining all these effects, we make a simple continuous model to describe the energy difference of cation intermixtures for a more quantitative understanding. For energy difference per interface cell, the simple model leads to (the derivation is in Appendix A.4):

$$\Delta E(d,\eta) = \begin{cases} 4kd(\eta^2+\eta) & \text{(Sr-La)} \\ 4kd(\eta^2-\eta)+b\eta & \text{(Ti-Al)} \end{cases} \tag{3.35}$$

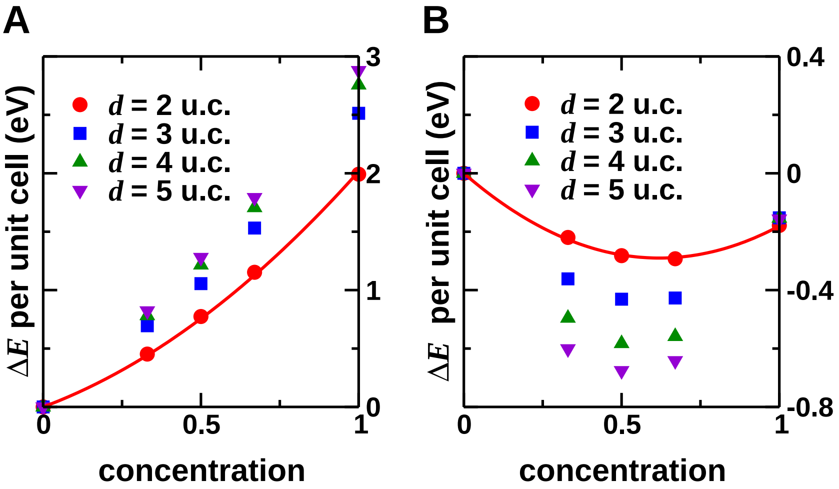

Figure 3.18: Concentration dependence of energy differences between the structure with cation intermixture and the ideal structures. d is the thickness of $LaAlO_3$. The solid line is the fitting using Eq. (3.35). **A**) Sr-La intermixtures and **B**) Ti-Al intermixtures.

where k and b are two fitting parameters. For the case of $d = 2$, the fitting yields excellent agreement with the DFT calculations for both types of intermixtures. It is worthy to mention that if we treat $LaAlO_3$ as continuous media in a rectangular box, k can be written as $\pi e^2/(2a^2\epsilon_{\text{LAO}})$. Quoting $\epsilon_{\text{LAO}} = 41$ from our ealier calculations [26], we can obtain $k = 0.037$ eV/Å. From the fitting, we find $k = 0.034$ eV/Å for Sr-La intermixtures and $k = 0.026$ eV/Å for Ti-Al intermixtures, which demonstrates that a simple continuous model based on electrostatics is a reasonable description for cation intermixtures.

At thickness other than 2 unit cells, qualitatively the energy differences have same dependence on concentration. However, quantitatively the simple model Eq. (3.35) breaks down because the polar catastrophe occurs at some concentration as the $LaAlO_3$ thickness is above 2 unit cells. Fig. 3.19 shows the integrated Ti-d states below the Fermi level. At $d = 2$ unit cells, for both types of intermixtures the structures remains insulating at all the concentrations. Fig. 3.19A shows that from $d = 3$ unit cells, Sr-La intermixtures drive the system to be metallic. This crtical thickness is smaller than that of ideal structures,

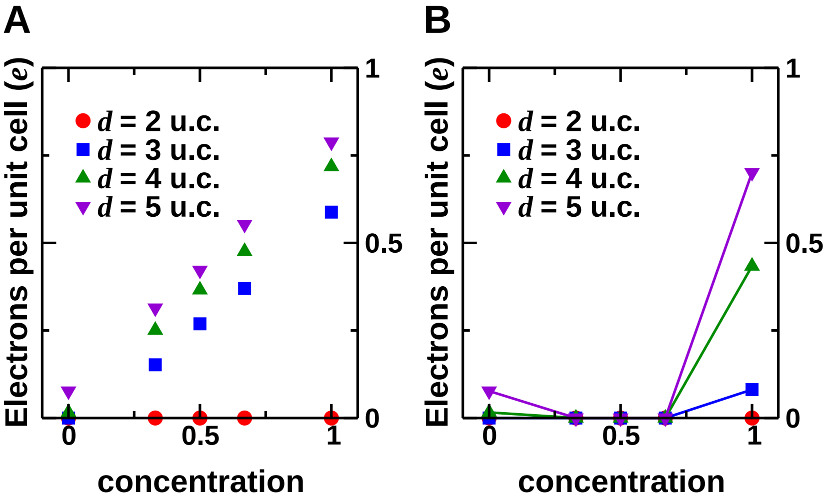

Figure 3.19: Concentration dependence of transferred electrons into the Ti-*d* states of $SrTiO_3$ conduction bands. *d* is the thickness of $LaAlO_3$. **A**) Sr-La intermixtures and **B**) Ti-Al intermixtures.

which is 4 unit cells. This is consistent with the electrostatic analysis in that the polar field is enhanced with Sr-La intermixtures and the system band gap is closed at a smaller thickness of $LaAlO_3$. The transferred electrons on Ti *d*-states are approximately linearly increasing with the intermixture concentration because the system band gap is fixed by the Ti *d*-states and the surface O *p*-states, and the internal field is strengthened linearly with the intermixtures. Therefore, electrons that transfer from surface to interface and compensate for any additional internal field induced by cation intermixtures should be proportional to the amount of intermixtures themselves. On the other hand, around 50% Ti-Al intermixtures almost cancel the internal polar field and the polar catastrophe is not expected to occur at any thickness, which is consistent with Fig. 3.19B. For ideal structures (the concentration is 0) and 100% Ti-Al intermixtures, the internal polar field is not compensated and with the increasing $LaAlO_3$ thickness, the polar catastrophe occurs at some critical point.

Discussion

The results of possible cation intermixtures presented in the previous section demonstrate that the pristine structures are not thermodynamically stable. Ti-Al intermixtures provide another mechanism to compensate for the polar field through $LaAlO_3$ thin films, in addition to the electronic reconstructions, the so-called polar catastrophe mechanism. However, we only study the thermodynamics from our DFT calculations. How cations find an optimal path to overcome energy barriers and reach the most favorable configurations is not clear. If energy barriers are high, such as for the case of Sr-La intermixtures, it is likely that the system is not in equilibrium, but rather gets stuck in a metastable state. A comprehensive investigation on kinetics of cation intermixtures is complicated, partly due to the lack of detailed information of optimal diffusion paths. However, our results do imply that in the growth chamber where the temperature is high and atoms have enough kinetic energy, it is possible that the atoms in the heterostructures are not "placed" at their ideal positions.

3.5.2 Oxygen vacancies on $LaAlO_3$ surfaces

Methodology

First of all, we need to clarify the definition of oxygen vacancy concentrations. Different from cations (Sr^{2+}, La^{3+}, etc.), there are two oxgyen atoms in each 1×1 in-plane cell. We define that with one oxygen vacancy every M 1×1 in-plane cell, the concentration ξ is $1/M$. Therefore 100% oxygen vacancy is one vancancy every 1×1 in-plane cell, but it does not mean all the oxygen atoms are gone (the other oxygen atom still remains in the cell). This convention to count oxygen vacancies could be sometimes confusing (with two oxygen atoms gone in the same 1×1 cell, the concentration is 200% by this definition), but we follow other researchers [20].

Since we are interested in oxygen vacancies with very low concentration (which is more realistic), we have only two unit cells of $SrTiO_3$ with the bottom layer fixed as bulk positions to simulate the substrate. The convergence of formation energy with the thickness of $SrTiO_3$ is discussed in the next section. Given the same concentration, oxygen vacancies can be arranged in different ways: either in stripes or in squares. Fig. 3.20 illustrates these two arrangements. For stripes, we use an in-plane cell $1 \times M$ ($M = 1, 2, ..8, 9$) to simulate

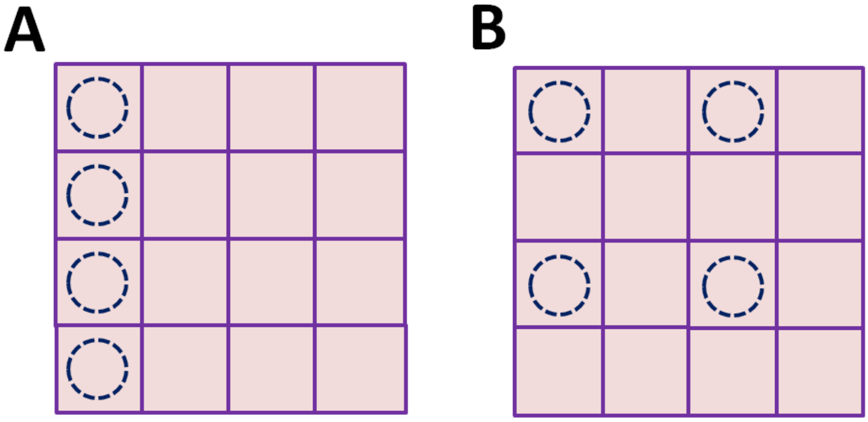

Figure 3.20: Schematics of different arrangements of oxygen vacancies. **A**) Oxygen vacancies are arranged in stripes. **B**) Oxygen vacancies are arranged in squares.

the concentrations from 100% to as low as 11%. For squares, we employ an in-plane cell $\sqrt{M} \times \sqrt{M}$ ($M = 1, 2, 4, 5, 8, 9, 10$) to simulate the concentrations: 10%, 11%, 12.5%, 25%, 50% and 100%. Formation energies of oxygen vacancies strongly depend on the arrangement, which is discussed in the next section in detail.

We also study the clustering of oxygen vacancies on $LaAlO_3$ surfaces. With a given concentration of oxygen vacancies, we double the lateral size of simulation cell and place two oxygen vacancies in the simulation cell. We calculate the total energy as a function of the separation between the two oxygen vacancies.

Formation energy

Oxygen vacancies are observed at $SrTiO_3/LaAlO_3$ interfaces in a number of experiments [59, 60, 61]. It is widely believed that oxygen vacancies can be created in $SrTiO_3$ substrates when the sample is grown at low oxygen partial pressure, which leads to a three-dimensional mobile electron gas. However, after annealing at high oxygen partial pressure, the mobile electron gas becomes essentially two-dimensional, indicating that most oxygen vacancies in $SrTiO_3$ are eliminated [69]. We are now interested in the question that with an ideal n-type interface, is there any intrinsic mechanism (no growth condition involved) to generate oxygen vacancies? In fact, it is proposed that oxygen vacancies may be created on $LaAlO_3$

surfaces to compensate for the polar field in $LaAlO_3$ thin films [20] and recently theoretical calculations show that when the polar field is not completely compensated, $LaAlO_3$ surfaces are the energetically most favorable places for oxygen vacancies to occur [92]. Here we focus on oxygen vacancies on $LaAlO_3$ surfaces and perform a comprehensive thermodynamical analysis on their formation energies. We focus on two important and relevant variables: one is the thickness of $LaAlO_3$, denoted by d and the other is the concentration ξ.

The formation energy of oxygen vacancies is defined as [93]:

$$E_{\mathrm{f}}(V_{\mathrm{O}}) = E_{\mathrm{tot}}(\mathrm{defect}) - E_{\mathrm{tot}}(\mathrm{perfect}) + \frac{1}{2}E_{\mathrm{O}_2} + \mu_{\mathrm{O}} \tag{3.36}$$

E_{O_2} is the total energy of an oxygen molecule and μ_{O} is the chemical potential of oxygen. $E_{\mathrm{tot}}(\mathrm{defect})$ is the total energy of the structure with one oxygen vacancy and $E_{\mathrm{tot}}(\mathrm{perfect})$ is the total energy of pristine structure. Like the study of cation intermixtures, we assume that electrostatic energies dominate. From the electrostatic analysis, $0.5e$ per 2D unit cell is enough to completely compensate for the internal polar field through $LaAlO_3$. Since every oxygen vacancy can donate at most two electrons, the critical concentration is 25%. Above 25%, $0.5e$ per 2D unit cell is transferred from the surface to the interface to completely cancel the internal polar field through $LaAlO_3$ thin films, and each oxygen vacancy on the surface is partially ionized. Below the concentration of 25%, each oxgyen vacancy completely donates two electrons, but the internal polar field is only partially compensated (due to low ξ). Based on this simple model, we can analytically derive the oxgyen vacancy formation energy as a function of $LaAlO_3$ thickness d and concentration ξ (See the appendix for details on derivation).

$$E_{\mathrm{f}}(V_{\mathrm{O}})(\xi, d) = \begin{cases} \alpha + \beta d(4\xi - 2) & (\xi \leq 25\%) \\ \alpha + \beta d/(4\xi) & (\xi > 25\%) \end{cases} \tag{3.37}$$

where α and β are two fitting parameters.

Before we test our simple electrostatic model Eq. (3.37) and go into details of defect calculations, we first need to calculate E_{O_2} and μ_{O}. As is well known, local density approximation describes oxygen bonds poorly [94]. The binding energy of oxygen bonds

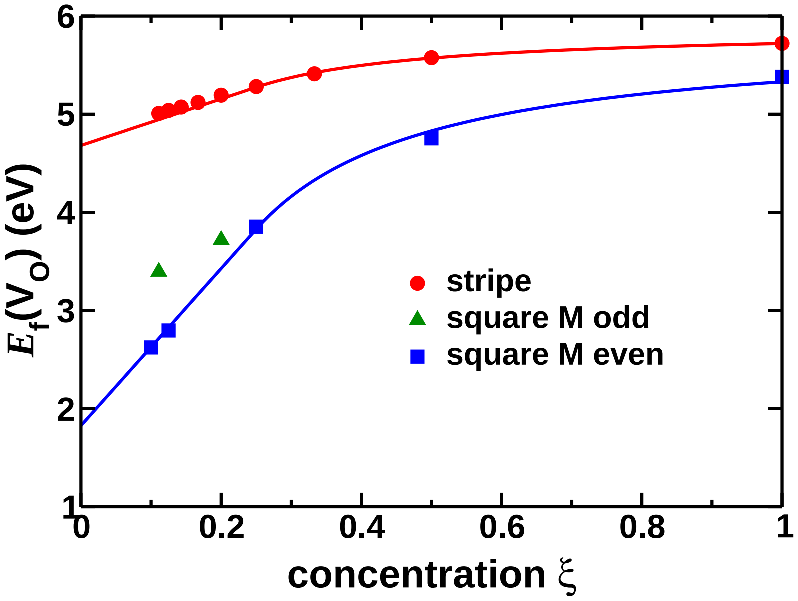

Figure 3.21: Comparison of formation energy of oxygen vacancies with different arrangements. The thickness of $LaAlO_3$ is 2 unit cells. The solid lines are fitting results using Eq. (3.37).

is defined as follows:

$$E_{\text{bind}} = 2E_{\text{O}} - E_{\text{O}_2} \tag{3.38}$$

The experimental value of E_{bind} is 5.23 eV and our LDA calculation yields E_{bind} =7.45 eV. Such a big error is consistent with previous calculations [94]. The reason is that local density approximation is not accurate enough for chemical bonds where electron density is far from uniform. On the other hand, we assume that an isolated oxgyen atom is reasonably described by local density approximation, since no bonding mechanism is involved. In order to better calculate E_{O_2}, we use the experimental value of $E_{\text{bind}}^{\text{exp}}$, LDA-calculated E_{O} and Eq. (3.38) to obtain a corrected E_{O_2}. Therefore we have:

$$E_{\text{O}_2}^{\text{corr}} = E_{\text{O}_2}^{\text{LDA}} + \left(E_{\text{bind}}^{\text{LDA}} - E_{\text{bind}}^{\text{exp}}\right) = E_{\text{O}_2}^{\text{LDA}} + 2.22 \text{ eV} \tag{3.39}$$

We use $E_{\text{O}_2}^{\text{corr}}$ throughout the remainder of discussion. The chemical potential of oxygen is

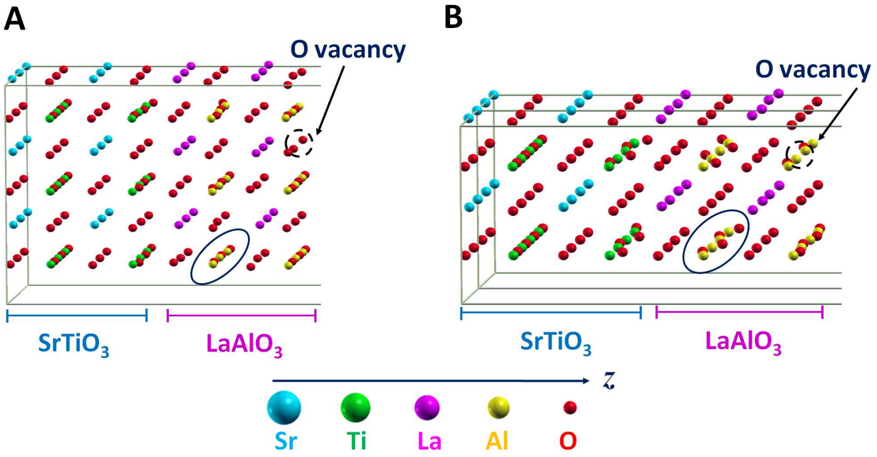

Figure 3.22: Comparison of different in-plane $\sqrt{M} \times \sqrt{M}$ simulation cells. **A**) 3×3 (M is odd) in-plane cell in which $GdFeO_3$ distortions are suppressed. **B**) 2×2 (M is even) in-plane cell which accommodates the $GdFeO_3$ distortions and lowers the oxygen vacancy formation energies.

tabulated as a function of temperature and pressure. Under the typical growth conditions (temperature T=1100 K and partial oxygen pressure p_{O_2}=10^{-6} atm), the chemical potential $\mu_O = -1.93$ eV. The details of how to calculate oxygen chemical potential μ_O are in the Appendix A.6.

Now we discuss the defect calculations in details. We first focus on 2 unit cells of $LaAlO_3$. The results are shown in Fig. 3.21. The symbols are DFT data and the solid lines are fitting results using the simple model Eq. (3.37). Just as we point out in the previous section, oxygen vacancies can be arranged differently, either in stripes or in squares (see Fig. 3.20). Fig. 3.21 shows that the formation energy of oxygen vacancies arranged in squares are significantly lower than that of oxygen vacancies arranged in stripes. The reason is that different arrangements (i.e. corresponding to different simulation cells) allow for different degrees of freedom. As oxygen vacancies are formed on square lattices (i.e. $\sqrt{M} \times \sqrt{M}$), and as M is even, $GdFeO_3$ distortions can be accommodated, which lowers the formation energy [9]. As M is odd, $GdFeO_3$ distortions are suppressed. If oxygen vacancies are formed in stripes, then the $1 \times M$ in-plane simulation cell completely disables $GdFeO_3$ distortions and also raises the total energy due to the repulsion between the charged vacancies, both of which lead to the much larger formation energy. A comparison

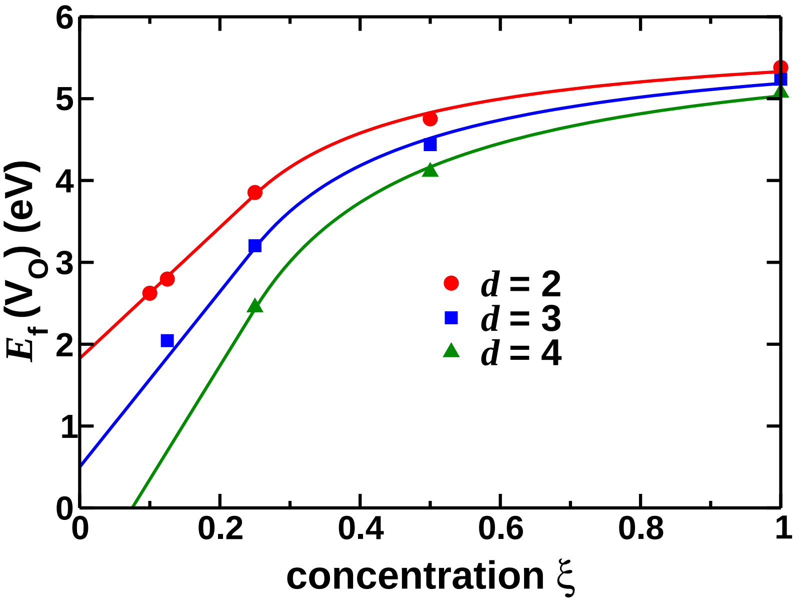

Figure 3.23: Dependence of oxygen vacancy formation energies on the thickness of $LaAlO_3$. All the calculations are done with the arrangement of oxygen vacancies in $\sqrt{M} \times \sqrt{M}$ in-plane cell (M is even).

of structures between 3 × 3 (11% oxygen vacancies) and 2 × 2 (25% oxygen vacancies) is shown in Fig. 3.22. In the even M case (Fig. 3.22B), the strong zig-zag chain pattern in AlO_2 layers is the direct evidence of $GdFeO_3$ distortions, which is suppressed in the odd M case (Fig. 3.22A).

From now on, we focus on the geometry with oxygen vacancies arranged in squares (i.e. $\sqrt{M} \times \sqrt{M}$) and M being even, which accommodates $GdFeO_3$ distortions and leads to the lowest formation energy of oxygen vacancies. Fig. 3.21 shows that at the thickness of $LaAlO_3$ $d = 2$ unit cells, the formation energy of an isolated oxygen vacancy is 1.87 eV, extracted out from the simple model Eq. (3.37). From the preceding analysis of electrostatics, increasing the thickness of $LaAlO_3$ d could lower the formation energy, as is shown in Eq. (3.37). We perform DFT simulations to support this analysis, with the results shown in Fig. 3.23. From the fitting, we find that increasing the thickness of $LaAlO_3$ could significantly lower the formation energy of oxygen vacancies, especially at low concentrations. At $d = 4$ unit cells, below 8% of concentration, the formation energy of oxygen vacancy

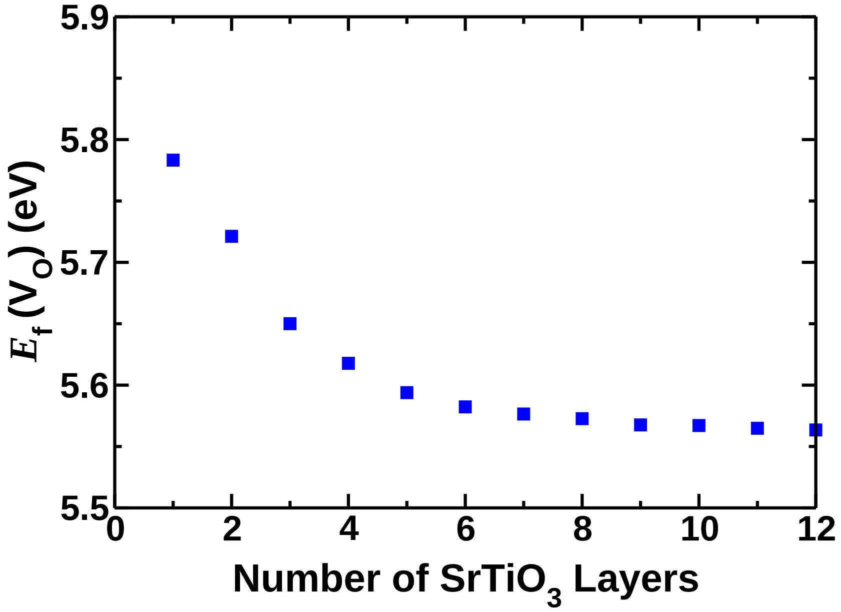

Figure 3.24: Convergence check of the oxygen vacancy formation energy on the thickness of SrTiO$_3$. The concentration of oxygen vacancies is 100% and the calculation is performed in a 1×1 unit cell.

becomes negative, indicating that oxygen vancacies can be spontaneously formed and an insulating-to-metallic transition occurs. This is an interesting result, which shows that due to the polar field through LaAlO$_3$, oxygen vacancies can be formed on the surface of 4 unit cells of LaAlO$_3$ and donate electrons from surface to interface. This fortuituously agrees with the critical thickness observed in experiment but more importantly provides a scenario in which there are only electrons at the interface and no holes on the surface.

Before we conclude the discussion of formation energy of oxygen vacancies, we need to finally mention that due to the computation limitations, we only include two unit cells of SrTiO$_3$ to simulate the SrTiO$_3$ substrate. We study the effect of thickness of SrTiO$_3$ on the formation energy by calculating 100% concentration of oxygen vacancies. Since the in-plane cell is only 1×1, we can include thick SrTiO$_3$ to check the convergence. The result is shown in Fig. 3.24. With the SrTiO$_3$ substrate thickens, the formation energy decreases and finally converges around 9 unit cells of SrTiO$_3$. For other lower concentrations (e.g. 50%), we observe a similar trend but the computation limitation does not allow us to

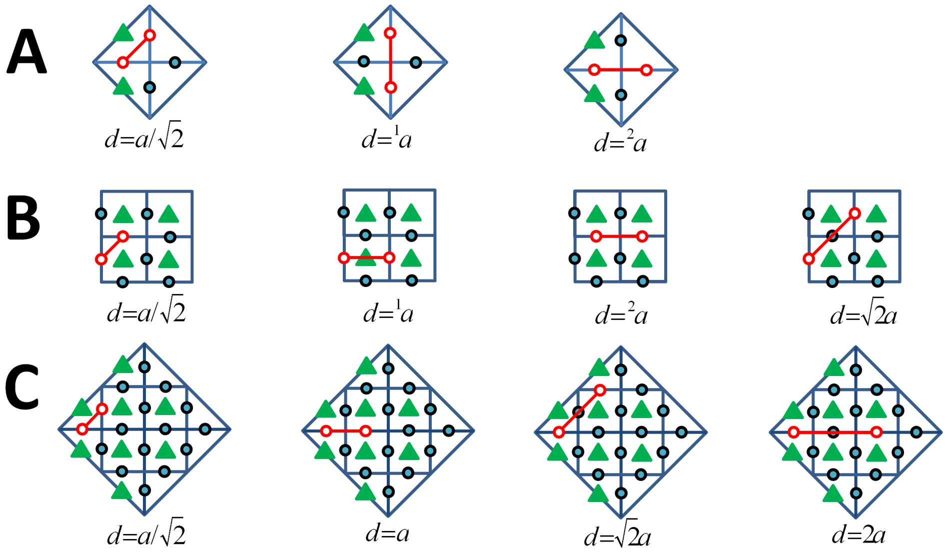

Figure 3.25: Schematics of top view of the simulation cell which includes two oxygen vacancies. The green triangle is Al, the solid circle is O and the empty circle is the oxygen vacancies. The distance between the two oxygen vacancies is highlighted by the red solid line. **A**) 100% oxygen vacancies in a $c(2 \times 2)$ cell. The superscript 1 and 2 are two distinct configurations, because $GdFeO_3$ distortions removes 90 degree rotation symmetry. **B**) 50% oxygen vacancies in a 2×2 cell. The superscript 1 and 2 are two different configurations because of the relative position to Al. **C**) 25% oxygen vacancies in a $\sqrt{8} \times \sqrt{8}$ cell.

reach the converged value. However, the energy change between 2 unit cells and 9 unit cells is around 0.2 eV, while the formation energy is on the order of a few electron volts. Therefore we can take the calculated formation energies in Fig. 3.21 and Fig. 3.23 as a good upper limit, which implies that the real critical thickness d_c could be even smaller than the estimated one $d_c = 4$ unit cells.

Clustering

In the previous section, we calculated the formation energy of oxygen vacancies, provided that they were uniformly distributed. However, it is possible that oxygen vacancies could cluster and lead to phase separation. In order to test whether clustering occurs, we introduce two oxygen vacancies in the simulation cell. Fig. 3.25 shows the schematics of the 100% oxygen vacancy in a $c(2 \times 2)$ cell, 50% oxygen vacancy in a 2×2 and 25% oxygen vacancy in a $\sqrt{8} \times \sqrt{8}$ cell. The distances of the two oxygen vacancies are highlighted by the red solid line and the total energies as a function of separation distance d are calculated

Table 3.5: Total energies with two oxgyen vacancies in the simulation cell. η is the concentration. d is the separation distance between two oxygen vacancies. The superscript refers to different configurations with the same separation d, whose definitions are in the caption of Fig. 3.25.

η	100%			
distance d	$a/\sqrt{2}$	^1a	^2a	
ΔE (eV)	-1.06	-0.32	ref	
η	50%			
distance d	$a/\sqrt{2}$	^1a	^2a	$\sqrt{2}a$
ΔE (eV)	-0.122	+0.122	+0.095	ref
η	25%			
distance d	$a/\sqrt{2}$	a	$\sqrt{2}a$	$2a$
ΔE (eV)	+0.023	+0.108	-0.070	ref

and compared with each other. We choose the total energy with the furtherest separation of two oxygen vacancies as the reference. The results are summarized in Table 3.5. We can see the general trend is that with the concentration ξ increasing, oxygen vacancies prefer to cluster and form a pair (i.e. the shortest distance $d = a/\sqrt{2}$ yields the lowest total energy). The explanation is as follows: as $\xi > 25\%$, oxygen vacancies on the $LaAlO_3$ surface are not fully ionized. The (mobile) electrons associated with oxygen vacancies can form a bond and therefore oxygen vacancies tend to cluster and form pairs at high concentrations. As $\xi \leq 25\%$, oxygen vacancies are fully ionized and no bonding mechanism is in play and hence no tendency for clustering is expected. Therefore the oxygen vacancy formation energy of concentration below 25% extracted out in Fig. 3.23 is reliable, while above 25% concentration, phase separation may occur and lower the formation energy that is calculated based on uniform distribution assumption.

Discussion

Oxygen vacancies on $LaAlO_3$ surfaces provide a plausible scenario to explain the formation of two-dimensional electron gas on $LaAlO_3/SrTiO_3$ interfaces. Unlike cation intermixtures, the formation of oxygen vacancies does not involve diffusion process. The oxygen atom on the surface can easily fly off the sample in the growth, the process of which does not need to overcome energy barriers. The electrons donated by oxygen vacancies either directly tunnel into the interface or through defect states in $LaAlO_3$ thin films. Different from the prediction of polar catastrophe, the only mobile carriers in this scenario are electrons that transfer from surface to interface. This might provide an explanation that mobile holes are not convincingly detected in experiment. More importantly, our study of oxygen vacancies on $LaAlO_3$ surfaces furnishes a general model to study defects on polar surfaces. For example, if we are interested in adsorption of water molecules on $LaAlO_3$ surfaces, the underlying process that water molecules denote electrons to compensate for the polar field in $LaAlO_3$ thin films remains unchanged, though the physical donor is different.

3.5.3 Possible cation vacancies in $SrTiO_3$ substrates

Methodology

To explore the possibility of cation vacancies in $SrTiO_3$ substrates, we calculate the formation energy of an isolated cation vacancy. We employ the following three different configurations: i) a bulk calculation of $N \times N \times N$ unit cells of $SrTiO_3$ with one vacancy; ii) a slab calculation of $N \times N \times N$ unit cells of $SrTiO_3$ with one vacancy (along the z direction, ~ 20 Å thick vacumm is inserted to separate periodic copies); iii) one vacancy in $N \times N \times N$ unit cells of $SrTiO_3$ slab capped with one full layer of $LaAlO_3$ (the thickness of vacuum is around 20 Å).

Formation energy

Different from cation intermixtures and oxygen vacancies in the previous two sections, there is no direct evidence of cation vacancies in the $SrTiO_3$ substrates of the n-type interface. However, before the annealing, samples are reported to be n-doped [59, 69]. Therefore the Fermi level does not lie in the band gap of $SrTiO_3$, but close to the conduction band edge or even in the conduction band of $SrTiO_3$. This alignment of Fermi level could significantly reduce the formation energy of negatively charged cation vacancies (V_{Sr}^{2-} or V_{Ti}^{4-}) [93]. In this section, we discuss the possibility of cation vacancies in $SrTiO_3$ substrates and, if they exist, their possible consequences. As an example, we only focus on V_{Sr} for the remainder of discussion. The treatment of V_{Ti} is very similar.

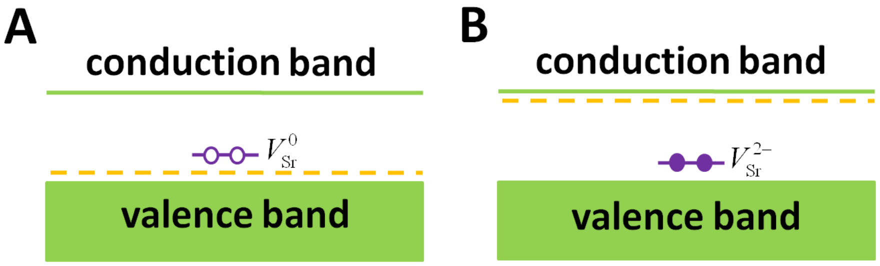

Figure 3.26: Schematic of neutral and charged Sr vacancies. **A**) neutral Sr vacancy. The Fermi level lies between the vacancy state and valence band maximum. **B**) charged Sr vacancy. The Fermi level lies close to the conduction band minimum or even into the conduction band due to the n-doped environment.

The formation energy of an isolated Sr vacancies V_{Sr}^{q} in the n-doped environment is:

$$E_{\mathrm{f}}(V_{\mathrm{Sr}}^{q}) = E_{\mathrm{tot}}(\mathrm{defect}) - E_{\mathrm{tot}}(\mathrm{perfect}) + E_{\mathrm{Sr}} + q\tilde{\varepsilon}_F + \mu_{\mathrm{Sr}} \tag{3.40}$$

where q is the charged state of V_{Sr}^{q}. In the previous section, we only discussed charge neutral oxygen vacancies. For simplicity, we omitted $q = 0$ in the preceding discussion. E_{Sr} is the total energy of Sr per atom in bulk form. Here $\tilde{\varepsilon}_F$ is the Fermi level with respect to valence band edge. For neutral vacancies, the term $q\tilde{\varepsilon}_F$ drops out and Eq. (3.40) is the analogue of Eq. (3.36) for Sr vacancy. As Fig. 3.26 shows, the defect state of a Sr vacancy is acceptorlike and lies close to the valence band edge. If the sample is insulating, so the Fermi level is located between the valence band edge and the isolated Sr vacancy defect state and therefore the charge state of V_{Sr} is $q = 0$. However, before annealing, samples of LaAlO$_3$/SrTiO$_3$ interfaces are reported to be n-doped, then the Fermi level is shifted up to the conduction band edge or even into the conduction band of SrTiO$_3$. As a rough approximation, the Fermi level is shifted by the band gap of SrTiO$_3$ (3.2 eV). The consequence of this shift in Fermi level is that the Sr vacancy becomes fully ionized (i.e. $q = -2$) and the additional term $q\tilde{\varepsilon}_F$ reduces the formation energy by 6.4 eV. Like oxygen vacancies, if the formation energy is negative, then Sr vacancies can be spontaneously formed.

In order to obtain the formation energy, we need to estimate the chemical potential of Sr metal. Unlike the chemical potential of oxygen which is tabulated as a function of temperature and pressure and can be uniquely determined under growth conditions, the chemical potential of Sr metal can only be estimated from the phase diagram of $SrTiO_3$. Considering that $SrTiO_3$ is stable in the chamber under growth conditions and it is in equilibrium with Sr, Ti and O, we have the following relations:

$$\mu_{\mathrm{Sr}} + \mu_{\mathrm{Ti}} + 3\mu_{\mathrm{O}} = E_{\mathrm{SrTiO_3}} - E_{\mathrm{Sr}} - E_{\mathrm{Ti}} - \frac{3}{2}E_{\mathrm{O_2}} \tag{3.41}$$

where $E_{\mathrm{SrTiO_3}}$, E_{Sr} and E_{Ti} are the total energies of bulk $SrTiO_3$, Sr metal and Ti metal per formula. $E_{\mathrm{O_2}}$ is the total energy of an oxygen molecule.

In order to avoid phase separation, we need following restrictions on chemical potentials:

$$\mu_{\mathrm{Sr}} \leq 0 \tag{3.42}$$

$$\mu_{\mathrm{Ti}} \leq 0 \tag{3.43}$$

$$\mu_{\mathrm{Ti}} + 2\mu_{\mathrm{O}} \leq E_{\mathrm{TiO_2}} - E_{\mathrm{Ti}} - E_{\mathrm{O_2}} \tag{3.44}$$

$$\mu_{\mathrm{Sr}} + \mu_{\mathrm{O}} \leq E_{\mathrm{SrO}} - E_{\mathrm{Sr}} - \frac{1}{2}E_{\mathrm{O_2}} \tag{3.45}$$

Fig. 3.27 shows the phase diagram of $SrTiO_3$ in the $(\mu_{\mathrm{O}}, \mu_{\mathrm{Sr}})$ plane with μ_{Ti} fixed by Eq. (3.41). The four solid lines in Fig. 3.27 are the boundaries set by Eq. (3.42-3.45). The phase space in which $SrTiO_3$ is stable is highlighted in the orange shaded area. In order to estimate the chemical potential of Sr, we draw the vertical dashed line which is the chemical potential of oxygen under growth conditions determined in the previous section ($\mu_{\mathrm{O}} = -1.93$ eV). The two crossing points between μ_{O} and the $SrTiO_3$ stable phase area constrain μ_{Sr} from -5.7 eV to -4.3 eV.

Given the range of Sr chemical potential (-5.7 eV $< \mu_{\mathrm{Sr}} <$ -4.3 eV), we calculate the formation energy of isolated Sr vacancy in different environments. The calculations are performed in the undoped environments (since we can not *a priori* estimate the density

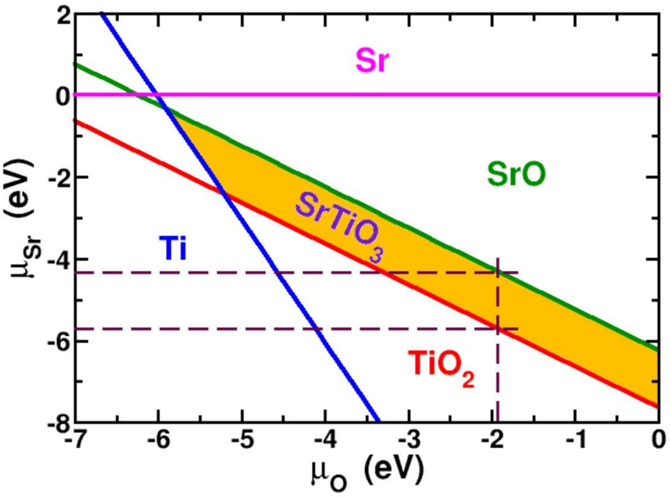

Figure 3.27: The phase diagram of $SrTiO_3$. The orange shaded area is the phase space in which $SrTiO_3$ is stable. The vertical dashed line highlights the chemical potential of oxygen μ_{O} under growth conditions. The horizontal dashed lines highlight the range of Sr chemical potential μ_{Sr} in which $SrTiO_3$ is the only stable phase.

of n-type carriers before annealing). However, in order to simulate the n-doped environment, we approximate the term $q\tilde{\varepsilon}_F$ by $-2 \times 3.2 = -6.4$ eV. The results are summaried in Table 3.6. We can see in all enviroments, the Sr formation energy becomes very negative, indicating the possibility of spontaneously formed Sr vacancies. However, the reason that Sr vacancies are not directly observed in experiments might be that although thermodynamically Sr vacancies are favored, kinetically they do not have enough energy to overcome the barriers and escape the samples. Since Sr ions are bigger than O ions, it is anticipated that Sr ions move with more difficultly than O ions through $SrTiO_3$ substrates. However, a comprehensive investigation of energy barriers of Sr ions in $SrTiO_3$ substrates is beyond the current study. We hope that our results might stimulate further theoretical and experimental work on possible defects in $SrTiO_3$ substrates.

Discussion

Before concluding, we briefly discuss the possible consequences of Sr vacancies, if they exist. With the presence of Sr vacancies, La could diffuse into $SrTiO_3$ substrates more easily and

Table 3.6: The formation energy of Sr vacancies in different configurations. ‘bulk’ means periodic boundary conditions posed along all three directions. ‘slab’ means periodic boundary conditions posed only in the x and y directions and both terminations are TiO_2 (i.e. the slabs are not stoichiometric.). ‘LAO’ means that one unit cell of $LaAlO_3$ is added on the stoichiometric $SrTiO_3$ slab. The interface is LaO/TiO_2.

	$E_f\left(V_{Sr}^q\right)$ (eV)	
configuration	lower bound	upper bound
$2 \times 2 \times 2$ (bulk)	-3.01	-1.61
$3 \times 3 \times 3$ (bulk)	-3.20	-1.80
$4 \times 4 \times 4$ (bulk)	-3.70	-2.30
$2 \times 2 \times 2$ (slab)	-4.10	-2.70
$3 \times 3 \times 3$ (slab)	-4.40	-3.00
$2 \times 2 \times 2$ (LAO-capped)	-3.45	-2.05
$3 \times 3 \times 3$ (LAO-capped)	-3.54	-2.14

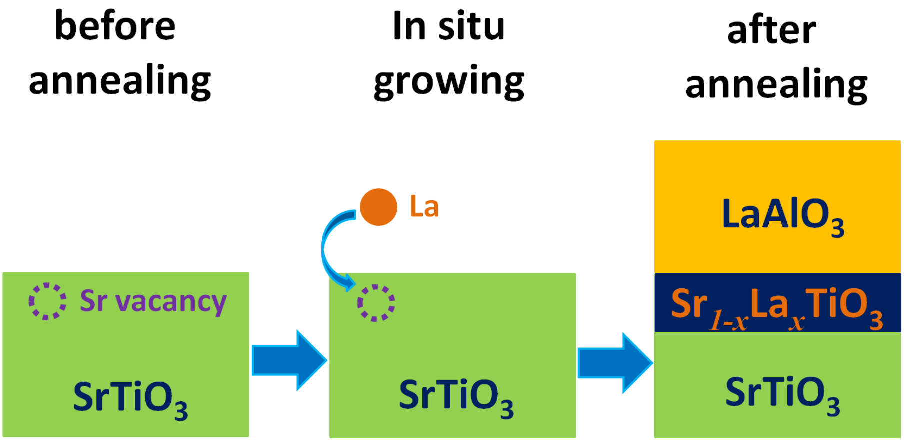

Figure 3.28: Schematic of how La diffusion can lead to the formation of metallic $Sr_{1-x}La_xTiO_3$, accompanying the possible creation of Sr vacancies in $SrTiO_3$ substrates.

donates electrons by forming $Sr_{1-x}La_xTiO_3$ [58]. If after the growth and annealing, the $LaAlO_3$ thin film itself remains stoichiometric, and some $Sr_{1-x}La_xTiO_3$ is formed at the interface between $LaAlO_3$ and $SrTiO_3$, then a metallic conducting channel could result, as is illustrated in Fig. 3.28. However, the details of how such a conducting layer is formed depends on the concentration of Sr vacancies and barriers of La diffusion.

3.6 Summary and outstanding puzzles

Concerning electronic reconstructions, we present a detailed study of ideal $LaAlO_3/SrTiO_3$ interfaces and a new class of quantum wells. In both systems, we confirm an intrinsic insulating-to-metallic transition. The observed transition can be triggered either by thickening the $LaAlO_3$ layers or by imposing an external electric field, both of which can be explained by the polar catastrophe mechanism. We show that for both the n-type interface and QW, the realistic critical separation (taking into account the underestimation of DFT band gap) is around 6 unit cells. We also show that, given a typical $SrTiO_3$ substrate thickness of 1mm, the lower bound for the critical voltage necessary to induce an insulating-to-metallic transition is estimated to be $\sim$ 300 V for the ideal n-type interface and $\sim$ 500 V for the QW. In addition to theoretically demonstrating the observed physical properties, we provide a microscropic explanation of the observed binding of conduction electrons at the n-type interface, a phenomenon which can not be described by the polar catastrophe mechanism alone. We demonstrate that the large La-Ti hopping matrix element at the n-type interface, which is absent in both bulk constituents and is unique to the n-type interface, lowers the energy of the Ti atom at the interface relative to all other Ti sites, thus binding the electrons. Futhermore, we develop a continuous model that captures the essence of polar structure and dielectric properties and predicts the thickness dependence of sheet carrier densities.

On atomic reconstructions, we study in great details the $LaAlO_3/SrTiO_3$ n-type interfaces. For cation intermixtures, we find less than 50% of Ti-Al mixing could lower the energetics of the n-type interface because the internal polar field is reduced, while Sr-La mixing always strengthens the internal polar field at any concentrations and thus increases the total energy. For oxygen vacancies on the $LaAlO_3$ surfaces, we carefully investigate their dependence on concentrations and $LaAlO_3$ thicknesses. By constructing an electrostatic model, we can extract out the formation of oxygen vacancies at arbitrary low concentrations and find an insulating-to-metallic transition at 4 unit cells of $LaAlO_3$, which provides another scenario for the origin of conducting electrons. Last, we study the possibility of cation vacancies in $SrTiO_3$ substrates due to the pre-annealing n-doped environment. We find that due to the shift of Fermi level and the large band gap of $SrTiO_3$, the formation energy of cation vacancies in $SrTiO_3$ could be significantly reduced, which might offer hosts for La diffusion in the growth and result in the formation of metallic $Sr_{1-x}La_xTiO_3$. In principle, there could be very many possibilities of atomic reconstructions at the n-type $LaAlO_3/SrTiO_3$ interface. We focus on those defects which are either experimentally observed or possibly relevant to the origin of emerging conducting electrons. We hope our study could stimulate further experiments on the investigations of atomic reconstructions and help elucidate the nature of two-dimensional mobile electron gas at the $LaAlO_3/SrTiO_3$ n-type interface.

Finally, we conclude by discussing some of the outstanding issues related to this system, which may stimulate further theoretical and experimental work.

3.6.1 Whence insulating n-type interfaces?

It is found in experiment that for samples grown at very high oxygen partial pressure ($> 10^{-2}$ mbar) [59] or annealed at 300 mbar during cooling [60], the n-type interfaces can become completely insulating. In fact, the conducting properties of n-type interfaces become poorer with increasing p_{O_2} during the growth process (from 10^{-6} to 10^{-3} mbar) [60]. With presumably better stoichiometry control, one would expect that the transport properties would converge to those of an ideal interface, where the polar catastrophe plays the dominant role. What is noticeable is that the high-pressure growth experimental results are at variance with these expectations.

At first glance, this phenomenon would imply that the observed interface conductivity comes only from the oxygen vacancies. With the higher p_{O_2} or post-annealing to repair the oxygen off-stoichiometry, the concentration of oxygen vacancies should decrease, resulting in higher sheet resistance and lower sheet carrier density. However, the sheet carrier density does show an abrupt jump at 4 unit cells of $LaAlO_3$ [19], which is difficult to explain using oxygen vacancy doping alone.

We mention here a number of possible scenarios and related questions. The first is that, for ideal n-type interfaces and for polar $LaAlO_3$, the polar catastrophe does not take place and that the theoretical models are unable to describe the correct physical properties. While logically possible, this scenario seems unlikely because the polar catastrophe for idealized interfaces is based on simple physical properties such as ionic charges of the cations. Next, one can consider the possibility that the theoretical results are correct but inapplicable; that the $LaAlO_3$ becomes non-polar when the samples are grown under high p_{O_2} or post-annealed. Perhaps, aside from removing oxygen vacancies, the oxidation has other side effects. The oxidation introduces oxygen atoms at the surfaces of the samples which then diffuse into the body of the materials. Does a larger flux of oxygen through the lattice affect the cation sublattice by enhancing disorder and/or intermixing? Does one achieve sharp and ideal interfaces or is the disorder sufficient to make the $LaAlO_3$ nonpolar?

Recent work by Segal *et al.* on molecular beam epitaxy grown $SrTiO_3/LaAlO_3$ interfaces yield a number of interesting findings concerning some of these questions. Similar to Thiel *et al.* [19], a critical separation of 4 unit cells of $LaAlO_3$ is found, as well as similar sheet carrier densities in transport. However, x-ray spectra of the La core states do not reveal the expected $LaAlO_3$ polar field. Quantitatively, the polar field is $\sim$10 times smaller than the typical theoretical value of $\sim$0.2 eV/Å for samples with $LaAlO_3$ thicknesses below and above the critical separation. This provides some evidence that the $LaAlO_3$ may not be polar in some samples. However, it also creates puzzles: if the $LaAlO_3$ is not strongly polar, then what mechanism leads to a critical thickness close to the expected value?

One direct experimental probe for these questions is the electron energy loss spectroscopy (EELS) performed in the scanning transmission electron microscope (STEM). Detailed studies of the Ti, La, and O core level have provided valuable information on the distributions of the cations and oxygen vacancies at n-type and p-type interfaces [66]. However, we are not aware of data published to date on the La core levels for relatively thin $LaAlO_3$ films close to the critical thickness. The existence of the polar field in $LaAlO_3$ will lead to an energy shift between neighboring La core levels along the (001) $LaAlO_3$ film direction. An expected shift of about 0.7 eV per $LaAlO_3$ unit cell is within present experimental resolution. That will allow for direct visualization of the strength of the $LaAlO_3$ polar field.

3.6.2 Are there multiple types of carriers?

The possibility of multiple types of carriers being present at the n-type interface has been suggested in both the published experimental [51] and theoretical [79, 68] literature. Recent experiments also invoke the same picture [95]. Brinkman *et al.* [51] speculate that the magnetic phenomena they observe are due to spin scattering of itinerant electrons off of localized electrons that serve as localized magnetic moments. Seo *et al.* [95] explain their optical measurements based on the simultaneous presence of a low density of high-mobility carriers that dominate the transport properties at low temperatures, together with a high density of low-mobility carriers localized close to the interface that dominate the optical spectra. The theoretical work uses the Anderson localization picture in 2D to argue that the bulk of the carriers, which are spatially localized close to the interface and highly 2D in nature, do not contribute to transport due to localization. The localization argument provides a possible explanation for why transport measurements on samples grown at higher $p_{\mathrm{O}_2} \sim 10^{-4}$ mbar show low sheet carrier densities when compared to the theoretical expectation of $0.5e/a_{\mathrm{STO}}^2$.

The optical approach of Seo *et al.* [95] is exciting, as it has the potential to separate out different contributions from different types of carriers. To date, these experiments have been performed on samples grown at low $p_{\mathrm{O}_2} \sim 10^{-6}$ mbar, with correspondingly high sheet densities of up to 3×10^{17} cm^{-2}, beyond the “intrinsic” limit of $0.5e/a_{\mathrm{STO}}^2$. The majority of carriers may stem from oxygen vacancies, swamping out any signal from the intrinsic electron gas at the interface more evident in samples grown at higher p_{O_2}.

Regarding the Anderson localization scenario, one experiment is to try to grow similar samples but to find a way to modify the degree of disorder at the interface. That could be induced by intentionally introducing a low density of isovalent cations during growth of the interface region or by introducing intentional off-stoichiometry. The required localization behavior requires mean free paths on the order of a few nanometers or less, which translates into point-like defects every nanometers as well. Since this spacing corresponds to only a few percent areal density per interface unit cell, the localization behavior should show strong dependence on the density of defects introduced on the percent level in the interface region. On the theoretical side, more detailed 2D transport modeling of the n-type interface, including scattering and thus localization, can help show whether the picture is applicable and under what conditions of disorder. In addition, the expected density and scattering efficacy of various defects (*e.g.*, oxygen vacancies or cation intermixtures) could be evaluated from first principles simulations.

3.6.3 Possible magnetic ordering?

Experimental studies of the magnetic properties of the n-type interface are an active and growing area. To date, some intriguing discoveries have been reported by various research teams based on both direct and indirect probes of magnetic behavior and ordering.

Measurements by Brinkman *et al.* [51] provided the first experimental evidence of magnetic behavior. Brinkman *et al.* [51] studied samples grown under a relatively high p_{O_2} $\sim 10^{-3}$ mbar, with sheet resistances $> 10^4$ Ω. They observe isotropic magnetoresistance, which they ascribe to spin scattering off localized magnetic moments at the interface, an interpretation bolstered by their observation of a minimum in the sheet resistance $R_s(T)$ with lowering temperature. This minimum is reminiscent of the Kondo effect, which stems from the interplay between localized magnetic moments and itinerant charges. Furthermore, they find that the magnetoresistance at 300 mK is hysteretic, implying the presence of ferromagnetic domains. However, the $R_s(T)$ minimum is not present for samples grown at lower p_{O_2} ($< 10^{-5}$ mbar). In contrast, Reyren *et al.* [16] grew a sample at a low oxygen partial pressure of 6×10^{-5} mbar, which is then annealed under conditions that (presumably) yield well oxidized samples. They find positive magnetoresistance, no minimum in $R_s(T)$, and no hysteresis in magnetoresistance. The two major differences between the experiments of Refs. [51] and [16] are the growth p_{O_2} (10^{-3} mbar versus 10^{-5} mbar) and the thickness of the $LaAlO_3$ film (26 u.c versus 8 u.c.). The former factor is known to affect the sheet resistance and mobility, while the latter modifies the sheet carrier density.

The $SrTiO_3/LaAlO_3$ samples investigated by van Zalk *et al.* [96] are grown under similar conditions to those used by Brinkman *et al.* [51]. This study reports hysteresis below 300 mK and magnetoresistance oscillations versus external field intensity B at 50 mK. Surprisingly, the oscillations are periodic in $\sqrt{B}$ instead of the standard Shubnikov-de Haas $1/B$ periodicity. The authors suggest that this stems from the commensurability condition of edge states. They also speculate that the magnetoresistance oscillation is related to ferromagnetic ordering, and that the quantum Hall effect might be present.

Shalom *et al.* [97] studied samples grown at a lower p_{O_2} of $10^{-4} - 10^{-5}$ mbar. In agreement with other observations [59, 19, 16], the sheet carrier density is $\sim 10^{13}$ cm^{-2} and the system becomes superconducting at 130 mK. In contrast to Refs. [51] and [96], however, the low temperature magnetoresistances are highly anisotropic and have different signs for fields parallel or perpendicular to the current. They find no hysteresis down to 130 mK, at which point their samples become superconducting. Based on these observations, they suggest an anti-ferromagnetic ordering at the interface below a Néel temperature of $\sim$35 K.

Very recently, new momentum has been obtained through a series of exciting papers [98, 99, 100, 101] on the study of magnetic properties of n-type LaAlO$_3$/SrTiO$_3$ interfaces. Ariando *et al.* [98] found electronic phase separation at the n-type interface. They report that the interface charges are separated into two regions: one is a quasi-two dimensional electron gas, ferromagnetic phase and the other is a (superconductor like) diamagnetic/paramagnetic phase. They show that the ferromagnetic phase is stabilized at high oxygen partial pressure while the superconducting state is favored at low pressure. At intermediate oxygen partial pressure in the growth, co-existence of ferromagnetism and superconductivity, which are adverse in normal metals, was reported by three groups using different techniques.

Dikin *et al.* [99] performed magnetoresistance, Hall and electric field dependence measurements and reported that there are two distint bands of charge carriers that contribute to the interface conductivity. Different from Ariando *et al.* in which the magnetic and superconducting paramagnetic regimes are quite distinct, Dikin *et al.* show coexistence of superconductivity and ferromagnetism in their samples. However, they do comment that the electronic properties of LaAlO$_3$/SrTiO$_3$ interfaces are extremely sensitive to growth conditions: samples grown by different groups with nominally identical growth conditions show some variations in electronic properties.

Bert *et al.* [101] used local imaging of the magnetization and magnetic susceptibility to directly observe a landscape of ferromagnetism, paramagnetism and superconductivity. They find submicrometre patches of ferromagnetism in a uniform background of paramagnetism, with a non-uniform, weak diamagnetic superconducting susceptibility at low temperature. They give a lower bound estimation of dipole moment density as $7.3 \pm 3.4 \times 10^{12}$ $\mu_B\mathrm{cm}^{-2} = 0.012 \pm 0.007$ μ_B per 1×1 interface unit cell.

On the other hand, Li *et al.* [100] combined high-resolution magnetic torque magnetometry and transport measurements and reported direct evidence of magnetic ordering of the two-dimensional electron liquid at the interface which also superconducts below 120 mK. They found a saturation magnetic moments of $\sim 0.3\mu_B$ per 1×1 interface unit cell and the easy axis of magnetic moment is in-plane.

Theoretically, there is controversy concerning the nature of magnetism at the interface between $LaAlO_3$ and $SrTiO_3$. Earlier work [52] suggests that the magnetism originates from localized Ti $3d$ states and accompanies checkboard charge ordering. Later work [102] demonstrates that the magnetism is due to rather confined electrons around O vacancies while the conductivity is a result of the two-dimensional electron gas caused by electronic reconstructions. More research is anticipated to clarity this subtle issue.

Chapter 4

Ferroelectric/manganite Interfaces

4.1 Introduction

Multiferroics have been one of the most intensively studied materials during the past decade [103, 104]. The coexistence of more than one order parameter in a single phase and their coupling may open new routes to the next generation of electronic devices. For instance, the possibility of controlling magnetization via external fields may find promising applications in spintronics.

The origin of multiferroicity lies in a nonzero magnetoelectric coupling, which can occur due to many different mechanisms (for recent reviews, see [105, 3]). The magnetic properties of an intrinsic bulk magnetoelectric, of which Cr_2O_3 is a prototype, can be modulated by an external field through the change of the magnetic cations' displacement relative to anions [106]. Extrinsic magnetoelectric couplings can be mediated by strain: in composites of piezomagnetic materials combined with electrostrictive materials, external fields modulate the polarization, as well as the shape of the piezoelectrics. This change in turn induces strain of the magnetic components and hence magnetization in the magnetostrictive materials [107]. However, although these bulk mechanisms are well understood, the magnitude of magnetoelectric couplings in bulk materials is generally small [108], impeding their applications in electronic devices. Beyond the bulk, artificial structures such as interfaces are promising candidates to realizing or even engineering magnetoelectric couplings. Recently, a variety of mechanisms were proposed to induce magnetoelectric coupling at interfaces. At ferromagnet/ferroelectric interfaces, the interfacial bond length can be altered by the presence of ferroelectric polarization, for example in Fe/$BaTiO_3$ [109], Co_2MnSi/$BaTiO_3$ [110] and Fe_3O_4/$BaTiO_3$ [111]. Another mechanism is to apply an external field and induce magnetization mediated by free screening carriers accumulated at ferromagnet/dielectric interfaces, for example $SrRuO_3$/$SrTiO_3$ [112]. A more complicated mechanism was recently predicted in theory [113] and realized in experiment [27] at the ferroelectric/manganite interface.

In the presence of ferroelectric polarization, screening charges are accumulated or depleted at the interface. Like $SrRuO_3$/$SrTiO_3$ interfaces in the presence of an external field, additional magnetization can be induced by screening charges (provided that the manganite is in the ferromagnetic doping phase). What is different is that accumulation of carriers may induce an interfacial ferromagnetic-to-antiferromagnetic phase transition, resulting in an anomalously large change in the magnetization due to a modification of spin configuration and hence a very large magnetoelectric coupling. Burton *et al.* [113] studied a representative heterostructure: $BaTiO_3$/$La_{1-x}Ba_xMnO_3$ with $x = 0.5$ which is the ferromagnetic-to-antiferromagnetic phase boundary of bulk $La_{1-x}Ba_xMnO_3$. They found that with the ferroelectric polarization flipped, the spin in the second unit cell from the interface changes its sign (labelled as $A2$ configuration). Interestingly, they expect that the spin-modified effect could occur in a range of stoichiometries near the magnetic transition point, but for the experimental doping level $x = 0.2$ which is far from the magnetic transition point, it is not necessarily expected that a magnetic transition should occur.

We quantitatively study the magnetoelectric phenomenon at the ferroelectric/manganite interface using first-principles calculations. We choose $PbTiO_3$/$La_{1-x}Sr_xMnO_3$ as a prototype. Though in experiments $PbTi_{0.8}Zr_{0.2}O_3$ replace $PbTiO_3$ as the ferroelectric [27] in order to reduce leakage, the key role ferroelectrics play is to induce screening charge due to their surface polarization, while the compositional details are secondary. Therefore we use $PbTiO_3$ instead to simplify the calculations. For the $La_{1-x}Sr_xMnO_3$ thin film, we choose the nominal hole doping to be $x = 0.2$ (unless otherwise specified) in order to directly compare to experiments [27].

Here we find that though the nominal doping $x = 0.2$ is far from the magnetic transition point, a spin-flipped transition does occur with the reversal of ferroelectric polarizations. However, different from the ground state Burton *et al.* found ($A2$ configuration), the spin flips in the first unit cell from the interface (labelled as $A1$ configuration). We calculate the evolution of ground state magnetic structures with nominal hole doping in $La_{1-x}Sr_xMnO_3$ and find the transition from $A1$ to $A2$ as the nominal hole doping increases ($0.2 < x < 0.5$). We develop a new method which can much more accurately count holes in the $La_{1-x}Sr_xMnO_3$ thin film than the Löwdin orbitals [85], and gives a direct supporting evidence that the holes on the interfacial Mn atom could be larger than the magnetic transition point ($x = 0.5$) due to ferroelectric polarizations, even though the nominal stoichiometry is only $x = 0.2$. This shows a robust feasibility of ferroelectric control of magnetism in manganites. In addition, we find that the magnetic structures sensitively depend on the details of exchange correlation functionals (LSDA+U). We build an Ising-like model to show that the dependence on Hubbard U can be well understood by introducing effective interactions between nearest Mn magnetic moments. We also find that though the spin-flipped effect is mainly due to the electronic screening, polar distortions at the interface need to be taken into account for a quantitative (instead of qualitative) link between bulk $La_{1-x}Sr_xMnO_3$ and the interfacial phase in $La_{1-x}Sr_xMnO_3$ thin films. Finally, we study the coupling of ferroelectrics to orbital occupancy in the manganites and propose a new approach to modulate the orbital ordering in perovskite oxides.

4.2 Computational details

Our calculations are performed using density functional theory within the *ab initio* supercell plane-wave approach [76], with the code PWscf in the Quantum-ESPRESSO package[1]. We employ ultrasoft pseudopotentials [45]. The semicore states and reference configuration of each element are shown in Table 4.1.

We use the local spin density approximation (LSDA) [12] for the exchange correlation functional as well as the Hubbard U correction method (LSDA+U) [114] to account for some of the strong electronic correlations on the localized d orbitals of Mn atoms. The

---

[1] See http://www.quantum-espresso.org

Table 4.1: The semicore states and reference configurations of our pseudopotentials. The cut-off radii are in units of Bohr.

Atom	Reference valence states	r_c^s	r_c^p	r_c^d
Pb	$5d^{10}6s^2 6p^2$	2.5	2.5	2.3
Ti	$3s^2 3p^6 3d^1 4s^2$	1.8	1.8	1.8
Sr	$4s^2 4p^6 5s^2$	2.0	1.8	2.0
La	$5s^2 5p^6 5d^1 6s^{1.5} 6p^{0.5}$	2.2	2.0	2.2
Mn	$3s^2 3p^6 3d^5 4s^2$	2.0	2.0	2.0
Pt	$5d^9 6s^1 6p^0$	1.0	1.0	1.2
O	$2s^2 2p^4$	1.3	1.3	–

plane wave basis energy cutoff and charge cutoff are 35 Ry and 280 Ry, respectively. We use a Gaussian smearing width of 5 mRy when sampling the Brillouin zone. For bulk $\mathrm{La}_{1-x}\mathrm{Sr}_x\mathrm{MnO}_3$, the k-grid sampling of the Brillouin zone is $20 \times 20 \times 20$ per formula unit. For interface calculations, the k-grid sampling is $20 \times 20 \times 2$ where the z-axis is orthogonal to the interface. For variable cell relaxations, the convergence threshold for pressure is 0.5 Kbar. For atom relaxations, the convergence threshold for every force component is 26 meV/Å. We check the convergence by increasing the k-point sampling density and reducing the stress and force threshold, and no significant difference is observed in atomic structures and physical quantities we are interested in.

The A-site $\mathrm{La}_{1-x}\mathrm{Sr}_x$ alloying is treated by the virtual crystal approximation [115, 116] which mixes the two elements and replaces them with a fictitious atom whose electron number is $(1-x)N_{\mathrm{La}} + xN_{\mathrm{Sr}}$, where N_{La} and N_{Sr} are the number of electrons of the La and Sr pseudo atoms, respectively. We stress that i) since the magnetic properties originate from Mn d-electrons and A-site atoms serve to donate electrons, we expect that the virtual crystal approximation is reasonable to describe the magnetic phase transition of manganites in the random distribution; ii) since the chemical properties mainly depend on the valence electrons, the approximation we make here is expected to be also good for Ca and Ba. The choice of Sr here is to permit direct comparison to experiment [27] and iii) our choice of pseudo potential and valence electrons shown in Table 4.1 ensures a very smooth interpolation between La and Sr as their pseudo valence electrons and nuclear pseudo charges only differ by one elementary charge. A simple test of 1:1 Sr-La alloying is

Table 4.2: Comparison between the virtual crystal approximation and supercell calculations. The nominal doping x is 0.5 in the virtual crystal approximation. A $c(2 \times 2) \times 2$ supercell is employed with La and Sr atoms forming a checker-board pattern (every nearest neighbor of Sr is La and vice versa). The lattice constants reported are those for A-type antiferromagnetic ordering. ΔE is the energy difference between ferromagnetic ordering and A-type antiferromagnetic ordering per Mn atom, defined by Eq. (4.1). A range of Hubbard U ($0 \leq U \leq 2$ eV) are tested.

Virtual crystal approximation							
U (eV)	ΔE (meV)	a (Å)		b (Å)		c (Å)	
		F	A	F	A	F	A
0	-34	5.345	5.363	7.561	7.385	5.386	5.408
1	-10	5.385	5.376	7.612	7.411	5.430	5.433
2	7	5.401	5.380	7.623	7.422	5.434	5.452
$c(2 \times 2) \times 2$ supercell							
U (eV)	ΔE (meV)	a (Å)		b (Å)		c (Å)	
		F	A	F	A	F	A
0	-37	5.327	5.366	7.482	7.372	5.381	5.411
1	-11	5.355	5.380	7.513	7.398	5.400	5.439
2	6	5.365	5.387	7.520	7.411	5.410	5.452

performed in a $c(2 \times 2) \times 2$ cell and the results are compared to the $x = 0.5$ virtual crystal approximation as shown in Table 4.2. We can see that virtual crystal approximations quantitatively reproduce the lattice constants and the energy differences between various magnetic orderings, compared to real atom calculations. The accuracy of magnetic energy differences between virtual crystal approximation and real atom calculations in our case is consistent with earlier calculations [117]. The nice agreement on lattice constants with real atom calculations gives further support to the validity of virtual crystal approximation.

4.3 Bulk manganites

4.3.1 Phase transition of magnetic ordering

Since, as we will show, the magnetic properties of $PbTiO_3/La_{1-x}Sr_xMnO_3$ interface can be understood qualitatively in terms of bulk $La_{1-x}Sr_xMnO_3$, we start the discussion with the phase diagram of bulk $La_{1-x}Sr_xMnO_3$ under different conditions. The parent compound of $La_{1-x}Sr_xMnO_3$ is $LaMnO_3$ which is an antiferromagnetic Mott insulator. Bulk $LaMnO_3$ has strong Jahn-Teller and $GdFeO_3$ distortions with *Pnma* symmetry [118] and its primitive cell is of size $c(2 \times 2) \times 2$ in units of the cubic perovskite. The smallest unit cell of $LaMnO_3$ has four formula units (20 atoms). Chemically doping $LaMnO_3$ with Sr induces holes on the Mn d-orbitals, leading to conduction and various magnetic orderings. For a random alloy distribution, we assume that bulk $La_{1-x}Sr_xMnO_3$ has the same symmetry as $LaMnO_3$ (*Pnma*). In DFT simulations, we replace La with the fictitious atom $La_{1-x}Sr_x$ in the virtual crystal approximation and calculate the energy difference between ferromagnetic ordering (F) and A-type antiferromagnetic ordering (A) as a function of doping x.

$$\Delta E = E(A) - E(F) \tag{4.1}$$

In addition to the doping dependence x, we also study the effect of strain, structural distortions and Hubbard U on the phase diagram of bulk $La_{1-x}Sr_xMnO_3$.

Doping dependence

Fig. 4.1a shows a representative bulk phase diagram of $La_{1-x}Sr_xMnO_3$ as a function of doping x. The calculation is performed in the LSDA (i.e. Hubbard U=0). DFT-LSDA reproduces the ferromagnetic-to-antiferromagnetic phase transition that is observed in experiment. The doping dependence can be understood as follows: the ferromagnetic ordering is stablized by the double exchange mechanism which relies on the hopping of the lone e_g electrons among the Mn^{3+} ions [119]. With the increasing hole doping x, the itinerant electrons (i.e. Mn^{3+} ions) are drained and the hopping processes are suppressed. Therefore the double exchange mechanism becomes less operative and the ferromagnetic ordering gets more unstable as x is increased. We need to point out that in the experimental phase diagram for $x < 0.1$, $La_{1-x}Sr_xMnO_3$ is a spin-canted insulator (a magnetic structure close to A-type antiferromagnetic ordering but the magnetic moment is not exactly cancelled due to weak spin-canting) [28]. As x increases to 0.2, there is an insulating-to-metallic transition and the appearance of the ferromagnetic ordering which is not reproduced in

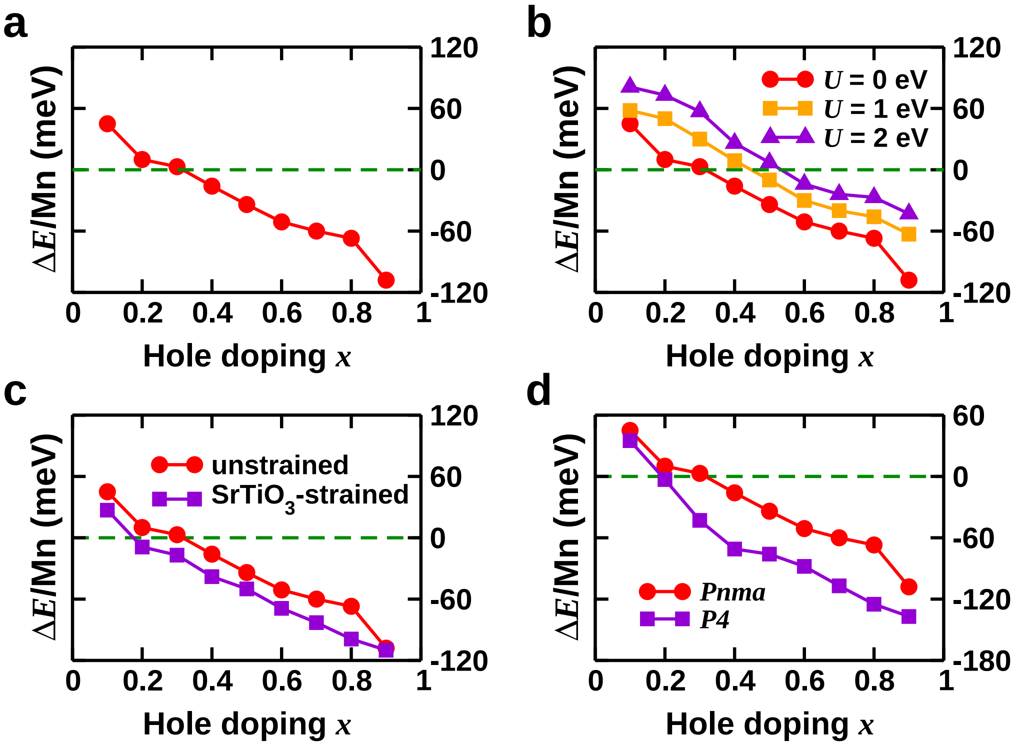

Figure 4.1: Phase diagram of bulk $La_{1-x}Sr_xMnO_3$. ΔE is defined in Eq. (4.1). Above zero, the ground state is ferromagnetic and below zero it is A-type antiferromagnetic. **a)** Hole doping dependence within LSDA. **b)** Hubbard U dependence. **c)** Strain dependence. **d)** Structural distortion dependence.

the DFT-LSDA calculation, since the LSDA ground state is metallic in the whole doping range. Turning on the Hubbard U does not change the metallicity of ferromagnetic $La_{1-x}Sr_xMnO_3$. We argue that even though LSDA or LSDA+U is not accurate enough to reproduce the spin-canted ground state at very low doping nor the insulating-to-metallic transition around $x \simeq 0.2$, it correctly produces the metallic ferromagnetic to metallic antiferromagnetic phase transition at larger x, which is the key to understanding the spin-modified magnetic structure of manganites in the presence of ferroelectrics.

Hubbard U dependence

Fig. 4.1b shows a comparison of LSDA and LSDA+U calculations for bulk $La_{1-x}Sr_xMnO_3$. The ferromagnetic-to-antiferromagnetic phase transition is well reproduced in both LSDA and LSDA+U calculations, but the transition point, i.e. the critical hole density where the ground state changes magnetic ordering, depends on the value of the Hubbard U. With an increasing U, the transition point moves to larger doping values while the overall features of the transition remain unchanged. The Hubbard U dependence originates as follows: antiferromagnetism is favored by the superexchange mechanism which involves the virtual hopping of electrons between low and high energy sites with the same spin [120]. A larger U increases the energy splitting and thus the virtual hopping is suppressed. Therefore the superexchange mechanism is suppressed as U increases, and the antiferromagnetic ordering accordingly becomes less stable, resulting in the upward shift of phase transition curve (favoring ferromagnetism). Empirically in order to correctly locate the transition point at the experimental value of $x \simeq 0.5$, we need a Hubbard U in the range of 1 eV< U <2 eV in the LSDA+U approximation (as illustrated in Fig. 4.1b).

Strain dependence

Since the $La_{1-x}Sr_xMnO_3$ thin film is grown coherently on an $SrTiO_3$ substrate, we also study the phase diagram of $SrTiO_3$-strained $La_{1-x}Sr_xMnO_3$ and compare it with unstrained bulk $La_{1-x}Sr_xMnO_3$ in Fig. 4.1c. $La_{1-x}Sr_xMnO_3$ in the whole doping range is under weak tensile strain (within 1%) when on an $SrTiO_3$ substrate. Tensile (compressive) strain removes the degeneracy of Mn e_g orbitals and favors $d_{x^2-y^2}$ ($d_{3z^2-r^2}$) orbitals due to the change of crystal field [121]. Based on the double exchange mechanism, ferromagnetism is isotropic with equal hoppings between Mn atoms along x, y and z directions. A-type antiferromagnetism is ferromagnetic in-plane and alternates its spin orientation layer by layer along the out-of-plane axis [122]. Due to the tensile strain, the occupancy of $d_{3d^2-r^2}$ is lowered and the hopping between Mn atoms becomes essentially two-dimensional, suppressing ferromagnetism. Therefore with tensile strain, ferromagnetism is destablized and the whole transition curve is shifted downwards (favoring A-type antiferromagnetic ordering) as seen in Fig. 4.1c.

Structural distortions

Distortions away from cubic symmetry play a crucial role in the magnetism of manganites [123]. Bulk $\mathrm{La}_{1-x}\mathrm{Sr}_x\mathrm{MnO}_3$ has complicated structural distortions with $Pnma$ symmetry (the unit cell is $c(2\times2)\times2$ with 20 atoms). However, we also theoretically study 'artificial' $\mathrm{La}_{1-x}\mathrm{Sr}_x\mathrm{MnO}_3$ with only tetragonal distortions (the symmetry is $P4$ and the unit cell is $1\times1\times2$). The main reason we consider the high symmetry phase ($P4$) and compare it to the low symmetry structure ($Pnma$) is computational: the $P4$ symmetry allows for the use of a smaller 1×1 interface unit cell which allows for simulation of much thicker films and substrates. Therefore we need to understand the main differences, if any, between the two phases for what follows below. In addition, a comparison allows us to elucidate the role of structural distortions.

Fig. 4.1d shows a representative phase diagram versus doping for both $Pnma$ and $P4$ $\mathrm{La}_{1-x}\mathrm{Sr}_x\mathrm{MnO}_3$ in the LSDA approximation. To understand these results, we begin with the fact that the effective hopping matrix element t between neighbouring Mn atoms depends on the Mn-O-Mn bond angle [124]. In the $P4$ case, the bond angle is 180° and the hopping is maximized, while in the $Pnma$ case, the bond angle is smaller than 180° and the hopping is reduced. The double exchange mechanism depends linearly on this effective hopping matrix element t, while the superexchange mechanism lowers the energy of antiferromagnetism by $\propto t^2$ from second-order perturbation theory [124]. Therefore as we increase the hopping matrix element t, superexhange is more significantly enhanced than double exchange, thus favoring antiferromagnetism. Compared to the $Pnma$ case, the $P4$ case has a larger effective hopping and the transition curve is shifted to favor antiferromagnetic ordering. This trend holds for both LSDA and LSDA+U calculations. Therefore, phenomenologically we can map $Pnma$ $\mathrm{La}_{1-x}\mathrm{Sr}_x\mathrm{MnO}_3$ to $P4$ $\mathrm{La}_{1-x}\mathrm{Sr}_x\mathrm{MnO}_3$ by choosing an appropriate Hubbard U. We find that in order to reproduce the ferromagnetic-to-antiferromagnetic transition around $x \simeq 0.5$ in the $P4$ case, we need 3 eV $< U <$ 4 eV. By comparison, to locate the correct transition point for $Pnma$ $\mathrm{La}_{1-x}\mathrm{Sr}_x\mathrm{MnO}_3$, U must be in the range of 1 eV $< U <$ 2 eV (see Fig. 4.1b).

Table 4.3: LSDA+U study of bulk $LaMnO_3$. The italic M means metallic and the itallic I means insulating. F refers to ferromagnetic ordering. A, C and G refer to A-type, C-type and G-type antiferromagnetic ordering, respectively [122]. ΔE is the energy difference between the ferromagnetic ordering and A-type antiferromagentic ordering per Mn atom, defined by Eq. 4.1. The unit cell is orthorombic. The experimental value of lattice constants is: $a = 5.742$ Å, $b = 7.668$ Å and $c = 5.532$ Å [118]. The calculated lattice constants are for A-type antiferromagnetic ordering because the experimental ground state is A-type antiferromagnetic. In the parenthesis lists the relative difference between experimental and theoretical lattice constants.

U (eV)	ΔE (meV)	magnetic ordering
0	40	$F(M) < A(M) < C(M) < G(M)$
2	61	$F(M) < A(M) < C(M) < G(I)$
4	65	$F(M) < A(I) < C(I) < G(I)$
6	76	$F(M) < A(I) < C(I) < G(I)$
8	98	$F(M) < A(I) < C(I) < G(I)$

U (eV)	a(Å)	b(Å)	c(Å)
0	5.402 (-5.9%)	7.468 (-2.6%)	5.458 (-1.3%)
2	5.567 (-3.0%)	7.560 (-1.4%)	5.435 (-1.8%)
4	5.644 (-1.7%)	7.584 (-1.1%)	5.448 (-1.5%)
6	5.699 (-0.8%)	7.624 (-0.6%)	5.465 (-1.2%)
8	5.743 (0.02%)	7.694 (0.3%)	5.482 (-0.9%)

4.3.2 Choosing Hubbard U

LSDA+U is commonly used in the study of manganites [118]. However, the choice of Hubbard U is not unanimous. In the previous section, we show that in order to correctly locate the magnetic transition point for *Pnma* manganites, we need 1 eV< U < 2 eV. In this section, we discuss two other methods to determine U, demonstrating that various approaches yield different ranges of U, some of which do not overlap. The point we want to make here is that *there is no most reliable way to determine* U. Since magnetic properties usually sensitively depend on Hubbard U, a general understanding of how Hubbard U affects magnetic properties is more important than a specific prediction of magnetic structure for a given U. The Hubbard U dependence of the ferroelectric/manganite interfaces is discussed in great details in the latter part of the paper.

Table 4.4: LSDA+U study of bulk $LaMnO_3$ using experimental coordinates and lattice constants. The italic M means metallic and the itallic I means insulating. ΔE is the energy difference between the ferromagnetic ordering and A-type antiferromagentic ordering per Mn atom, defined by Eq. 4.1.

U (eV)	magnetic ordering	ΔE (meV)
0	$A(I) < F(M)$	-15
1	$A(I) < F(M)$	-4
2	$F(M) < A(I)$	4
3	$F(M) < A(I)$	10
4	$F(M) < A(I)$	17

Bulk $LaMnO_3$

First we may ask what U value properly describes the parent material: bulk $LaMnO_3$. Taking into account the structural distortions by using a $c(2 \times 2) \times 2$ unit cell [118], we calculate the total energies of different magnetic orderings and find their energy sequence. The result is shown in Table 4.3. In particular, we explicitly list ΔE, defined by Eq. (4.1) in the table. We can see that within a wide range of U, the ground state is not the experimentally observed A-type antiferromagnet, nor is there any tendency that ferromagnetism could yield to A-type antiferromagnetism in the large U limit. However, in order to reproduce the insulating properties of A-type antiferromagnetism, we require that $U \geq 4$eV. As an aside, we also perform a self-consistent calculation on $LaMnO_3$ using the experimental coordinates and lattice constants. By changing the Hubbard U, the experimentally observed insulating A-type magnetic ordering is obtained when U is around 1 eV (see Table 4.4). For a more comprehensive study on bulk $LaMnO_3$, please refer to [8] and references therein.

Linear response approach of self-consistent U

Second, we may ask for an *ab initio* value of U based on the linear response approach [48, 125]. We focus on $P4$ $La_{1-x}Sr_xMnO_3$ as an example. We run a series of linear response calculations [48] on $2 \times 2 \times 2$ unit cells of $P4$ $La_{1-x}Sr_xMnO_3$. The ground state is calculated with the approximation of LSDA+U with a range of $0 < U_{in} < 5$ eV. For

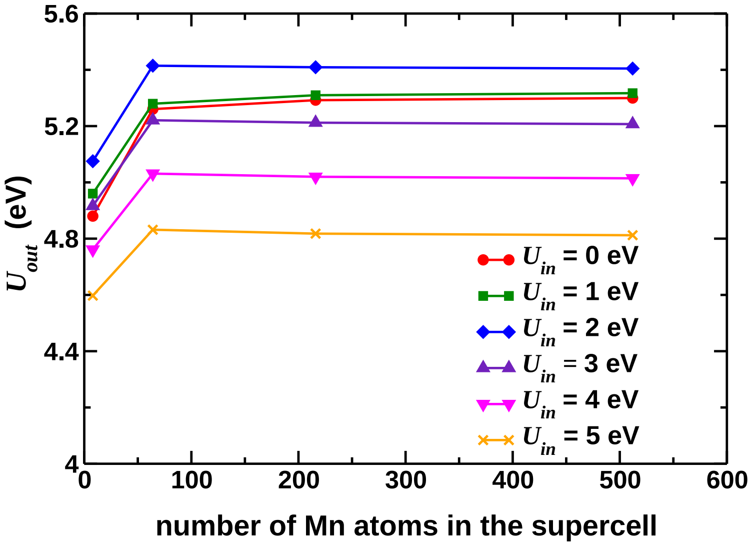

Figure 4.2: Linear response calculations of self-consistent U. The ground state is calculated with the approximation of LSDA+U. For each U_{in}, a converged U_{out} is obtained through an extraopolation scheme in Ref. [48].

each value of U_{in}, we use the extrapolation scheme in Ref. [48] to get the converged value of U_{out}. The results are shown in Fig. 4.2. Then in Fig. 4.3, we collect all the converged U_{out} as a function of U_{in} and extract out U_{scf} [125] from the linear region, which is 5.8 eV. We note that in order to reproduce a ferromagnetic-to-antiferromagnetic transition at $x \simeq 0.5$, we need 3 eV $< U <$ 4 eV for $P4$ $La_{1-x}Sr_xMnO_3$. The value of self-consistent U is significantly larger.

4.4 Ferroelectric/manganite interfaces

4.4.1 Methodology

Our computational supercell for interface calculations is schematically illustrated in Fig. 4.13. The x and y directions of the simulation cell are subject to periodic boundary conditions and their lengths are fixed to our computed theoretical lattice constant of $SrTiO_3$ $a =$ 3.85 Å (1.5% smaller than the experimental value), because in experiments $La_{1-x}Sr_xMnO_3$ are epitaxially grown on $SrTiO_3$ substrate [27]. In order to directly compare to the experiment

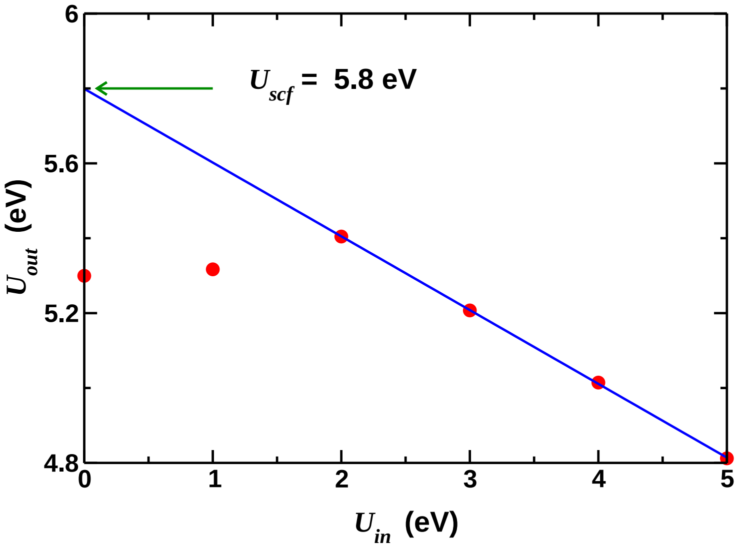

Figure 4.3: From linear response calculations of self-consistent U, converged U_{out} are obtained as a function of U_{in}. From the linear region, we extract out U_{scf} [125], which is 5.8 eV.

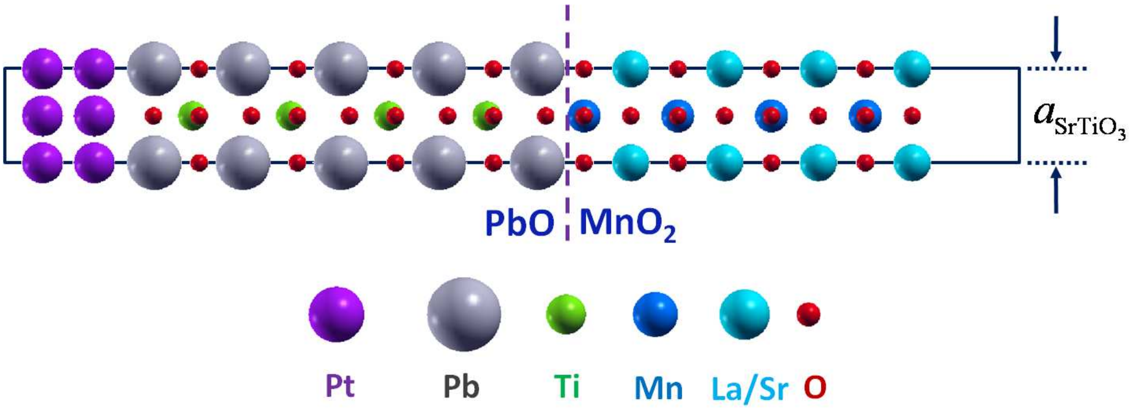

Figure 4.4: Illustration of the computational supercell. The dashed line highlights the PbO/MnO$_2$ interface. The whole structure is coherently strained to the lattice constant of SrTiO$_3$. Vacuum $\simeq$ 20 Å thick is introduced to separate periodic copies and an XO (X=La/Sr) atomic layer faces the vacuum.

[27], all the results shown below are from calculations with the nominal doping level chosen as $x = 0.2$ (unless otherwise specified). In addition to PbTiO$_3$ and La$_{1-x}$Sr$_x$MnO$_3$, we also include the electrode Pt to provide an electron reservior and $\simeq$ 20 Å vacuum to separate

periodic copies. In the simulation cell (Fig. 4.4), we do not include $SrTiO_3$ substrate because the effects of $SrTiO_3$ substrate on the *interfacial* structrual and magnetic properties of $PbTiO_3/La_{1-x}Sr_xMnO_3$ heterostructures are negligible when $La_{1-x}Sr_xMnO_3$ is of 4 unit cells or thicker. Tests on the effects of $SrTiO_3$ substrate are in Appendix B.1. However, we strain the in-plane lattice constant of the whole structure to that of bulk $SrTiO_3$ to preserve the correct stress. In addition to reducing the computational burden, the absence of $SrTiO_3$ substrate creates a manganite surface that allows us to apply a counting method which can much more accurately calculate the hole spatial distribution than the Löwdin orbitals [85], (see Appendix B.2 for details). Since the $SrTiO_3$ substrate is usually TiO_2-terminated and we assume that the manganites are deposited stoichiometrically and epitaxially, the resulting interface between ferroelectric and manganite is taken to be PbO/MnO_2. Based on the Berry phase method [46], the $SrTiO_3$-strained $PbTiO_3$ has bulk polarization 0.74 C/m^2. For the two different directions of ferroelectric polarization, we define two distinct states: accumulation state in which extra holes are induced into $La_{1-x}Sr_xMnO_3$ and depletion state in which extra electrons are induced into $La_{1-x}Sr_xMnO_3$ or equivalently holes are driven out of $La_{1-x}Sr_xMnO_3$. One unit cell of $PbTiO_3$ in the interior is fixed to the bulk ferroelectric $PbTiO_3$ positions in order to simulate a thick $PbTiO_3$ film. In Fig. 4.5, we show the cation-oxygen z-axis displacements of a representative $PbTiO_3$ thin film. The fixed one unit cell is highlighted by the two solid purple lines. The two interfaces (one faces $La_{1-x}Sr_xMnO_3$ and the other faces Pt electrodes) are shown by the orange dashed lines. The sign of the displacements indicates polarization directions. We can see that in the relaxed $PbTiO_3$, there is no reversal of ferroelectric polarization and the magnitude of polarization is homogeneous. In addition, we also calculate an artificial state in which one unit cell of $PbTiO_3$ is fixed to be paraelectric. For the remaining relaxed $PbTiO_3$, cation-oxygen z-axis displacements are very small except for the PbO atomic layer that faces Pt electrodes. We make sure that the ferroelectric $PbTiO_3$ thin film has bulk-like polarization states and serves as hole/electron injectors. Finally, we need to mention that most of results presented below are calculated in an in-plane $c(2 \times 2)$ simulation cell which could accommodate the structural distortions in $Pnma$ $La_{1-x}Sr_xMnO_3$. Such calculations are referred to as $c(2 \times 2)$ $La_{1-x}Sr_xMnO_3$ interface calculations. In order to converge the

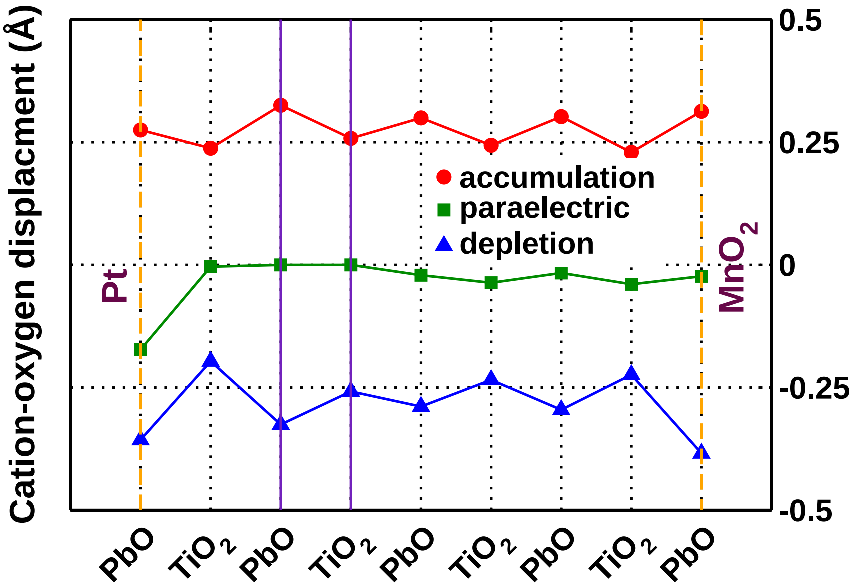

Figure 4.5: Cation-oxygen displacements along z-axis. The two purple solid lines highlights the one unit cell of $PbTiO_3$ that is fixed to bulk positions. The two orange dashed lines show the interfaces: left is the one facing Pt electrodes and right is the one that faces $La_{1-x}Sr_xMnO_3$.

hole distribution, we increase the thickness of manganites by reducing the in-plane cell to 1×1. Those calculations are referred to as 1×1 $La_{1-x}Sr_xMnO_3$ interface calculations.

4.4.2 Charge modulation

We first study the effect of charge modulation from switching the ferroelectric polarization of $PbTiO_3$. In the presence of ferroelectric $PbTiO_3$, the charge density of $La_{1-x}Sr_xMnO_3$ at the interface differs from its bulk value because the polarization of $PbTiO_3$ terminates at the interface and results in the surface charge (the surface charge density is $\sigma = \mathbf{P} \cdot \mathbf{n} = P_z$). Since $La_{1-x}Sr_xMnO_3$ is metallic, this surface charge induces screening charge in the $La_{1-x}Sr_xMnO_3$ equal in magnitude but opposite in sign to the surface charge. When the $PbTiO_3$ switches its polarization, the surface charge changes sign and so does the screening charge. Therefore a net change of charge density ($\Delta\sigma = 2P_z$) is induced in the $La_{1-x}Sr_xMnO_3$ thin film.

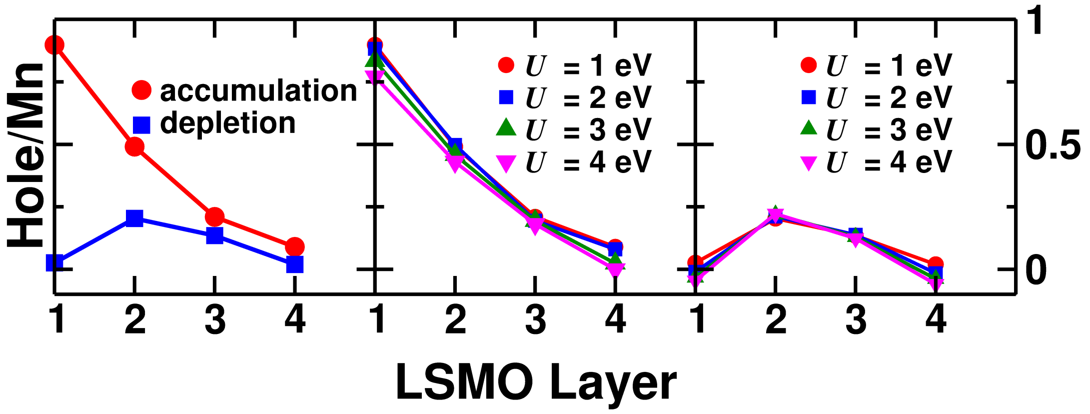

Figure 4.6: Left panel: hole distributions of the accumulation and depletion states of $c(2{\times}2)$ $La_{1-x}Sr_xMnO_3$ ($U = 1$ eV). Middle panel: Hubbard U dependence of hole distribution in the accumulation state. Right panel: Hubbard U dependence of hole distribution in the depletion state.

The left panel of Fig. 4.6 shows the hole distribution of a 4 unit cells thick $La_{1-x}Sr_xMnO_3$ film on $PbTiO_3$. The method of counting holes is described in the Appendix B.2. The nominal doping is $x = 0.2$, highlighted by the dashed line. This calculation is performed on $c(2 \times 2)$ $La_{1-x}Sr_xMnO_3$ with LSDA+U ($U = 1$ eV). The PbO/MnO_2 interface is at layer 1, and layer 4 is the artificial surface. As expected, the hole distribution accumulates (depletes) at the interface when the surface charge is negative (positive).

The middle and right panel of Fig. 4.6 show the Hubbard U dependence of spatial hole distribution for the accumulation and depletion states, respectively. The calculation is performed on the same structure as in the left panel of Fig. 4.6. Since the induced holes (or electrons) extend into the $La_{1-x}Sr_xMnO_3$ within the screening length which does not strongly depend on the correlation, it is not surprising that Hubbard U does not significantly change the hole distribution. As a good approximation, we assume that the hole distribution does not depend on Hubbard U.

In order to get a spatial distribution of holes that is well converged with the manganite thickness, we run a calculation with 8 unit cells of 1×1 $La_{1-x}Sr_xMnO_3$. This calculation is performed with LSDA+U (U=4 eV). The results are shown in Fig. 4.7. From Fig. 4.7a, the screening length of the accumulation state is estimated to be 3 unit cells while the screening length of depletion state seems to be only 1 unit cell. The asymmetry is due to the fact that there are two factors affecting the hole distribution. One is the induced screening charge and the other is the presence of PbO/MnO_2 interface itself. To demonstrate the role of the interface, we perform a test calculation in which the $PbTiO_3$ thin film is forced to be paraelectric and find (see the orange triangle symbols in Fig. 4.7a) that the resulting hole distribution is not uniform nor equal to the nominial doping ($x = 0.2$) at the interface. This non-uniform hole distribution can be considered as a background, owing to the chemistry of the PbO/MnO_2 interface. If we substract the hole distributions of accumulation and depletion states from this background, we can see that the "net" hole distributions of accumulation and depletion states now become more symmetric, with the screening length of depletion state a little larger than that of accumulation state (Fig. 4.7b). This is consistent with the Thomas-Fermi picture that depletion states have less carriers (holes) and therefore a larger screening length. To further verify this Thomas-Fermi picture, we perform the same calculation with another nominal hole doping $x = 0.5$ and find very similar results (see Fig. 4.7c and d).

4.4.3 Magnetization modulation

In this section, we study in detail whether the charge modulation can induce a spin modified configuration in the ground state. This means that the change of the magnetization is not simply proportional to that of the charge density (i.e. simple filling/emptying of Mn orbitals with fixed spin polarization) but involves a more dramatic change of magnetic structure at the interface. The mechanism is as follows: in the accumulation state, the local hole distribution adjacent to the interface could be higher than $x = 0.5$, the critical value for the ferro-to-antiferromagnetic transition. Therefore the spins at the interfacial region could flip. However, in the depletion state, such a local spin-flip is not expected to occur. Therefore from now on, we only focus on the accumulations state. In order to study whether this local phase transition does occur at the interface by switching the polarization, we consider three relevant spin configurations (F, $A1$ and $A2$), illustrated in Fig 4.8.

When all the spins are ferromagnetically coupled, this configuration is denoted as F

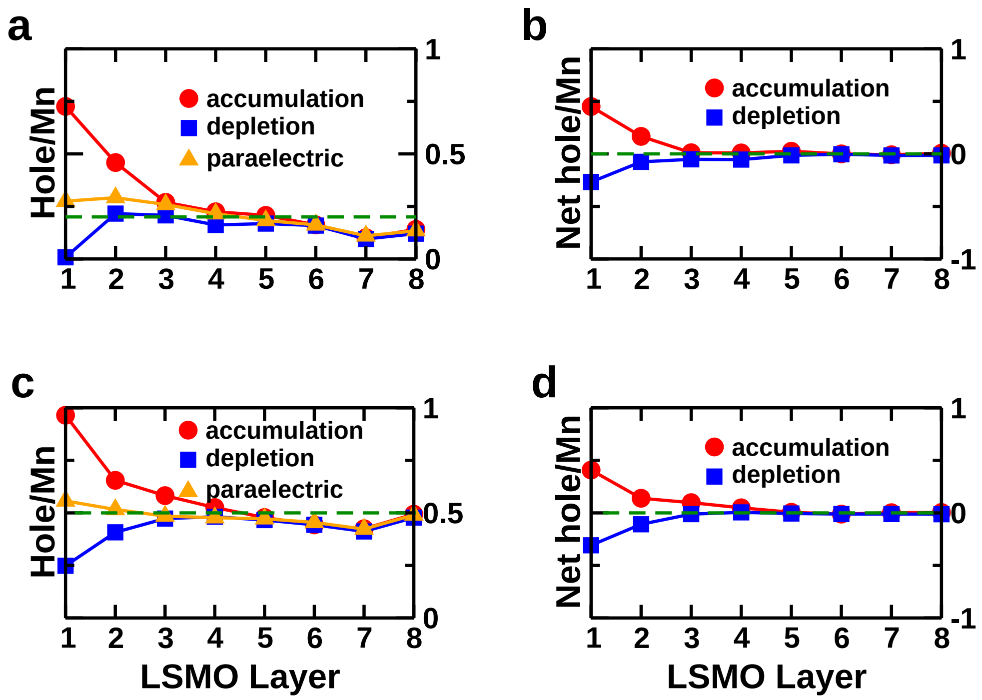

Figure 4.7: **a)** Hole distributions of 1 × 1 $La_{1-x}Sr_xMnO_3$ 8 unit cells thick with $x = 0.2$ ($U = 4$ eV). In addition to accumulation and depletion states, a test calculation in which $PbTiO_3$ is fixed to be paraelectric is done and the resulting hole distribution is shown with orange triangles. **b)** "Net" hole distributions of 1 × 1 $La_{1-x}Sr_xMnO_3$ 8 unit cells thick with $x = 0.2$ ($U = 4$ eV): the paraelectric state background (see **a)**) is substracted from the hole distributions of accumulation and depletion states. **c)** Hole distributions of 1 × 1 $La_{1-x}Sr_xMnO_3$ 8 unit cells thick with $x = 0.5$ ($U = 4$ eV). **d)** "Net" hole distributions in 1 × 1 $La_{1-x}Sr_xMnO_3$ 8 unit cells thick with $x = 0.5$ ($U = 4$ eV).

(Fig. 4.8a). If the spin is flipped in the first unit cell of manganite from the interace, this configuration is denoted by $A1$ (Fig. 4.8b). Finally, if the spin is flipped in the second unit cell of manganite, then we denote it by $A2$ (Fig. 4.8c). We address three important and related questions below: i) whether the ground state magnetic structure depends on U? ii) given a reasonable U, whether the manganite nominal doping x could change the final magnetic structure? iii) how the structural distortions at the interface may affect the magnetic structures?

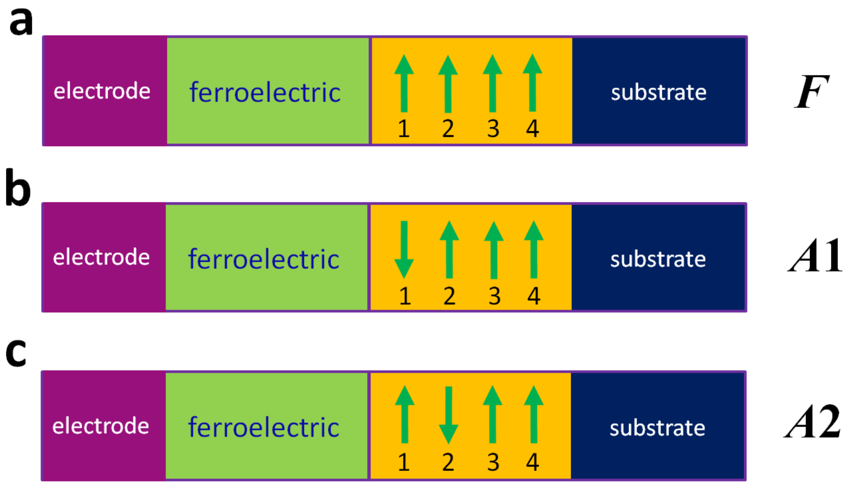

Figure 4.8: Illustration of different magnetic structures. **a)** Ferromagnetic configuration, denoted by F. **b)** Spin flips in the first unit cell, denoted by $A1$. **c)** Spin flips in the second unit cell, denoted by $A2$.

Hubbard U dependence

We obtain the total energies of these three spin configurations with a range of Hubbard U and collect all the results in Fig. 4.9. We use the following definitions of energy differences:

$$\Delta E_1 = E(A1) - E(F) \tag{4.2}$$

$$\Delta E_2 = E(A2) - E(F) \tag{4.3}$$

From Fig. 4.9 we can see that the magnetic structure of the ground state evolves with Hubbard U. When U is small ($U < 0.9$ eV), the ground state has the magnetic structure of $A2$. With U increasing (0.9 eV $< U <$ 2.4 eV), the ground state evolves into $A1$. When U gets even larger ($U >$ 2.4 eV), we have F as the ground state. Therefore any prediction of the magnetic properties of the interface depends greatly on the choice of U. Before we pick a reasonable value of U, we need to understand why the magnetic structure is so sensitive to the Hubbard U. The answer is that U changes the bulk phase transition point so that for the same hole distribution, the preferred local magnetic phase also changes. We can see from Fig. 4.9 that increasing the Hubbard U drives the local phase at the interface

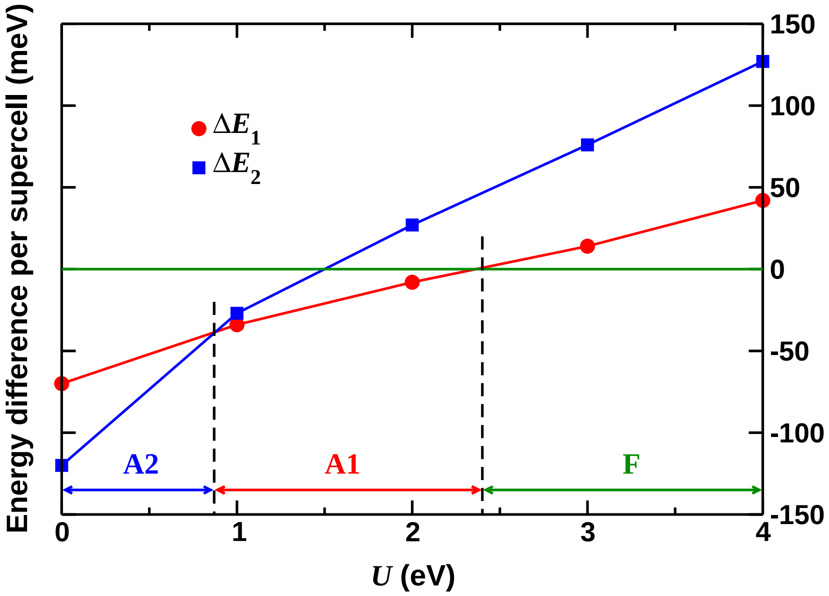

Figure 4.9: Energy sequence dependence on Hubbard U. $\Delta E_1 = E(A1) - E(F)$ and $\Delta E_2 = E(A2) - E(F)$. The labels ($F$, $A1$ and $A2$) show the ground state in different regions of Hubbard U. The boundary between F and $A1$ is 2.4 eV and that between $A1$ and $A2$ is 0.9 eV.

from antiferromagnetic to ferromagnetic, which is consistent with the U dependence in the bulk (see Fig. 4.1b). In order to more quantitatively describe the energy sequence, we construct an Ising-like model which is based on the interaction between nearest neighbor Mn magnetic moments:

$$E = -\sum_{<ij>} J_{ij} m_i m_j \tag{4.4}$$

where $< ij >$ range is over all nearest neighbors and m_i is the magnetization in each MnO$_2$ layer of the manganites. The labelling of manganite layers is shown in Fig. 4.8. We assume that the hole spatial distribution does not sensitively depend on magnetic structures [2], and obtain:

---

[2] We used a Löwdin orbital analysis and found that the change in the hole spatial distribution between different magnetic structures is insignificant. However, just as we argued in the appendix, the Löwdin method itself is not highly accurate and can only be considered to provide indirect evidence.

$$\Delta E_1 = 2J_{12}|m_1 m_2| \tag{4.5}$$

$$\Delta E_2 = 2J_{12}|m_1 m_2| + 2J_{23}|m_2 m_3| \tag{4.6}$$

In order to get an energy sequence, we need to know the signs of J_{12} and J_{23}. From the bulk calculations, at a given hole doping x and assuming half-metallicity, the magnetization is related to the hole doping x by $m = (4 - x)\mu_B$ where μ_B is the Bohr magneton. The exchange coupling J can be extracted out by:

$$J = \frac{E(A) - E(F)}{2m^2} \tag{4.7}$$

where the energy difference $\Delta E = E(A) - E(F)$ is from the bulk calculations, shown in Fig. 4.1. J changes sign at the transition point. From Eq. (4.7), J is positive for ferromagnetic phase and negative for A-type antiferromagnetic phase. At the interface, however, the hole spatial distribution is not uniform (see Fig. 4.7). We assume that the interface coupling J_{ij} is that of bulk $La_{1-x}Sr_xMnO_3$ but for a doping value that is the average of the neighboring layers i and j:

$$J_{ij} \simeq J_{\text{bulk}} \left(\frac{x_i + x_j}{2} \right) \tag{4.8}$$

We need a final good approximation, which is verified in Fig. 4.6, that the hole distribution does not sensitively depend on Hubbard U. Based on Eq. (4.5-4.8), we start with a large Hubbard U. Since large U favors ferromagnetism (see Fig. 4.1b), the bulk phase is ferromagnetic and both J_{12} and J_{23} are positive. Thus $0 < \Delta E_1 < \Delta E_2$ and we have the following energy sequence: $F < A1 < A2$. We denote this by case 1. With a decreasing U, the transition point is moved to smaller hole doping region. Noting that the hole distribution monotonically decays from the interface (see Fig. 4.7), we always have $(x_1 + x_2)/2 > (x_2 + x_3)/2$. Hence J_{12} changes sign earlier than J_{23} as U decreases. If U is in such a range that J_{12} just becomes negative but $J_{23} > 0$, we have $\Delta E_1 < 0$ and $\Delta E_2 > 0$. The energy sequence is now $A1 < F < A2$, which is denoted by case 2.

Table 4.5: The energy sequence predicted from the simple model and the comparison with the DFT calculations with different Hubbard U.

model		DFT		
case	energy sequence	U (eV)	ΔE_1 (meV)	ΔE_2 (meV)
1	$0 < \Delta E_1 < \Delta E_2$	3	14	76
2	$\Delta E_1 < 0 < \Delta E_2$	2	-8	27
3	$\Delta E_1 < \Delta E_2 < 0$	1	-34	-27
4	$\Delta E_2 < \Delta E_1 < 0$	0	-70	-120

As U further decreases, so that J_{12} becomes very negative and J_{23} remains positive but $J_{12}|m_1| + J_{23}|m_3| < 0$, then we have $\Delta E_1 < \Delta E_2 < 0$. The energy sequence becomes $A1 < A2 < F$. This is case 3. With U further decreasing, the bulk phase becomes always antiferromagnetic, both J_{12} and J_{23} become negative, and we have $\Delta E_2 < \Delta E_1 < 0$. The final possible energy sequence is $A2 < A1 < F$, which is denoted by case 4. These four energy sequences exhaust all the possibilities and are summarized in Table 4.5. Now we compare the DFT results (see Fig. 3.18) to the energy sequence predicted from the model (see Table 4.5). As the Hubbard U evolves from 0 to 4 eV, we find all four cases. For example, $U = 3$ eV corresponds to $F < A1 < A2$; $U = 2$ eV to $A1 < F < A2$; $U = 1$ eV to $A1 < A2 < F$ and $U = 0$ eV to $A2 < A1 < F$. The exact boundaries of Hubbard U for each energy sequence can be found in Fig. 3.18.

Since the Hubbard U changes the transition point and the magnetic structure of the ground state of the $PbTiO_3/La_{1-x}Sr_xMnO_3$ interface, we need to determine what is the reasonable value of U. Following Ref. [113], we argue that because the magnetic structures sensitively depend on the transition point, we need to choose a range of U so that the ferromagnetic-to-antiferromagnetic transition occurs around $x \simeq 0.5$. From bulk calculations, we know that as 1 eV $< U <$ 2 eV for $Pnma$ $La_{1-x}Sr_xMnO_3$, this criterion is satisfied. On the other hand, when U is in this range, the magnetic structure of the ground state is always $A1$. Therefore by switching the $PbTiO_3$ polarization, we do find a spin-modified configuration in the DFT simulation, provided that our choice of U is reasonable. This prediction is consistent with the recent experiment [27] which observes an anomously large change in the magnetization as the polarization of ferroelectrics is switched and which

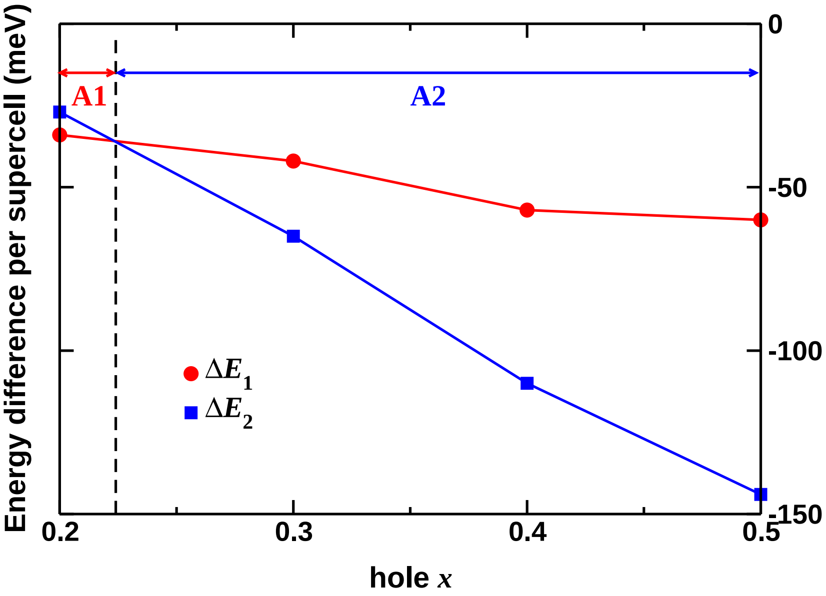

Figure 4.10: Energy sequence dependence on nominal doping of manganite. $\Delta E_1 = E(A1) - E(F)$ and $\Delta E_2 = E(A2) - E(F)$. The labels ($A1$ and $A2$) show the ground state in different regions of nominal doping. The boundary between $A1$ and $A2$ is $x_c = 0.22$. The calculations are performed with LSDA+U (U=1 eV).

assigns this to a spin-flip on the Mn atom closest to the interface.

Nominal hole dependence

The ground state magnetic structure we found ($A1$ configuration) is consistent with the experimental conjecture, but is different from that of a similar multiferroelectric structure $BaTiO_3/La_{1-x}Ba_xMnO_3$ with $x = 0.5$, which is $A2$. We explain that the difference of ground state magnetic structures lies in the nominal doping of manganites. Given $U = 1$ eV, we calculate the ground state with different nominal doping x of manganites and show the results in Fig. 4.10

At $U = 1$ eV, as the nominal doping is *near* the magnetic transition point $x = 0.5$, the ground state is $A2$, consistent with Ref. [113]. However, as the nominal doping is far below the magnetic transition point, the ground state could be $A1$. The exact phase boundary between $A1$ and $A2$ is $x_c = 0.22$ for $U = 1$ eV. This transition could be easily understood by the model we build above. Each pair of Mn magnetic moments could be either ferromagnetic or antiferromagnetically coupled, depending on the average holes on the two Mn atoms. As the nominal doping is low, ferroelectrics can only inject enough holes to make (m_1, m_2) pair to be antiferromagnetic, leaving the remaing manganites ferromagnetic. This is $A1$ configuration. If the nominal doping is higher, then the injected holes could make both (m_1, m_2) and (m_2, m_3) pairs antiferromagnetically coupled. We need to further comment here: i) due to the screening length of manganite (see Fig 4.7), the injected holes can not diffuse too far into the manganites and therefore we do not expect antiferromagnetism to occur in the first three pairs or even further. ii) we are only interested in the nominal doping smaller than 0.5, so that before ferroelectric doping, the manganite is in the ferromagnetic state and a spin-flip process could be expected due to injected holes. iii) from our Ising-like model, the phase transition point between $A1$ and $A2$ depends on Hubbard U. As U does not favor antiferromagnetism, a larger U increases x_c (i.e, requiring more holes to make it antiferromagnetic).

Structural distortion dependence

Due to the presence of ferroelectric polarization, significant distortions that deviate from bulk manganites are observed in the relaxed ground state structures. Concerning each oxygen octahedron that encloses Mn atoms, we calculate c/a ratio and rumplings δ/a in each MnO_2 layer, where c is the distance between the two apical oxygen atoms along the z direction, δ is the vertical displacement between Mn and O, and a is the lattice constant of $SrTiO_3$ substrate. The results are summarized in Table 4.6. Since the spin-flipped process occurs at the interface in the accumulation state, we only show c/a ratio and δ/a of the first and second manganite layers from the interface, and from now on the discussion is constrained to the accumulation state. From Table 4.6, we can see that in the accumulation state, there are significant polar distortions at the interface (δ/a is as large as 6%). It was shown in Ref. [113] that the spin-flipped process is mainly of electronic origin rather than due to the polar distortions at the interface. In this section, we use detailed comparisons to show that though the spin-modified configuration is due to electronic reconstructions, polar distortions need to be taken into account in order to make a quantitative (instead of

Table 4.6: The c/a ratio of each oxygen octahedron that encloses Mn atoms and rumplings δ/a of each MnO_2 layer for both accumulation and depletion states. c is the distance between the two apical oxygen atoms along the z direction. δ is the rumplings of MnO_2 layer, and a is the lattice constant of $SrTiO_3$ substrate. Layer1 and layer2 refer to the first and second unit cell of manganites from the interface.

accumulation state			depletion state		
	layer1	layer2		layer1	layer2
c/a	0.97	0.94	c/a	1.05	0.98
δ/a	0.06	0.02	δ/a	0.01	0.001

qualitative) link between the interface phase and bulk phases.

Now we look at the Ising-like model Eq. (4.5-4.8) more closely. The model is based on the assumption that the local magnetic structure can be predicted from bulk manganites of the same hole doping. In Table 4.7, we list the energy difference between F and $A1$ interfacial configurations from the interface calculations, defined by

$$\Delta E_I = E(A1) - E(F) \tag{4.9}$$

where $E(F)$ and $E(A1)$ are the total energies of F and $A1$ configurations, respectively. We also calculate the average hole density between the first and second layers, i.e. $\overline{x} = (x_1 + x_2)/2$. Next, we list the *bulk* energy difference ΔE_B, defined as

$$\Delta E_B = \frac{1}{2}\left(E_B(A) - E_B(F)\right) \tag{4.10}$$

where $E_B(F)$ and $E_B(A)$ are the total energies of $SrTiO_3$-strained $La_{1-x}Sr_xMnO_3$ with ferromagnetic and A-type antiferromagnetic ordering, respectively. The factor $\frac{1}{2}$ is included because in the bulk form wherever a Mn atom flips its spin, there are two Mn-Mn bonds involved owing to periodic boundary conditions, whereas at the interface a Mn spin flip only involves one Mn-Mn bond. Hence, we need a factor $\frac{1}{2}$ so that both ΔE_I and ΔE_B describe the energy difference *per* Mn-Mn bond. The nominal hole doping x is chosen as the same as $\overline{x}$ from the supercell calculations. Table 4.7 shows that although the trend versus U is the same in both supercell and bulk calculations, the magnitudes of ΔE do

Table 4.7: The comparison of energy difference between the interface calculations and bulk $La_{1-x}Sr_xMnO_3$ calculations. $\overline{x} = (x_1 + x_2)/2$ is the average hole in the first and second $La_{1-x}Sr_xMnO_3$ layers closest to the interface. For different Hubbard U, $\overline{x}$ does not change significantly. ΔE_I is the energy difference between phases $A1$ and F from the supercell calculations. ΔE_B is the energy difference of $SrTiO_3$-strained *bulk* $La_{1-x}Sr_xMnO_3$ between A-type antiferromagnetism (A) and ferromagnetism (F). ΔE_{BP} is the energy difference between $E(A)$ and $E(F)$ of $SrTiO_3$-strained *bulk* $La_{1-x}Sr_xMnO_3$, with the interfacial polar distortions manually included and c-axis optimized. For bulk calculations (ΔE_B and ΔE_{BP}), the nominal hole density is chosen as $\overline{x}$.

U (eV)	$\overline{x}$	ΔE_I (meV)	ΔE_B (meV)	ΔE_{BP} (meV)
1	0.7	-34	-112	-47
2	0.7	-8	-70	-17
3	0.65	14	-24	16
4	0.6	42	19	57

not agree at all. There must be something at the interface which is absent in bulk phase and significantly affects the energy difference between antiferro- and ferromagnetism.

We find that, due to the presence of ferroelectric $PbTiO_3$, strong polar distortions are induced at the interface layer of MnO_2 in the accumulation state (Table 4.6), as is illustrated in Fig. 4.11a. The cation-oxygen vertical displacement in MnO_2 at the interface is $\delta = 0.2$ Å. Such a strong polar distortion (distinguished from the structural distortions of $Pnma$ symmetry) is absent in bulk $La_{1-x}Sr_xMnO_3$ and is a direct consequence of the ferroelectric/manganite interface. In order to show explicitly how this interfacial polar distortion affects the energy difference between F and A-type magnetic orderings, we perform the following thought experiment, which is schematically illustrated in Fig. 4.11b. We focus on the two layers of $La_{1-x}Sr_xMnO_3$ closest to the interface in interface calculations, use their relaxed atomic positions and choose an x that is equal to the average hole doping $\overline{x} = (x_1 + x_2)/2$ from interface calculations. In this way, we create such artificial $La_{1-\overline{x}}Sr_{\overline{x}}MnO_3$ with the same built-in polar distortions and the same average hole doping as the two manganite layers at the interface. We impose periodic boundary conditions on this artificial $La_{1-\overline{x}}Sr_{\overline{x}}MnO_3$, fix all atom positions and in-plane lattice constants, and optimize the c-axis to minimize the out-of-plane stress. We tune c separately for both ferromagnetism and A-type antiferromagnetism. A similar energy difference ΔE_{BP} (subscript

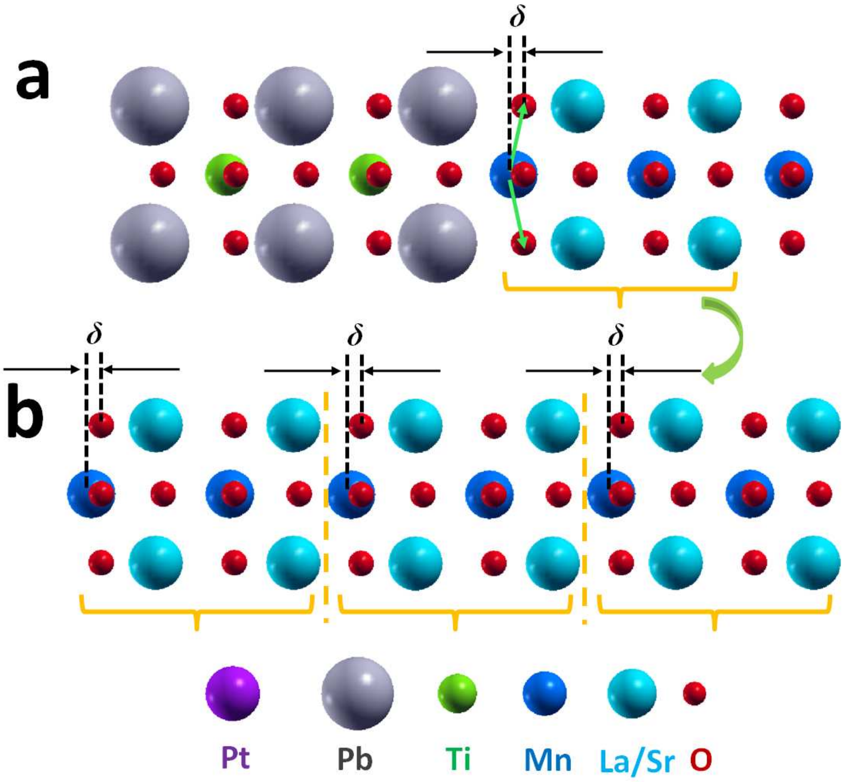

Figure 4.11: **a)** Strong polar distortion is induced at the interface layer of MnO_2 due to the presence of $PbTiO_3$. **b)** Schematics of copying the two interfacial $La_{1-x}Sr_xMnO_3$ layers and forming artificial bulk $La_{1-\overline{x}}Sr_{\overline{x}}MnO_3$ with built-in polar distortions.

P means 'polarized') is defined as

$$\Delta E_{BP} = \frac{1}{2}\left(E_{BP}(A) - E_{BP}(F)\right) \tag{4.11}$$

where $E_{BP}(F)$ and $E_{BP}(A)$ are the total energies of the artificially constructed $La_{1-\overline{x}}Sr_{\overline{x}}MnO_3$ with ferromagnetic and A-type antiferromagnetic ordering, respectively. We can see from Table 4.7 that ΔE_{BP} is much closer to ΔE_I than the raw bulk data ΔE_B, demonstrating that in order to quantitatively connect the phase evolution of the ferroelectric/manganite interface from the bulk manganite phases, the polar distortion induced in interfacial manganites is an essential ingredient in modelling.

4.4.4 Orbital modulation

In this section, we study the ferroelectric control of orbital ordering in the manganites. First we need to understand the orbital degree of freedom in perovskite oxides. Elementary considerations show that the introduction of transition metals into the cubic perovskite crystal lattice creates crystal splittings of the d orbitals into low energy t_{2g} (3-fold degenerate d_{xy}, d_{yz} and d_{zx}) and higher energy e_g (2-fold degenerate $d_{x^2-y^2}$ and $d_{3z^2-r^2}$) manifolds [29]. These orbital degeneracies can be removed in many ways, e.g. by Jahn-Teller distortions, which makes for unequal electronic occupations between the orbitals. This leads to the anisotropy of charge distribution and in turn affects transport properties and magnetic orderings [117]. Therefore removing orbital degeneracy and controlling various orbital orderings may play an important role in tailoring properties of TMOs and their surfaces as well as interfaces [126, 127, 128, 129, 63, 130].

Among perovskite oxides, manganites stand out as an important class [29], in which the e_g orbital degree of freedom is active and strongly correlates with magnetic orderings. For bulk $La_{1-x}Sr_xMnO_3$ (LSMO), Mn has valence 3+ or 4+ (average 3+x). Hunds' rule causes the three t_{2g} majority-spin orbitals to be completely filled up, resulting in a 3/2 core spin. The remaining lone electron hops among the Mn e_g orbitals with a spin essentially parallel to the core spin, based on the double exchange mechanism [119, 124]. When the two e_g orbitals are degenerate, the hopping is maximized and this favors the ferromagnetic ordering of the Mn core spins. Then statistically they have equal occupancy, which favors ferromagnetic ordering for a wide range of hole doping $0.2 < x < 0.5$ [28]. However, if the orbital degeneracy is removed, other magnetic orderings could be energetically favored: lowering the in-plane orbital $d_{x^2-y^2}$ stabilizes A-type antiferromagnetism while lowering the out-of-plane orbital $d_{3z^2-r^2}$ favors C-type antiferromagnetic ordering [117, 123].

Although structural distortions (e.g. Jahn-Teller or $GdFeO_3$ distortions) are common bulk perovskite manganites, they only weakly remove orbital degeneracy. With the development of thin film growth techniques and the introduction of epitaxial strain, orbital degeneracy can be more effectively removed through strain-induced Jahn-Tell distortions. Tensile (compressive) strain makes for $c/a < 1$ ($c/a > 1$) which in turn changes the crystal field to favor the in-plane orbital $d_{x^2-y^2}$ (out-of-plane orbital $d_{3z^2-r^2}$). Unforunately,

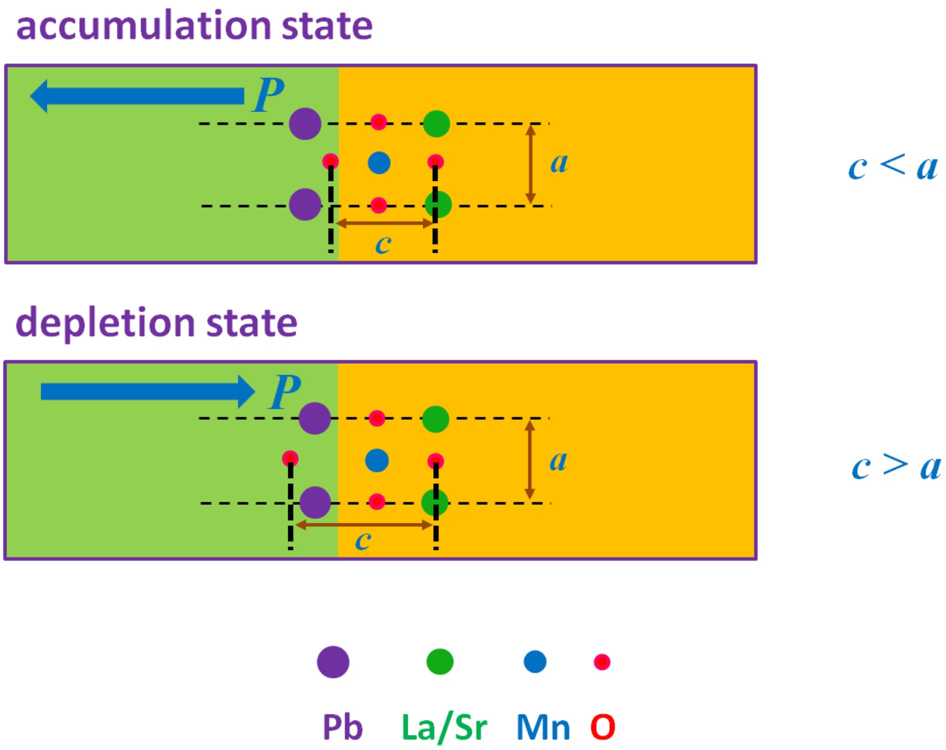

Figure 4.12: Schematic of a $PbTiO_3$/LSMO interface. Yellow parts represent LSMO and green parts are $PbTiO_3$. The interface is PbO/MnO_2. The oxygen octahedron enclosing the interfacial Mn atom has different c/a ratio as the ferroelectric polarization flips.

utilizing strain is a static approach to tailoring the c/a ratio and the desired orbital [121]. In this Letter, we describe a *dynamic* (i.e., flippable) approach to modulate the orbital ordering in manganites.

Motivated by the recent experimental realization of $Pb(Zr_{0.2}Ti_{0.8})O_3$/LSMO interface [27], we show that switching the ferroelectric polarization at ferroelectric/manganite interfaces can strongly modulate the Mn e_g orbital ordering at the interface. For simplicity, we focus on $PbTiO_3$/LSMO as a prototype. Fig. 4.12 shows the schematic of such an artificial structure with a PbO/MnO_2 interface. Due to the presence of ferroelectric polarization (surface) charges, screening charges (in the form of mobile doped holes) appear at manganite interface. Two states are possible: accumulation or depletion of holes at the interface as illustrated in Fig. 4.12. In the accumulation state, the interfacial PbO layer is polarized so that its O anion is pushed towards the Mn at the interface, which should lead

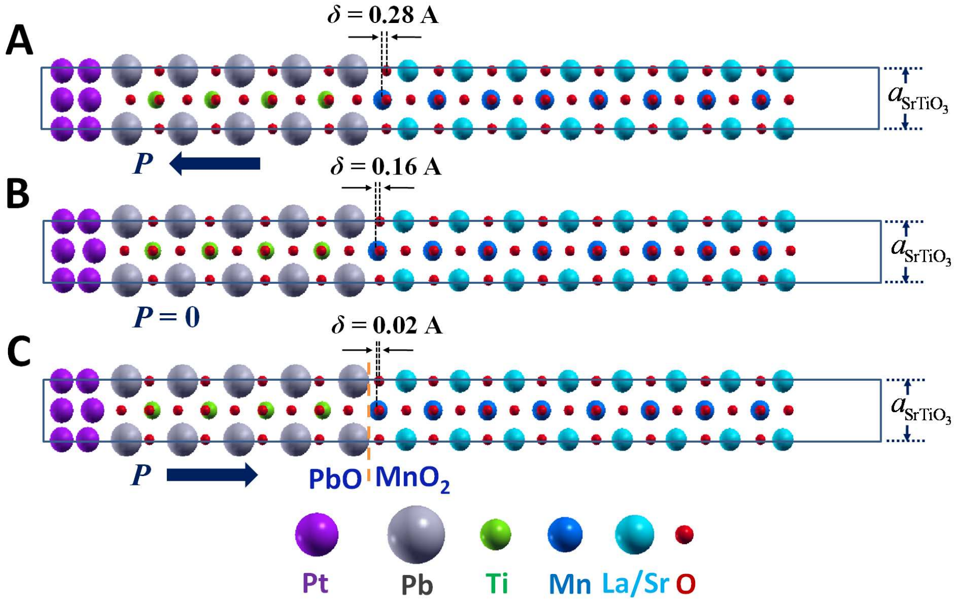

Figure 4.13: Illustration of the supercell. The orange dashed line highlights the PbO/MnO$_2$ interface. The whole structure is strained to a SrTiO$_3$ substrate (substrate not shown in the figure). **A**) accumulation state. **B**) paraelectric state. **C**) depletion state. δ is the Mn-O displacement.

to $c < a$ and stabilization of $d_{x^2-y^2}$. On the other hand, in the depletion state the oxygen is pushed away from the Mn, leading to $c > a$ and favoring $d_{3z^2-r^2}$.

Following the above schematics, we simulate the PbTiO$_3$/La$_{1-x}$Sr$_x$MnO$_3$ interface using the local spin density approximation (LSDA) [12] and the LSDA+U method with Hubbard $U = 4$ eV [114] to take into account the strong electronic correlations on the Mn d orbitals [3]. The schematic of our supercell is illustrated in Fig. 4.13.

To quantify the orbital ordering, we define a layer-resolved orbital polarziation as in Ref. [131]

$$P^i_{\text{orb}} = \frac{n^i_{d_{x^2-y^2}} - n^i_{d_{3z^2-r^2}}}{n^i_{d_{x^2-y^2}} + n^i_{d_{3z^2-r^2}}} \tag{4.12}$$

where n^i is the occupancy of an orbital in the ith unit cell of the LSMO calculated by using

---

[3] In all our calculations, we focus on $P4$ LSMO rather than the more complex $Pnma$ LSMO to reduce the computational burden and to study thick LSMO thin films. The choice of U is based on the experimental fact that a ferromagnetic-to-antiferromagnetic transition occurs as hole doping is around 0.5. However, the mechanism we propose here depends on the atomic configuration, thus arguably insensitive to strong correlations. For the details of how to choose the Hubbard U and how to map $P4$ LSMO to $Pnma$ LSMO, please refer to [30].

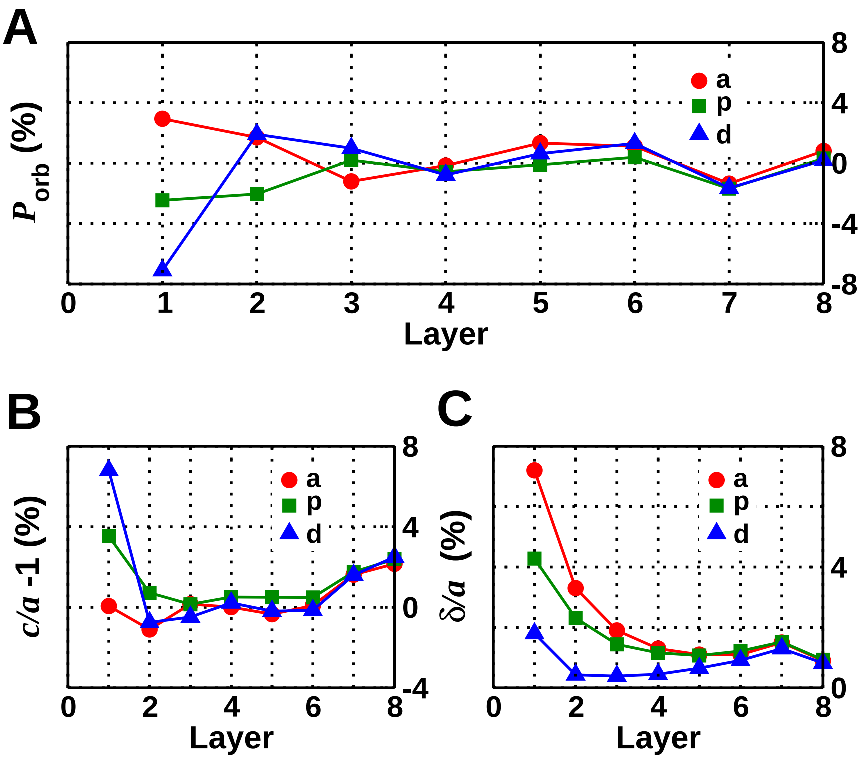

Figure 4.14: **A**) Layer-resolved orbital polarization of $PbTiO_3$/LSMO interface. “a”, “p” and “d” refer to accumulation, paraelectric and depletion state, respectively. **B**) c/a ratio. a is the lattice constant of $SrTiO_3$. **C**) Mn-O displacement δ of the interfacial MnO_2 layer.

Löwdin projection [85]. We show the layer-resolved orbital polarization P^i_{orb} in Fig. 4.14A. We study three different configurations: accumulation, depletion, and a test reference state in which the $PbTiO_3$ film is fixed to its bulk paraelectric state. The relaxed atomic structures are illustrated in Fig. 4.13. We can see from Fig. 4.14A that the orbital polarizations of the interfacial Mn layer are non-zero in both accumulation and depletion. The positive interfacial orbital polarization in accumulation indicates that $d_{x^2-y^2}$ is stabilized while in depletion the negative polarization means $d_{3z^2-r^2}$ is more populated. Qualitatively, these results are consistent with the above simple schematics. However, quantitatively we find that in addition to the c/a ratio, the ferroelectric cation displacement of the interfacial MnO_2 layer also contributes significantly to the orbital polarization, a degree of freedom missing in the simple schematics. We show in Fig. 4.14B, the c/a ratios of each oxygen octahedron enclosing a Mn atom; in Fig. 4.14C we present the ferroelectric Mn-O rumplings in each MnO_2 atomic layer. In depletion, c is significantly larger than a for the interface Mn layer, while c is almost equal to a in accumulation. On the other hand, the rumplings of the MnO_2 layers are largest in accumulation, decrease for the paraelectric state, and are smallest for depletion. These ferroelectric interfacial rumplings in the LSMO have two causes. The first is elementary and extrinsic due to the ferroelectricity in the $PbTiO_3$ whose rumplings propagate into the interface (similar to what is seen in ferroelectric superlattices of $BaTiO_3/SrTiO_3$ [132] and $PbTiO_3/SrTiO_3$ [133] where minimization of electrostatic potential at the interface causes polarization in otherwise paraelectric $SrTiO_3$). Second is a pure intrinsic interfacial chemistry effect where the rumpling is present even in the paraelectric state as shown clearly in Fig. 4.13B), and which is also observed for other heterostructures [131]. Therefore, in accumulation (Fig. 4.13A) the rumplings in LSMO are enhanced since the extrinsic and intrinsic effects work together while in depletion the rumplings are suppressed since the two effects counteract.

We find that just as the canonical Jahn-Teller (c/a ratio) effect can remove the degeneracy of Mn e_g orbitals, so can the MnO_2 cation-anion displacement. In fact, they could be equally strong and create orbital polarization of the same order and thus must both be considered on equal footing for the interfacial system. This is most easily illustrated for bulk LSMO. Fig. 4.15 shows P_{orb} for bulk LSMO as a function of c/a and MnO_2 rumplings. Fig. 4.15A shows data for tetragonal LSMO where c/a is changed manually. The resulting P_{orb} is consistent with the elementary expectation from crystal field theory (a detailed analysis is in Appendix B.5). Fig. 4.15B shows the effect on P_{orb} of manually creating a Mn-O rumpling int the MnO_2 of bulk LSMO. P_{orb} increases ($d_{x^2-y^2}$ is more populated) as the rumpling δ becomes bigger. Combining Fig. 4.14 and Fig. 4.15, we see that in accumulation the the interfacial P_{orb} is actually not due to $c < a$ but instead due to the large Mn-O rumplings stabilizing $d_{x^2-y^2}$. On the hand, the octahedron elongation $c > a$ is the dominating factor for depletion, which favors $d_{3z^2-r^2}$.

We note that Mn-O rumplings always stabilize $d_{x^2-y^2}$ (Fig. 4.15B). This is straightforward from elementary tight-binding considerations [134]. In a cubic ABO_3 perovskite, the conduction band minimum e_g states at the Γ point are pure metal orbitals due to the vanishing of B-O hopping elements. B-O rumplings break symmetry and allow for mixing of B and O orbitals: i.e., for rumplings along z, the $d_{3z^2-r^2}$ can mix with O p_z

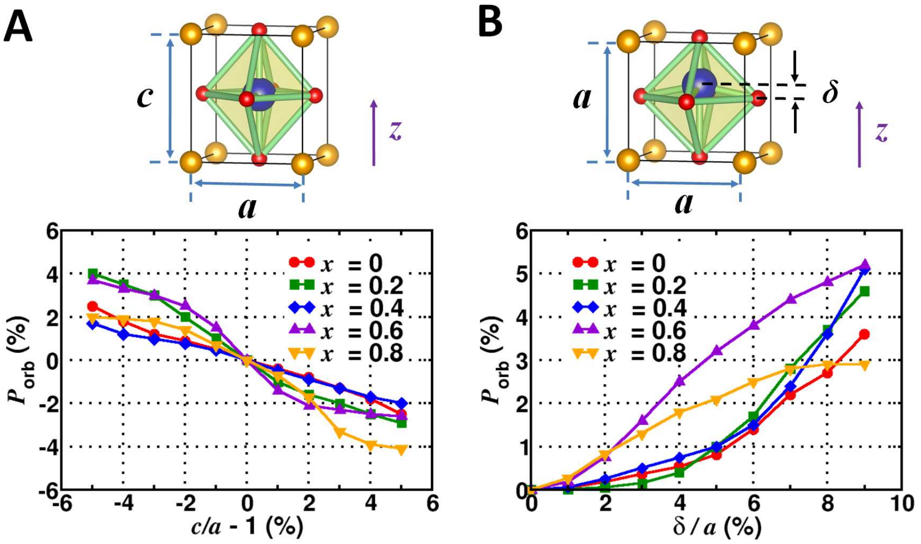

Figure 4.15: Orbital polarization of bulk LSMO. **A**) tetragonal LSMO. **B**) cubic LSMO with the Mn atom shifted along z direction.

orbitals to become more antibonding and rise in energy at Γ, and the unchanged $d_{x^2-y^2}$ now constitutes the conduction band minimum (see Appendix B.5 for a more detailed analysis).

Finally, we examine the robustness of our findings for modulating interfacial orbital polarization. To simulate differing ferroelectric polarizations, we fix the electric polarization throughout the $PbTiO_3$ thin film and manually vary its magnitude from 0.44 to 1.04 C/m^2 (bulk $PbTiO_3$ has a ferroelectric polarization of 0.7 C/m^2). Fig. 4.16A shows that the orbital degeneracy of the interfacial MnO_2 is significantly removed over this range. The difference of orbital polarization ranges from 7% to 10%, which might be directly detectable by the recently invented orbital reflectometry [131], especially since by flipping polarization, the measure focus on the change of interfacial orbital polarization, thus canceling backgrounds and the bulk of the films.

We need to mention that in accumulation, $c/a \approx 1$ as the polarization changes its magnitude (Fig. 4.16C) while δ increases with polarization (Fig. 4.16D). However, P_{orb} decreases as the electric polarization exceeds 0.6 C/m^2, which seems at odds with the argument that the Mn-O rumpling δ favors $d_{x^2-y^2}$ (as per Fig. 4.15B). However, a careful study of Fig. 4.15B shows that at fixed hole density x, P_{orb} increases with δ, but that for

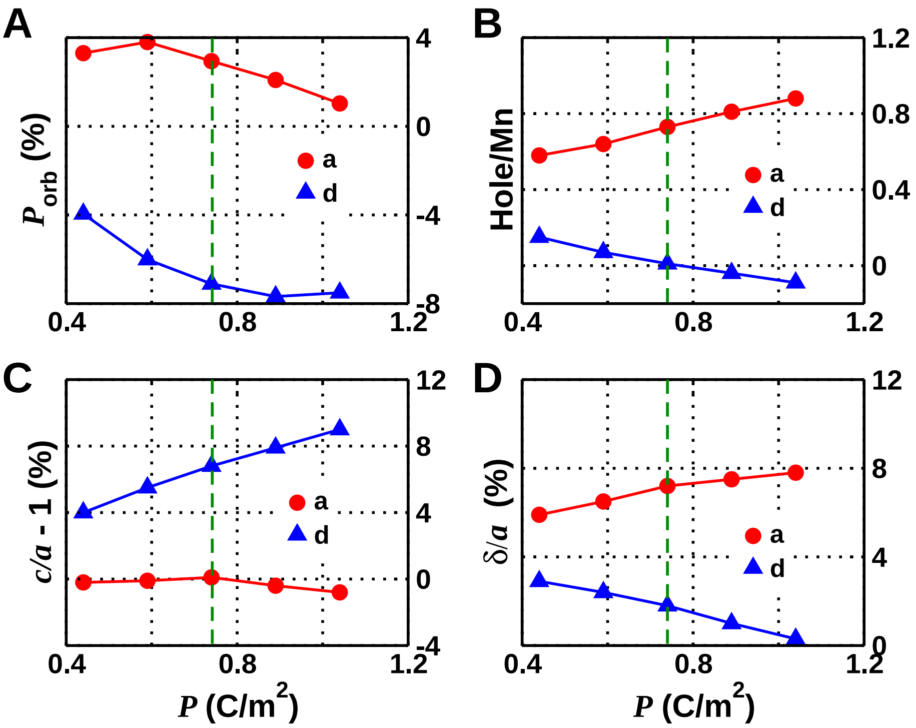

Figure 4.16: **A**) Orbital polarization of the interfacial Mn atom versus electric polarization. "a" and "d" refer to accumulation and depletion state, respectively. **B**) Holes on the interfacial Mn atom versus electric polarization. **C**) c/a ratio versus electric polarization. a is the lattice constant of $SrTiO_3$. **D**) Mn-O displacement of the interfacial MnO_2 layer versus electric polarization. The green dashed lines correspond to the calculated polarization of $SrTiO_3$-strained bulk $PbTiO_3$.

a fixed δ $P_{\rm orb}$ decreases strongly as $x > 0.6$. When we increase the electric polarization, δ is enhanced (see Fig. 4.16D), so is the hole density of the interfacial Mn atom (see Fig. 4.16B). Therefore, for small electric polarizations below 0.6 C/m^2, δ dominates so that $P_{\rm orb}$ increases. For larger electric polarizations, the hole factor takes over and $P_{\rm orb}$ decreases. In brief, this non-monotonic behavior of $P_{\rm orb}$ on electric polarization shows that in addition to c/a and the rumpling δ, the hole density is also a critical factor controlling $P_{\rm orb}$: in our system it is determined by the screening in response to the ferroelectric, but in principle this density could be modified by chemically doping the interfacial layer.

4.5 Conclusion

We systematically study the $PbTiO_3/La_{1-x}Sr_xMnO_3$ interface as a prototype interface between ferroeletrics and manganites. We develop a method to accurately count the holes in each layer of the manganite and show explicitly the hole distribution of the manganite in the accumulation and depletion states. The hole distribution is consistent with the charge modulation due to the screening of ferroelectric polarization. We also carefully compare the energy difference between different magnetic orderings. We find that the magnetic structure of the ground state sensitively depends on the Hubbard U. We make a simple model to explain the evolution of the ground state magnetic structure as a function of U. The energy sequence predicted from the simple model is well reproduced by the DFT calculations. Aided by the bulk phase diagram of $La_{1-x}Sr_xMnO_3$, we argue that in order to obtain the correct ferromagnetic-to-antiferromagnetic transition point, the value of Hubbard U should range from 1 to 2 eV. Within this range, the magnetic structure of the ground state is $A1$, which is consistent with the experimentally proposed spin-modified configuration, which attempts to explain the observed anomalously large change in the magnetization with the switching of ferroelectric polarization. However, we want to comment that our conclusion on the ground state magnetic structure is not *ab initio*. Different criteria to determine the Hubbard U can easily change the final prediction, sounding a note of caution when using LSDA+U. We believe that the main limitation is due to the LSDA+U method itself. While including of U does improve over plain LSDA, the method is still not accurate enough to properly describe all the key correlations in complex strong correlated materials such as manganites.

We also show that ferroelectric/manganite interfaces present a system where one can dynamically remove and control orbital degeneracy by modifying the ferroelectric polarization. In addition to the Jahn-Teller effect at the interface, the propagation of the ferroelectric mode into the interfacial manganite also creates orbital polarization, a degree of freedom absent in bulk LSMO and which is quantitatively as important as the Jahn-Teller effect. The predicted changes of orbital polarization are up to $\sim$10%, which might be accessible by cutting-edge experimental methods. We hope our work stimulates further studies on control of orbital orderings at oxides interface.

Chapter 5

Theory of Interfacial Ferroelectricity

5.1 Introduction

Integrating ferroelectrics into the next generation of complementary metal oxide semiconductor (CMOS) is promising for applications in nanoelectronics [135]. A ferroelectric thin film between electrodes yields the simplest form of nanocapacitor [136]. However, with the thickness of ferroelectric film shrinking down to nano scales, deleterious effects such as imperfect screening of electrodes could significantly worsen the functions of nanocapcitors [137, 138]. Recently, Stengel *et al.* found that at metal/AO-terminated perovskite oxides interfaces, a pair of metal-O bonds could become unstable, which leads to the enhancement of ferroelectric instability [33]. In particular, at Pt/$BaTiO_3$ interfaces, the polarization in $BaTiO_3$ thin film is found to be increased beyond its bulk value [139], which is contrary to the prediction of simple electrostatic model that finite screening length of realistic electrodes suppresses polarization in ultra thin ferroelectric films and results in a critical thickness below which ferroelectric polarization disappears [140, 32]. This novel property of $BaTiO_3$ with metal electrodes is very appealing for the design of realistic ultra small devices. However, for other perovskite ferroelectric oxides, e.g. $PbTiO_3$ and chemically similiar isostructural oxides $SrTiO_3$ and $CaTiO_3$, the ferroelectric instability of metal-O bonds are missing at the AO termination (A=Pb, Sr, Ca) [33]. This arouses the question whether $BaTiO_3$ is the only material that could circumvent the bottleneck of size effects in thin film devices. If not, then what is the general principle for other materials that have the same advantageous property with metal electrods as $BaTiO_3$?

Here aided by Density Functional Theory calculations [11, 12], we build step by step a microscopic understanding of the ferroelectric instability of metal-O bonds at electrode-AO terminated interfaces. We show that the ferroelectric instability of interfacial bonds, or so-called interfacial ferroelectricity, is mainly induced by the giant size of A atom while the chemical properties of bonds are secondary. This mechanism is quite general and the emergent phenomenon of interfacial ferroelectricity is neither restricted to peroskite structures nor to oxides. More importantly, the ferroelectric instability of interfacial bonds is independent of the ferroelectric properties of the bulk phase of the materials. Bulk paraelectrics can be driven into ferroelectric states when interfacial bonds are carefully established and electrodes are properly chosen. In addition, magnetism can also be combined with interfacial ferroelectricity to form a new type of multiferroic in ultra thin films.

5.2 Computational details

We run the simulations using Density Functional Theory [11, 12] within the *ab initio* supercell plane-wave approach [76]. The calculations are performed with the code PWscf in the Quantum-ESPRESSO package [1] within the local spin density approximation (LSDA) [12] and with ultrasoft pseudopotentials [45]. The plane wave basis energy cutoff and charge density cutoff are 35 Ry and 280 Ry, respectively. For all the key results, we repeat the calculation using much higher cutoffs 60Ry/480Ry to ensure convergence. We use a Gaussian smearing width of 10 mRy when sampling the Brillouin zone and the corresponding k-grid sampling of the Brillouin zone is $6 \times 6 \times 1$ where the z-axis is orthogonal to the interface. A lower smearing width (5 mRy) and a higher k-grid sampling ($10 \times 10 \times 1$) have been employed to check the convergence. The force threshold for atomic relaxation is 26 meV/Å. The key results are tested by reducing the threshold to 13 meV/Å and values reported below are converged to the precision shown For calculations that involve EuO, we turn on Hubbard U on Eu $4f$ orbitals to take into account the strong correlation effects on

---

[1] See http://www.quantum-espresso.org

localized orbitals. We choose the U to be 8 eV and the ground state of EuO is computed to be a ferromagnetic insulator with the magnetic moment $7\mu_B$ per formula. The energy cutoff and charge cutoff for EuO is 40 Ry and 320 Ry.

For all the calculations, the in-plane lattice constant is fixed to be theoretical value of a_{STO} except for the study of strain effects where the in-plane lattice constant is varied. Around 20 Å vacuum is inserted in all simulations to separate the heterostructures along the z direction. The interface properties are well converged as the electrodes are much thicker than their screening length which is on the order of Å for simple metals.

5.3 Instability criterion

Fig. 5.1A shows the schematic of the interface geometry we are interested in. We assume that the thin film has two compositionally identical terminations and it is sandwiched between metal electrodes. Therefore we have a pair of metal-O bonds at the two interfaces. In the centrosymmetric geometry, i.e. paraelectric state, the separation between metal and O at the interface is denoted by r_e. For small ferroelectric perturbations, the change of total interfacial energy is approximately:

$$E(r_e+\delta)+E(r_e-\delta)-2E(r_e)\simeq E''(r_e)\delta^2 \tag{5.1}$$

where $E(r)$ is the binding energy of metal-O bonds and δ is a small displacement along the bond direction. A typical curve of $E(r)$ is illustrated in Fig. 5.1B in which we define the critical turning point r_c of metal-O bond as:

$$E''(r_c)=0 \tag{5.2}$$

Thus the onset of interfacial ferroelectric instability at the interface is given by the condition:

$$r_e > r_c \tag{5.3}$$

We will quantitatively test the condition Eq. (5.3) in microscopic simulations and more

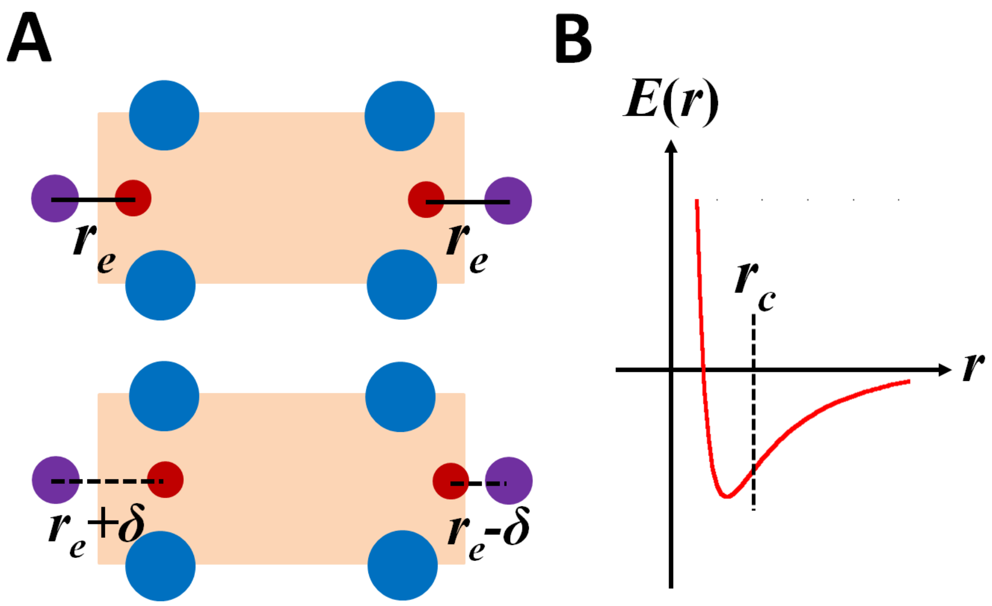

Figure 5.1: **A**) Schematics of the metal-oxide interface. The red circles are oxygen atoms. The purple circles are metal electrode atoms. The giant blue atoms are the A atoms (e.g. A is Ba for $BaTiO_3$). The separation of metal and oxygen atoms is r_e. δ is a smaller perturbation along the bond. **B**) Schematics of typical binding energy of a metal-O bond. r_c is the critical bonding length where the curvature vanishes.

importantly, find out what factors affect r_e and r_c, so that we can engineer the materials to induce a ferroelectric instability at the interface.

We start the calculations from the simplest structure: a square lattice on which each oxygen atom is sandwiched by two Pt atoms. The square lattice constant is equal to the theoretical lattice constant of $SrTiO_3$ $a_{\mathrm{STO}} = 3.85$ Å (1.5% smaller than the experimental value. The in-plane lattice constant is always fixed to be a_{STO} unless otherwise specified). A schematic of the simulation cell (both side view and top view) is shown in Fig. 5.2A. The solid rectangular represents the periodic boundary conditions. Around 20 Å thick vacuum is inserted in the simulation cell to separation the system along the z direction. We vary the distance between the Pt and O atoms (on both sides) and calculate the total energy. The binding energy is shown in Fig. 5.2B. The zero point is chosen as the binding energy at the furtherest separation. The turning point r_c is extracted to be $0.58a_{\mathrm{STO}}$. Then we include Ba atoms which form a co-planar square lattice as O atoms, and show the schematics in Fig. 5.2C. In order to test whether the co-planar BaO layer is stable or not, we employ a

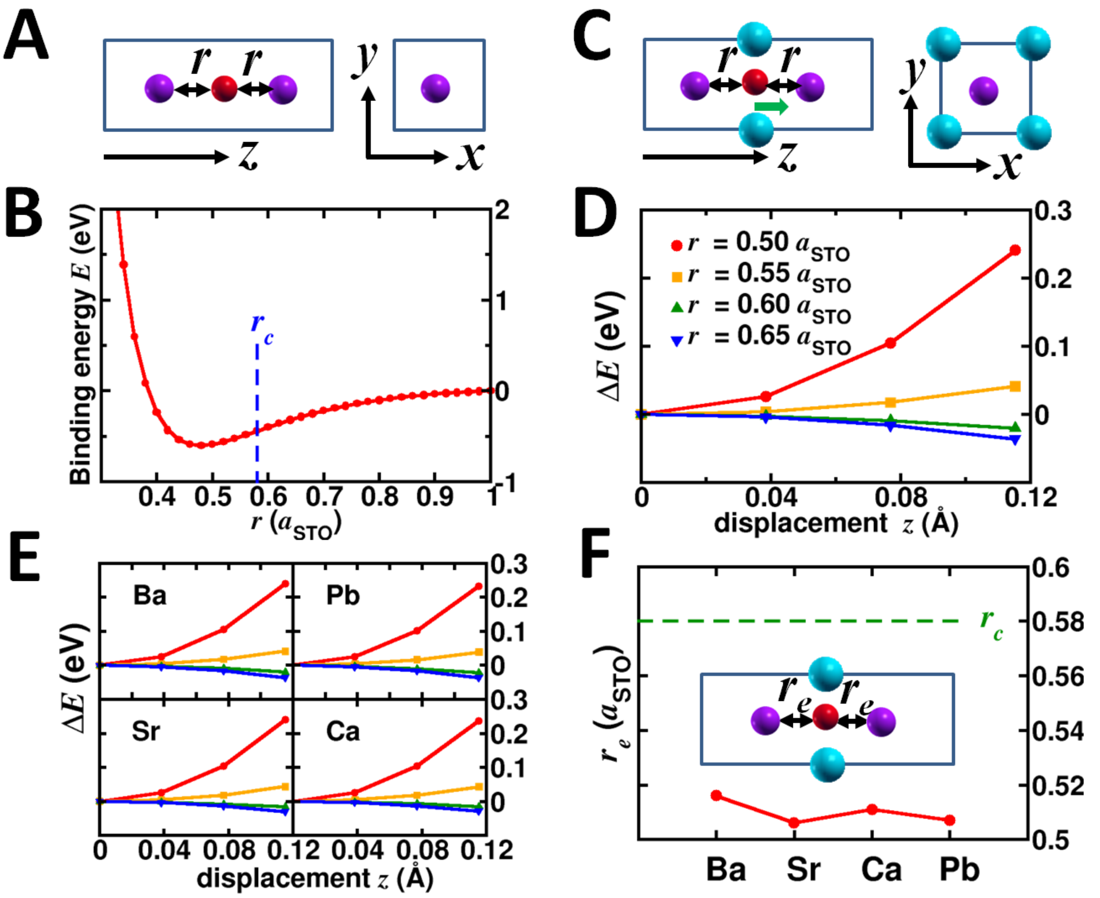

Figure 5.2: **A**) Side view and top view of the simulation cell in which a single atomic layer of oxygens is sandwiched by two monolayers of Pt atoms. **B**) Binding energy of Pt-O bonds as a function of separation r, which is illustrated in **A**). **C**) Side view and top view of the simulation cell in which a single atomic layer of BaO is sandwiched by two monolayers of Pt atoms. **D**) For a given Pt-O separation r (shown in **B**), the change of total energy of the BaO/Pt interface with respect to the displacement of central O atom along z direction. **E**)The same experiment as in Fig. 5.2C and Fig. 5.2D. The results of BaO, PbO, SrO and CaO are collected together for a comparison. **F**) The relaxed Pt-O distance r_e in the centralsymmetric geometry as a function of elements. The illustrated structure is the BaO/Pt interface as a representative. r_e for all the elements considered (Ba, Pb, Sr and Ca) are smaller than r_c extracted out from Fig. 5.2A and Fig. 5.2B.

frozen phonon approach (see Fig. 5.2D). We fix the Pt atoms at two symmetrical positions with respect to the origin, the separation of which is denoted by r. The centrosymmetric geometry (i.e. Ba and O atoms are co-planar) is chosen as the reference. Then with everything else fixed, the O atom is manually shifted along the z direction by different steps. For each step, a self-consistent calculation is performed to compare the total energy to the reference configuration. Just as we expect, if the separation r between the Pt and O atom is smaller than r_c, then the Pt-O bonds in the reference configuration are stable, i.e. the system is paraelectric. On the other hand, if $r > r_c$, the instability of Pt-O bonds in the reference configuration leads to rumplings in the BaO layer and therefore the system becomes ferroelectric. In addition to Ba, we also perform the same frozen-phonon analysis on Sr, Ca and Pb, and collect the results in Fig. 5.2E for a comparison. From Fig. 5.2E, we find that, to a very good precision, the frozen-phonon results do not depend on the type of A atom, indicating that r_c is indeed an intrinsic property of Pt-O bond. Therefore, given a Pt-O bond (i.e. r_c is intrinsically determined), whether the interface has ferroelectric instability depends on the *relaxed* Pt-O separation r_e in the centrosymmetric configuration with the presence of A atom. In order to obtain r_e, we relax all the atoms while enforcing inversion symmetry and show the results in Fig. 5.2F. We can see that r_e does depend on the type of A atom, but for all the types considered, r_e is always smaller than r_c. As a consistent check, we manually break the inversion symmetry constraint and perturb the system. For all the types of A atom considered, the ground state is paraelectric. Though no interfacial ferroelectricity is found in the ground state of these simplest monolayer oxide systems, they show clearly that the criterion $r_e > r_c$ by which ferroelectricity can be induced at metal-oxide interfaces holds at the microscropic scales. This will be our guide for further analysis.

A single atomic layer of Pt is a dramatic oversimplification of real electrodes. We increase the thickness of Pt to four atomic layers on both sides, so that all the interface properties (binding energy, r_c, r_e, etc) are well converged [2]. The sideview of the simulation cell is shown in Fig. 5.3A. The inserted ~ 20 Å vacuum to separate periodic systems along the z direction is not explicitly shown in Fig. 5.3A. Concerning r_c, we fix the Pt-O distances on both sides, which is highlighted by r, and then relax all the other atoms. The binding energy (same definition of zero point) versus the separation r is shown in Fig. 5.3B and r_c is extracted out to be $0.595 a_{\mathrm{STO}}$. Then we include the A atom and show the schematic of simulation cells in Fig. 5.3C. The interesting result is that if we now relax all the atoms

---

[2] Pt is a very good metal with a screening length ~ 1 Å. Therefore four atomic layers of Pt (~ 8 Å) is thick enough to screen any electric fields at the interface.

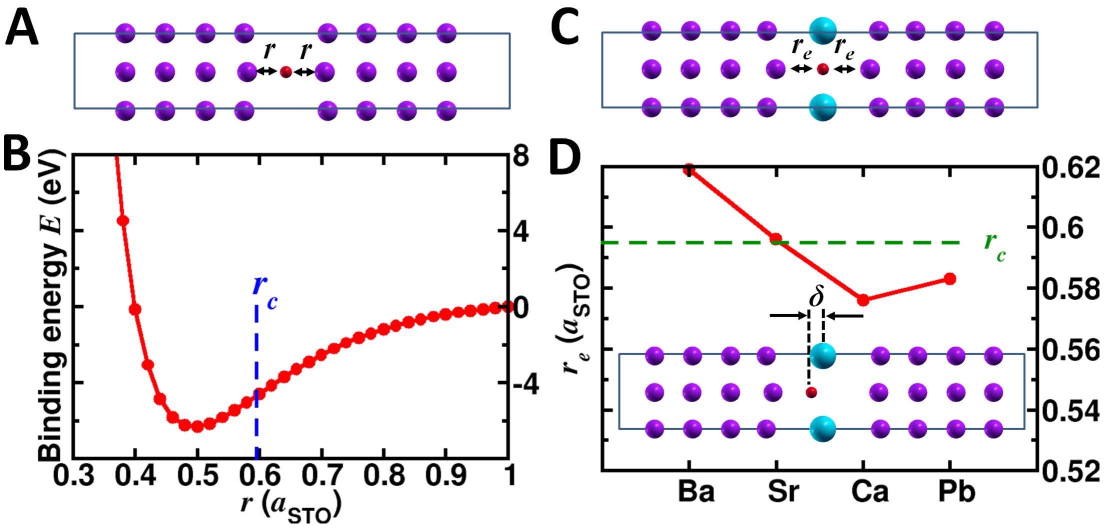

Figure 5.3: **A**) Side view of the simulation cell in which a single atomic layer of oxygens is sandwiched by Pt electrodes. **B**) Side view of the simulation cell in which a single atomic layer of BaO is sandwiched by Pt electrodes. The relaxed Pt-O distance in the centrosymmetric geometry is labelled as r_e. **C**) Binding energy of Pt-O bonds as a function of separation r, which is illustrated in **A**). **D**) The relaxed Pt-O distance r_e in the centrosymmetric geometry as a function of elements. For BaO and SrO, r_e is larger r_c and therefore the ground states of BaO/Pt and SrO/Pt interfaces are ferroelectric. The illustrated structure is the fully relaxed BaO/Pt interface as a representative.

in the centrosymmetric configuration, the r_e for Ba and Sr case could exceed r_c, signaling the instability of paraelectric state. Consistently, we remove the inversion symmetry and relax the atoms again, and the resulting ground states for Ba and Sr case are indeed ferroelectric. The relaxed atomic structure of Ba case is shown in Fig. 5.3D. We can see a clear rumpling δ in BaO layer, which is 0.60 Å (For Sr case, $\delta = 0.47$ Å). This result is consistent with earlier calculations of Pt/BaTiO$_3$ interfaces, in which the rumpling in BaO layer is 0.52 Å for the thinnest 1.5 unit cells of BaTiO$_3$ [139]. The significant enhancement in r_e can be understood as follows: now the Pt atom at the interface not only binds to the oxygen atom, but also to the surrounding Pt atoms. Since the total charge is conserved, we can intuitively find that, the more neighbors the interfacial Pt atom binds to, the weaker any single bond such as the Pt-O bond. We need to comment that the ferroelectricity of a single atomic layer of BaO (SrO) between Pt electrodes is a remarkable result, since unlike BaTiO$_3$, bulk BaO (SrO) itself is paraelectric. We can also rule out strain as the driving

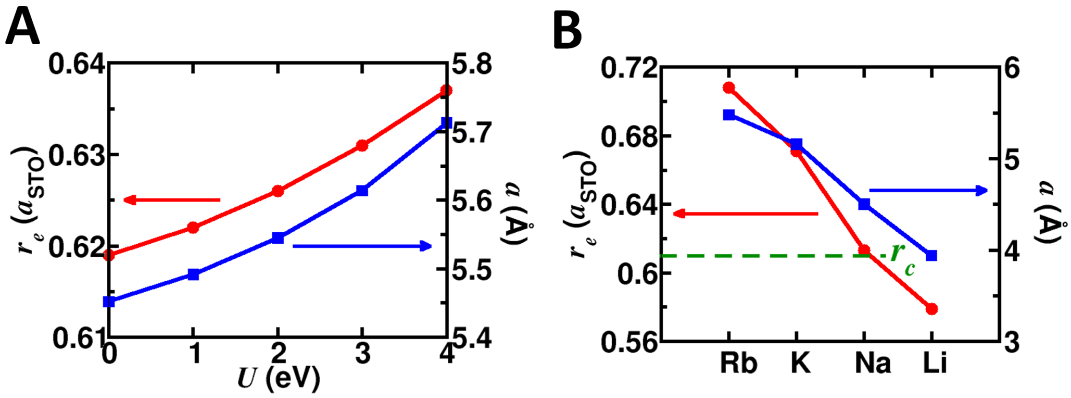

Figure 5.4: The study of size effects. **A**) Left side: the relaxed Pt-O distance r_e in the centrosymmetric BaO/Pt interface geometry as a function of Hubbard U on Ba 5d states. Right side: the relaxed lattice constant of BaO as a function of Hubbard U on Ba 5d states. **B**) Left side: the relaxed Pt-F distance r_e in the centrosymmetric AF/Pt interface geometry as a function of elements (A=Li, Na, K, Rb). Right side: the relaxed lattice constant of AF as a function of elements (A=Li, Na, K, Rb). The critical turning point r_c of Pt-F bonds is extracted out similarly as in Fig. 5.3A and Fig. 5.3C. Since r_e for the case of RbF, KF and NaF are larger than r_c, the fully relaxed RbF/Pt, KF/Pt and NaF/Pt interfaces are ferroelectric.

force here, since when strained by theoretical $SrTiO_3$ lattice constant, BaO is under 0.8% compressive strain and SrO under 5% tensile strain. In bulk phase, we need 1.3% and 5.1% compressive strains to induce out-of-plane ferroelectricity in BaO and SrO [141].

5.4 Correlation of A cation size and r_e

Now we understand that in order to induce interfacial ferroelectricity, we need to find a proper type of A atom to make r_e big enough. Here we show that the magnitude of r_e mainly correlates with the size of A atom, rather than the chemical properties of metal-O bonds. As a thought experiment, we turn on the Hubbard U [47, 48] on Ba 5d orbitals. The blue square symbols in Fig. 5.4A shows the lattice constant of BaO with different Hubbard U. We can see that the effect of this artificial Hubbard U is to increase the size of Ba atoms. Consistently, we relax the Pt/BaO interface (the configuration shown in Fig. 5.3B) with the inversion symmetry and obtain r_e for different Hubbard U. Consistently, with the enhancement of Ba size, r_e increases accordingly. To provide more convincing evidences that the interfacial ferroelectricity more correlates with the A atom size rather than the chemical properties of metal-O bonds, we switch to another class of compounds, rocksalt fluorides. Nominally, F has valence 1- and we use A atoms that are alkaline metals (Li, Na, K, Rb) to preserve charge balance and insulating properties. We first calculate the theoretical lattice constants of AF (all of which are $\simeq 3.5\%$ smaller than the experimental ones). With more and more filled shells, the ion size of alkaline metals A monotonically increases as does the lattice constant of AF. Following the same precedure, we calculate the binding energy of Pt-F bonds and extract out r_c. Though metal/oxides and metal/fluorides have different chemical properties, we conjecture that an alkaline metal ion whose size is big enough so that r_e could exceed r_c would induce the same interfacial phenomenon at metal/flurides interfaces as alkaline earth metals Ba and Sr do at metal/oxides interfaces. In fact, our calculations do show that in the case of Rb, K and Na, r_e in the centrosymmetric configuration exceeds r_c and therefore once the inversion symmetry is removed, a single atomic layer of RbF, KF and NaF sandwiched by Pt electrodes under the strain of $SrTiO_3$ does become ferroelectric. The characteristic rumplings δ are 0.73 Å, 0.60 Å and 0.34 Å, for RbF, KF and NaF, respectively. From the above analysis, we further comment that the fact that the giant size of A cation drives the interfacial bonds to be unstable naturally explains why the enhanced ferroelectric instability is only observed at AO-termination of peroskite oxides because the typical size of A cation (e.g. Ba^{2+}) is much larger than B cation (e.g. Ti^{4+}).

5.5 Finite thickness effects and strain engineering

In order to find more practical applications as realistic nanoelectrics, we need to explore the interfacial ferroelectric instability at finite thickness of oxides (or fluorides) rather than at single atomic layers. Before we proceed, we need to clarify a subtle point. The oxides (or fluorides) we are interested in might be ferroelectric in bulk (e.g. $BaTiO_3$) or driven into ferroelectric states by strain (e.g. BaO). However, what we attempt to study is whether the interfacial Pt-O (or Pt-F) bonds become unstable or not, which is independent of the ferroelectric properties of bulk materials. As we will show by a phenomenological Landau

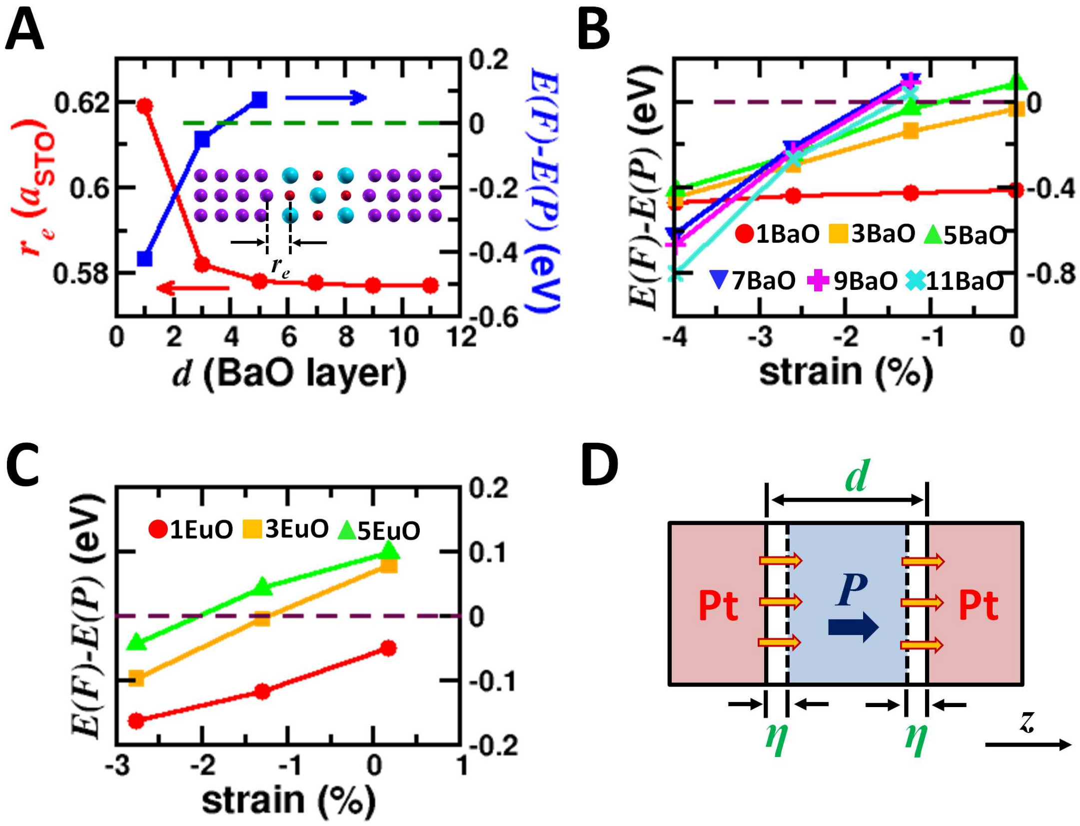

Figure 5.5: **A**) Left side: the relaxed Pt-O distance r_e of centrosymmetric BaO/Pt interfaces imposed by $SrTiO_3$ substrates as a function of the thickness of BaO layers d. Right side: the energy difference between the ferroelectric and paraelectric (i.e. centrosymmetric) states of different thickness of BaO layers. At 1 and 3 atomic layers of BaO, the ground state is ferroelectric. Thicker than 3 atomic layers, the ground state of BaO/Pt interfaces becomes paraelectric. **B**) Energy difference between ferroelectric and paraelectric states of BaO/Pt interfaces as a function of BaO thickness and imposed in-plane strain. The strain is defined as $\xi = (a - a_{\mathrm{BaO}})/a_{\mathrm{BaO}}$ where a_{BaO} is the theoretical lattice constant of BaO. **C**) Energy difference between ferroelectric and paraelectric states of EuO/Cu interfaces as a function of EuO thickness and imposed in-plane strain. The strain is defined as $\xi = (a - a_{\mathrm{EuO}})/a_{\mathrm{EuO}}$ where a_{EuO} is the theoretical lattice constant of EuO. **D**) Schematic of metal electrodes and oxides interfaces. The red shaded parts are electrods (Pt is chosen as an example). The blue shaded part is oxides. The unshaded parts are the interface regions in which a flippable polarization is built in. The thickness of oxides is d and the characteristic length of interface regions is η.

approach at the end of the discussion, if electrodes are properly chosen, interfacial ferroelectricity could either enhance the polarization in bulk ferroelectric, or induce polarization in otherwise paraelectric materials. We study Pt/BaO/Pt heterostructures as a representative. With the in-plane lattice constant being fixed to that of $SrTiO_3$, we increase the thickness d of BaO sandwiched by Pt electrodes, as illustrated in Fig. 5.5A. We still define r_e as the distance between O and Pt atoms at the interface in the centrosymmetric geometry. From Fig. 5.5A, we find that as the thickness d is increased, the interfacial Pt-O distance r_e drops and saturates as d reaches 9 atomic layers. For heterostructures of each thickness, we manually break the inversion symmetry and perturb the system to find out whether the interfacial Pt-O bonds become unstable. If the heterostructure is finally in a polarized state due to the unstable Pt-O bonds, we call such a configuration 'ferroelectric', whose total energy is denoted by $E(F)$. The total energy of the heterstructure in the centrosymmetric geometry is labelled as $E(P)$. $\Delta E = E(F) - E(P)$ is shown in Fig. 5.5A. It turns out that at 1 and 3 atomic layers of BaO, the heterostructure is ferroelectric. At larger thicknesses, interfacial ferroelectricity can not be stabilized. This is consistent with the decreasing trend of r_e [3]. The reason that r_e gets smaller with increasing thickness of BaO is that in the centrosymmtric geometry with a single atomic layer of BaO, Ba and O atoms have to be co-planar because of inversion symmetry, i.e. O atom does not have any degree of freedom. At finite thickness of BaO, even with inversion symmetry, the O atom at the interface could relax along z to form a stronger bond with Pt atoms. To summarize the results in Fig. 5.5A, we need to increase r_e at finite thickness of BaO to get ferroelectricity and therefore at this point, we attempt to play with strain by changing the in-plane lattice constant. We expect that compressive strain may increase r_e and thus possibly stabilize interfacial ferroelectricity. The strain is defined as $\xi = (a - a_{\mathrm{BaO}})/a_{\mathrm{BaO}}$ where a_{BaO} is the theoretical lattice constant of BaO (1.5% smaller than the experimental value). At different in-plane lattice constants, we relax heterostructures of increasing thickness of BaO layers to find out whether the pair of Pt-O bonds can be made unstable. The results of $\Delta E = E(F) - E(P)$ are collected in Fig. 5.5B. We can see that at 1 atomic layer of BaO, interfacial ferroelectricity is stabilized even without any compressive strain. As the thickness d increases, r_e decreases and thus we need some compressive strain to induce

---

[3] To be very precise, we need to calculate r_c at each thickness of BaO and test that $r_e > r_c$ breaks down at or beyond 5 atomic layers of BaO. However, for practical purposes, we only need to know whether the interfacial Pt-O bonds are unstable or not at a given thickness of BaO and find an approach to increase r_e.

the ferroelectric instability in Pt-O bonds. It turns out that at or above approximately 1.6% compressive strain, the Pt-O bonds of Pt/BaO/Pt heterostructures at any thickness of BaO considered become unstable and interfacial ferroelectricity is induced.

The results in Fig. 5.5B show great promise for use of simple rocksalt binary oxides as candidates of ultra thin ferroelectric devices. In addition to Pt/BaO/Pt heterostructures, we also consider insulating magnetic oxides and attempt to achieve multiferroicity by combining magnetism with interfacial ferroelectricity. We consider EuO which is a ferromagnetic insulator. However, EuO has big lattice mismatch with Pt. Instead, we choose Cu which has nice lattice match with EuO (lattice mismatch 0.7%). Again we define in-plane strain similarly $\xi = (a - a_{\mathrm{EuO}})/a_{\mathrm{EuO}}$ where a_{EuO} is the theoretical lattice constant of EuO which is 1.2% smaller than the experimental value. The results are shown in Fig. 5.5C. Like Pt/BaO/Pt heterostructures, one atomic layer of EuO is ferroelectric when sandwiched between two Cu electrodes even without any strain. With increasing thickness of EuO, we need compressive strain to stabilize interfacial ferroelectricity in ultra thin EuO layers. At 5 atomic layers of EuO, the critical compressive strain is 2%, which should be achievable by choosing proper substrates.

5.6 Phenomenological Landau free energy approach

Finally, we attempt to construct a Landau free energy to describe the metal-oxides interfaces, as illustrated in Fig. 5.5D. The shallow red shaded areas are electrodes (Pt is chosen as an example). The shallow blue shaded area represents an oxide (BaO, $BaTiO_3$, EuO, etc.). The unshaded areas are the interfacial regions. We have shown previously that metal-O bonds can be made unstable by adequate compressive strain. Now let us start from the assumption that the interfacial ferroelectricity is already stabilized. Therefore, a built-in flippable polarization P_I is highlighted in the interfacial regions. The Landau free energy is constructed as a function of polarization P in the oxide sandwiched between the electrodes (the derivation can be found in the Appendix C.1).

$$F = F_0 - \int_0^P E_{dep}(P')dP' = F_0 + \frac{4\pi}{d+2\lambda}\left((\eta+\lambda)P^2 - 2\eta P_I P\right) \tag{5.4}$$

where E_{dep} is the uncompensated depolarization field in the oxides due to the finite screening and interface effects. η is the characteristic length of interface region and λ is the finite screening length of the electrode material. Though both P and P_I can flip their signs (i.e. directions), electrostatics require that P and P_I take the same sign in order to reduce the interface bound charge, i.e. if $P \to -P$, then $P_I \to -P_I$. Therefore Eq. (5.4) is an even function of P. Without loss of generality, we assume $P > 0$ and $P_I > 0$. F_0 is the Landau free energy of the oxide in bulk form. To distinguish bulk ferroelectrics (e.g. $BaTiO_3$) and paraelectrics (e.g. BaO), we have:

$$F_0 = \begin{cases} \frac{\Delta E_0}{P_0^4}\left(P^4 - 2P_0^2 P^2\right) d & \text{ferroelectric} \\ 4\pi\alpha P^2 d & \text{paraelectric} \end{cases}$$

where $\Delta E_0 > 0$ is the double-well depth of ferroelectrics and $P_0 > 0$ is bulk ferroelectric polarization and d is the thickness of thin film. $\alpha > 0$ is proportional to the susceptibility for paraelectrics. For ferroelectrics, minimization of F with P leads to:

$$F'(P) = \frac{4\Delta E_0}{P_0^4} P\left(P^2 - P_0^2\right) + \frac{2\pi}{d+2\lambda}\left(2(\eta+\lambda)P - 2\eta P_I\right) = 0 \tag{5.5}$$

Though we can get the analytical solution to Eq. (5.5), a simple analysis will be more useful. As P gets very large, Eq. (5.5) is reduced to $F'(P) \propto P^3$ and positively diverges. Now let us look at $F'(P_0)$:

$$F'(P_0) = -\frac{4\pi}{d+2\lambda}\left(P_I - P_0(1+\lambda/\eta)\right) \tag{5.6}$$

If $P_I > P_0(1+\lambda/\eta)$, then $F'(P_0) < 0$ and there must be a solution to $F'(P) = 0$ for some P larger than P_0. This is the case of Pt/$BaTiO_3$ interfaces in which not only the ferroelectric instability is enhanced, but the magnitude of polarization is also increased at finite thickness of $BaTiO_3$. However, if $P_I \le P_0(1+\lambda/\eta)$, then $F'(P_0) \ge 0$ and noting that $F'(0) = -\frac{4\pi\eta}{d+2\lambda}P_I < 0$, then the solution is no larger than P_0. This is the case of Au/$BaTiO_3$ interfaces in which the ferroelectric instability is enhanced but the polarization of $BaTiO_3$ is essentially bulk-like. The interesting thing is that for paraelectrics, we can get a simple analytical solution to $F'(P) = 0$:

$$P = P_I \frac{\eta}{\alpha d(d + 2\lambda) + (\eta + \lambda)} \tag{5.7}$$

which shows that the presence of interfacial polarization P_I can induce ferroelectric polarization in paraelectrics that decays as $1/d^2$. Therefore in ultra thin films, we expect that the induced polarization could be comparable in magnitude to those of normal ferroelectrics. This is what we have observed in the single atomic layer of BaO sandwiched by Pt electrodes.

5.7 Conclusion

In conclusion, we build step by step a microscopic understanding of ferroelectric instability of interfacial metal-O (or metal-F) bonds. The onset of interfacial ferroelectricity depends on the simple criterion $r_e > r_c$, where r_c is the intrinsic critical turning point of metal-O bonds and r_e is the *relaxed* metal-O separation in the centrosymmetric geometry. r_e mainly correlates with the size of A atom, which provides guidance to engineering interfacial bonds. At finite thickness of oxides d, r_e decreases as d is thickened, and we need compressive strain to help stabilize interfacial ferroelectricity. Finally, a Landau free energy is constructed with a built-in interfacial polarization P_I, which naturally explains that interfacial ferroelectricty could enhance the polarization of ferroelectrics, or induce polarization in otherwise paraelectrics. Our finding of ferroelectricity in ultra thin BaO and EuO between realistic electrodes may stimulate further experiments to explore new ferroelectric and multiferroelectric phenomena in ultra small devices.

Chapter 6

Outlook

In this thesis, we have presented our work on three different oxide interfaces. Conclusions on each topic have been placed at the end of corresponding chapters. Here we make some comments on the opportunities and challenges of oxide interfaces.

At the oxide interfaces we have studied, rich phenomena are exhibited, including insulating-to-metallic transitions, gate-voltage control, ferroelectricity and various magnetic orderings. A microscopic knowledge of oxide interfaces, including structural, electronic and magnetic properties, is not only of basic scientific interest, but also of practical applied value. The most appealing feature of oxide interfaces is that many new phenomena or properties emerge. Some are due to electronic or atomic reconstructions, others are owing to the coupling of different order parameters in dissimilar materials. With advances in oxide epitaxy growth techniques, we can in principle create more combinations of different oxide properties: feroelectric, ferromagnetic, antiferromagnetic and superconducting. By carefully engineering interface structures, unexpected properties that are absent in both bulk constituents may appear and enhance the overall functions of oxide heterostructures. A broad spectrum of unknown novel phenomena of oxide interfaces is waiting ahead of us.

From our studies, DFT proves to be a powerful tool to simulating oxide interfaces at microscopic scales. With the rapid development of parallel computer clusters and super computers, computational capability is increasing exponentially, allowing us to investigate more and more complicated interface structures, atomic reconstructions, and low doping effects. However, despite the huge success DFT has achieved in material simulations, we need to face the fact that the approximation we make for exchange and correlation may not be accurate enough to describe the strong correlation effects when localized $3d$ orbitals are involved. We have used the local density approximation (LDA) throughout this thesis. Arguably a more popular approximation of exchange correlation functional is generalized gradient approximation (GGA). However, either the LDA nor GGA exactly cancels the unphysical self-interaction of an electron itself as does Hartree Fock approximation[1] [47]. When it comes to localized orbitals, self-interaction correction is important and the deficiency of the LDA (or GGA) becomes clear. For example, DFT-LDA predicts that transition metal oxides like $LaTiO_3$ [122] and $LaMnO_3$ [123] are metallic while in experiment they are Mott insulators, i.e. they have an odd number of electrons per Ti/Mn site, but the strong correlation on d orbitals makes the electrons localized and thus insulating. Such strong correlation effects are modelled by Hubbard Hamiltonian. For its simplest incarnation, the single-orbital Hubbard Hamiltonian at half filling (i.e. one electron per site), mean field solutions show that the degeneracy of the two states (spin up and spin down) associated with each site is completely removed, leading to an empty state (upper Hubbard band) and a filled state (lower Hubbard band), which are separated by Hubbard U in energy. The Fermi level lies between the two states and a Mott gap is developed [142]. However, LDA (or GGA) fails to reproduce such Mott physics and therefore predicts a metallic ground state for many such Mott insulators. Since Mott insulators are common in transition metal oxides and more importantly are host to high temperature superconductivity, improvements over LDA are highly anticipated. LDA+U (introduced in Chapter 2) is one of them [47, 48], which takes into account the Hubbard U correction in a mean-field manner. There are two issues with LDA+U: one is that for a given U, the Hubbard term is treated in a mean-field manner. To describe strong correlation effects, the Hubbard term may need to be handled more accurately than in a single-particle description. The other issue is that we can not *a priori* determine Hubbard U and the predictions of magnetic properties can depend sensitively on Hubbard U, as we demonstrated in Chapter 4. To solve the first issue, we need to go beyond DFT and presently Dynamical Mean Field Theory (DMFT) [143] is a promising tool which incorporates correlation effects

---

[1] However, Hartree-Fock has its own disvantages that screening effect is not taken into account.

more accurately than LDA+U, though its high computational burden may hamper from its applications to complicated systems. The second issue is common to both LDA+U and DMFT. The recent developed self-consistent linear response approach may provide some useful estimations on Hubbard U [48]. However, there are some cases in which the Hubbard U predicted from the self-consistent approach does not correctly reproduce the observed magnetic properties. Therefore, a practical solution is to fit DFT results with some experimental inputs and once the Hubard U is determined, LDA+U is employed to make new predictions. Though widely used, this practical solution is unsatisfactory. First fitting experimental data goes against the spirit of "*ab initio*" calculations. Furthermore, fitting different data can lead to different Hubbard U. To us, Mott physics and related magnetic orderings are among the most intriguing properties of transition metal oxides. Designing a better exchange correlation functional without fitting parameters to reproduce Mott physics within band theory is challenging but highly rewarding. Hybrid functionals [144] are one attempt people have made toward this goal. However, compared to LDA+U, they are much more computationally intensive, which limits its applications. Further research is still on-going in this direction.

Appendix A

Appendix to $LaAlO_3/SrTiO_3$ Interfaces and Their Variants

A.1 Conduction electron and hole densities

In this appendix, we explain how we calculate the *conduction* electron and hole densities for the symmetric superlattices and stoichiometric interface systems. The basic tool we use is the local density of states (LDOS) for the system

$$D(\mathbf{r}, E) = \sum_{n\mathbf{k}} |\psi_{n\mathbf{k}}(\mathbf{r})|^2 \delta(E - \epsilon_{n\mathbf{k}}) \tag{A.1}$$

which we integrate over the appropriate energy range.

A.1.1 Double n-type and p-type superlattices

The symmetric nonstoichiometric double n-type (p-type) superlattice is shown in Fig. 3.1a (Fig. 3.1b). The corresponding electron (hole) denisty is presented in Fig. 3.2a (Fig. 3.2b). For the symmetric superlattices, there is no polar field and analysis of the density of states shows that there is an easily identifiable energy gap at all locations in the film; the Fermi level is either above the conduction band edge for the the n-type superlattice or below the conduction band for the p-type superlattice. For the transferred electron density (Fig. 3.2a), we integrate the LDOS from the middle of the band gap to the Fermi level,

$$\eta(\mathbf{r}) = \int_{\mathcal{E}}^{E_F} D(\mathbf{r}, E)dE \tag{A.2}$$

where $\mathcal{E}$ is the energy in the middle of the band gap. We are in fact counting all the electrons in the conduction bands. For the transferred hole density (Fig. 3.2b), similarly we integrate the LDOS from the Fermi level to the middle of the band gap,

$$\xi(\mathbf{r}) = \int_{E_F}^{\mathcal{E}} D(\mathbf{r}, E)dE \tag{A.3}$$

i.e. counting all the holes in the valence bands. The integrated LDOS $\eta(\mathbf{r})$ and $\xi(\mathbf{r})$ are then averaged over the xy plane and finally plotted along the z direction.

A.1.2 Stoichiometric n-type and p-type interface systems

The stoichiometric n-type (p-type) interface system is shown in Fig. 3.3b (Fig. 3.3c). The corresponding *conduction* electron (hole) density is shown in Fig. 3.2c (Fig. 3.2d). For the stoichiometric n-type and p-type interfaces, the polar field ensures that the bands edges in the $LaAlO_3$ are not flat and that the Fermi level will intersect the band edges of the $SrTiO_3$ as well as the surface of the $LaAlO_3$ film (see Fig. 3.3). However, the local density of states in the $SrTiO_3$ film still clearly shows a band gap. Therefore, we can also compute the transferred charges at the interface using the above formula. The only complication is that in addition to showing the transferred charges in the interface region, $\eta(\mathbf{r})$ and $\xi(\mathbf{r})$ will necessarily have contributions localized at the surface region of $LaAlO_3$ which are not of direct interest when studying the interface alone; the choice of axis range in Fig. 3.2c and 3.2d effectively excludes this contribution. As a consistency check, we can also compute the transferred charge by computing the atomic projections of all Bloch states in the system and identifying all those states with the proper atomic character: Ti-d or La-d character and partial occupancy for the n-type interface, and O-p character and partial occupancy for the p-type interface. One can then manually sum up these particular contributions to get the electron and hole distributions, and the results agree with the previous method in the relevant regions.

A.2 Periodic boundary condition effects

When we perform a slab calculation, the materials in the simulation are generally polarized either due to intrinsic polar fields (*e.g.* $LaAlO_3$) or external electric fields. In DFT calculations, the periodic boundary conditions (PBC) imposed on the simulation cell influence the screening properties of the materials. We will show in the following two sections that the presence of PBCs does not significantly affect the polarization due to intrinsic polar fields in the system, but it does induce large artificial effects when one studies the response of the system to an external field, requiring a careful set up of the simulation and interpretation of the results.

A.2.1 Polarization due to intrinsic fields

In this section, we illustrate that in the $SrTiO_3/LaAlO_3$ interface system, PBCs induce an artificial field through $SrTiO_3$, but we show that this effect is neglegible.

As shown in Fig. A.1a, the two boundary conditions of displacement $\mathbf{D}$ at each interface give:

$$D_{\mathrm{LAO}} - D_{\mathrm{STO}} = 4\pi\sigma \tag{A.4}$$

$$D_{\mathrm{STO}} - D_{\mathrm{V}} = 0 \tag{A.5}$$

PBCs require that the total potential drop over the whole simulation cell is equal to zero:

$$E_{\mathrm{STO}}s + E_{\mathrm{LAO}}l + E_{\mathrm{V}}v = 0 \tag{A.6}$$

where s, l and v are the thicknesses of $SrTiO_3$, $LaAlO_3$ and vacuum, respectively. Considering that $E_i = D_i/\epsilon_i$ (i is $SrTiO_3$, $LaAlO_3$ or vacuum), we can solve D_{STO} and D_{LAO} explicitly,

$$D_{\mathrm{STO}} = -4\pi\sigma \frac{l/\epsilon_{\mathrm{LAO}}}{s/\epsilon_{\mathrm{STO}} + l/\epsilon_{\mathrm{LAO}} + v/\epsilon_{\mathrm{V}}} \tag{A.7}$$

$$D_{\text{LAO}} = 4\pi\sigma \frac{s/\epsilon_{\text{STO}} + v}{s/\epsilon_{\text{STO}} + l/\epsilon_{\text{LAO}} + v/\epsilon_{\text{V}}} \tag{A.8}$$

The dielectric constants of $SrTiO_3$, $LaAlO_3$ and vacuum are roughly:

$$\epsilon_{\text{STO}} \simeq 300 \gg \epsilon_{\text{LAO}} \simeq 25 \gg \epsilon_{\text{V}} = 1 \tag{A.9}$$

and the thicknesses of $SrTiO_3$, $LaAlO_3$ and vacuum in the simulation cell are on the same order of magnitude (within a factor of two), therefore we have the following simplifications:

$$E_{\text{LAO}} \simeq \frac{4\pi\sigma}{\epsilon_{\text{LAO}}} \tag{A.10}$$

$$E_{\text{STO}} \simeq -\frac{4\pi\sigma}{\epsilon_{\text{LAO}}\epsilon_{\text{STO}}}\frac{l}{v} = -\frac{l}{v\epsilon_{\text{STO}}}E_{\text{LAO}} \to |E_{\text{STO}}| \ll |E_{\text{LAO}}| \tag{A.11}$$

$$E_{\text{V}} \simeq -\frac{4\pi\sigma}{\epsilon_{\text{LAO}}}\frac{l}{v} = -\frac{l}{v}E_{\text{LAO}} \to E_{\text{V}}v \simeq -E_{\text{LAO}}l \tag{A.12}$$

Eq. (A.11) and Eq. (A.12) show that though $SrTiO_3$ is artificially polarized due to the PBCs, the electric field through $SrTiO_3$ is much smaller than the intrinsic field through $LaAlO_3$ and the voltage built across the $LaAlO_3$ film mostly drops in the vacuum. Based on the above approximate dielectric constants, the field in $SrTiO_3$ is only $\sim 0.3\%$ of that in $LaAlO_3$. In addition, we can further reduce the field in $SrTiO_3$ by increasing the thickness of the vacuum v; the above relations give a quantitative measure of the (small) error for any finite value of v.

A.2.2 Polarization due to an applied external electric field

We illustrate in this section that when we use a slab calculation and a sawtooth potential to simulate an external electric field through nonpolar materials (*e.g.* $SrTiO_3$), PBCs will artificially undermine the screening and give rise to a significantly smaller dielectric constant.

Fig. A.1b shows a schematic of how an external electric field E_{ext} along the z direction is screened in a nonpolar material. There are two induced electric fields. The one in the material is the stardard depolarization field E_{dep} and the other field, which we call the outside field E_{out}, is in the vacuum with the opposite direction. E_{ext}, E_{dep} and E_{out} are the *magnitudes* of each field; their directions are explicitly shown in Fig. A.1b. We denote the size of the unit cell along the z direction by L and the thickness of the slab by d. The sawtooth potential automatically satisfies the periodic boundary condition (the reversed part is not shown in Fig. A.1b). Therefore, the induced electric fields required to satisfy the periodic boundary condition are given by:

$$E_{dep}d = E_{out}(L - d) \tag{A.13}$$

On the other hand, Gauss's law gives:

$$4\pi\Sigma = E_{dep} + E_{out} \tag{A.14}$$

where the surface charge density Σ is related to the polarization in the material by

$$\Sigma = \mathbf{n} \cdot \mathbf{P} = P \tag{A.15}$$

and the polarization P is related to the total electric field E_{tot} by

$$P = \chi E_{tot} \tag{A.16}$$

where χ is the permitivity. From Fig. A.1b, it is easy to see that

$$E_{tot} = E_{ext} - E_{dep} \tag{A.17}$$

Combining Eq. (A.13-A.17) gives

$$E_{tot} = \frac{E_{ext}}{1 + 4\pi\chi\left(1 - \frac{d}{L}\right)} \tag{A.18}$$

Now we can identify the dielectric constant ϵ

$$\epsilon = \frac{E_{ext}}{E_{tot}} = 1 + 4\pi\chi\left(1 - \frac{d}{L}\right) \tag{A.19}$$

Eq. (A.19) is different from the familiar formula $\epsilon = 1 + 4\pi\chi$ in that we have an extra factor $(1 - d/L)$. In typical slab calculations $(1 - d/L) \sim 30\%$ and for high-k materials (*e.g.* $SrTiO_3$) $\chi \gg 1$ so that ϵ is dominated by the second term in Eq. (A.19) and thus the reduction factor is a significant error.

A.2.3 A remedy

The origin of the deviation of the dielectric constant from the correct value of $1 + 4\pi\chi$ is that the electric field induced by the bound charge $\pm\Sigma$ does not completely serve as the depolarization field, but is instead split into two parts, E_{dep} and E_{out}. The presence of E_{out} is purely due to the imposed periodic boundary condition, and is unphysical. However, in practical slab calculations it is too computationally expensive to make d/L small.

In order to get rid of E_{out}, we need a simulation cell in which the depolarization field automatically satisfies periodic boundary conditions. Therefore, we use a mirror-symmetric simulation cell in which the external electric field is also mirror-symmetrically distributed. By symmetry, E_{dep} automatically satisfies periodic boundary conditions and E_{out} is guaranteed to be zero in the vacuum. Thus, the external electric field is correctly screened, but with a relatively modest increase in computational expense due to doubling the simulation cell along one direction.

A.3 Field dependence of dielectric constant

The Landau theory phenomenologically describes the field dependence of the dielectric constant [87, 88]. It is assumed that the free energy of the system $F(P, T)$ can be expanded in even powers of the polarization P:

$$F(P, T) = F_0 + AP^2 + BP^4 + CP^6 + ... \tag{A.20}$$

where the coefficients $A, B, C...$ may depend on the temperature T. Keeping only terms in F to the fourth order, we obtain:

$$E = \frac{\partial F}{\partial P} = 2AP + 4BP^3 \tag{A.21}$$

and the permitivity follows:

$$\frac{1}{\chi} = \frac{\partial E}{\partial P} = 2A + 12BP^2 \tag{A.22}$$

Eq. (A.21) and Eq. (A.22) uniquely determine $\chi = \chi(P)$ and $P = P(E)$. The analytical solution to Eq. (A.21) $P = P(E)$ is complicated, but we can find a useful interpolation scheme [87, 88] by noting that as P is small, $\chi \to (2A)^{-1}$ and as P is large, $\chi \propto P^{-2}$ and $E \propto P^3$, that is $\chi \propto E^{-2/3}$, so

$$\chi \simeq \chi_0 \left(1 + \left(\frac{E}{\mathcal{E}_0}\right)^2\right)^{-1/3} \tag{A.23}$$

For high-k materials, we can also approximate $\epsilon \simeq 4\pi\chi \gg 1$, giving the final expression:

$$\epsilon \simeq \epsilon_0 \left(1 + \left(\frac{E}{\mathcal{E}_0}\right)^2\right)^{-1/3} \tag{A.24}$$

where ϵ_0 and $\mathcal{E}_0$ are fitting parameters.

We note that the truncation of Eq. (A.20) is based on the assumption that P is small (*i.e.* E is small). However, the Landau theory itself does not give a characteristic polarization or electric field. Instead, we consider $\mathcal{E}_0$ as a characteristic electric field whose value is determined by the fitting. Thus, data points much larger than $\mathcal{E}_0$ should not be used in the fitting because Eq. (A.20) would break down. This is a self-consistent check.

A.3.1 LaAlO$_3$

Before we calculate the dielectric constant ϵ_L of LaAlO$_3$, we need to elucidate a subtle point. The ϵ_L we calculate here is only well defined in the thin slab of LaAlO$_3$, not in the bulk. This is because we are in the region of very strong electric field (~ 0.7 V/a_{LAO}). With a few unit cells, the potential difference built across the slab will be larger than the band gap of LaAlO$_3$, and Zener tunneling will occur. Bulk LaAlO$_3$ can not accommodate such a large electric field and the Berry phase method [89] for calculating the dielectric constant breaks down in this regime. Instead, we resort to a mirror-symmetric slab calculation (see Fig. A.2 and Appendix A.2). We turn on a mirror-symmetric external electric field E_{ext}

and calculate the macro-averaged electric field E_{tot} through the material. The dielectric constant is then defined as:

$$\epsilon_L(E_{tot}) = \frac{E_{ext}}{E_{tot}} \tag{A.25}$$

The raw data and the fitting curve using Eq. (A.24) are shown in Fig. A.3. The fitting results are:

$$\epsilon_0 = 40.95, \;\; \mathcal{E}_0 = 0.15\mathrm{V/Å} \tag{A.26}$$

A.3.2 SrTiO$_3$

Since SrTiO$_3$ is a nonpolar material with a large dielectric constant, the typical internal electric field through SrTiO$_3$ is much smaller than that through LaAlO$_3$. The dielectric constant we are interested in can be defined in the bulk (based on the argument of metastable states) and calculated using the Berry phase method. In order to accurately determine the atom positions, we use $6 \times 6 \times 20$ k-point sampling and lower the force convergence threshold to 8 meV/ Å. We directly calculate the total polarization P_{tot} (both ionic and electronic) in the unit cell at a given total electric field E_{tot} and the dielectric constant follows straightforwardly:

$$\epsilon_S(E_{tot}) = 4\pi \frac{P_{tot}}{\Omega E_{tot}} + 1 \tag{A.27}$$

where Ω is the volume of unit cell. The raw data and fitting curve are shown in Fig. A.3, with the fitting results:

$$\epsilon_0^S = 309.6, \mathcal{E}_0^S = 49.2\mathrm{V}/\mu\mathrm{m} = 4.92 \times 10^{-2}\mathrm{V/Å} \tag{A.28}$$

A.4 Model for cation intermixtures

In this section, we derive Eq.(3.35). We assume that the electrostatic energy dominates at the LaAlO$_3$ /SrTiO$_3$ heterostructures, which can be expressed as [145]:

$$E_{\text{tot}} = \frac{\epsilon_{\text{LAO}}}{8\pi} \int |\mathbf{E}|^2 d\tau = \frac{\epsilon_{\text{LAO}}}{8\pi} |\mathbf{E}|^2 V \tag{A.29}$$

where $\mathbf{E}$ is the average internal electric field through $LaAlO_3$, ϵ_{LAO} is the dielectric constant of $LaAlO_3$ and V is the volume of $LaAlO_3$. Since $LaAlO_3$ is polar and $SrTiO_3$ is non-polar, the average electric field is only through $LaAlO_3$. Note that since $SrTiO_3$ is nonpolar, there is no average electrostatic potential in $SrTiO_3$. Therefore the $SrTiO_3$ substrate does not contribute to Eq. (A.29). With the continuous approximation, the volume V can be written as $V = da^2/\eta$ where d is the thickness of $LaAlO_3$, a is the lattice constant of $SrTiO_3$ (the $LaAlO_3$ thin film is coherently strained on the $SrTiO_3$ substrate) and η is the concentration of cation intermixture. For ideal $LaAlO_3$ /$SrTiO_3$ heterostructures, the nominal average electron per unit cell is $0.5e$ and therefore

$$E_{\text{tot}} = \frac{\epsilon_{\text{LAO}}}{8\pi} \left| 4\pi \frac{0.5e}{a^2 \epsilon_{\text{LAO}}} \right|^2 \left(\frac{da^2}{\eta} \right) = k \frac{d}{\eta} \tag{A.30}$$

where $k = \pi e^2 / (2a^2 \epsilon_{\text{LAO}})$ is a constant. With cation intermixture, in addition to the original internal electric field, an extra field is induced by intermixtures, the manitude of which depends on the concentration η and the direction depends on the type of intermixture. For Sr-La intermixture, the internal electric field is enhanced while Ti-Al intermixture suppresses the internal field. The total energy is therefore changed as

$$E_{\text{tot}} = \begin{cases} k \frac{d}{\eta} \frac{(0.5+\eta)^2}{(0.5)^2} & \text{(Sr-La)} \\ k \frac{d}{\eta} \frac{(0.5-\eta)^2}{(0.5)^2} & \text{(Ti-Al)} \end{cases} \tag{A.31}$$

The energy difference per intermixture is the substraction between Eq. (A.31) and Eq. (A.30). A little algebra leads to:

$$E_{\text{diff}} = \begin{cases} 4kd(\eta + 1) & \text{(Sr-La)} \\ 4kd(\eta - 1) & \text{(Ti-Al)} \end{cases} \tag{A.32}$$

It turns out that as the intermixture is on the surface (for Ti-Al intermixture), there could be some surface effects which also play a role in energetics. In order to describe surface effects, we introduce another parameter b to account for the surfac energy per intermixture.

Hence, the energy dependence per intermixtures on LaAlO3 thickness and concentration is:

$$E_{\text{diff}}(d,\eta) = \begin{cases} 4kd(\eta+1) & \text{(Sr-La)} \\ 4kd(\eta-1)+b & \text{(Ti-Al)} \end{cases} \tag{A.33}$$

Finally, for the sake of comparison to DFT calculations, we define energy difference per 1×1 interface cell ΔE, which is simply related to $E_{\text{diff}}(d,\eta)$ by $\Delta E = \eta E_{\text{diff}}$, and obtain the final expression:

$$\Delta E(d,\eta) = \begin{cases} 4kd(\eta^2+\eta) & \text{(Sr-La)} \\ 4kd(\eta^2-\eta)+b\eta & \text{(Ti-Al)} \end{cases} \tag{A.34}$$

A.5 Model for oxygen vacancies

In this section, we derive Eq.(3.37). Our starting point is the definition of formation energy:

$$E_{\text{f}}(V_{\text{O}}) = E_{\text{tot}}(\text{defect}) - E_{\text{tot}}(\text{perfect}) + \frac{1}{2}E_{\text{O}_2} + \mu_{\text{O}} \tag{A.35}$$

We assume that electrostatic energy dominates. In pristine structures, the internal polar field through LaAlO3 is generated by $0.5e$ per 2D unit cell. Above the concentration of 25% oxygen vacancies, the internal polar field through LaAlO3 is completely compensated. Recalling Eq. (A.29), we approxmiate that the first term in Eq. (A.35) does not contribute to the electrostatic energy. Both E_{O_2} and μ_{O} are constants, therefore Eq. (A.35) is modelled as:

$$E_{\text{f}}(V_{\text{O}}) = \alpha - \beta(0.5)^2\frac{d}{\xi} = \alpha - \beta\frac{d}{4\xi} \quad (\xi > 25\%) \tag{A.36}$$

where ξ is the concentration of oxygen vacancies and d is the thicknes of LaAlO3 . α and β are both fitting parameters.

As the concentration ξ is lower than 25%, each oxygen vacancy is fully ionized, i.e. donating two electrons completely from surface to interface. However, since the total donated electrons are less than $0.5e$, a residual internal field remains through LaAlO3 and the electrostatic energy now has two contributions in Eq. (A.35): one is from the first term and the other from the second term. As $\xi \leq 25\%$, each oxygen vacancy denotes two electrons, we have:

$$E_{\mathrm{f}}(V_{\mathrm{O}}) = \alpha + \beta \left[(0.5 - 2\xi)^2 \frac{d}{\xi} - (0.5)^2 \frac{d}{\xi} \right] = \alpha + \beta(4\xi - 2)d \ \ (\xi \leq 25\%) \tag{A.37}$$

Combining Eq. (A.36) and Eq. (A.37), we finally establish the dependence of oxygen vacancies formation energy on concentration ξ and $\mathrm{LaAlO_3}$ thickness d:

$$E_{\mathrm{f}}(V_{\mathrm{O}})(\xi, d) = \begin{cases} \alpha + \beta d(4\xi - 2) & (\xi \leq 25\%) \\ \alpha + \beta d/(4\xi) & (\xi > 25\%) \end{cases} \tag{A.38}$$

A.6 Chemical potential of oxygen

In this section, we show the details of how to calculate the chemical potential of oxygen. The chemical potential is tabulated as follows:

$$\mu = \mu_0(T) + \frac{1}{2} T \log(p/p_0) \tag{A.39}$$

where T is the temperature and p is the pressure. p_o is 1 atomosphere and μ_0 is the chemical potential at standard conditions (i.e. at 1 atmosphere). The temperature dependence of μ_0 is tabulated as follows:

$$\mu_0(T) = \frac{1}{2} \left(H_0(T) - S_0(T) \right) \tag{A.40}$$

where $H_0(T)$ and $S_0(T)$ are standard enthalpy and entropy, respectivly. They are tabulated as follows:

$$H_0(T) = a_1 t + \frac{1}{2} a_2 t^2 + \frac{1}{3} a_3 t^3 + \frac{1}{4} a_4 t^4 - a_5/t + a_6 \tag{A.41}$$

$$S_0(T) = a_1 \log(t) + a_2 t + \frac{1}{2} a_3 t^2 + \frac{1}{3} a_4 t^3 - a_5/(2t^2) + a_7 \tag{A.42}$$

Table A.1: Coefficients of polynomials in Eq. (A.41) and Eq. (A.42), which tabulate the standard enthalpy and entropy as a function of temperature.

temperature (K)	100-700	700-2000
a_1	31.322	30.032
a_2	-20.235	8.773
a_3	57.866	-3.988
a_4	-36.506	0.788
a_5	-0.007	-0.742
a_6	-8.903	-11.325
a_7	246.795	236.166

where $t = T/1000\text{K}$ and the unit for H_0 is kJ/mol and for S_0 is J/mol/K. All the coefficients are collected in Table A.1 [1].

---

[1] NIST Chemistry WebBook. http://webbook.nist.gov/chemistry/

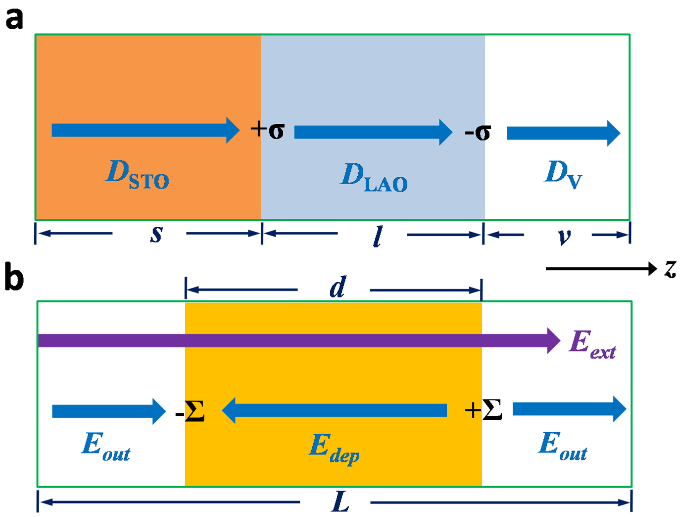

Figure A.1: Schematics of how the periodic boundary condition affects the screening of the electric fields. **a)** Polarization due to intrinsic fields. The shaded parts are $SrTiO_3$ and $LaAlO_3$, respectively. The interface is n-type. The unshaded part denotes vacuum. **b)** Polarization due to an applied electric field. The shaded part is a general nonpolar material and the empty part is vacuum.

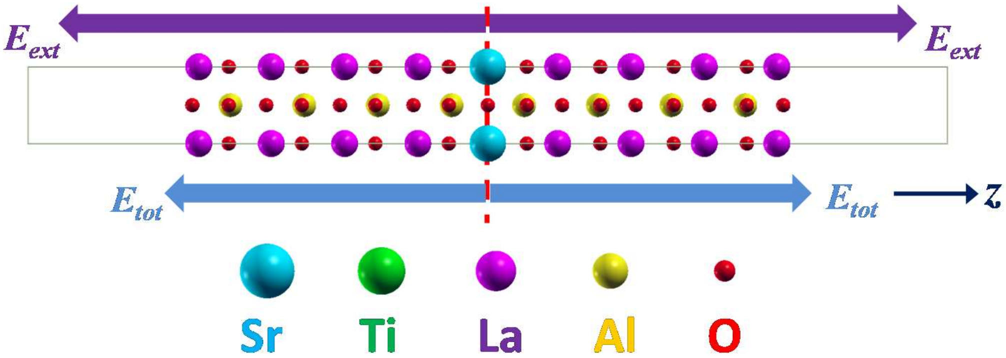

Figure A.2: Schematics of the simulation cell of $LaAlO_3$ slab calculations. Both the simulation cell and the external electric field are mirror-symmetric. All fields through $LaAlO_3$ are along the z direction (perpendicular to the interface).

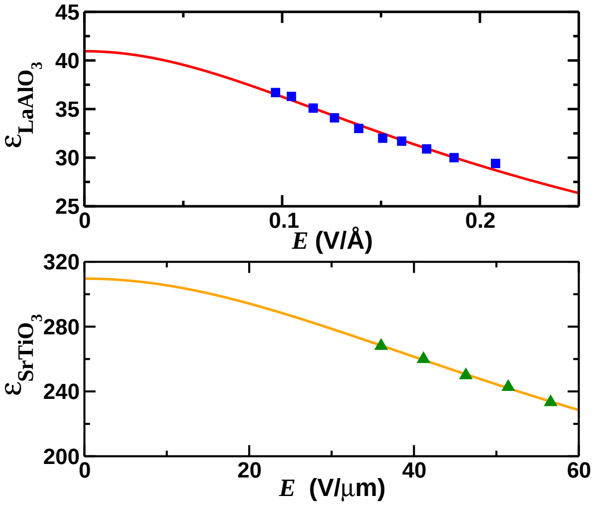

Figure A.3: Electric field dependence of dielectric constants of $LaAlO_3$ and $SrTiO_3$. The solid squares are the results of the slab calculations and the solid triangles are the results of Berry phase calculations. The solid lines are the fitting results using Eq. (A.24).

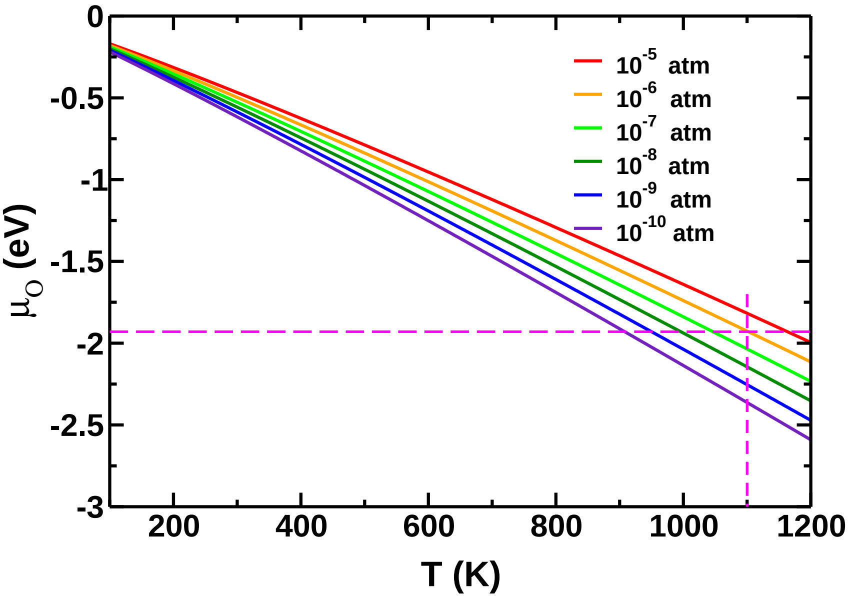

Figure A.4: Chemical potential of oxygen at different temperature and pressure. The growth temperature and pressure are highlighted by the dashed lines.

Appendix B

Appendix to Ferroelectric/manganite Interfaces

B.1 The effects of $SrTiO_3$ substrate

Inclusion of $SrTiO_3$ substrate in the simulation of $PbTiO_3/La_{1-x}Sr_xMnO_3$ heterostructures is computationally intensive. In this section, we test the effects of $SrTiO_3$ substrate on structrual and magnetic properties on the $PbTiO_3/La_{1-x}Sr_xMnO_3$ interface. We compare two calculations: one with three unit cells of $SrTiO_3$ and the other without $SrTiO_3$. $La_{1-x}Sr_xMnO_3$ is four unit cells thick with nominal doping $x = 0.2$. $PbTiO_3$ thin film is polarized so that both calculations are in the accumulation state. In terms of structural properties, we focus on two important quantities. One is the c/a ratio of each oxygen octahedron that encloses Mn atoms. The other is the rumpling δ of each MnO_2 layer. The results are shown in Fig. B.1A. Layer 1 is the interface. Layer 4 is the artificial surface when $SrTiO_3$ is absent. The solid symbols are with $SrTiO_3$ and the open symbols are without $SrTiO_3$. We can see that the structural properties with or without $SrTiO_3$ substrate quickly converge as the interface is approached. At Layer 1, the difference is negligible. In terms of magnetic properties, we calculate the d-orbital magnetic moment of each Mn atom, using the Löwdin orbitals approach [85]. Fig. B.1B shows the comparison between with $SrTiO_3$ substrate (solid symbols) and without $SrTiO_3$ substrate (open symbols). Similar to structural properties, the effects of $SrTiO_3$ substrate on magnetic

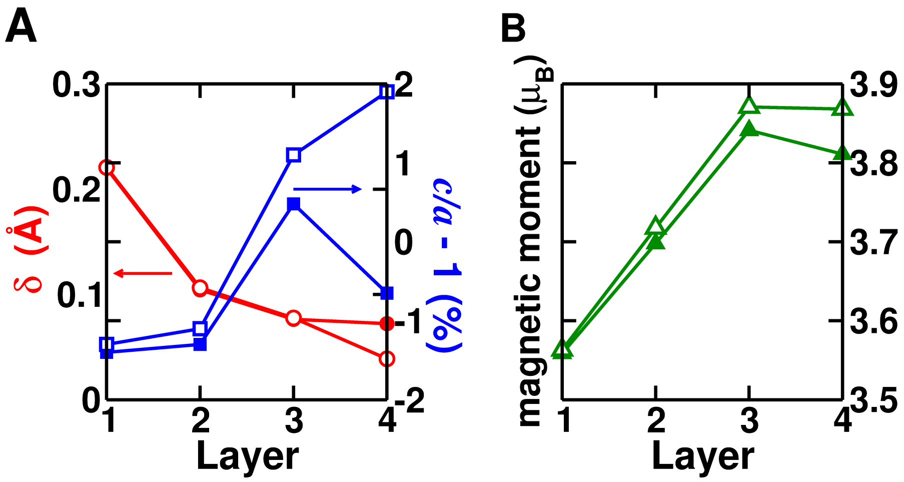

Figure B.1: The effects of $SrTiO_3$ substrate on structural and magnetic properties at the $PbTiO_3/La_{1-x}Sr_xMnO_3$ interface. The solid symbols correspond to the data with $SrTiO_3$ substrate. The open symbols correspond to the data without $SrTiO_3$ substrate. **A)** rumplings of each MnO_2 layer and c/a ratio of each oxygen octahedron that encloses Mn atoms. **B)** d-orbital magnetic moment of each Mn atom, calculated by using Löwdin orbitals.

properties are generally very small and diminish at the interface. Therefore we do not include $SrTiO_3$ substrate in our simulation, not only to reduce the computation burden but also to introduce an artificial surface so that we can apply a counting method (see Appendix B.2) to accurately calculate hole distribution in $La_{1-x}Sr_xMnO_3$.

B.2 The method to count holes

The number of holes and the magnetization of Mn atoms can be calculated approximately using Löwdin orbitals [85]. However, due to their incompleteness as a basis, Löwdin orbitals are not accurate enough (the typical error is around 0.2 hole) to calculate the magnetization or hole profiles we require here. The most accurate and direct method to count holes is to use the charge density. The difficulty lies in that the boundary between each manganite layer is not straightforward to determine in the thin film of $La_{1-x}Sr_xMnO_3$. We develop a method to unambiguously set the boundary between each manganite layer, provided that the manganite is half-metallic.

For a half-metallic manganite, there are no states at the Fermi level in the minority

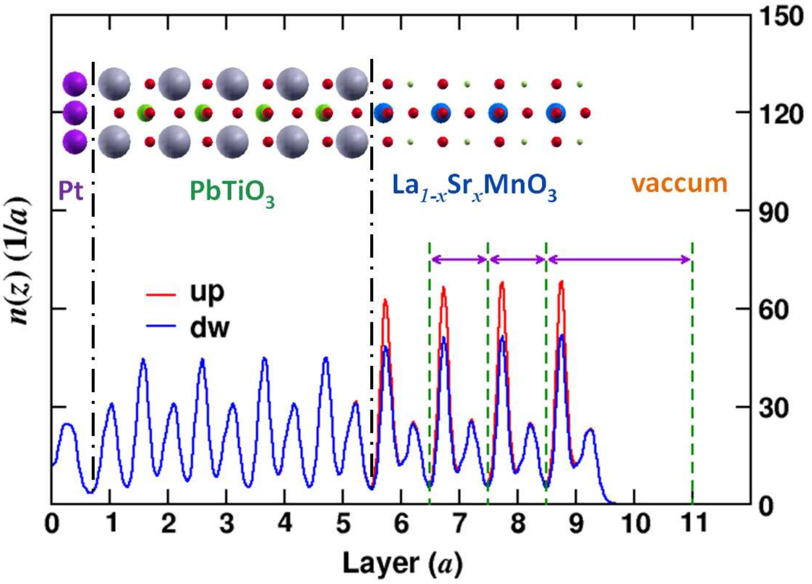

Figure B.2: Illustration of how to count the charge in each layer of La$_{1-x}$Sr$_x$MnO$_3$. The spin polarized part is La$_{1-x}$Sr$_x$MnO$_3$. The green dashed lines highlight the computed boundaries of each layer.

spin channel, so that there must be a definite integer number of electrons N_c filled in the minority spin channel. N_c depends on the details of pseudopotentials. For our pseudo atoms (see Table 4.1), for doping level x, we have La^{3+}: $5s^2 5p^6 5d^0 6s^0$, Sr^{2+}: $4s^2 4p^6 5s^0$, O^{2-}: $2s^2 2p^6$ and due to charge conservation, Mn ion is nominally $+(3+x)$ with an electron configuration $3s^2 3p^6 3d^{4-x} 4s^0$. For one unit cell of La$_{1-x}$Sr$_x$MnO$_3$, since spin polarization only comes from the electrons on Mn d-orbitals, we can sum all the other electrons that are formally spin unpolarized: $8 \times (1-x) + 8 \times x + 8 \times 3 + 8 = 40$. The four terms are from La^{3+}, Sr^{2+}, three O^{2-} and the Mn ion without d-electrons. Hence $N_c = 40/2 = 20$, which is independent of hole doping. Now we start from the vacuum (see Fig. B.2) where there is no charge. We integrate the minority spin channel moving into the film until the integral is equal to 20. Then this position determines the boundary of the first layer. Next we restart the integral from this boundary until it reaches 20 again. This determines the boundary of the second layer. Repeating the procedure yields the boundaries of each manganite layer. Once the boundaries are determined, we integrate the charge density of both majority

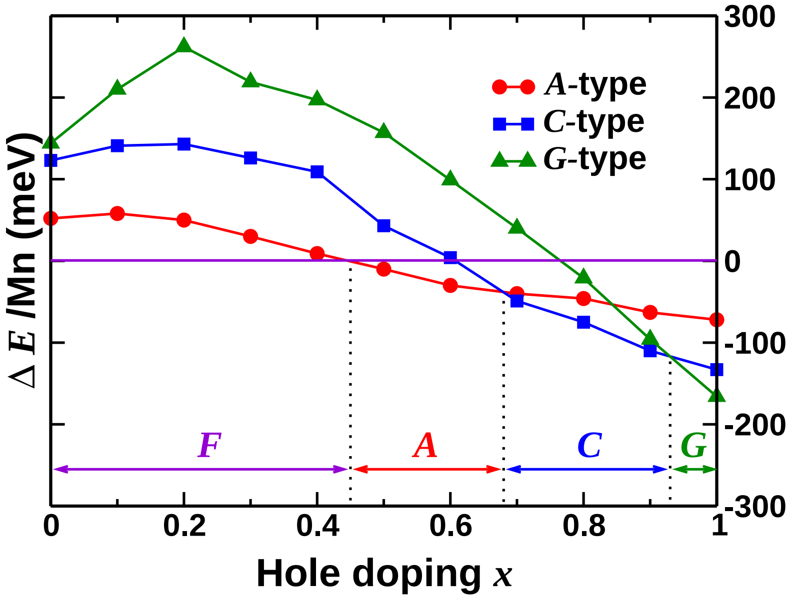

Figure B.3: The complete magnetic phase diagram of $La_{1-x}Sr_xMnO_3$ (4 formula, 20 atoms). The calculation is based on LSDA+U with $U = 1$ eV. ΔE is the energy difference between ferromagnetism and various types of anti-ferromagnetism. The labels F, A, C and G refer to ferromagnetism, A-type, C-type and G-type antiferromagnetism, respectively. Each label highlights the ground state magnetic structure of the given hole doping region.

and minority spins in each layer and thus layer-resolved holes and magntization follow straightforwardly.

We comment that in DFT calculations, as long as the Hubbard U is larger than a critical value U_c, the manganites become half-metallic in the ferromagnetic phase. For $SrTiO_3$-strained $Pnma$ $La_{1-x}Sr_xMnO_3$, we find $U_c \simeq 1$ eV. Therefore, for the useful and reasonable range of U, our method is valid.

B.3 The phase diagram of manganites from LSDA+U

In this section, we provide the complete magnetic phase diagram of $La_{1-x}Sr_xMnO_3$ in Fig. B.3 based on LSDA+U with $U = 1$ eV. In the high doping region ($x > 0.4$), LSDA+U does reproduce the experimentally observed sequence of different magnetic ground states [117]:

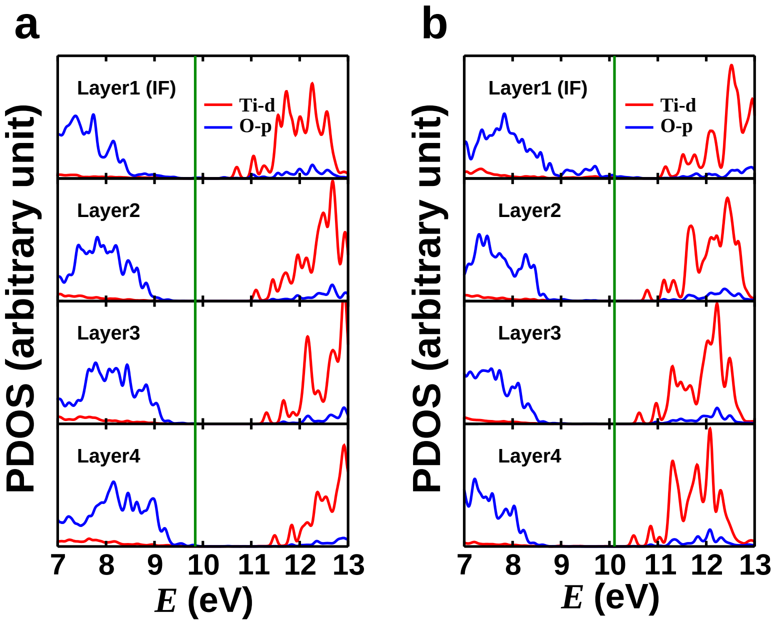

Figure B.4: Atomic projected density of states (PDOS) of PbTiO$_3$/La$_{1-x}$Sr$_x$MO$_3$/Pt. The red curves are Ti-d projected states and the blue curves are O-p projected states. Layer1 refers to the interface between PbTiO$_3$ and La$_{1-x}$Sr$_x$MnO$_3$ (the interface we are interested in) and Layer4 is the interface between PbTiO$_3$ and Pt. The green solid line is the Fermi level.

FM $\rightarrow A-$ AFM $\rightarrow C-$ AFM $\rightarrow G-$ AFM as the hole doping x increases. Our result is consistent with previous calculations [113], though the exact transition points depend on the Hubbard U and the type of exchange correlation functionals.

B.4 Test of band alignment and possible charge spillage

Due to the underestimation of band gap in DFT calculations, band alignment and possible artificial charge spillage into conduction bands could lead to unrealistic ground states when simulating the interface between ferroelectrics and metals [146]. We check our calculations of PbTiO$_3$/La$_{1-x}$Sr$_x$MO$_3$/Pt interface and find that the Fermi level is in the band gap of PbTiO$_3$. A typical projected density of states (PDOS) is illustrated in Fig. B.4, where Layer1 refers to the interface between PbTiO$_3$ and La$_{1-x}$Sr$_x$MnO$_3$ (the interface we are interested in) and Layer4 is the interface between PbTiO$_3$ and Pt. We can see that the

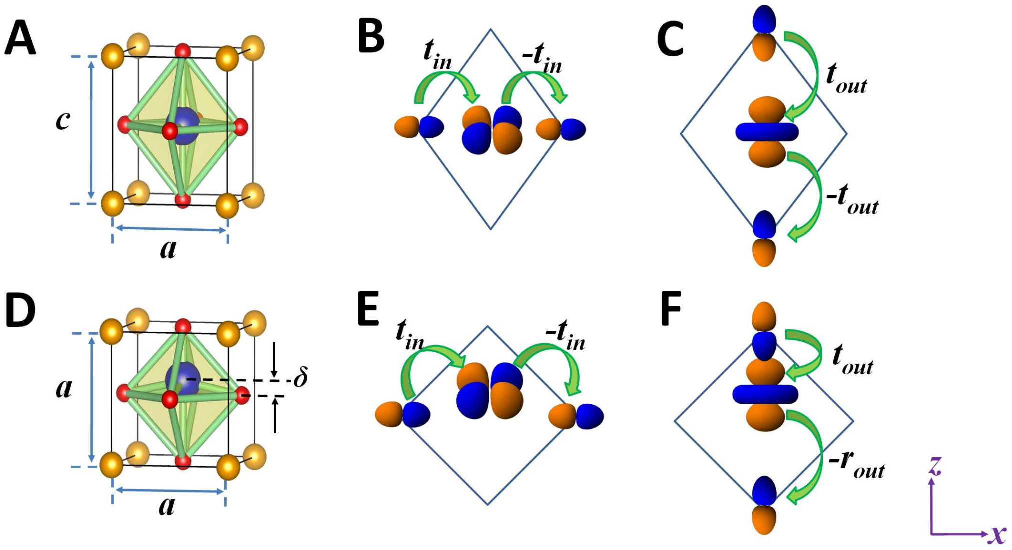

Figure B.5: **A**) Jahn-Teller distortions of tetragonal perovskite oxides. **B**) in-plane hopping t_{in} between oxygen p_x orbitals and $d_{x^2-y^2}$ orbital of B atom. **C)** out-of-plane hopping t_{out} between oxygen p_z orbitals and $d_{3z^2-r^2}$ orbital of B atom. **D**) BO rumplings of cubic perovskite oxides. δ is the B-O displacement. **E**) same as **B**). **F**) same as **C**).

interior of PbTiO_3 remains insulating. We need to point out that both terminations of PbTiO_3 are PbO layers in our calculations, instead of the pathological TiO_2 termination which leads to a metallic ferroelectric ground state in other similar systems [146].

B.5 Tight binding analysis of orbital polarization in perovskite oxides

We are focused on two structural distortions, both of which induce orbital polarization in pervskite oxides: Jahn-Teller distortions and BO displacments. Fig. B.5A) shows a typical Jahn-Teller distortion in which c/a deviates from unit. Fig. B.5B) illustrates the in-plane hopping t_{in} between oxygen p_x orbitals and $d_{x^2-y^2}$ orbital of B atom. Fig. B.5C) illustrates the out-of-plane hopping t_{out} between oxygen p_z orbitals and $d_{3z^2-r^2}$ orbital of B atom. In the cubic structure, $t_{\text{in}} = t_{\text{out}}$ due to symmetry. Considering that the d-orbital is an anti-bonding state, as $c/a > 1$ ($c/a < 1$), we have $t_{\text{out}} < t_{\text{in}}$ ($t_{\text{in}} < t_{\text{out}}$) so that $d_{3z^2-r^2}$ ($d_{x^2-y^2}$) becomes less antibonding and thus more energetically favorable. A quantitative orbital polarization is shown in Fig. 4A in the main text. Fig. B.5D) shows a rumpling of

BO layer in cubic perovskite oxides. The B atom moves along the z direction while the in-plane O atoms are fixed. Fig. B.5E) illustrates the in-plane hopping t_{in} between oxygen p_x orbitals and $d_{x^2-y^2}$ orbital of B atom. Fig. B.5F) illustrates the out-of-plane hopping t_{out} between oxygen p_z orbitals and $d_{3z^2-r^2}$ orbital of B atom. Since the distances from the B atom to the two apical O atoms are different, the hoppings are generally different, denoted by t_{out} and r_{out}. The minus sign reflects the fact that p_z has odd parity while $d_{3z^2-r^2}$ has even parity along z direction. Owing to the periodic boundary conditions, the effective in-plane hopping at Γ $(k = 0)$ is $t_{\text{in}}+(-t_{\text{in}})e^{ika} = 0$, i.e. a pair of non-bonding states is formed and the $d_{x^2-y^2}$ orbital constitutes the conduction band minimum. However, with the BO rumplings, the effective out-of-plane hopping at Γ is no longer zero because $t_{\text{out}} \neq r_{\text{out}}$. A net out-of-plane hopping mixes O p_z orbitals and the $d_{3z^2-r^2}$ orbitals of B atom, making the latter more antibonding and thus less occupied. First-principle calculations, shown in Fig. 4B in the main text, are consistent with this crude tight-binding analysis.

Appendix C

Appendix to Theory of Interfacial Ferroelectricity

C.1 Landau free energy for interfacial ferroelectricity

In this section, we derive how to construct a Landau free energy for interfacial ferroelectricity. Before doing that, we first briefly derive a Landau free energy for the normal interface between ferroelectrics and realistic electrodes with finite screening length λ [32]. As is illustrated in Fig. C.1A, the ferroelectric polarization P terminates at the interface and causes the surface charge $\sigma = P$. Because of the finite screening length λ, we model the system that the screening charge σ_s does not lie right at the interface, but at a separation λ away from the interface. The elaboration of this modelling could be made but the qualitative picture is not altered [147].

The voltage drop across the whole heterostructure is zero since electrodes on both sides effectively screen the potential and the interior of electrodes is bulk-like. Therefore we have:

$$4\pi\sigma d - 4\pi\sigma_s(d + 2\lambda) = 0 \tag{C.1}$$

Eq. (C.1) shows that σ_s is always smaller than σ, leading to the depolarization field in the ferroelectrics.

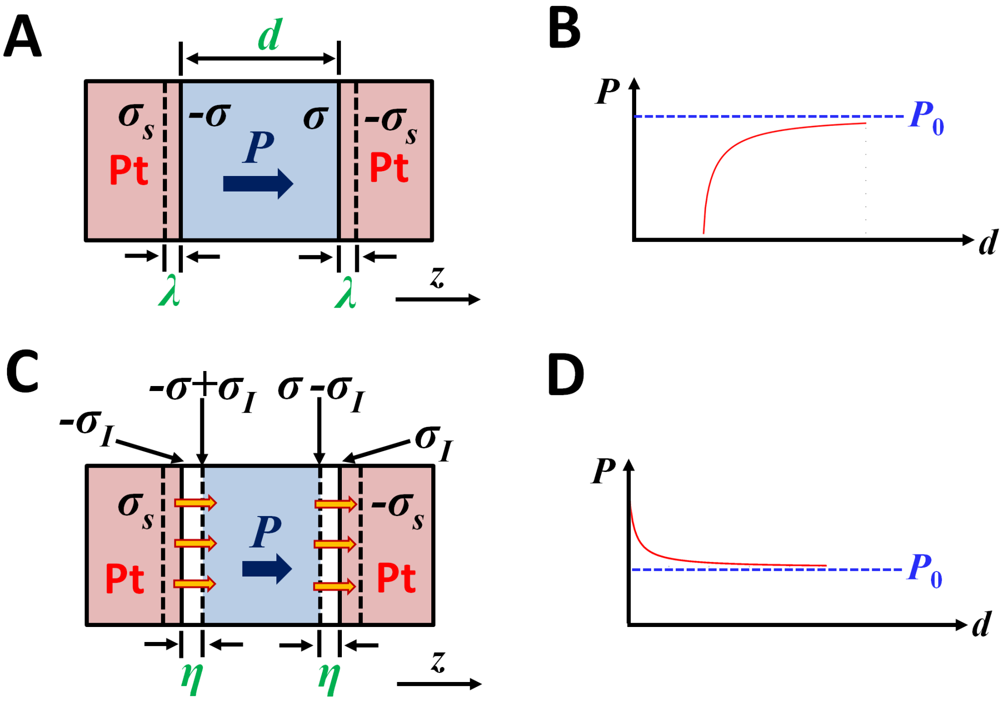

Figure C.1: **A**) Schematic of normal metal/ferroelectric heterostructures. The realistic electrodes have finite screening lengths λ. **B**) Polarization of thin film ferroelectrics as a function of film thickness d. As d is comparable to the screening length λ, ferroelectric polarization is severely suppressed. **C**) Schematic of metal/ferroelectric heterostructures with built-in interfacial ferroelectric polarization P_I. The unshaded areas are the interfacial region with a characteristic length η. **D**) If $P_I > P(1 + \lambda/\eta)$, then the polarization of ferroelectric thin film could be enhanced by the unstable interfacial metal-O bonds at any finite film thickness.

$$E_{dep} = -4\pi(\sigma - \sigma_s) = -4\pi\sigma\frac{2\lambda}{d + 2\lambda} = -4\pi P\frac{2\lambda}{d + 2\lambda} \tag{C.2}$$

where P is the ferroelectric polarization. The minus sign shows that the direction of depolarization field is always opposite to the polarization P. The Landau free energy is then:

$$F = F_0 + \int^{P} E_{dep}(P')dP' \tag{C.3}$$

where F_0 is the double-well Landau free energy for bulk ferroelectrics

$$F_0(P) = \frac{\Delta E_0}{P_0^4}\left(P^4 - 2P_0^2P^2\right) \tag{C.4}$$

where P_0 is the bulk ferroelectric polarization and ΔE_0 is the energy difference between ferroelectric and paraelectric states. Minimization of Eq. (C.3) with respect to P leads to:

$$P = P_0\sqrt{1 - \frac{d_c + 2\lambda}{d + 2\lambda}} \tag{C.5}$$

where

$$d_c = 2\lambda\left(\pi\frac{P_0^2}{\Delta E_0} - 1\right) \tag{C.6}$$

is the critical thickness below which the polarization of ferroelectric thin film vanishes due to imperfect screening. A schematic of Eq. (C.5) is shown in Fig. C.1B.

Now we introduce some built-in polarization P_I in the interfacial regions within the ferroelectrics. The unshaded areas and yellow arrows in Fig. C.1C highlight the interfacial ferroelectricity induced by the unstable metal-O bonds. We assume that the magnitude of P_I is fixed but its sign (i.e. direction) is flippable. Because of the P_I, Eq. (C.1) now becomes:

$$4\pi(\sigma - \sigma_I)(d - 2\lambda) + 4\pi\sigma_I d - 4\pi\sigma_s(d + 2\lambda) = 0 \tag{C.7}$$

where $\sigma = P$ and $\sigma_I = P_I$. The definition of depolarization field remains the same:

$$E_{dep} = -4\pi(\sigma - \sigma_s) = -4\pi\left[\frac{P(2\lambda + 2\eta) - P_I \cdot 2\eta}{d + 2\lambda}\right] \tag{C.8}$$

The Landau free energy is constructed similarly,

$$F = F_0 + \int^P E_{dep}(P')dP' = F_0 + \frac{4\pi}{d + 2\lambda}\left((\eta + \lambda)P^2 - 2\eta P_I P\right) \tag{C.9}$$

It is interesting to examine Eq. (C.8). If P_I is much smaller than P, then like Eq. (C.2), E_{dep} always has the opposite direction of P and suppresses the polarization. However, if $P_I > P(1 + \lambda/\eta)$, then E_{dep} is parallel with P and therefore could enhance the ferroelectric polarization. Fig. C.1D shows the case in which the polarization of the thin film is enhanced by the unstable interfacial metal-O bonds. Such effects are found in the numerical simulations of Pt/$BaTiO_3$ interfaces [33].

Bibliography

[1] Pavlo Zubko, Stefano Gariglio, Marc Gabay, Philippe Ghosez, and Jean-Marc Triscone. Interface physics in complex oxide heterostructures. *Annual Review of Condensed Matter Physics*, 2(1):141–165, 2011.

[2] James M. Rondinelli and Nicola A. Spaldin. Structure and properties of functional oxide thin films: Insights from electronic-structure calculations. *Advanced Materials*, 23(30):3363–3381, 2011.

[3] Carlos A. F. Vaz, Jason Hoffman, Charles H. Ahn, and Ramamoorthy Ramesh. Magnetoelectric coupling effects in multiferroic complex oxide composite structures. *Advanced Materials*, 22(26-27):2900–2918, 2010.

[4] E. Dagotto. *Science*, 318:1076, 2007.

[5] Masashi Kawasaki, Kazuhiro Takahashi, Tatsuro Maeda, Ryuta Tsuchiya, Makoto Shinohara, Osamu Ishiyama, Takuzo Yonezawa, Mamoru Yoshimoto, and Hideomi Koinuma. *Science*, 266:1540, 1994.

[6] Yoshinori Tokura and Harold Hwang. Condensed-matter physics: Complex oxides on fire. *Nat. Mat.*, 7:694, 2008.

[7] John Tully. Crisp: The center for research on interface structures and phenomena, yale university. *Advanced Materials*, 22(26-27):2837–2837, 2010.

[8] T. Hashimoto, S. Ishibashi, and K. Terakura. Jahn-teller distortion and magnetic structure in $lamno_3$: A first-principles theoretical study with full structure optimizations. *Phys. Rev. B*, 82(4):045124, Jul 2010.

[9] Z. Zhong and P. J. Kelly. *Europhys. Lett.*, 84:27001, 2008.

[10] Eric Bousquet, Matthew Dawber, Nicolas Stucki, Céline Lichtensteiger, Patrick Hermet, Stefano Gariglio, Jean-Marc Triscone, and Philippe Ghosez. *Nature*, 452:732, 2007.

[11] P. Hohenberg and W. Kohn. Inhomogeneous electron gas. *Phys. Rev.*, 136(3B):B864–B871, Nov 1964.

[12] W. Kohn and L. J. Sham. Self-consistent equations including exchange and correlation effects. *Phys. Rev.*, 140(4A):A1133–A1138, Nov 1965.

[13] Craig J. Fennie. Ferroelectrically induced weak ferromagnetism by design. *Phys. Rev. Lett.*, 100:167203, 2008.

[14] A. Ohtomo and H. Y. Hwang. *Nature*, 427:423, 2004.

[15] M. Huijben, G. Rijnders, D. H. A. Blank, S. Bals, S. Van Aert, J. Verbeeck, G. Van Tendeloo, A. Brinkman, and H. Hilgenkamp. *Nature Mater.*, 5:556, 2006.

[16] N. Reyren, S. Thiel, A. D. Caviglia, L. Fitting Kourkoutis, G. Hammerl, C. Ricther, C. W. Schneider, T. Kopp, A. S. Rüetschi, D. Jaccard, M. Gabay, D. A. Muller, J. M. Triscone, and J. Mannhart. *Science*, 317:1196, 2007.

[17] C. Bell, S. Harashima, Y. Kozuka, M. Kim, B. G. Kim, Y. Hikita, and H. Y. Hwang. Dominant mobility modulation by the electric field effect at the laalo$_3$/srtio$_3$ interface. *Phys. Rev. Lett.*, 103:226802, 2009.

[18] A. D. Caviglia, S. Gariglio, N. Reyren, D. Jaccard, T. Schneider, M. Gabay, S. Thiel, G. Hammerl, J. Mannhart, and J. M. Triscone. *Nature*, 456:624, 2008.

[19] S. Thiel, G. Hammerl, A. Schmehl, C. W. Schneider, and J. Mannhart. *Science*, 313:1942, 2006.

[20] C. Cen, S. Thiel, G. Hammerl, C. W. Schneider, K. E. Andersen, C. S. Hellberg, J. Mannhart, and J. Levy. *Nature Mater.*, 7:298, 2008.

[21] Cheng Cen, Stefan Thiel, Jochen Mannhart, and Jeremy Levy. *Science*, 323:1026, 2009.

[22] Hanghui Chen, Alexie M. Kolpak, and Sohrab Ismail-Beigi. Electronic and magnetic properties of srtio3/laalo3 interfaces from first principles. *Advanced Materials*, 22(26-27):2881–2899, 2010.

[23] Mark Huijben, Alexander Brinkman, Gertjan Koster, Guus Rijnders, Hans Hilgenkamp, and Dave H. A. Blank. Structure-property relation of srtio[sub 3]/laalo[sub 3] interfaces. *Adv. Mat.*, 21:1665, 2009.

[24] Hanghui Chen, Alexie Kolpak, and Sohrab Ismail-Beigi. Fundamental asymmetry in interfacial electronic reconstruction between insulating oxides: An ab initio study. *Phys. Rev. B*, 79(16):161402, 2009.

[25] Hanghui Chen and Sohrab Ismail-Beigi. Atomic reconstructions at laalo$_3$/srtio$_3$ interfaces. *(in preparation)*, 2012.

[26] Hanghui Chen, Alexie Kolpak, and Sohrab Ismail-Beigi. First-principles study of electronic reconstructions of laalo$_3$/srtio$_3$ heterointerfaces and their variants. *Phys. Rev. B*, 82:085430, Aug 2010.

[27] C. A. F. Vaz, J. Hoffman, Y. Segal, J. W. Reiner, R. D. Grober, Z. Zhang, C. H. Ahn, and F. J. Walker. Origin of the magnetoelectric coupling effect in $pb(zr_{0.2}ti_{0.8})o_3/la_{0.8}sr_{0.2}mno_3$ multiferroic heterostructures. *Phys. Rev. Lett.*, 104(12):127202, Mar 2010.

[28] Y Tokura. Critical features of colossal magnetoresistive manganites. *Rep. Prog. Phys.*, 69(3):797, 2006.

[29] Y. Tokura and N. Nagaosa. Obital physics in transition-metal oxides. *Science*, 288:462, 2000.

[30] Hanghui Chen and Sohrab Ismail-Beigi. Ferroelectric control of magnetization in the manganites. *(in preparation)*, 2011.

[31] Hanghui Chen and Sohrab Ismail-Beigi. Ferroelectric modulation of orbital polarization in the manganites. *in preparation*, 2011.

[32] J. Junquera and P. Ghosez. Critical thickness for ferroelectricity in perovskite ultrathin films. *Nature*, 422:506, 2003.

[33] M. Stengel, David Vanderbilt, and N. A. Spaldin. Enhancement of ferroelectricity at metaloxide interfaces. *Nat. Mat.*, 8:392, 2009.

[34] Hanghui Chen and Sohrab Ismail-Beigi. Theory of interfacial ferroelectricty. *(in preparation)*, 2012.

[35] Neil W. Ashcroft and N. David Mermin. *Solid State Physics*. Thomson Learning, 1976.

[36] J. P. Perdew and Alex Zunger. Self-interaction correction to density-functional approximations for many-electron systems. *Phys. Rev. B*, 23:5048–5079, 1981.

[37] John P. Perdew and Wang Yue. Accurate and simple density functional for the electronic exchange energy: Generalized gradient approximation. *Phys. Rev. B*, 33:8800–8802, 1986.

[38] John P. Perdew, Kieron Burke, and Matthias Ernzerhof. Generalized gradient approximation made simple. *Phys. Rev. Lett.*, 77:3865–3868, 1996.

[39] R. P. Feynman. Forces in molecules. *Phys. Rev.*, 56:340–343, 1939.

[40] D. R. Hamann, M. Schlüter, and C. Chiang. Norm-conserving pseudopotentials. *Phys. Rev. Lett.*, 43:1494–1497, 1979.

[41] James C. Phillips. Energy-band interpolation scheme based on a pseudopotential. *Phys. Rev.*, 112:685–695, 1958.

[42] Leonard Kleinman and James C. Phillips. Crystal potential and energy bands of semiconductors. i. self-consistent calculations for diamond. *Phys. Rev.*, 116:880–884, 1959.

[43] J. D. Joannopoulos, Th. Starkloff, and Marc Kastner. Theory of pressure dependence of the density of states and reflectivity of selenium. *Phys. Rev. Lett.*, 38:660–663, 1977.

[44] Th. Starkloff and J. D. Joannopoulos. Local pseudopotential theory for transition metals. *Phys. Rev. B*, 16:5212–5215, 1977.

[45] David Vanderbilt. Soft self-consistent pseudopotentials in a generalized eigenvalue formalism. *Phys. Rev. B*, 41(11):7892–7895, Apr 1990.

[46] R. D. King-Smith and David Vanderbilt. Theory of polarization of crystalline solids. *Phys. Rev. B*, 47:1651–1654, 1993.

[47] Vladimir I. Anisimov, Jan Zaanen, and Ole K. Andersen. Band theory and mott insulators: Hubbard U instead of stoner *I*. *Phys. Rev. B*, 44:943–954, 1991.

[48] Matteo Cococcioni and Stefano de Gironcoli. Linear response approach to the calculation of the effective interaction parameters in the $lda+u$ method. *Phys. Rev. B*, 71(3):035105, Jan 2005.

[49] J. F. Janak. *Phys. Rev. B*, 18:7165–7168, 1978.

[50] C. Bell, S. Harashima, Y. Hikita, and H. Y. Hwang. Thickness dependence of the mobility at the laalo[sub 3]/srtio[sub 3] interface. *Appl. Phys. Lett.*, 94(22):222111, 2009.

[51] A. Brinkman, M. Huijben, M. Van Zalk, J. Huijben, U. Zeitler, J. C. Maan, W. G. Van der Wiel, G. Rijnders, D. H. A. Blank, and H. Hilgenkamp. *Nature Mater.*, 6:493, 2007.

[52] R. Pentcheva and W. E. Pickett. *Phys. Rev. B*, 74:035112, 2006.

[53] R. Pentcheva and W. E. Pickett. *Phys. Rev. B*, 78:205106, 2008.

[54] M. S. Park, S. H. Rhim, and A. J. Freeman. *Phys. Rev. B*, 74:205416, 2006.

[55] J. M. Albina, M. Mrovec, B.Meyer, and C. Elsässer. *Phys. Rev. B*, 76:165103, 2007.

[56] K. Janicka, J. P. Velev, and E. Y. Tsymbal. *Phys. Rev. Lett.*, 102:106803, 2009.

[57] Jaekwang Lee and Alexander A. Demkov. *Phys. Rev. B*, 78:193104, 2008.

[58] P. R. Willmott, S. A. Pauli, R. Herger, C. M. Schlepütz, D. Martoccia, B. D. Patterson, B. Delley, R. Clarke, D. Kumah, C. Cionca, and Y. Yacoby. *Phys. Rev. Lett.*, 99:155502, 2007.

[59] A. Kalabukhov, R. Gunnarsson, J. Börjesson, E. Olsson, T. Claeson, and D. Winkler. *Phys. Rev. B*, 75:121404(R), 2007.

[60] G. Herranz, M. Basletić, M. Bibes, C. Carrétéro, E. Tafra, E. Jacquet, K. Bouzehouane, C. Deranlot, A. Hamzić, J. M. Broto, A. Barthélémy, and A. Fert. *Phys. Rev. Lett.*, 98:216803, 2007.

[61] W. Siemons, G. Koster, H. Yamamoto, W. A. Harrison, G. Lucovsky, T. H. Geballe, D. H. A. Blank, and M. R. Beasley. *Phys. Rev. Lett.*, 98:196802, 2007.

[62] M. Sing, G. Berner, A. Möller K. Goβ, A. Ruff, A. Wetscherek, S. Thiel, J. Mannhart, S. A. Pauli, C. W. Schneider, P. R. Willmott, M. Gorgoi, F. Schäfers, and R. Claessen. *Phys. Rev. Lett.*, 102:176805, 2009.

[63] M. Salluzzo, J. C. Cezar, N. B. Brookes, V. Bisogni, G. M. De Luca, C. Richter, S. Thiel, J. Mannhart, M. Huijben, A. Brinkman, G. Rijnders, and G. Ghiringhelli. Orbital reconstruction and the two-dimensional electron gas at the laalo[sub 3]/srtio[sub 3] interface. *Phys. Rev. Lett.*, 102(16):166804, 2009.

[64] S. Thiel, C. W. Schneider, L. Fitting Kourkoutis, D. A. Muller, N. Reyren, A. D. Caviglia, S. Gariglio, J.-M. Triscone, and J. Mannhart. Electron scattering at dislocations inlaalo[sub 3]/ srtio[sub 3] interfaces. *Phys. Rev. Lett.*, 102(4):046809, 2009.

[65] J. N. Eckstein. *Nature Mater.*, 6:473, 2007.

[66] N. Nakagawa, H. Y. Hwang, and D. A. Muller. *Nature Mater.*, 5:204, 2006.

[67] R. Pentcheva and W. E. Pickett. *Phys. Rev. Lett*, 102:107602, 2009.

[68] Won joon Son, Eunae Cho, Bora Lee, Jaichan Lee, and Seungwu Han. Density and spatial distribution of charge carriers in the intrinsic n-type laalo[sub 3]-srtio[sub 3] interface. *Phys. Rev. B*, 79(24):245411, 2009.

[69] M. Basletic, J.-L. Mauric, C. Carrétéro, G. Herranz, O. Copie, M. Bibes, É. Jacquet, K. Bouzehouane, S. Fusil, and A. Barthélémy. *Nature Mater.*, 7:621, 2008.

[70] M. Takizawa, Y. Hotta, T. Susaki, Y. Ishida, H. Wadati, Y. Takata, K. Horiba, M. Matsunami, S. Shin, M. Yabashi, K. Tamasaku, Y. Nishino, T. Ishikawa, A. Fujimori, and H. Y. Hwang. Spectroscopic evidence for competing reconstructions in polar multilayers laalo[sub 3]/lavo[sub 3]/laalo[sub 3]. *Phys. Rev. Lett.*, 102(23):236401, 2009.

[71] Y. Segal, J. H. Ngai, J. W. Reiner, F. J. Walker, and C. H. Ahn. X-ray photoemission studies of the metal-insulator transition in $laalo_3/srtio_3$ structures grown by molecular beam epitaxy. *Phys. Rev. B*, 80(24):241107, 2009.

[72] A. Kalabukhov, R. Gunnarsson, T. Claeson, and D. Winkler. Electrical transport properties of polar heterointerface between ktao3 and srtio3. *arXiv.org:0704.1050*, 2007.

[73] Franklin J. Wong, Rajesh V. Chopdekar, and Yuri Suzuki. Disorder and localization at the laalo$_3$/srtio$_3$ heterointerface. *Phys. Rev. B*, 82:165413, Oct 2010.

[74] Zhicheng Zhong, P. X. Xu, and Paul J. Kelly. Polarity-induced oxygen vacancies at laalo$_3$srtio$_3$ interfaces. *Phys. Rev. B*, 82:165127, Oct 2010.

[75] N. C. Bristowe, P. B. Littlewood, and Emilio Artacho. Surface defects and conduction in polar oxide heterostructures. *Phys. Rev. B*, 83:205405, May 2011.

[76] M. C. Payne, M. P. Teter, D. C. Allan, T. A. Arias, and J. D. Joannopoulos. Iterative minimization techniques for ab initio total-energy calculations: molecular dynamics and conjugate gradients. *Rev. Mod. Phys.*, 64(4):1045–1097, Oct 1992.

[77] S. Gemming and G. Seifert. *Acta Mater.*, 54:4299, 2006.

[78] K. Janicka, J. P. Velev, and E. Y. Tsymbal. *J. Appl. Phys.*, 103:07B508, 2008.

[79] Zoran S. Popović, Sashi Satpathy, and Richard M. Martin. Origin of the two-dimensional electron gas carrier density at the laalo[sub 3] on srtio[sub 3] interface. *Phys. Rev. Lett.*, 101(25):256801, 2008.

[80] Jaekwang Lee and Alexander A. Demkov. Band alignment of laalo3/srtio3. *Mater. Res. Soc. Symp. Proc.*, 0966-T07-33, 2007.

[81] M Peressi, N Binggeli, and A Baldereschi. Band engineering at interfaces: theory and numerical experiments. *J. Phys. D*, 31(11):1273, 1998.

[82] Alfonso Baldereschi, Stefano Baroni, and Raffaele Resta. Band offsets in lattice-matched heterojunctions: A model and first-principles calculations for gaas/alas. *Phys. Rev. Lett.*, 61(6):734, Aug 1988.

[83] L. Colombo, R. Resta, and S. Baroni. Valence-band offsets at strained si/ge interfaces. *Phys. Rev. B*, 44(11):5572, 1991.

[84] R. Pentcheva, M. Huijben, K. Otte, W. E. Pickett, J. E. Kleibeuker, J. Huijben, H. Boschker, D. Kockmann, W. Siemons, G. Koster, H. J. W. Zandvliet, G. Rijnders, D. H. A. Blank, H. Hilgenkamp, and A. Brinkman. Parallel electron-hole bilayer conductivity from electronic interface reconstruction. *Phys. Rev. Lett.*, 104:166804, Apr 2010.

[85] Per-Olov Löwdin. On the non-orthogonality problem connected with the use of atomic wave functions in the theory of molecules and crystals. *J. Chem. Phys.*, 18(3):365, 1950.

[86] S. Satpathy. Eigenstates of wannier excitons near a semiconductor surface. *Phys. Rev. B*, 28(8):4585–4592, Oct 1983.

[87] A. F. Devonshire. *Philos. Mag.*, 40:1040, 1949.

[88] Armin Antons, J. B. Neaton, Karin M. Rabe, and David Vanderbilt. Tunability of the dielectric response of epitaxially strained *srtio*3 from first principles. *Phys. Rev. B*, 71(2):024102, Jan 2005.

[89] Ivo Souza, Jorge Íñiguez, and David Vanderbilt. First-principles approach to insulators in finite electric fields. *Phys. Rev. Lett.*, 89(11):117602, Aug 2002.

[90] M. A. Saifi and L. E. Cross. Dielectric properties of strontium titanate at low temperature. *Phys. Rev. B*, 2(3):677–684, Aug 1970.

[91] S.A. Chambers, M.H. Engelhard, V. Shutthanandan, Z. Zhu, T.C. Droubay, L. Qiao, P.V. Sushko, T. Feng, H.D. Lee, T. Gustafsson, E. Garfunkel, A.B. Shah, J.-M. Zuo, and Q.M. Ramasse. Instability, intermixing and electronic structure at the epitaxial heterojunction. *Surface Science Reports*, 65(10-12):317 – 352, 2010.

[92] Yun Li, Sutassana Na Phattalung, Sukit Limpijumnong, Jiyeon Kim, and Jaejun Yu. Formation of oxygen vacancies and charge carriers induced in the n-type interface of a $laalo_3$ overlayer on $srtio_3(001)$. *Phys. Rev. B*, 84:245307, Dec 2011.

[93] Tomohito Tanaka, Katsuyuki Matsunaga, Yuichi Ikuhara, and Takahisa Yamamoto. First-principles study on structures and energetics of intrinsic vacancies in $srtio_3$. *Phys. Rev. B*, 68:205213, Nov 2003.

[94] B. Hammer, L. B. Hansen, and J. K. Nørskov. Improved adsorption energetics within density-functional theory using revised perdew-burke-ernzerhof functionals. *Phys. Rev. B*, 59:7413–7421, Mar 1999.

[95] S. S. A. Seo, Z. Marton, W. S. Choi, G. W. J. Hassink, D. H. A. Blank, H. Y. Hwang, T. W. Noh, T. Egami, and H. N. Lee. Multiple conducting carriers generated in laalo[sub 3]/srtio[sub 3] heterostructures. *Appl. Phys. Lett.*, 95(8):082107, 2009.

[96] M. van Zalk, J. Huijben, A. J. M. Giesbers, M. Huijben, U. Zeitler, J. C. Maan, W. G. van der Wiel, G. Rijnders, D. H. A. Blank, H. Hilgenkamp, and A. Brinkman. Magnetoresistance oscillations and relaxation effects at the srtio3-laalo3 interface. *arXiv.org:0806.4450*, 2008.

[97] M. Ben Shalom, C. W. Tai, Y. Lereah, M. Sachs, E. Levy, D. Rakhmilevitch, A. Palevski, and Y. Dagan. Anisotropic magnetotransport at the srtio[sub 3]/laalo[sub 3] interface. *Phys. Rev. B*, 80(14):140403, 2009.

[98] Ariando, X. Wang, G. Baskaran, Z. Q. Liu, J. Huijben, J. B. Yi, A. Annadi, A. Roy Barman, A. Rusydi, S. Dhar, Y. P. Feng, J. Ding, H. Hilgenkamp, and T. Venkatesan. Electronic phase separation at the laalo3/srtio3 interface. *Nat. Commun.*, 2:188, 2011.

[99] D. A. Dikin, M. Mehta, C. W. Bark, C. M. Folkman, C. B. Eom, and V. Chandrasekhar. Coexistence of superconductivity and ferromagnetism in two dimensions. *Phys. Rev. Lett.*, 107:056802, 2011.

[100] Li Lu, Richter C., Mannhart J., and Ashoori R. C. Coexistence of magnetic order and two-dimensional superconductivity at laalo3/srtio3 interfaces. *Nat. Phys.*, 7:762, 2011.

[101] Julie A. Bert, Beena Kalisky, Christopher Bell, Minu Kim, Yasuyuki Hikita, Harold Y. Hwang, and Kathryn A. Moler. Direct imaging of the coexistence of ferromagnetism and superconductivity at the laalo3/srtio3 interface. *Nat. Phys.*, 7:767, 2011.

[102] N. Pavlenko, T. Kopp, E. Y. Tsymbal, G. A. Sawatzky, and J. Mannhart. Magnetic and superconducting phases at the laalo$_3$/srtio$_3$ interface: The role of interfacial ti 3d electrons. *Phys. Rev. B*, 85:020407, 2012.

[103] W. Eerenstein, N. D. Mathur, and J. F. Scott. Multiferroic and magnetoelectric materials. *Nature*, 442:759–765, 2006.

[104] R. Ramesh and N. A. Spaldin. Multiferroics: progress and prospects in thin films. *Nat. Mater.*, 6:21–29, 2007.

[105] K. F. Wang, J. M. Liu, and Z. F. Ren. Multiferroicity: the coupling between magnetic and polarization orders. *Adv. Phys.*, 58:321, 2009.

[106] I Dzyaloshinskii. On the magneto-electric effect in antiferromagnets. *Soviet Phys. J. Expt. Theor. Phys.*, 10:628629, 1960.

[107] G. Srinivasan, E. T. Rasmussen, J. Gallegos, R. Srinivasan, Yu. I. Bokhan, and V. M. Laletin. Magnetoelectric bilayer and multilayer structures of magnetostrictive and piezoelectric oxides. *Phys. Rev. B*, 64(21):214408, Nov 2001.

[108] Nicola A. Spaldin and Manfred Fiebig. The renaissance of magnetoelectric multiferroics. *Science*, 309(5733):391, 2005.

[109] Chun-Gang Duan, S. S. Jaswal, and E. Y. Tsymbal. Predicted magnetoelectric effect in $fe/batio_3$ multilayers: Ferroelectric control of magnetism. *Phys. Rev. Lett.*, 97(4):047201, Jul 2006.

[110] Kunihiko Yamauchi, Biplab Sanyal, and Silvia Picozzi. Interface effects at a half-metal/ferroelectric junction. *Appl. Phys. Lett.*, 91(6):062506, 2007.

[111] Manish K. Niranjan, Julian P. Velev, Chun-Gang Duan, S. S. Jaswal, and Evgeny Y. Tsymbal. Magnetoelectric effect at the $fe_3o_4/batio_3$ (001) interface: A first-principles study. *Phys. Rev. B*, 78(10):104405, Sep 2008.

[112] J. M. Rondinelli, M. Stengel, and N. A. Spaldin. Carrier-mediated magnetoelectricity in complex oxide heterostructures. *Nat. Nanotech.*, 3:46, 2008.

[113] J. D. Burton and E. Y. Tsymbal. Prediction of electrically induced magnetic reconstruction at the manganite/ferroelectric interface. *Phys. Rev. B*, 80(17):174406, Nov 2009.

[114] V. I. Anisimov, F. Aryasetiawan, and A. I. Lichtenstein. *J. Phys.: Condens. Matter*, 9:767, 1997.

[115] L Nordheim. *Ann. Phys. (Leipzig)*, 9:607, 1931.

[116] L. Bellaiche and David Vanderbilt. Virtual crystal approximation revisited: Application to dielectric and piezoelectric properties of perovskites. *Phys. Rev. B*, 61(12):7877–7882, Mar 2000.

[117] Z. Fang, I. V. Solovyev, and K. Terakura. Phase diagram of tetragonal manganites. *Phys. Rev. Lett.*, 84(14):3169–3172, Apr 2000.

[118] G. Trimarchi and N. Binggeli. Structural and electronic properties of $lamno_3$ under pressure: An ab initio $lda + u$ study. *Phys. Rev. B*, 71(3):035101, Jan 2005.

[119] Clarence Zener. Interaction between the d-shells in the transition metals. ii. ferromagnetic compounds of manganese with perovskite structure. *Phys. Rev.*, 82(3):403–405, May 1951.

[120] H. A. Kramers. *Physica*, 1:182, 1934.

[121] Aymeric Sadoc, Bernard Mercey, Charles Simon, Dominique Grebille, Wilfrid Prellier, and Marie-Bernadette Lepetit. Large increase of the curie temperature by orbital ordering control. *Phys. Rev. Lett.*, 104(4):046804, Jan 2010.

[122] I. V. Solovyev. Lattice distortion and magnetic ground state of $ytio_3$ and $latio_3$. *Phys. Rev. B*, 69(13):134403, Apr 2004.

[123] Igor Solovyev, Noriaki Hamada, and Kiyoyuki Terakura. Crucial role of the lattice distortion in the magnetism of $lamno_3$. *Phys. Rev. Lett.*, 76(25):4825–4828, Jun 1996.

[124] P. W. Anderson and H. Hasegawa. Considerations on double exchange. *Phys. Rev.*, 100(2):675–681, Oct 1955.

[125] Heather J. Kulik, Matteo Cococcioni, Damian A. Scherlis, and Nicola Marzari. Density functional theory in transition-metal chemistry: A self-consistent hubbard u approach. *Phys. Rev. Lett.*, 97(10):103001, 2006.

[126] J. Chakhalian, J. W. Freeland, H.-U. Habermeier, G. Cristiani, G. Khaliullin, M. van Veenendaal, and B. Keimer. Orbital reconstruction and covalent bonding at an oxide interface. *Science*, 318:1115, 2007.

[127] A. D. Rata, A. Herklotz, K. Nenkov, L. Schultz, and K. Dörr. Strain-induced insulator state and giant gauge factor of $la0.7sr0.3coo3$ films. *Phys. Rev. Lett.*, 100(7):076401, Feb 2008.

[128] A. Tebano, C. Aruta, S. Sanna, P. G. Medaglia, G. Balestrino, A. A. Sidorenko, R. De Renzi, G. Ghiringhelli, L. Braicovich, V. Bisogni, and N. B. Brookes. Evidence of orbital reconstruction at interfaces in ultrathin $la0.67sr0.33mno3$ films. *Phys. Rev. Lett.*, 100(13):137401, Apr 2008.

[129] M. Huijben, L. W. Martin, Y.-H. Chu, M. B. Holcomb, P. Yu, G. Rijnders, D. H. A. Blank, and R. Ramesh. Critical thickness and orbital ordering in ultrathin $la0.7sr0.3mno3$ films. *Phys. Rev. B*, 78(9):094413, Sep 2008.

[130] P. Yu, J.-S. Lee, S. Okamoto, M. D. Rossell, M. Huijben, C.-H. Yang, Q. He, J. X. Zhang, S. Y. Yang, M. J. Lee, Q. M. Ramasse, R. Erni, Y.-H. Chu, D. A. Arena, C.-C.

Kao, L. W. Martin, and R. Ramesh. Interface ferromagnetism and orbital reconstruction in $bifeo3 - la0.7sr0.3mno3$ heterostructures. *Phys. Rev. Lett.*, 105(2):027201, Jul 2010.

[131] Eva Benckiser, Maurits W. Haverkort, Sebastian Brck, Eberhard Goering, Sebastian Macke, Alex Fra, Xiaoping Yang, Ole K. Andersen, Georg Cristiani, Hanns-Ulrich Habermeier, Alexander V. Boris, Ioannis Zegkinoglou, Peter Wochner, Heon-Jung Kim, Vladimir Hinkov, and Bernhard Keimer. Orbital reflectometry of oxides heterostructures. *Nat. Mater.*, 10:189, 2011.

[132] Karen Johnston, Xiangyang Huang, J. B. Neaton, and Karin M. Rabe. First-principles study of symmetry lowering and polarization in $batio_3?srtio_3$ superlattices with in-plane expansion. *Phys. Rev. B*, 71(10):100103, Mar 2005.

[133] M. Dawber, C. Lichtensteiger, M. Cantoni, M. Veithen, P. Ghosez, K. Johnston, K. M. Rabe, and J.-M. Triscone. Unusual behavior of the ferroelectric polarization in $pbtio_3/srtio_3$ superlattices. *Phys. Rev. Lett.*, 95(17):177601, Oct 2005.

[134] Thomas Wolfram and Sinasi Ellialtioglu. *Electronic and Optical Properties of d-Band Perovskites.* Cambridge University Press, 2006.

[135] M. Dawber, K. M. Rabe, and J. F. Scott. Physics of thin-film ferroelectric oxides. *Rev. Mod. Phys.*, 77:1083–1130, Oct 2005.

[136] Na Sai, Alexie M. Kolpak, and Andrew M. Rappe. Ferroelectricity in ultrathin perovskite films. *Phys. Rev. B*, 72:020101, 2005.

[137] Cheol Seong Hwang. Thickness-dependent dielectric constants of (ba,sr)tio[sub 3] thin films with pt or conducting oxide electrodes. *Journal of Applied Physics*, 92(1):432–437, 2002.

[138] R. Plonka, R. Dittmann, N. A. Pertsev, E. Vasco, and R. Waser. Impact of the top-electrode material on the permittivity of single-crystalline ba[sub 0.7]sr[sub 0.3]tio[sub 3] thin films. *App. Phys. Lett.*, 86(20):202908, 2005.

[139] Massimiliano Stengel, David Vanderbilt, and Nicola A. Spaldin. First-principles modeling of ferroelectric capacitors via constrained displacement field calculations. *Phys. Rev. B*, 80:224110, 2009.

[140] D. J. Kim, J. Y. Jo, Y. S. Kim, Y. J. Chang, J. S. Lee, Jong-Gul Yoon, T. K. Song, and T. W. Noh. Polarization relaxation induced by a depolarization field in ultrathin ferroelectric $batio_3$ capacitors. *Phys. Rev. Lett.*, 95:237602, 2005.

[141] Eric Bousquet, Nicola A. Spaldin, and Philippe Ghosez. Strain-induced ferroelectricity in simple rocksalt binary oxides. *Phys. Rev. Lett.*, 104:037601, 2010.

[142] Gerald D. Manhan. *Many-Particle Physics.* Kluwer Academic/Plenum Publishers, 2000.

[143] G. Kotliar, S. Y. Savrasov, K. Haule, V. S. Oudovenko, O. Parcollet, and C. A. Marianetti. Electronic structure calculations with dynamical mean-field theory. *Rev. Mod. Phys.*, 78:865–951, 2006.

[144] Axel D. Becke. A new mixing of hartree–fock and local density-functional theories. *The Journal of Chemical Physics*, 98(2):1372–1377, 1993.

[145] John David Jackson. *Classical Electrodynamics*. Wiley, 1999.

[146] Massimiliano Stengel, Pablo Aguado-Puente, Nicola A. Spaldin, and Javier Junquera. Band alignment at metal/ferroelectric interfaces: Insights and artifacts from first principles. *Phys. Rev. B*, 83:235112, Jun 2011.

[147] J. W. Reiner, F. J. Walker, R. A. McKee, C. A. Billman, J. Junquera, K. M. Rabe, and C. H. Ahn. Ferroelectric stability of batio3 in a crystalline oxide on semiconductor structure. *physica status solidi (b)*, 241(10):2287–2290, 2004.